NAVAL POSTGRADUATE SCHOOL

MONTEREY, CALIFORNIA

DISSERTATION

DIAPYCNAL TRANSPORT AND PATTERN FORMATION IN DOUBLE-DIFFUSIVE CONVECTION

by

Erick L. Edwards

December 2015

Dissertation Supervisor   Timour Radko

THIS PAGE INTENTIONALLY LEFT BLANK

REPORT DOCUMENTATION PAGE		*Form Approved OMB No. 0704–0188*

Public reporting burden for this collection of information is estimated to average 1 hour per response, including the time for reviewing instruction, searching existing data sources, gathering and maintaining the data needed, and completing and reviewing the collection of information. Send comments regarding this burden estimate or any other aspect of this collection of information, including suggestions for reducing this burden, to Washington headquarters Services, Directorate for Information Operations and Reports, 1215 Jefferson Davis Highway, Suite 1204, Arlington, VA 22202-4302, and to the Office of Management and Budget, Paperwork Reduction Project (0704-0188) Washington, DC 20503.

1. AGENCY USE ONLY *(Leave blank)*	2. REPORT DATE December 2015	3. REPORT TYPE AND DATES COVERED Dissertation	
4. TITLE AND SUBTITLE DIAPYCNAL TRANSPORT AND PATTERN FORMATION IN DOUBLE-DIFFUSIVE CONVECTION		5. FUNDING NUMBERS	
6. AUTHOR(S) Erick L. Edwards			
7. PERFORMING ORGANIZATION NAME(S) AND ADDRESS(ES) Naval Postgraduate School Monterey, CA 93943-5000		8. PERFORMING ORGANIZATION REPORT NUMBER	
9. SPONSORING /MONITORING AGENCY NAME(S) AND ADDRESS(ES) N/A		10. SPONSORING/ MONITORING AGENCY REPORT NUMBER	

11. SUPPLEMENTARY NOTES The views expressed in this dissertation are those of the author and do not reflect the official policy or position of the Department of Defense or the U.S. Government. IRB Protocol number ____N/A____.

12a. DISTRIBUTION / AVAILABILITY STATEMENT Approved for public release; distribution is unlimited	12b. DISTRIBUTION CODE

13. ABSTRACT (maximum 200 words)

This work analyzes the role of double-diffusive convection in constraining diapycnal velocity in the mid-latitude thermocline and in the initiation and maintenance of the deep convection associated with polynya and sea ice thinning events. Previously, no comprehensive high-resolution modeling studies of the possible role of double-diffusion in these areas have been conducted. A series of simulations using a numerical, multi-scale, MPI-based general circulation model is presented to remedy this dearth of knowledge. The effects of turbulent-dominated and purely double-diffusive regimes are compared to dual turbulent/double-diffusive systems and results are used to assess the likely roles of double-diffusion in constraining diapycnal velocity and delaying convection onset in high-latitude regions of marginal water column stability. High-resolution numerical modeling indicates that when both double-diffusion and turbulence are present, the constraints on diapycnal velocity loosen (tighten) with the increase of the fraction of the overall mixing attributed to turbulence (double-diffusion). The results of this study also indicate that double-diffusion could play an important role in delaying the onset of deep convection in the vicinity of Maud Rise in the eastern Weddell Sea, and may contribute to polynya formation and the persistence of interannual sea ice thinning.

14. SUBJECT TERMS double-diffusion, diffusive convection, salt fingering, diffusive flux, diapycnal velocity, Weddell Sea polynya			15. NUMBER OF PAGES 215
			16. PRICE CODE
17. SECURITY CLASSIFICATION OF REPORT Unclassified	18. SECURITY CLASSIFICATION OF THIS PAGE Unclassified	19. SECURITY CLASSIFICATION OF ABSTRACT Unclassified	20. LIMITATION OF ABSTRACT UU

THIS PAGE INTENTIONALLY LEFT BLANK

DIAPYCNAL TRANSPORT AND PATTERN FORMATION IN DOUBLE-DIFFUSIVE CONVECTION

Erick L. Edwards
Lieutenant Commander, United States Navy
B.S., United States Naval Academy, 1998
M.S., Naval Postgraduate School, 2008

Submitted in partial fulfillment of the
requirements for the degree of

DOCTOR OF PHILOSOPHY IN PHYSICAL OCEANOGRAPHY

from the

NAVAL POSTGRADUATE SCHOOL
December 2015

Author: Erick L. Edwards

Approved by: Timour Radko
               Professor of Oceanography
               Dissertation Supervisor / Dissertation Committee Chair

               Timothy Stanton   William Shaw
               Professor of Oceanography   Professor of Oceanography

               Francis Giraldo   John Colosi
               Professor of Mathematics   Professor of Oceanography

Approved by: Peter Chu, Chair, Department of Oceanography

Approved by: Douglas Moses, Vice Provost for Academic Affairs

iii

THIS PAGE INTENTIONALLY LEFT BLANK

ABSTRACT

This work analyzes the role of double-diffusive convection in constraining diapycnal velocity in the mid-latitude thermocline and in the initiation and maintenance of the deep convection associated with polynya and sea ice thinning events. Previously, no comprehensive high-resolution modeling studies of the possible role of double-diffusion in these areas have been conducted. A series of simulations using a numerical, multi-scale, MPI-based general circulation model is presented to remedy this dearth of knowledge. The effects of turbulent-dominated and purely double-diffusive regimes are compared to dual turbulent/double-diffusive systems, and results are used to assess the likely roles of double-diffusion in constraining diapycnal velocity and delaying convection onset in high-latitude regions of marginal water column stability. High-resolution numerical modeling indicates that when both double-diffusion and turbulence are present, the constraints on diapycnal velocity loosen (tighten) with the increase of the fraction of the overall mixing attributed to turbulence (double-diffusion). The results of this study also indicate that double-diffusion could play an important role in delaying the onset of deep convection in the vicinity of Maud Rise in the eastern Weddell Sea, and may contribute to polynya formation and the persistence of interannual sea ice thinning.

THIS PAGE INTENTIONALLY LEFT BLANK

TABLE OF CONTENTS

LIST OF FIGURES

x

THIS PAGE INTENTIONALLY LEFT BLANK

LIST OF TABLES

THIS PAGE INTENTIONALLY LEFT BLANK

LIST OF ACRONYMS, ABBREVIATIONS, AND SPECIAL TERMS

DNS	direct numerical simulation
GCM	general circulation model
KPP	K-profile parameterization scheme
MITgcm	Massachusetts Institute of Technology general circulation model
MOC	meridional overturning circulation
NPS	Naval Postgraduate School
ODE	ordinary differential equation
psu	practical salinity units
R_ρ	density ratio for salt fingering $\left(\text{i.e.,} \dfrac{\alpha\, \partial T/\partial z}{\beta\, \partial S/\partial z} \right)$
R_ρ^*	density ratio for diffusive convection $\left(\dfrac{\beta\, \partial S/\partial z}{\alpha\, \partial T/\partial z} \right)$
Tu	Turner angle
WP	Weddell Sea polynya
γ	Flux ratio $\left(\dfrac{\alpha F_T}{\beta F_S} \text{ and } \dfrac{\alpha K_T\, \partial T/\partial z}{\beta K_S\, \partial S/\partial z} \right)$ for salt fingering
γ^*	Flux ratio $\left(\dfrac{\beta F_S}{\alpha F_T} \text{ and } \dfrac{\beta K_S\, \partial S/\partial z}{\alpha K_T\, \partial T/\partial z} \right)$ for diffusive convection
θ	Potential temperature (*theta*)

THIS PAGE INTENTIONALLY LEFT BLANK

ACKNOWLEDGMENTS

Patience!

I would like to thank everyone for their incredible, near super-human patience with me over the last three years as I completed this most important milestone of my academic and professional career. The best way to eat an elephant is one bite at a time and I've been steadily chewing since before September of 2012 to finish. In a (sort of) chronological order, I'd like to express my sincerest gratitude to:

Mr. Clarence White, fellow Virginian and shipmate, for helping me with the initial, vitally important administrative matters that allowed me to apply to the doctoral program in the first place.

CAPT Sam Howard, USN (Ret.), former USS BATAAN CO, for his recommendation, which I know was a key factor in my selection to the Navy's Ph.D. program.

CAPT Bill Nisley, USN, whose endorsement was really a highly supportive recommendation, and again, a key factor in allowing me to break out among a group of highly qualified applicants.

Mr. and Professor Gera for helping my family find a house in the area and for hosting my wife, Julia, and infant son, Evan, for a month until I could make it out to Monterey with the rest of the family.

All of my professors (most of the Physical Oceanography department) during the initial qualification process for teaching me what I needed to know (again).

Ms. Marla Stone and Mr. Tarry Rago for being great "office neighbors" when I used to be downstairs and for their continued support even after I moved upstairs.

Ms. Susan Valeriano for helping me with the little things that made life in Spanagel easier.

My academic committee, as a group, for their enduring patience with me from proposal to final draft.

Professor John Colosi and Professor Frank Giraldo for their time, support, kind words, and insightful input.

Professor Bill Shaw for his extensive guidance during the initial stages of the project and his even more extensive, candid, and extremely constructive criticism during the final stages.

Professor Tim Stanton for his unwavering patience, sustained belief in me, wise counsel, and continued enthusiasm and sympathy in the face of severe (and admittedly, sometimes self-inflicted) modeling difficulties. I look forward to our continuing collaboration on all sorts of sea ice modeling; I've simply invested too much time learning how to do it to quit now.

Professor Timour Radko for everything. In *Nicomachean Ethics*, Aristotle advances the idea of virtue as the mean between the extreme states of excess and deficiency. In light of this definition, you are, indeed, a virtuous mentor. Your advice and encouragement, enthusiasm and direction shaped me profoundly even as you gave me the space to learn and develop my own skills and confidence as a researcher. Thank you for always believing that I was vastly more capable than I thought myself to be. You are a true friend.

All of my friends and family, too numerous to name individually, for all of their support of me and the rest of my family during the entire process.

My sons, Lucian, Cezar, and Evan, for keeping things interesting at home.

Finally, they say that behind every successful man is a surprised mother-in-law, so I would like to thank Teodora and my father-in-law, Valeriu, for bringing my beautiful wife, Julia, into this world. It was Julia's patience that was most tested during this entire process. A separate dissertation could not recount all of Julia's hard work and daily sacrifices that made this present work possible. Her loving support, forbearance, and wholehearted commitment to my success make this dissertation just as much hers as mine.

I. INTRODUCTION

A. DOUBLE-DIFFUSIVE CONVECTION

Seawater density is determined by its temperature, its salinity, and the pressure it experiences. The diffusivity rates of two of these determinants, heat and salt, differ by two orders of magnitude leading to many interesting phenomena. Chief among these is double-diffusive convection. Double-diffusive convection is a mixing process that occurs when a liquid contains two components that diffuse at different rates. When seawater density increases with depth, the water column is statically stable. However, because heat and salt diffuse at different rates in seawater, a column of water can be unstable even if density increases with depth. In the ocean, this form of instability occurs in two different ways. The first regime is found in tropical and subtropical waters when both temperature and salinity decrease with depth. In this case, warm and salty water overlies cold and fresh water, and a phenomenon known as salt fingering is observed. In high latitude portions of the world ocean, however, a second type of double-diffusion is realized. Colder, fresher water lies above relatively warmer and saltier water in these regions. This condition leads to diffusive layering, which is a form of vertical stratification marked by well-mixed layers separated by thin interfaces with strong vertical gradients of temperature and salinity.

But what is double-diffusive convection? How is heat transported across a diffusive layer interface? Why does the difference in diffusivity matter? And why is double-diffusion important?

Double-diffusive convection is a form of fluid mixing that can occur when there are gradients of two (or more) density-determining properties with different molecular diffusivities (Turner 1973). Because two of the components that determine the density of seawater, heat and salinity, have such a large difference in their molecular diffusivities, much of the World Ocean is susceptible to double-diffusion (You 2002). Specifically, double-diffusion occurs in the ocean wherever the vertical gradients of heat and salinity have the same sign (either both positive or both negative) and seawater density increases

1

with depth. The mechanisms governing heat transport are illustrated in Figure 1.1 for salt fingering and in Figure 1.2 for diffusive convection.

In the low and mid-latitude portions of the World Ocean, evaporation and surface heating commonly produce a warm, salty upper layer with a relatively cooler, fresher layer beneath, as illustrated in the first panel of Figure 1.1. This fluid is stably stratified, has a stable thermal gradient, but an unstable salinity gradient (1). Some disturbance displaces a parcel from the upper layer to the lower layer. Because the diffusivity of heat is 100 times faster than that of salt, the parcel loses heat much faster than it loses salt (2). The parcel, now having the same temperature as the lower layer but with a higher salinity, is denser than its surroundings (3). The parcel sinks further into the lower layer forming a finger-like structure that is denser than the surrounding fluid. This is known as a salt finger.

Now consider Figure 1.2, illustrating the dynamics of diffusive layering. In this case, the fluid is stably stratified despite an unstable thermal gradient. Due to some disturbance, a parcel of warm, salty water is displaced upward across the interface into the cooler, fresher layer (1). The parcel is warmer and saltier than its surroundings and diffuses its heat and salt content into the upper layer (2). Because the diffusivity of heat is 100 times faster than that of salt, the parcel loses heat much faster than it loses salt. The parcel, now having the same temperature as the upper layer but with a higher salinity, is now denser (3). It sinks, crossing the interface again. Heat diffuses into the parcel (now cooler than its surroundings) in the lower layer (4), and the cycle can repeat with a gradually amplifying amplitude.

In these two ways, double-diffusive mixing increases the density of the denser layers while decreasing the density of the lighter layers, both processes occurring due to the large disparity in the order of magnitudes between the heat and salt diffusivities (Radko 2013). Although a small-scale phenomenon, double-diffusive convection may significantly affect global circulation patterns and world climate due (i) to its ability to transport heat and salt and (ii) due to its tendency to constrain diapycnal volume transport. The latter property has been largely overlooked by extant studies and will be explored in the current work.

The significance of double-diffusive convection is manifold. Double-diffusion could exert a tremendous influence on the climate, given its role in meridional overturning circulation (MOC) and high latitude convection in regions of deepwater formation. Furthermore, double-diffusion affects the undersea warfare area of military operations. Double-diffusive processes can produce patterns that have a profound effect on acoustic detection of subsurface contacts. Surface signatures derived from undersea platforms traveling through the homogeneous vertical layers produced by double-diffusion could be exploited as a form of hydrodynamically based detection as well. Finally, the formulation of oceanographic models requires the inclusion of double-diffusion if observed heat and salt fluxes are to be properly represented in forecasts.

B.   INVESTIGATING DOUBLE-DIFFUSIVE CONVECTION

Conditions favorable for double-diffusive convection occur over much of the subtropical and high-latitude portions of the World Ocean (Radko 2013, Batteen 2015) giving oceanographers a wide variety of locations to study double-diffusion. For example, some estimates place the areal extent of conditions favorable for the formation of salt fingers at 90% in the Atlantic (Knauss 1997) and You (2002) estimates that conditions conducive to double-diffusion occur in almost 50% of the Earth's ocean volume. The widespread nature of this phenomenon demands that its contribution to overall vertical mixing processes be fully investigated to understand potential impacts on motions across a spectrum of scales, from meridional overturning circulation and deep convection to diapycnal transport.

Specifically, this work analyzes the role of double-diffusive convection in constraining diapycnal velocity in the mid-latitude thermocline and in the initiation and maintenance of the deep convection associated with polynya and sea ice thinning events in high latitude regions. Previously, no comprehensive high-resolution modeling studies of the possible role of double-diffusion in these areas have been conducted. A series of simulations using a numerical, multi-scale, MPI-based general circulation model is presented here. The effects of turbulent-dominated and purely double-diffusive regimes are compared to dual turbulent/double-diffusive systems and these results are used to

assess the likely roles of double-diffusion in constraining diapycnal velocity and delaying convection onset in high-latitude regions of marginal water column stability.

Chapter II details the first investigation into the constraints on diapycnal velocity in the thermocline of a subtropical gyre where salt fingering is prevalent, with results indicating that double-diffusion severely limits the magnitude of cross-isopycnal transport. The role of double-diffusion in the onset and maintenance of deep convection during sea ice thinning and polynya formation events is presented in Chapter 0. Double-diffusion is found to be a significant contributor to the persistence of interannual thinning of sea ice in the vicinity of Maud Rise and may even be responsible for the initiation of polynya events in the presence of a preconditioned water column. A summary of this work concludes both investigations in Chapter IV.

II. CONSTRAINTS ON DIAPYCNAL VELOCITY IN THE DOUBLE-DIFFUSIVE THERMOCLINE

A. INTRODUCTION

An ongoing challenge in the further development of the theory of thermohaline circulation is associated with the role of diapycnal mixing in the establishment and maintenance of the meridional overturning circulation (MOC). Early classical views (Robinson and Stommel 1959, Munk 1966) consider the main governing process of the MOC to be a vertical advective-diffusive balance in the ocean interior. Other studies (Welander 1986 and Whitehead 1995) support this conception. A number of studies, however, have challenged this classical theory and advocate an alternative adiabatic view of meridional overturning, the view that emphasizes the importance of isopycnal advection and wind forcing (Toggwieler and Samuels 1998, Gnanadesikan 1999, Radko 2007b, Radko and Kamenkovich 2011). Attempts have been made to combine the classical and mixing-driven views into a unified framework (Salmon 1990, Samelson and Vallis 1997). These newer theories advance a two-thermocline ocean model: an upper thermocline subject to isopycnal advection and wind-driven forcing over a lower thermocline where the classical vertical advective-diffusive balance dominates. Numerical simulations (e.g., Hallberg and Gnanadesikan 2006) indicate that the adiabatic effects may indeed be essential in controlling the pattern and strength of the MOC. However, the diabatic mode, driven by diapycnal fluxes, is quite substantial. Radko et al. (2008), for instance, estimate that the diabatic mode of circulation accounts for approximately one third of the inter-hemispheric water mass transport in the global ocean.

While diabatic mixing is an important process in maintaining the diapycnal overturning mode, a continuing question concerns whether this mixing takes on a passive role in influencing the pattern and strength of the MOC, or whether this form mixing plays a more active role. This same question was posed in Radko et al. (2008) and they found that the MOC was largely influenced by adiabatic processes. But the answer could also depend on the particular type of mixing as well. When diapycnal diffusion is

dominated by mechanically generated turbulence, which tends to mix the temperature and salinity at the same rate, then diapycnal transport is not actively constrained by mixing. Generally, it is possible to construct consistent steady-state solutions for mid-latitude circulation for a wide range of diapycnal velocities.

However, the dynamics of diapycnal transport can change dramatically when the dominant mixing agent is double-diffusion. Unlike mechanically generated turbulence, double-diffusion is characterized by unequal eddy diffusivities of heat and salt, which depend on the background density ratio (R_ρ). In an attempt to identify the key differences in the way double-diffusion and turbulence control diapycnal velocity, a series of large-scale numerical simulations were performed. The vertical mixing of heat and salt in these models is parameterized as a function of the corresponding large-scale gradients (Fick's diffusion model):

$$\begin{cases} F_T = -K_T \dfrac{\partial T}{\partial z} \\ F_S = -K_S \dfrac{\partial S}{\partial z} \end{cases} \tag{2.1}$$

These simulations reveal that for comparable values of mixing coefficients (K_T, K_S), the average diapycnal velocity (w^*) in double-diffusive experiments is less, by at least an order of magnitude, than w^* in the corresponding turbulent systems.

In order to rationalize this theory of double-diffusive insulation, three arguments are proposed. The first argument applies to the strongly diabatic regime representative of the lower (diffusive) thermocline that is often described by Munk's (1966) vertical advection-diffusion balance. Numerical solutions indicate that steady one-dimensional solutions in double-diffusive systems are possible only for a very narrow range of diapycnal velocities. The second argument extends the first through an analysis of diapycnal velocity in a double-diffusive regime with a variable, rather than constant, flux ratio. Solutions indicate that diapycnal velocities remain constrained by double-diffusion and the range of diapycnal velocity magnitudes is found to be proportional to the variation in the flux ratio.

The third argument is more relevant for the central thermocline, where double-diffusive processes are most common. Dynamics of the main thermocline are fundamentally three-dimensional (Luyten et al. 1983); the overall water-mass distribution is set by large-scale advection whereas diapycnal mixing is relatively weak. Nevertheless, in this regime it is still possible to predict the impact of higher order diabatic processes on cross-isopycnal transfer using the technique originally developed by Rhines and Young (1982). The crux of this approach is the integration of governing equations along closed streamlines, which effectively eliminates the zero order advective terms in integral balances. Adapting this procedure to the double-diffusive problem makes it possible to evaluate the average diapycnal velocity in regions bounded by closed streamlines and, ultimately, to explain the insulation effect from first principles. Thus, for both advectively dominated and diffusively dominated regimes, there are theoretical reasons to expect the suppression of diapycnal volume flux by double-diffusion.

This chapter is organized as follows. An analysis of a one-dimensional vertical advective-diffusive balance of temperature and salinity of Munk's (1966) type is covered in Section B. This analysis, albeit highly idealized, suggests that fundamental differences may exist in the way turbulent and double-diffusive mixing affect diapycnal volume transport. In Section C, solutions for a model of double-diffusion with a weak variation in flux ratio is explored. These solutions show that double-diffusion could severely constrain diapycnal velocities, even when the constant flux ratio assumption is relaxed. Motivated by these possibilities, a series of large-scale three-dimensional multi-century numerical simulations are detailed in Section D, which also consistently reflect the tendency of double-diffusion to constrain diapycnal volume transport. In Section E, an analytical model of the double-diffusive insulation in a three-dimensional setting is developed. Summary and conclusions follow in Section F.

B. ANALYSIS OF A ONE-DIMENSIONAL VERTICAL ADVECTIVE-DIFFUSIVE BALANCE OF TEMPERATURE AND SALINITY

Consider a one-dimensional model consisting of the steady state temperature and salinity equations:

$$\begin{cases} w\dfrac{\partial T}{\partial z} = -\dfrac{\partial F_T}{\partial z} \\[4mm] w\dfrac{\partial S}{\partial z} = -\dfrac{\partial F_S}{\partial z}, \end{cases} \tag{2.2}$$

where $T(z)$ and $S(z)$ are the large-scale temperature and salinity of the sea-water; w is the upward vertical velocity. The temperature and salinity fluxes (F_T, F_S) are attributed to small-scale mixing processes and related to large-scale gradients through (2.1). We are interested in solving (2.2) for the given boundary conditions:

$$\begin{cases} (T,S) = \left(T_{top}, S_{top}\right) & \text{at } z = -H_{top} = -H_{bot} + H \\[2mm] (T,S) = \left(T_{bot}, S_{bot}\right) & \text{at } z = -H_{bot}, \end{cases} \tag{2.3}$$

where $z = -H_{top}$ ($z = -H_{bot}$) represents the top (bottom) of the mixing zone and H is its thickness (see the schematic in Figure 2.1). Differences in the possible solutions of (2.2) and (2.3) for the cases in which vertical mixing is controlled by: *a*) mechanical turbulence, *b*) double-diffusion, and *c*) a combination thereof provide the original motivation of the inquiry into the link between double-diffusive mixing and associated diapycnal volume transport.

1.   Turbulent Mixing

To illustrate the basic properties of system (2.2), consider first the simplest model of turbulent mixing characterized by constant and equal eddy diffusivities of heat and salt:

$$K_T = K_S = K^{turb}. \tag{2.4}$$

In this case, (2.2) and (2.3) can be solved for any value of diapycnal velocity (w):

$$\begin{cases} T = (T_{top} - T_{bot})\dfrac{\exp(w(z - z_{bot})/K^{turb}) - 1}{\exp(wH/K^{turb}) - 1} + T_{bot} \\[5mm] S = (S_{top} - S_{bot})\dfrac{\exp(w(z - z_{bot})/K^{turb}) - 1}{\exp(wH/K^{turb}) - 1} + S_{bot} \end{cases} \quad \text{for } w \neq 0, \tag{2.5}$$

and

8

$$\begin{cases} T = (T_{top} - T_{bot})(z - z_{bot})/H + T_{bot} \\ S = (S_{top} - S_{bot})(z - z_{bot})/H + S_{bot} \end{cases} \quad \text{for} \quad w = 0. \quad (2.6)$$

Thus, the turbulent mixing model (2.4) represents an extreme case of a completely passive system that offers no restrictions on diapycnal velocity. For any value of w it is possible to construct a consistent solution of the T-S advection-diffusion equations satisfying the boundary conditions at $z = z_{bot}$ and $z = z_{top}$. In order to demonstrate that this feature does not necessarily apply to other types of mixing, we now turn to a very different configuration that demands a unique value of w—the constant flux ratio model of double-diffusion.

2. Double-Diffusion: The Constant Flux Ratio Model

Double-diffusion occurs in the ocean in locations where the vertical gradients of temperature and salinity both have the same sign and density increases with depth. Two distinct forms of double-diffusion are possible, salt fingering and diffusive convection. The salt fingering regime is realized when the gradients of temperature and salinity are both positive, with warmer, saltier water near the surface becoming both cooler and fresher with depth. This condition is commonly found in the subtropical thermocline. Diffusive convection occurs when the gradients of temperature and salinity are both negative, with warmer, saltier water being found at depth over cooler, fresher water. Conditions favorable to diffusive convection are typical in high-latitude oceans. The following analysis is relevant to both forms of double-diffusion, but to be specific, the discussion will be focused on the example of the salt finger regime.

The single most important indicator of the nature of diapycnal mixing in regions dominated by double-diffusion is the local density ratio (Radko and Stern 2011)

$$R_\rho = \frac{\alpha T_z}{\beta S_z}, \quad (2.7)$$

where α and β are the expansion/contraction coefficients in the linear equation of state—see the discussion in Schmitt (1994, 2003) and Radko (2013). The magnitude of

double-diffusive transport is therefore frequently parameterized by formulating the eddy diffusivities of heat and salt (K_T, K_S) as functions of R_ρ (Radko and Stern 2011). The flux ratio (γ) is the ratio of thermal and haline density fluxes and is another indicator of double-diffusive activity. Although less justified, a commonly used approximation sets γ to a constant value:

$$\frac{\alpha F_T}{\beta F_S} = \gamma_0 = const . \tag{2.8}$$

Radko and Stern (2011) call attention to particular examples of constant flux ratio parameterizations that can be found in works by Schmitt (1981), Zhang et al. (1998), and Merryfield et al. (1999).

For our formulation, we begin with (2.2) and perform the following operations

$$\begin{cases} \alpha\left(w\dfrac{\partial T}{\partial z} = -\dfrac{\partial F_T}{\partial z}\right) \\ -\beta\gamma_0\left(w\dfrac{\partial S}{\partial z} = -\dfrac{\partial F_S}{\partial z}\right) \end{cases} \text{ substituting } \quad F_S = \frac{\alpha F_T}{\beta\gamma_0}. \tag{2.2a}$$

Combining (2.2) with (2.7) and (2.8) to arrive at:

$$w\left(\frac{R_\rho}{\gamma_0} - 1\right) = 0 . \tag{2.9}$$

To maintain salt fingering convection, the loss of potential energy stored in salt stratification should exceed the energy gain by heat stratification and therefore $\gamma_0 < 1$. The density ratio, on the other hand, has to exceed unity in order for density to decrease upward. Hence, $\dfrac{R_\rho}{\gamma_0} > 1$ and therefore (2.9) can be satisfied only if $w = 0$. Thus, in contrast with the turbulent mixing model, the double-diffusive system actively controls diapycnal velocity.

3.   The Combined Effects of Double-Diffusion and Turbulence

Because small-scale mixing in the ocean is controlled by a combination of double-diffusion and mechanically generated turbulence, it is of interest to examine the constraints on diapycnal velocity in a model that includes both mixing processes. For that, the foregoing analyses are extended by considering the following closure:

$$K_T = K_T^{dd}(R_\rho) + K^{turb}, \quad K_S = K_S^{dd}(R_\rho) + K^{turb}, \quad \frac{\alpha K_T^{dd} T_z}{\beta K_S^{dd} S_z} = \gamma, \qquad (2.10)$$

which assumes equal and uniform diffusivities of heat and salt due to turbulence (K^{turb}). There have been at least two attempts to evaluate the flux ratio based on oceanographic field measurements (Schmitt et al. 1987, Schmitt et al. 2005). Both estimates were mutually consistent, suggesting a flux ratio of

$$\gamma \approx 0.85. \qquad (2.11)$$

The individual values of salt finger fluxes, and in particular the pattern of their variation with R_ρ, are more difficult to infer from observations. Therefore, the parameterization proposed by Radko and Smith (2012) on the basis of high-resolution DNS is adopted:

$$\begin{cases} K_S = k_T \left[\dfrac{a_S}{\sqrt{R_\rho - 1}} + b_S \right] R_\rho & \text{for} \quad 1 < R_\rho < R_{cutoff} \\ K_S = 0 & \text{for} \quad R_\rho > R_{cutoff} \end{cases} \qquad (2.12)$$

where $(a_S, b_S, R_{cutoff}) = (135.7, -62.75, 5.67)$ and

$$K_T = \frac{\gamma K_S}{R_\rho}. \qquad (2.13)$$

Assume parameter values representative of mid-latitude thermocline:

$$\Delta T \equiv T_{top} - T_{bot} = 10^{\circ}C, \ R_0 = 2, \ \Delta S \equiv S_{top} - S_{bot} = \frac{\alpha \Delta T}{\beta R_0} = 1.3 psu, \ H = 1000m, \qquad (2.14)$$

11

where $R_0 = \dfrac{\alpha \Delta T}{\beta \Delta S}$. Next, we systematically vary K^{turb} in an attempt to determine how it affects the range of diapycnal velocities.

The system (2.2), (2.11)-(2.14) was coded in the Maple software package and solutions were sought using the numerical ODE solver for a range of (w, K^{turb}). The results are shown in Figure 2.2. Calculations resulting in regular solutions are indicated by the heavy dots while light dots represent conditions under which no solutions were found. Figure 2.2 indicates that the constraints on diapycnal velocity loosen (tighten) with the increase (decrease) in $K^{turb}/K_T^{dd}(R_0)$—a quantity measuring the relative contributions from turbulence and double-diffusion to net mixing.

Despite considerable uncertainties in the estimated magnitudes of double-diffusive and turbulent mixing, it is plausible that in the central thermocline of the Atlantic Ocean their diffusivities are comparable (e.g., St. Laurent and Schmitt 1999). For $K^{turb}/K_T^{dd}(R_0) \sim 1$ the following constraint on the (dimensional) diapycnal velocity is obtained:

$$\max |w| \sim 10^{-7} ms^{-1} \sim 3m/year , \tag{2.15}$$

which is similar to the data-based estimates of the diapycnal velocity in regions susceptible to both double-diffusive and turbulent mixing (St. Laurent and Schmitt 1999).

In summary, the foregoing calculations indicate that *a)* in the turbulent model, the assumed vertical T-S balances do not impose any internal constraints on diapycnal transport, *b)* in the double-diffusive model the diapycnal transport is zero, and *c)* the hybrid model, which takes into account both double-diffusion and turbulence, allows only a finite range of diapycnal velocities. Of course, the selection of a unique w in the purely double-diffusive model could be a consequence of the chosen flux laws; of particular concern is the constant flux ratio approximation. To address this concern, the next section presents a variable flux ratio model to explore the effect of double-diffusion on the range of diapycnal velocities.

C. ASYMPTOTIC SOLUTIONS FOR A DOUBLE-DIFFUSIVE MODEL WITH WEAK VARIATION IN THE FLUX RATIO

The one-dimensional advection-diffusion equations (2.2) are non-dimensionalized using H as the unit of length and k_T/H as the unit of velocity. The expansion/contraction coefficients of the linear equation of state (α, β) are incorporated in (T, S), and $\alpha(T_{top} - T_{bot})$ is used as the scale for both temperature and salinity. This non-dimensionalization is similar to those found in previous works by Radko (2003, 2005, and others) and is implemented as follows:

$$\begin{cases} z \rightarrow zH - H_{bot} \\ w \rightarrow \dfrac{K_0}{H} w \\ T \rightarrow \left(T_{top} - T_{bot}\right)T + T_{bot} \\ S \rightarrow \dfrac{\alpha}{\beta}\left(T_{top} - T_{bot}\right)S + S_{bot} \end{cases} \tag{2.16}$$

The governing equations (2.2) and boundary conditions (2.3) in non-dimensional units reduce to:

$$\begin{cases} w\dfrac{\partial T}{\partial z} = \dfrac{\partial}{\partial z}\left(\dfrac{K_T}{k_T}\dfrac{\partial T}{\partial z}\right) \\ w\dfrac{\partial S}{\partial z} = \dfrac{\partial}{\partial z}\left(\dfrac{K_S}{k_S}\dfrac{\partial S}{\partial z}\right) \end{cases} \quad \text{and} \quad \begin{cases} (T,S) = \left(1, R_0^{-1}\right) & \text{at } z = 1 \\ (T,S) = (0,0) & \text{at } z = 0. \end{cases} \tag{2.17}$$

The purpose of the following theory is to examine solutions of (2.17) in the regime where the heat/salt buoyancy flux ratio γ is nearly uniform. The value of the flux ratio is constrained by the requirement that the heat contribution to density flux must be less than that of the salinity flux. Therefore, the flux ratio must be less than one. This energy requirement, viz. that the loss of potential energy by salt must exceed the energy gain of the heat component through thermal stratification, makes flux ratio one of the most stable characteristics in locations with active salt fingering (Radko 2005). If double-diffusive fluxes are determined by local gradients, then the flux ratio can be formulated as a function of the local density ratio: $\gamma = \gamma(R_\rho)$ (cf., Radko 2003). The variation in the

13

flux ratio is fairly gentle, which makes it tempting to approximate γ by a constant in theoretical models (Schmitt 1981, Stern et al. 2001). However, this approximation, while simplifying the analytical development, also filters out some key processes affecting the dynamics of double-diffusive fluids (e.g., Walsh and Ruddick 2000, Radko 2003, 2005).

1.   General Solutions

In order to extend the double-diffusive constant flux ratio model in Section B, we consider the case when the variation in flux ratio is small but non-zero:

$$\gamma = \gamma_0 + \varepsilon^2 \gamma_1(R_\rho),\qquad(2.18)$$

where $\varepsilon \ll 1$. As is common in weakly nonlinear models (e.g., Malkus and Veronis 1958), we search for a solution of the governing equations (2.17) using the power series in ε:

$$\begin{cases} T = T_0(z) + \varepsilon T_1(z) + \varepsilon^2 T_2(z) + ... \\ S = S_0(z) + \varepsilon S_1(z) + \varepsilon^2 S_2(z) + ... \\ w = w_0 + \varepsilon w_1 + \varepsilon^2 w_2 + ... \end{cases}\qquad(2.19)$$

These power series are substituted into the governing equations (2.17) and the terms of the same order in ε are collected. At the zero order, we essentially arrive at the constant flux ratio model discussed in Section B, which requires zero diapycnal velocity. The zero order equations for $T_0(z)$ and $S_0(z)$ are satisfied by the linear gradients:

$$\begin{cases} T_0 = z \\ S_0 = R_0^{-1}z \\ w_0 = 0. \end{cases}\qquad(2.20)$$

The boundary conditions for the individual *T-S* components become:

$$T_i(0) = S_i(0) = T_i(1) = S_i(1) \quad \text{for} \quad i = 1, 2, \ ... \ .\qquad(2.21)$$

The first order equations are given by

14

$$\begin{cases} K'_S(R_0)\gamma_0\left(\dfrac{\partial^2 T_1}{\partial z^2} - R_0\dfrac{\partial^2 S_1}{\partial z^2}\right) + K_S(R_0)\gamma_0\dfrac{\partial^2 S_1}{\partial z^2} = w_1 \\[4mm] K'_S(R_0)\left(\dfrac{\partial^2 T_1}{\partial z^2} - R_0\dfrac{\partial^2 S_1}{\partial z^2}\right) + K_S(R_0)\dfrac{\partial^2 S_1}{\partial z^2} = \dfrac{w_1}{R_0} \end{cases} \tag{2.22}$$

Multiplying the second equation by γ_0 and subtracting from the first yields:

$$w_1 = 0, \tag{2.23}$$

and by integrating (2.22) twice in z, subject to (2.23) and the boundary conditions (2.21), we arrive at:

$$T_1 = \frac{K'_S(R_0)R_0 - K_S(R_0)}{K'_S(R_0)}S_1. \tag{2.24}$$

Using (2.23) and (2.24), we write down the second order equations:

$$\begin{cases} K'_S(R_0)\gamma_0\left(\dfrac{\partial^2 T_2}{\partial z^2} - R_0\dfrac{\partial^2 S_2}{\partial z^2}\right) + K_S(R_0)\gamma_0\dfrac{\partial^2 S_2}{\partial z^2} + \dfrac{\gamma_0 R_0 K''_S(R_0)K_S^2(R_0)}{K'^2_S(R_0)}\dfrac{\partial S_1}{\partial z}\dfrac{\partial^2 S_1}{\partial z^2} = w_2 \\[4mm] K'_S(R_0)\left(\dfrac{\partial^2 T_2}{\partial z^2} - R_0\dfrac{\partial^2 S_2}{\partial z^2}\right) + K_S(R_0)\dfrac{\partial^2 S_2}{\partial z^2} + \dfrac{R_0 K''_S(R_0)K_S^2(R_0)}{K'^2_S(R_0)}\dfrac{\partial S_1}{\partial z}\dfrac{\partial^2 S_1}{\partial z^2} = \dfrac{w_2}{R_0} \end{cases} \tag{2.25}$$

Multiplying the second equation in (2.25) by γ_0 and subtracting from the first yields:

$$w_2 = 0, \tag{2.26}$$

and the third order T-S equations are obtained in a similar manner. When the third order salinity equation is multiplied by γ_0 and subtracted from the third order temperature equation, we obtain:

$$K_S^2(R_0)\gamma'_1(R_0)\frac{\partial^2 S_1}{\partial z^2} = w_3 K'_S(R_0)(\gamma_0 - R_0), \tag{2.27}$$

which is solved for $S_1(z)$ using the boundary conditions (2.21):

$$S_1 = \frac{1}{2}\frac{w_3 K'_S(R_0)(\gamma_0 - R_0)z(z-1)}{K_S^2(R_0)\gamma'_1(R_0)R_0}. \tag{2.28}$$

15

Combining (2.28) with (2.24), we obtain an explicit expression for $T_1(z)$:

$$T_1 = \frac{1}{2} \frac{w_3 \left(K_S'(R_0)R_0 - K_S(R_0) \right)(\gamma_0 - R_0)z(z-1)}{K_S^2(R_0)\gamma_1'(R_0)R_0}. \qquad (2.29)$$

The expansion can be similarly extended to higher orders. The significance of the foregoing analysis lies in the suggestion that similarity solutions exist in the asymptotic sector

$$(T', S', w) \propto \left(\varepsilon, \varepsilon, \varepsilon^3 \right), \qquad (2.30)$$

where $(T', S') \propto (T, S) - (T_0, S_0)$.

2. Specific Solutions

To illustrate the structure of the asymptotic solution and examine its accuracy, we now consider specific patterns of $K_T(R_\rho)$ and $K_S(R_\rho)$ in (2.12) and (2.13). The flux ratio is taken as

$$\gamma(R_\rho) = \gamma_0 + \delta(R_\rho - 1), \qquad (2.31)$$

which conforms to the assumed asymptotic pattern (2.18) for $\varepsilon = \sqrt{|\delta|}$. The following explicit expressions are obtained for $R_0 = 2$, $\gamma_0 = 0.85$, and $(w_1, w_2, w_3, w_4, w_5, ...) = (0, 0, W, 0, 0, ...)$. In this case,

$$w = \varepsilon^3 W, \qquad (2.32)$$

and Eqs. (2.28), (2.29) reduce to:

$$\begin{cases} T_1 = 3.67 \cdot 10^{-3} W z(1-z) \\ S_1 = 8.48 \cdot 10^{-3} W z(1-z). \end{cases} \qquad (2.33)$$

Further extending the asymptotic expansion, we obtain the second order

$$\begin{cases} T_2 = 7.99 \cdot 10^{-6} W^2 z(z-1)(2z-1) \\ S_2 = 1.20 \cdot 10^{-6} W^2 z(z-1)(2z-1), \end{cases} \qquad (2.34)$$

16

and third order *T-S* components:

$$\begin{cases} T_3 = Wz(1-z)(8.19\cdot10^{-8}W^2z^2 - 8.19\cdot10^{-8}W^2z + 1.13\cdot10^{-8}W^2 + 2.40\cdot10^{-4}) \\ S_3 = Wz(1-z)(1.34\cdot10^{-8}W^2z^2 - 1.34\cdot10^{-8}W^2z + 2.59\cdot10^{-9}W^2 + 9.77\cdot10^{-4}). \end{cases} \quad (2.35)$$

To validate the foregoing asymptotic theory, the governing equations are also solved using the numerical ODE solver of the Maple software package. A meaningful comparison of the asymptotic and numerical solutions requires some information about relevant values of δ, which represents the variation in the flux ratio. The pattern of the flux ratio $\gamma = \gamma(R_\rho)$ has been studied analytically (Schmitt 1979a), numerically (Stern et al. 2001, Radko and Smith 2012), experimentally (Schmitt 1979b) and observationally (St. Laurent and Schmitt 1999). These studies are mutually consistent, suggesting that a reasonable choice of δ in the ocean would be $|\delta| \sim 0.1-0.2$. Therefore, Figure 2.3 presents the numerical and asymptotic solutions for $R_0 = 2$, $\delta = 0.1$ (corresponding to $\varepsilon = 0.32$) and $W = -500$ (corresponding to $w = -15.81$). The black curve represents the numerical solution for the (non-dimensional) departure of temperature profile from the uniform gradient $T'(z) = T(z) - z$. The blue, green, and red curves represent the power series in ε that are truncated at the first, second, and third order respectively. The analytical curves rapidly converge to the numerical solution with increasing order of the expansion. The third order asymptotic closely approximates the fully nonlinear solution even for the relatively large ε used for the calculation in Figure 2.3.

3.   Constraints on the Diapycnal Velocity

In addition to the parameters used in Figure 2.3, numerous other cases were examined, all of which indicate that the asymptotic series in ε are remarkably accurate in describing the steady solutions of the one-dimensional advection-diffusion equations (2.17) provided that such solutions exist. The question arises whether these series could be used to formulate simple explicit conditions for the existence of solutions.

If $|W| \leq O(1)$, then all coefficients of the power series in ε for *T* and *S* are of order one. Such series are generally characterized by a finite radius of convergence. This

implies that for $|W| \le O(1)$, solutions always exist as long as ε is sufficiently small. What happens when $|W| \gg 1$? In this case, the asymptotic series for temperature and salinity can be approximated by

$$\begin{cases} T = a_0 + (W\varepsilon)a_1 + (W\varepsilon)^2 a_2 + (W\varepsilon)^3 a_3 + ... \\ S = b_0 + (W\varepsilon)b_1 + (W\varepsilon)^2 b_2 + (W\varepsilon)^3 b_3 + ... \end{cases} \tag{2.36}$$

where the coefficients (a_i, b_i) are independent of W and ε. These power series for $(W\varepsilon)$ are also valid only within a finite radius of convergence. Thus, denoting the radius of convergence of the series in (2.36) by r_C, we can expect the existence of regular solutions for T and S for as long as

$$|W\varepsilon| < r_C . \tag{2.37}$$

When (2.37) is rewritten in terms of $w = \varepsilon^3 W$ and $|\delta| = \varepsilon^2$, we arrive at the explicit constraint on the diapycnal velocity:

$$|w| < |\delta| r_C . \tag{2.38}$$

This result is highly suggestive—(2.38) implies that the range of diapycnal velocities is proportional to the effective variation in the flux ratio. To systematically test this prediction, a series of numerical calculations were performed using the Maple ODE solver in which δ and w are varied. The results obtained with $R_0 = 2$ and the flux parameterizations in (2.12), (2.13) and (2.31) are shown in Figure 2.4. The dots in (δ, w) parameter space represent all attempts to solve the governing equations. The experiments in which regular solutions have been found are indicated by heavy dots, whereas the light dots represent conditions for which the numerical search for solutions failed. The results in Figure 2.4 are consistent with the theoretical prediction in (2.38). All solutions are largely confined to two sectors—corresponding to positive and negative δ—bounded by straight lines emanating from the (0,0) point in the (δ, w) parameter space.

It is also of interest to examine the relevant range of diapycnal velocities in the double-diffusive zone in Figure 2.4. Assuming that the variation of flux ratio in the ocean

18

is $\delta \approx 0.15$, we obtain a non-dimensional constraint of $|w| \leq 40$. This estimate can be expressed in terms of dimensional variables by reverting the non-dimensionalization (2.16). For $k_T = 1.4 \cdot 10^{-7} m^2 s^{-1}$ and $H \sim 1000m$, we obtain the maximum dimensional diapycnal velocity of

$$\max |w_{\text{dim}}| \sim 5 \cdot 10^{-9} ms^{-1}. \tag{2.39}$$

This estimate suggests that double-diffusion could severely constrain diapycnal velocity. To interpret (2.39) in the global circulation context, let us recall that the nominal value of diapycnal velocity, commonly used in climate models (see the review by Wunsch and Ferrari 2004), is $\sim 10^{-7} ms^{-1}$, exceeding (2.39) by more than an order of magnitude. Thus, the diapycnal transport, both upward and downward, can be essentially blocked in the ocean regions where mixing is dominated by double-diffusion.

These findings, of course, should be interpreted with great caution—the ability of any one-dimensional model to reflect the inherently three-dimensional dynamics of ocean circulation is suspect. Perhaps it is most profitable to interpret these one-dimensional solutions as the result of the averaging of the advection-diffusion equations along isopycnals, although this conceptualization immediately raises the question whether such averaging is physically justified. Nevertheless, the profound differences in the way various mixing models affect diapycnal transport provide a compelling reason to launch a more comprehensive investigation of this phenomenon using more realistic—three-dimensional and time-dependent—models. We now proceed with the analysis of double-diffusive insulation based on a series of large-scale numerical simulations.

D.   LARGE-SCALE NUMERICAL SIMULATIONS

1.   Model Formulation

The MIT General Circulation Model (MITgcm), described in Marshall et al. (1997a, b), was used to simulate an ocean of equatorial to sub-arctic meridional extent with a zonal width comparable to that of the North Atlantic. This model solves the incompressible Boussinesq equations of motion with the linear equation of state. The model geometry is a rectangular domain with dimensions

$$(L_x, L_y, L_z) = (6400km, 6400km, 3000m), \tag{2.40}$$

resolved by $64 \times 64 \times 60$ Cartesian grid points with $\Delta x, \Delta y = 10^5 m$ and $\Delta z = 50m$. The relatively coarse horizontal resolution prevents generation of mesoscale variability, thereby isolating the phenomena of interest—double-diffusive and turbulent diapycnal mixing. Thermohaline forcing is represented by strong relaxation of the surface temperature and salinity to the zonally uniform target patterns shown in Figure 2.5. The surface temperature and salinity vary linearly with latitude from $T_{South} = 30\,^\circ C$ and $S_{South} = 37.75$ to $T_{North} = 5.67\,^\circ C$, and $S_{North} = 34.22$. Surface forcing also includes y-dependent zonal wind stress (Figure 2.5c) prescribed as follows:

$$\tau(y) = -\tau_0 \sin\left(2\pi \frac{y}{L_y}\right), \quad 0 < y < L_y, \tag{2.41}$$

where $\tau_0 = 0.05 Nm^{-2}$. The variation in the Coriolis parameter (f) is represented by the beta-plane approximation:

$$f = \beta_c y, \tag{2.42}$$

where $\beta_c = 10^{-11} m^{-1} s^{-1}$.

The model was initialized from rest with a *T-S* distribution that is zonally uniform but varies linearly in *y* and *z*. The target temperatures and salinities (Figure 2.5) served as initial surface values as well and initial bottom values were $T_{abyss} = 4.6\,^\circ C$ and $S_{abyss} = 34.1$. The corresponding density ratios monotonically increase from $R_\rho = 1.88$ at $y = 0$ to $R_\rho = 2.35$ at $y = L_y$. Horizontal and vertical eddy viscosities were set to $A_H = 4 \cdot 10^5 m^2 s^{-1}$ and $A_Z = 5 \cdot 10^{-4} m^2 s^{-1}$. The nonlocal K-Profile Parameterization (KPP) scheme of Large et al. (1994) was used to model convective and near-surface mixing processes. Geostrophic eddy parameterization followed Gent and McWilliams (1990). To reduce spurious interactions with KPP and to isolate the dynamics of interest, isopycnal diffusivity was set to the minimal value $(\kappa_\rho = 10m^2 s^{-1})$ required to maintain the

numerical stability of the model. Vertical mixing of temperature and salinity was represented by a combination of double-diffusion and turbulence. Double-diffusion was parameterized using (2.12)-(2.13). The interior turbulent diffusivity (K^{turb}) associated with overturning gravity waves is assumed to be spatially uniform and equal for temperature and salinity. In a series of simulations K^{turb} was systematically varied from 0 to $2 \cdot 10^{-4} m^2 s^{-1}$. In the region of western intensification ($x < L_{int}$), however, K^{turb} was maintained at the minimum value of $K^{turb}_{\min WBC} = 2 \cdot 10^{-4} m^2 s^{-1}$. This restriction was implemented to prevent excessive convection in the regions where the western boundary current, transporting relatively warm and light water northward, enters locations with much higher target surface density. Each simulation was integrated forward for at least 200 years using a time step of $480s$, which was sufficient to produce quasi-steady circulation patterns.

Figure 2.6 and Figure 2.7 present a typical final state realized in these numerical experiments. This simulation was performed assuming purely double-diffusive interior mixing, with $K^{turb} = 0$ for $x > L_{int} = 1000 km$. Figure 2.6a shows the horizontal temperature distribution and the velocity pattern at $z = -500m$. As expected, the flow field is dominated by clockwise circulation in the subtropical region ($\frac{1}{4} L_y < y < \frac{3}{4} L_y$) where wind forcing is anticyclonic. A vertical zonal section of temperature at $y = 0.5L_y$ is shown in Figure 2.6b. Clearly visible is a well-defined thermocline with relatively warm water extending several hundred meters downward from the surface. Figure 2.7 presents a three-dimensional view of the isopycnal $\rho = \rho_{av}$, where

$$\rho_{av} = \frac{\rho_{\max} + \rho_{\min}}{2}, \tag{2.43}$$

and $\rho_{\max}$ ($\rho_{\min}$) represents the maximum (minimum) density in the computational domain. The color coding represents the values of the density ratio on this isopycnal. The observed range of density ratios $1 < R_\rho < 3$ indicates that salt fingering is active on this isopycnal and that its intensity is relatively high.

2. Diapycnal Velocity

The analyses in Sections B and C pertained to steady one-dimensional systems in which diapycnal volume transport is associated with vertical advection. To quantify diapycnal fluxes in a more realistic three-dimensional setting, the diagnostics of large-scale simulations will be focused on diapycnal velocity w^* (Pedlosky 1987, Radko and Marshall 2004), which is generally dissimilar to the vertical velocity (w). Diapycnal velocity can be defined by rewriting governing equations in terms of density (rather than z) as a vertical coordinate:

$$w^* = w(x, y, \rho) - \frac{d}{dt} z(\rho), \tag{2.44}$$

where

$$\frac{d}{dt} z(\rho) \equiv \frac{\partial z(\rho)}{\partial t} + u \frac{\partial z(\rho)}{\partial x} + v \frac{\partial z(\rho)}{\partial y}. \tag{2.45}$$

In (2.45), $\dfrac{\partial z(\rho)}{\partial x} = -\dfrac{\rho_x}{\rho_z}$ and $\dfrac{\partial z(\rho)}{\partial y} = -\dfrac{\rho_y}{\rho_z}$ represent the slopes of isopycnal surfaces in x and y. For steady-state circulation patterns, (2.44) reduces to

$$w^* = \frac{u\rho_x + v\rho_y + w\rho_z}{\rho_z}. \tag{2.46}$$

Figure 2.8 illustrates the following physical interpretation of diapycnal velocity. Consider a Lagrangian particle initially located at the motionless isopycnal surface ρ (point A). In the presence of a finite cross-isopycnal flow, this particle will be advected by velocity $\vec{v} = (u, v, w)$ to a new point B, located off the isopycnal. Let C be the vertical projection of the point B onto the isopycnal surface. In this configuration, the diapycnal velocity in (2.46) represents the rate of increase of the vertical separation of our Lagrangian point from the density surface: $w^* = \dfrac{d}{dt}[BC] = \dfrac{dz_B}{dt} - \dfrac{dz_C}{dt}$. Note that the shadow point C, which remains on the isopycnal, can also alter its z-level and the corresponding vertical velocity can be expressed as

$$w_\rho = \frac{d}{dt}z_C = -u\frac{\rho_x}{\rho_z} - v\frac{\rho_y}{\rho_z}. \qquad (2.47)$$

Thus, the isopycnal ascent rate w_ρ and diapycnal velocity w^* represent two distinct components of vertical velocity:

$$w = w^* + w_\rho. \qquad (2.48)$$

Equation (2.46) indicates that in the absence of any diabatic water-mass transformation, $\frac{d\rho}{dt} = \vec{v} \cdot \nabla\rho = 0$ and therefore diapycnal velocity is zero. Curiously, the reverse statement is not necessarily correct. The double-diffusive example in Section B indicates that diapycnal velocity can still be zero even in the presence of substantial diabatic mixing. The following analysis will therefore attempt to determine whether w^* is suppressed by double-diffusion in the more realistic three-dimensional systems.

3. Diapycnal Transport in the Ocean: Double-Diffusive and Turbulent Regimes

First, the proposed diagnostics have been applied to the double-diffusive experiment shown in Figure 2.6 and Figure 2.7. The diapycnal velocity was computed using (2.46) and evaluated at the isopycnal surface $\rho = \rho_{av}$. The results are plotted (Figure 2.9a) for the interior region $(L_{int} < x < L_x)$ where mixing is exclusively double-diffusive. The same procedure was then applied to the turbulent experiment (Figure 2.9b). The latter was designed in the same way as the baseline double-diffusive run, save the vertical mixing was assumed to be exclusively turbulent with

$$K^{turb} = 2 \cdot 10^{-5} m^2 s^{-1}. \qquad (2.49)$$

The comparison of diapycnal velocities in these experiments reflects the dramatic difference in the way double-diffusion and turbulence affect diapycnal transport. Over most of the isopycnal surface, the double-diffusive w^* values are on the order of $\sim 5 \cdot 10^{-9} ms^{-1}$ or less (both positive and negative values are observed). On the other hand, the turbulent values of w^* are mostly positive and larger by at least an order of magnitude

23

$(\sim 5 \cdot 10^{-8} ms^{-1})$. The difference between Figure 2.9a and Figure 2.9b becomes particularly striking when we recall that typical *T-S* diffusivities in the two experiments are comparable. For instance, the volume-averaged diffusivities in the double-diffusive experiment are $\left(\overline{K}_T^{dd}, \overline{K}_S^{dd} \right) = (1.07, 2.18) \cdot 10^{-5} m^2 s^{-1}$, and these values are similar to the turbulent diffusivity (2.49).

Figure 2.10a presents the mean diapycnal velocity evaluated at various isopycnal surfaces $w_{iso}^*(\rho)$. In computing w_{iso}^*, two regions with elevated turbulent diffusivity were excluded: *a)* the western intensification region $(x < L_{int})$ and *b)* the near surface region $(z > -250m)$ where some isopycnal surfaces enter the mixed layer, particularly in the cold northern parts of the domain. Diapycnal velocity w_{iso}^* was evaluated for both turbulent and double-diffusive experiments and referenced (Figure 2.10a) to the average depth of isopycnal surfaces $h_{iso}(\rho)$. Figure 2.10a shows that the turbulent diapycnal velocity (blue curve) substantially exceeds the double-diffusive w_{iso}^* (green curve) for most isopycnals. In both cases, relatively large values of w_{iso}^* were found at the base of the main thermocline $(h_{av} \sim 1000m)$. Diapycnal velocity in the turbulent experiment was also greatly amplified in the abyssal region $(h \to 3000m)$ whereas no such amplification occurred in the double-diffusive simulation. It is interesting to note that the patterns of isopycnal-averaged diapycnal velocity are qualitatively similar to the corresponding local vertical profiles. For instance, Figure 2.10b shows the diapycnal velocity profile at the center of the model domain: $w_{loc}^* = w^*(0.5L_x, 0.5L_y, z)$. The local diagnostics also indicate that diapycnal velocity in the turbulent ocean greatly exceeds the double-diffusive w^*. Thus, the double-diffusive insulation effect considered in this study represents both the integral and the local property of large-scale flows.

An attempt has also been made to determine the constraints on diapycnal velocity in an ocean experiencing vertical mixing due to a combination of double-diffusion and mechanically generated turbulence. A series of simulations in which K^{turb} was systematically varied, while retaining the parameterization (2.11)-(2.13) for double-

diffusion was performed. Diapycnal velocity was computed and evaluated as previously (Figure 2.9, Figure 2.10). As expected, we find that the diapycnal transport intensifies with the increase of the fraction of the overall mixing attributed to turbulence. Figure 2.11 presents the variation of the isopycnal-averaged diapycnal velocity $w_{av}^* = w_{iso}^*(\rho_{av})$ at the isopycnal surfaces $\rho = \rho_{av}$ in (2.43) as a function of K^{turb}. These diagnostics also support the interpretation of double-diffusive mixing as an insulating mechanism. When K^{turb} is less than typical values for K_S^{dd} and K_T^{dd}, the overall system behaves like the fully double-diffusive case (e.g., Figure 2.9a). Values of mean diapycnal velocity are on the order of $\sim 5 \cdot 10^{-9} ms^{-1}$ or less for experiments with $K^{turb} \leq 2 \cdot 10^{-6} m^2 s^{-1}$. Conversely, simulations with $K^{turb} \geq K_S^{dd}, K_T^{dd} \sim 2 \cdot 10^{-5} m^2 s^{-1}$ are characterized by w^* on the order of $\sim 5 \cdot 10^{-8} ms^{-1}$ or greater.

4. The Role of the Flux Ratio

The foregoing experiments have illustrated the dramatic differences in diapycnal volume flux in double-diffusive and turbulent systems. The question that naturally arises at this point is what aspect of double-diffusion makes it so effective in blocking the diapycnal volume transport? Theoretical arguments presented in Section C suggest that, at least in one-dimensional models, the range of diapycnal velocities is controlled by the effective variation in the flux ratio (γ). Double-diffusive systems are characterized by relatively uniform γ. For instance, Radko and Smith (2012) find that as the density ratio increases from $R_\rho = 1.1$ to $R_\rho = 3$, the flux ratio decreases by $\Delta\gamma \sim 0.15$. The flux ratio realized in turbulent fluids $(\gamma = R_\rho)$ varies over the same interval much more $(\Delta\gamma = 1.9)$, which suggests significantly larger values of diapycnal velocity. In particular, the one-dimensional model (Section C) predicts that $w^* \propto \Delta\gamma$. To determine whether these conclusions remain relevant for three-dimensional systems, an additional series of four double-diffusive simulations with variable flux ratio patterns were performed.

These new simulations were identical to the baseline double-diffusive experiment (Figure 2.6, Figure 2.7) in all respects except for the chosen flux ratio model, which assumed that γ varies linearly with the density ratio:

$$\gamma\left(R_\rho\right) = \gamma_0 + \delta\left(R_\rho - 1\right). \tag{2.50}$$

The flux ratio models used in these simulations are shown in Figure 2.12a, along with the baseline $(\delta = 0)$ experiment, and the corresponding parameter values are $(\delta = 0, 0.25, 0.5, 0.75, 1)$ and $(\gamma_0 = 0.85, 0.8875, 0.925, 0.9625, 1)$ respectively. Thus, the flux ratio pattern in Figure 2.12a gradually changes from the zero-slope baseline experiment $(\gamma = 0.85)$ to the one realized in the turbulent model $(\gamma = R_\rho)$. In all experiments, however, the double-diffusive mixing parameterization (2.12), (2.13) is retained; the corresponding $K_S(R_\rho)$ pattern is shown in Figure 2.12b.

As previously (e.g., Figure 2.11), this analysis is focused on the properties of w_{av}^* —the isopycnal-averaged diapycnal velocity calculated for each simulation along the density surface $\rho = \rho_{av}$ —and these results are summarized in Figure 2.13. The diapycnal velocity for the $\delta = 0$ case is very weak $(w^* \sim 10^{-9}\, ms^{-1})$ and negative. However, as δ increases and the flux ratio becomes less and less uniform, w_{av}^* monotonically increases. Finally, for $\delta = 1$, which corresponds to the turbulent flux ratio model $(\gamma = R_\rho)$, the average diapycnal velocity increases to $w_{av}^* \approx 5 \cdot 10^{-8}\, ms^{-1}$. Diapycnal velocities in this case become comparable to those realized in the fully turbulent model (Figure 2.9b). The pattern of $w_{av}^*(\delta)$ in Figure 2.13 can be reasonably well described as a linear relation and is broadly consistent with the one-dimensional theoretical model developed in Section C (see Figure 2.4). Thus, the range of diapycnal velocities realized in these three-dimensional double-diffusive simulations with weakly varying flux ratio is of the same order of magnitude as (2.39), supporting the theoretical framework previously constructed.

26

E. THEORETICAL MODEL OF DOUBLE-DIFFUSIVE INSULATION

The foregoing numerical simulations indicate that the double-diffusive insulation occurs over most of the thermocline and it is not limited to Munk's regions characterized by the vertical advective-diffusive balance. Therefore, the next step represents an attempt to rationalize this phenomenon without relying on the highly restrictive one-dimensional assumption used in Sections B and C. Over much of the main thermocline, small-scale mixing constitutes a numerically small component of the full advective-diffusive balance of temperature and salinity. Yet, this component is responsible for diabatic water-mass transformation and, ultimately, for the selection of diapycnal velocity. Diabatic dynamics can be brought to the fore and analyzed theoretically using a procedure analogous to the one used by Rhines and Young (1982), albeit in a very different context.

Consider a zero-order steady state of the ocean in the absence of mixing. This state is characterized by exact conservation of temperature, salinity, density and potential vorticity. This ideal basic state is slightly perturbed by including weak diapycnal fluxes of heat and salt in the advection-diffusion equations of motion. It is assumed that the perturbation results in only slight (first order) modification of the corresponding ideal zero order solution. The perturbed state is governed by

$$\begin{cases} \dfrac{d}{dt}T = \vec{v} \cdot \nabla T = \dfrac{d}{dt}\bigg|_{\rho} T + w^* \dfrac{\partial T}{\partial z} = -\dfrac{\partial F_T}{\partial z} \\[3mm] \dfrac{d}{dt}S = \vec{v} \cdot \nabla S = \dfrac{d}{dt}\bigg|_{\rho} S + w^* \dfrac{\partial S}{\partial z} = -\dfrac{\partial F_S}{\partial z}, \end{cases} \tag{2.51}$$

where $\dfrac{d}{dt}\bigg|_{\rho} \equiv u\dfrac{\partial}{\partial x} + v\dfrac{\partial}{\partial y} + w_{\rho}\dfrac{\partial}{\partial z}$ and w_{ρ} is given in (2.47). Figure 2.14 represents the typical circulation pattern in the subtropical ocean on an arbitrarily chosen isopycnal surface $\rho = \rho_0$. On this surface, we select a closed temperature contour $(T = T_0)$. Since temperature, salinity and density are assumed to be uniquely related through the linear equation of state, it follows that salinity is also constant along the chosen contours $(S = S_0)$. These contours closely follow the corresponding streamlines of the ideal basic state on which (T_0, S_0, ρ_0) are conserved exactly.

The following analysis is pivoted about the time integrals of (2.51) along such closed contours:

$$\begin{cases} \oint w^* \dfrac{\partial T}{\partial z}\, dt = -\oint \dfrac{\partial F_T}{\partial z}\, dt \\[4mm] \oint w^* \dfrac{\partial S}{\partial z}\, dt = -\oint \dfrac{\partial F_S}{\partial z}\, dt \, . \end{cases} \tag{2.52}$$

The major simplification here is achieved by elimination of the zero order advective terms. Combining (2.52) with the double-diffusive parameterization (2.8), we arrive at

$$\oint w^* \left(\alpha \dfrac{\partial T}{\partial z} - \gamma_0 \beta \dfrac{\partial S}{\partial z} \right) dt = 0 \, . \tag{2.53}$$

The next step is the change of the integration variable from time (t) to the length coordinate measured along the contours (l), which reduces (2.53) to

$$\oint w^* \left(\alpha \dfrac{\partial T}{\partial z} - \gamma_0 \beta \dfrac{\partial S}{\partial z} \right) \dfrac{dl}{\left| \vec{v}_h \right|} = 0 \tag{2.54}$$

where $\left| \vec{v}_h \right|$ is the absolute value of horizontal velocity. The mid-latitude circulation patterns (e.g., Figure 2.14) consist of two distinct regions: relatively slow geostrophic interior $(L_{\text{int}} < x < L_x)$ and swift western boundary currents $(0 < x < L_{\text{int}})$. The inspection of (2.54) indicates that even if a streamline passes through both regions (Figure 2.14), the dominant contribution to (2.54) comes from the interior geostrophic region, where $\left| \vec{v}_h \right|$ is much less (by a factor $L_x / L_{WBC} \gg 1$) than the velocity in the boundary current. Neglecting the small contribution from the region of western intensification allows us to focus exclusively on geostrophic dynamics and express the horizontal velocity components as follows:

$$\begin{cases} fv = \left. \dfrac{\partial M}{\partial x} \right|_{\rho=\rho_0} \\[4mm] fu = -\left. \dfrac{\partial M}{\partial y} \right|_{\rho=\rho_0} \, , \end{cases} \tag{2.55}$$

where M is the Montgomery potential. The system (2.55) indicates that the contours of integration in (2.54) at the leading order coincide with the isopleths of M. Another simplification brought by geostrophic approximation is that the Ertel potential vorticity in this case takes a relatively simple form

$$q = f \frac{\partial C}{\partial z}, \tag{2.56}$$

where C is any conservative tracer. Recall that the perturbed solution is assumed to be only slightly different from its adiabatic counterpart, which conserves temperature, salinity, and potential vorticity in the Lagrangian sense. Thus, we conclude that at the leading order *a)* potential vorticity q is conserved along the contours of integration and *b)* the tracer C can be represented by any combination of temperature and salinity. Given the structure of the line integral (2.54), we expect significant simplifications to occur for

$$C = \alpha T - \gamma_0 \beta S. \tag{2.57}$$

Since potential vorticity is approximately uniform along each streamline, we divide (2.54) by q, entering it directly into the integrand, which reduces the line integral to

$$\oint_{int} \frac{w^*}{f} \frac{dl}{|\vec{v}_h|} = 0. \tag{2.58}$$

Here, the notation "*int*" is used to emphasize that the integration is carried out only over the geostrophic interior. By virtue of (2.55), we further simplify (2.58) to

$$\oint_{int} w^* \frac{dl}{|\nabla M|} = 0. \tag{2.59}$$

The final step is the transition from the line integrals to the area integrals over the regions bounded by closed contours of the Montgomery potential $(M = M_0)$:

$$\iint_{\substack{M > M_0 \\ int}} w^* dx dy = 0. \tag{2.60}$$

Equation (2.60) shows that there could be no net diapycnal transport across broad regions on the isopycnal surfaces laterally bounded by closed streamlines, which

29

confirms and rationalizes the double-diffusive insulation effect discussed and numerically modeled in Section D. The foregoing arguments are certainly not relevant for the turbulent ocean. In this case, the flux laws do not satisfy (2.8) and therefore (2.53)—and all that follows—does not apply. Hence, no analogous constraints on diapycnal velocity are expected to arise in purely turbulent systems.

F. SUMMARY AND CONCLUSIONS

In the classical view of thermohaline circulation (Munk 1966), small-scale diapycnal mixing is assigned a role in the driving force of MOC. It is commonly assumed that the increase in diapycnal diffusion of temperature and salinity necessarily amplifies the diabatic component of overturning (e.g., Bryan 1987). This notion has profoundly affected the evolution of physical oceanography. It motivated development of the extensive small-scale mixing research program, largely aimed at quantification of the average diapycnal diffusivity in the ocean (Munk and Wunsch 1998, Wunsch and Ferrari 2004). This study presents a peculiar counter-example of this tendency by showing that mixing can have an adverse impact on overturning. Using a suite of basin-scale simulations and theoretical models, it is demonstrated that the inclusion of double-diffusive mixing of temperature and salinity—a fairly common small-scale process in the ocean—can place rather severe constraints on the magnitude of vertical diapycnal velocity. In the extreme case when vertical mixing is dominated by double-diffusion, the diapycnal transport is almost negligible. Simulations indicate that these constraints are realized both locally and in the isopycnal-average sense. Typical values of diapycnal velocity ($w^* \sim 5 \cdot 10^{-9} ms^{-1}$) are less, by at least an order of magnitude, than w^* driven by mechanically generated turbulence with comparable T-S diffusivities. In essence, double-diffusion acts to "seal" the thermocline by preventing the leakage of seawater (both upward and downward) across the isopycnal surfaces on which double-diffusion is a dominant mixing process.

The ability of double-diffusion to constrain diapycnal transport is contrasted with the properties of mechanically generated turbulence. The latter is characterized by equal diffusivities of temperature and salinity and offers no restrictions on diapycnal velocity.

When both double-diffusion and turbulence are present, the constraints on w^* loosen (tighten) with the increase (decrease) of the fraction of the overall mixing attributed to turbulence. When the contributions to mixing from double-diffusion and turbulence are comparable—the regime that is perhaps realized in the central Atlantic thermocline (St. Laurent and Schmitt 1999)—the maximum diapycnal velocity is on the order of $\sim 10^{-7} ms^{-1}$. This value is comparable to current estimates of diapycnal velocity, which raises an intriguing possibility that diapycnal transport could be controlled by constraints on w^* imposed by double-diffusion. This suggestion is distinct from the ideas expressed by mainstream models of thermohaline circulation (e.g., Welander 1971) in which the *T-S* advective-diffusive dynamics constitute only a part of the problem. Ultimately, diapycnal velocity is selected by invoking three-dimensional large-scale balances involving both momentum and density. It should be realized, however, that the latter proposition is based on mixing models with uniform and equal vertical diffusivity $(K_T = K_S = const)$. The examples in this study indicate that such models may not capture all the relevant dynamics and therefore caution is urged in conceptualizing the thermohaline circulation based on oversimplified mixing parameterizations.

Of course, there are a number of uncertainties in the presented model, particularly with regard to its ability to incorporate all relevant dynamics of the oceanic circulation. For instance, it is not clear how resilient the double-diffusive insulating blanket is in the presence of active mesoscale variability, which can also impact the diapycnal transport (Radko and Marshall, 2004). The processes discussed in this study could be affected by the nonlinearities of the equation of state (e.g., McDougall 1987). Thus, the quantitative accuracy of double-diffusive insulation theory is readily questioned. However, the differences in the way double-diffusion and turbulence affect diapycnal transport identified here are suggestive and are likely to be realized in the ocean. In this regard, it should be mentioned that GCM-based studies, which take into account double-diffusion (Gargett and Holloway 1992, Zhang et al. 1998, Merryfield et al. 1999), report systematic reduction in the strength of meridional overturning. Although the extent of this reduction varies considerably between models, it is possible that these results can be attributed to the double-diffusive insulation effect. Finally, it should be mentioned that while the

results of this study are based on particular parameterizations of double-diffusive mixing, which require further refinements and testing, additional experiments (not shown) indicate that the model results are not overly sensitive to the assumed relations for $K_T(R_\rho)$ and $K_S(R_\rho)$. Therefore, it is expected that these qualitative conclusions are sufficiently robust.

III. THE ROLE OF DOUBLE-DIFFUSION IN THE ONSET AND MAINTENANCE OF CONVECTION DURING WEDDELL SEA POLYNYA AND SEA ICE THINNING EVENTS

A. INTRODUCTION

The Weddell Sea Polynya was a large expanse of open water surrounded by sea ice that appeared in three consecutive austral winters from 1974 to 1976 in the Weddell Sea bordering Antarctica. No persistent polynyas of this magnitude have occurred in the same area since the 1970s, making it one of the more mysterious and interesting phenomena in high-latitude oceanography. Marginal water column stability in the Weddell Sea during winter leads to conditions favorable to diffusive convection, a form of double-diffusion prevalent in high-latitude regions. The role that diffusive convection plays in polynya formation and the onset of deep convection in this region is not fully understood. Polynyas affect global climate in two important ways. First, significant areas of open sea in otherwise ice-covered regions enable large amounts of sea-to-air heat flux to modify atmospheric conditions, affecting short-term weather. Second, this surface heat loss to the atmosphere substantially cools the near-surface ocean, increasing its density, and initiating convection. This ventilation process significantly affects the properties of the World Ocean's deep water and has long-term effects on the world's climate, so the importance of understanding polynya formation in the Weddell Sea cannot be understated. Apart from the natural desire to explain an anomaly, research into the preconditioning, onset, maintenance, and subsequent disappearance of the Weddell Sea Polynya can offer useful insights into the annual heat budget, nature of the cyclical ice cover and deep water formation in the region.

Many theories have been offered to explain the mechanisms of formation and maintenance of the Weddell Sea Polynya (hereafter WP). Gordon (1978) hypothesized that divergence caused by Ekman transport at the center of the Weddell Gyre led to increased sea ice production and, with its attendant brine rejection, densified the surface mixed layer. This process along with the upward heat flux associated with this vertical instability of the surface water could account for the onset and maintenance of the WP.

Carsey (1980) first detailed the seasonal behavior of the WP using satellite observations and ruled out formation mechanisms acting in isolation (such as wind-driven ice divergence and dynamic effects near Maud Rise enhancing upward heat flux from depth). Carsey suggested the WP was caused by Weddell Gyre eddies, consisting of water preconditioned in temperature and salinity profiles to respond to surface cooling by convection, interacting with other mechanisms. Martinson et al. (1981) offered a two-level convective model to simulate the life cycle of the WP and found vertical convection due to salt rejection into a preconditioned upper level with a shallow pycnocline could explain the appearance and maintenance of this feature. Its irregularity in occurrence was attributed to sensitivity in profile temperature and salinity and variability in freshwater input. Gordon (1981) speculated that either anomalously low precipitation or greater than normal brine rejection could have contributed to densification of surface water leading to increased vertical instability and convection, causing the Weddell Polynya's anomalous appearance in the mid-1970s. Gordon and Huber (1984) postulated that warm Weddell Deep Water advected into the deep ocean west of Maud Rise would eventually enter surface water through entrainment, decreasing pycnocline stability by increasing near-surface salinity, thus leading to a greater likelihood of convective events able to initiate open ocean polynyas.

Single-year polynya events along with periods of low ice concentration have been observed since the 1970s (Comiso and Gordon 1987, Drinkwater 1996, and Lindsay et al. 2004 and others), but there have been no multi-year, persistent events since the first microwave satellite observations. Comiso and Gordon (1987) attribute this subsequent lack of seasonal polynyas to a cessation of open water convection due to increased freshwater flux in the form of wind-induced sea ice advection into, followed by melting within, the polynya formation area.

Martinson (1990) used an analytical model to detail the complex interaction between heat flux and freshwater external forcing, density ratio, pycnocline depth and strength in relation to sea ice growth and winter sea ice thicknesses in the Southern Ocean. This study indicated that the stability of the water column is maintained by a system of negative feedbacks in the form of diffusive and entrainment heat fluxes.

Diffusive flux across the thin pycnocline is large due to its strong thermal gradient. This large flux limits significant sea ice growth, which would destabilize the water column through brine rejection. Entrainment flux further mitigates sea ice growth by providing an additional upward heat flux that is proportional to surface buoyancy loss. In this way, entrainment flux acts in concert with diffusive flux and both serve as negative feedback moderating ice growth. This effect is known as the "thermal barrier."

Equally important to understanding how the thermal barrier regulates sea ice thickness is understanding the mechanisms that can lead to its breakdown. Martinson (1990) details four parameters critical to maintaining the delicate balance of the thermal barrier: (i) the depth of the pycnocline, (ii) the ratio of heat to salt through the pycnocline, (iii) the strength of the pycnocline, and (iv) the magnitudes of external forcing in the form of heat loss to the atmosphere and freshwater input. Given these four critical parameters, a breakdown of the thermal barrier could naturally involve four factors. First, a shallower pycnocline would concentrate equal magnitudes of external forcing into a smaller volume, which would lead to larger buoyancy loss. Second, either a reduction of heat flux or an increase of salt flux in the pycnocline would reduce the stabilizing effects of heat flux in relation to the destabilizing salt flux. Third, the definition of destabilization can be thought of as the reduction of the density gradient across the pycnocline, so weakening the strength of the pycnocline would be a direct way to disrupt the thermal barrier feedback mechanisms. Finally, increasing heat flux to the atmosphere would stimulate further sea ice growth and brine rejection, which would destabilize the system (the present study concentrates on this mechanism exclusively). It is worth mentioning that the findings of Martinson (1990) are corroborated by the descriptive analysis provided by Gordon and Huber (1990).

Timmermann et al. (1999) concluded that multi-year appearances of the WP can occur from the positive feedback effects of the polynya on the lower atmosphere above it. Increased open ocean vertical heat flux induces a persistent low pressure area centered over the polynya itself with this area subject to divergent sea ice drift and a further increase of air-ocean heat flux due to Ekman pumping. Timescales of vertical motion and

diffusion allow a winter-time increase of near-surface salinity to persist until the following winter, preconditioning the column for a further appearance of the polynya.

McPhee et al. (1999) showed through an analysis of ANZFLUX data that winter ice cover in the vicinity of Maud Rise acts as a thermal "flywheel" maintaining constant heat flux to the atmosphere in conditions of varying heat flux below the mixed layer, evidenced by cycles of alternating sea ice bottom growth and melt. This mechanism relies on the interplay between heat loss to the atmosphere, interior oceanic heat flux, and sea ice growth. As oceanic heat flux increases, sea ice experiences bottom melting. As sea ice thickness diminishes from bottom melt, heat flux to the atmosphere increases. This increase in cooling halts sea ice bottom melt and can possibly lead to sea ice growth. Conversely, if oceanic heat flux decreases, sea ice thickens due to bottom freezing, heat loss to the atmosphere is diminished, and eventually sea ice growth is checked. This negative feedback can maintain a near-constant heat loss to the atmosphere despite large changes in oceanic heat flux. Thus, the thermal barrier of Martinson (1990) and the thermal flywheel of McPhee et al. (1999) complement each other as both mechanisms work to maintain constant sea ice thicknesses in the region.

Holland (2001) attributed the formation of the WP to purely dynamic causes, ruling out thermodynamic reasons for its formation, but acknowledged these mechanisms may have a role in its maintenance. Muench et al. (2001) detailed the warm pool, warm halo, and Taylor column features that extend the effects of Maud Rise bathymetry over a region twice as large as that of the area directly above the seamount. De Steur et al. (2007) modeled the region using both idealized and realistic topography and showed that the dynamics of a warm water "halo" surrounding the Maud Rise seamount could be responsible for preconditioning the area for polynya events like the ones observed in the mid-1970s.

More recently, Shaw and Stanton (2014) investigated the dependence of pycnocline diffusivity on the Froude number and density ratio generated by double diffusion and diapycnal cabbeling in this region. They found that diffusive heat flux across the pycnocline limits winter ice formation and subsequent densification at the surface and this could explain the consistently thin ice cover detailed in previous studies.

36

Flanagan et al. (2014) followed this with direct numerical simulation (DNS) modeling of the same region, examining the interaction of diffusive convection and shear. The Flanagan et al. model produces results corroborating the findings in Shaw and Stanton (2014) without the inclusion of cabbeling effects, indicating that the observations can be explained adequately by double-diffusion.

Even with this extensive array of previous works, there has been no comprehensive numerical modeling study of the possible role of double-diffusion in the onset and maintenance of convection during polynya and sea ice thinning events in the vicinity of Maud Rise in the eastern Weddell Sea. A simple thought experiment illustrates why it is reasonable to believe that double-diffusion could have a profound impact on this process and provides the overall impetus for this investigation.

The diffusive flux ratio ($\gamma*$) in regions experiencing diffusive convection is commonly formulated as:

$$\gamma* = \frac{\beta F_S}{\alpha F_T} \tag{3.1}$$

and represents the ratio of the haline contribution to density flux to the thermal contribution. In conditions dominated by turbulence, $\gamma* > 1$. This indicates that the haline contribution to density flux is greater than the thermal contribution, resulting in a positive density flux overall, leading to decreased static stability of the water column (Figure 3.1). However, when the water column temperature and salinity profiles produce conditions favorable for diffusive convection, $\gamma* < 1$. In this case, the thermal contribution to density flux is greater than the haline contribution. The sum of these two contributions results in a negative density flux overall, leading to increased stability of the water column (Figure 3.2). This ability of diffusive convection, so common in high-latitude regions, to transport heat upward while acting to increase static stability of the water column gives us a compelling reason to expect double-diffusion to promote sea ice thinning and polynya formation even while delaying the onset of convection in the Weddell Sea and is the subject of this study.

Further understanding of this region of marginal water column stability is desirable since double-diffusion could play a larger role than previously thought in the regional heat budget, the nature of seasonal ice cover, and the determination of water mass characteristics that affect deep water formation and ventilation. The eastern Weddell Sea in the vicinity of Maud Rise provides the ideal setting to investigate this intriguing possibility, made all the more fitting by its history of multi-year polynya events. This study aims to expand the already substantial body of knowledge concerning this region by investigating how double-diffusion, in its diffusive convection form, affects the onset and maintenance of convection during multi-year polynya and persistent sea ice thinning events in the region. To this end, a series of simulations using a numerical, multi-scale, MPI-based general circulation model was used. A model containing an idealized bathymetry featuring a seamount representative of Maud Rise along with open edge boundaries forms the basis of the investigation.

B. HIGH RESOLUTION NUMERICAL MODELING

Since the densification of surface water is thought to be an important factor in initiating turbulent convection in the vicinity of Maud Rise (Martinson et al. 1981, Gordon 1982 and others), a surface forcing prescribed to achieve this effect was included. Several potential choices of forcing were explored and an attempt was made to strike a workable balance between a mechanism that was simple and yet also observationally relevant. The robust nature of the negative feedback mechanisms of the thermal barrier (Martinson 1990) and the thermal flywheel (McPhee et al. 1999) in mitigating large variations in surface and subsurface heat fluxes while maintaining near-constant sea ice thicknesses made the use of surface heat flux forcing as the primary densification mechanism the most attractive option. This leaves the strength and depth of the pycnocline dependent on model physics only and allows the model's turbulent and double-diffusive mixing parameterizations to control heat and salt fluxes. Thus, only one of the critical parameters discussed in Martinson (1990) would need to be varied during each model run. This choice of surface heat flux forcing as the primary densification mechanism is also supported by the observations and analysis in McPhee et al. (1999). By prescribing surface heat flux, the thermal flywheel negative feedback is simulated.

38

Heat and salt fluxes across the pycnocline are free to vary as model physics demands, while surface heat flux remains as prescribed.

Given these two justifications, surface heat flux forcing was chosen as the main variable to achieve surface densification through sea ice growth and brine rejection. This was supplemented by a constant rate of precipitation in the form of snow to maintain observed thicknesses for insulation of sea ice (and as a possible restoring force for open ocean areas). It was hoped that the thermal barrier and thermal flywheel effects would make the model sufficiently robust in the face of large changes in both magnitude and variability of surface heat fluxes, allowing for a wide variety of surface heat flux forcing conditions to be investigated.

1. Base Model Formulation

High resolution numerical modeling of the eastern Weddell Sea in the vicinity of Maud Rise was conducted using the MIT General Circulation Model (MITgcm) as detailed in Marshall et al. (1997a, b). This model solves the incompressible Boussinesq equations of motion with the nonlinear equation of state given in McDougall et al. (2003). Model geometry consisted of a volume comprising 320 grid points in the zonal and 256 grid points in the meridional directions, 31 grid points in the vertical, in a spherical-polar coordinate system. The overall model domain was further subdivided into a "domain of interest" consisting of 148 grid points in the zonal and 128 grid points in the meridional directions (Figure 3.3). The remaining volume of the larger domain was used to minimize open boundary edge effects, ensure that overall background flow remained consistent throughout each model run, and prevent in-flow advection from dominating conditions in the smaller domain.

In the domain of interest, model resolution was 0.1° in the horizontal directions with meridional spacing equal to ~11 km and zonal spacing varying from ~4 km at the southern boundary to ~6 km at the northern boundary, framing a horizontal area representing 59° S to 71° S and 6° W to 8° E. Vertical layer thicknesses for the upper four layers were 4, 6, 8, and 10m with seven layers equal to 12m below these. The thickness of each successive, deeper layer was ~125% of the height of the layer preceding

it for a total mean depth of $5500m$. This layer thickness scheme provided increased granularity in the high-gradient near-surface levels of interest while avoiding an excessive number of levels at the deeper, lower-gradient depths, thus reducing computational cost. An idealized, Gaussian seamount was used to represent Maud Rise. It was centered at $(x, y) = (189, 112)$, representing 65° S, 2.5° E with a radius of 28 grid points at the $5000m$ isobath, rising to a peak at depth $2000m$. The ocean bottom was further altered by randomizing the bathymetry at each grid point within a range of $\pm 200m$, smoothed over three grid points. The bathymetry and seamount are depicted in Figure 3.4.

The model was initialized with values based on idealized austral winter climatology typical to the region investigated. Vertical profiles of initial temperature, salinity, and potential density anomaly are shown in Figure 3.5. Mean surface salinity was $34.4\,psu$ and mean surface temperature was $-1.89\,°C$. Initial mixed layer depth was set at $76m$. Below the mixed layer, salinity and temperature increased with depth to values of $34.7\,psu$ and $0.65\,°C$ at $200m$ to yield an initial density ratio (R_ρ^*) range of 1.6 to 2.8 throughout the column. Gradual smoothing of the salinity and temperature profiles from $200m$ downward provided a transition into the lower, stable region of the model that begins at a depth of $500m$. Density ratios in this intermediate region ranged from 1.6 to 2.5. Thus, the upper 20 levels of the model were dominated by conditions commonly found in high-latitude regions marked by negative gradients of both salinity and temperature where diffusive convection prevails.

Dynamic and thermohaline forcing was provided by zonally constant, meridionally varying wind stress, time-dependent surface heat flux, and constant freshwater flux in the form of snow precipitation. Winds were based on idealized climatology for the region and are constant through the model run (Figure 3.6). Air temperature was set at $-10\,°C$. The model was initialized with and maintained a constant $-0.05\,ms^{-1}$ zonal barotropic flow (negative value indicating westward flow). A baroclinic flow of $-0.01\,ms^{-1}$ was induced by maintaining a north-south salinity gradient. Net surface heat flux was prescribed under four general schemes: a constant net surface

heat flux, a high-slope, gradual linear increase as the model integrated forward, a low-slope gradual linear increase in time, and a periodic, cyclical net surface heat flux representing idealized annual variation. More specific details on surface heat flux forcing appear in the next section. Snow precipitation was $5 \cdot 10^{-10}$ ms^{-1} throughout each run and constituted the sole freshwater input.

The open boundaries of the model were prescribed to initial values for temperature, salinity, zonal velocity, sea ice concentration, and sea ice thickness and remain constant throughout each model run. An exponentially decaying relaxation of these same conditions alleviated model irregularities near the open boundaries and had no significant effect on the interior region of interest. Flow enters the open boundary at the east and exits the model domain through the open boundary to the west. The Gaussian seamount representing Maud Rise was placed an adequate distance away from the eastern boundary to prevent the advection of prescribed tracer values from dominating the domain of interest. This distance is sufficient to allow surface heat flux forcing to bring the model into an equilibrated state prior to flow entering the domain of interest (and impinging on the seamount). In this way, the model can employ prescribed open boundaries, a regional flow, and surface forcing in such a way that phenomena of interest are free to develop in the time-domain as a natural consequence of ocean physics and changes in the parameters being investigated.

The nonlocal K-Profile Parameterization (KPP) scheme of Large et al. (1994) was used to model boundary layer and internal vertical mixing processes, including double-diffusion. In this formulation, interior mixing is governed by shear instability, internal wave activity, and double-diffusion (when employed). A boundary layer depth is determined for each grid point by comparing the bulk Richardson number with the critical value of 0.3. Mixing is enhanced in this boundary layer and the boundary/interior layer profiles are matched at the boundary allowing boundary layer properties to penetrate into the interior layer and *vice versa*. Furthermore, a non-local term that is independent of vertical gradients enhances mixing under conditions of water column instability. The KPP scheme has been compared to observations (Large et al. 1997) and is used in many ocean models.

41

All models used free drift sea ice dynamics and the "zero-layer" thermodynamics of Semtner (1976) with a lead-closing parameter (Hibler 1979) of $0.1m$ instead of the model default of $0.5m$ (in light of Smedsrud and Martin 2015). Surface heat flux is computed following Parkinson and Washington (1979) and Manabe et al. (1979).

2.   Specific Model Formulations

Variations in model heat flux forcing at the surface boundary and vertical mixing schemes characterize the main differences in the models used in this study. These differences can be organized as a taxonomy of model types following a classification along three axes. First, models were constructed with either "fixed" or "free" surface heat flux forcing. Models with fixed surface heat flux forcing had heat flux to the atmosphere completely prescribed, with no allowance for variations in heat flux at the air-ocean or air-ice interface outside those prescribed. Models with free surface heat flux forcing, on the other hand, were forced as in the fixed cases with a prescribed surface heat flux across the interface, but also included physics that applied latent and sensible heat fluxes as well as a net longwave heat flux that freely varied as surface conditions warranted. Shortwave heat flux was not included in the "free" formulation due to its primary role as an inducer of negative density flux at the surface. As such, shortwave radiation would have opposed the cooling of the surface levels, acting against the overall scheme of using surface heat fluxes as the primary densification mechanism in the model. The "free" models allowed for differences in surface heat fluxes to the atmosphere as sea ice conditions varied. Each component of surface heat flux forcing is given below.

Sensible heat fluxes are given by

$$Q_{sh} = C_D c_p \rho_{air} U (T_{air} - T_{surf})$$
(3.2)

where $C_D = 1.75 \cdot 10^{-3}$ is the heat transfer coefficient for "free" models ($C_D = 0$ for "fixed" models), $c_p = 1004 \, J \, kg^{-1} K^{-1}$ is the specific heat of air, $\rho_{air} = 1.3 \, kg \, m^{-3}$ is the air density, U is wind speed at the sea surface $(m \, s^{-1})$, and the difference in atmospheric and sea surface temperature (K) appears last.

42

Similarly, latent heat flux is

$$Q_{lh} = C_D h_l \rho_{air} U \left(q_{air} - q_{surf} \right), \tag{3.3}$$

with $h_l = 2.5 \cdot 10^6 \ J \, kg^{-1}$ is the latent heat of evaporation and the difference in atmospheric humidity and specific humidity at the surface $(kg \ kg^{-1})$ appearing last.

Net longwave heat flux for each model is

$$Q_{lw} = Q_{pr} + c_f \varepsilon \sigma T_{surf}^4 \tag{3.4}$$

with Q_{pr} the prescribed longwave flux (Wm^{-2}), ε the surface emissivity, σ the Stefan-Boltzmann constant $(5.67 \cdot 10^{-8} \ Wm^{-2} K^{-4})$, and T_{surf}^4 the surface temperature to the fourth power. The variable c_f controls net longwave flux over that prescribed. In the "fixed" models c_f is zero and in the "free" models $c_f = 0.03$. In the "free" models, a net 3% of the outgoing longwave radiation is added to the longwave radiation that is prescribed. Or, put another way, back radiation equals 97% of calculated outgoing longwave flux in the "free" models. The terms "fixed" and "free" are used to differentiate the surface heat flux forcing in these model types from the next series of parameter choices that follow.

All models included a prescribed surface heat flux in the form of longwave radiation. The exact type of prescription forms the second classification in our model taxonomy. Four types of surface heat flux forcing were used, based on how this forcing varied in the time domain: steady; high-slope, linearly increasing; low-slope, linearly increasing; and seasonal. The first three were forced with outgoing longwave radiation while the seasonal types were forced with heat flux that oscillated between heating and cooling the ocean surface. Models with "steady" forcing saw no change in initial surface heat flux forcing with time. This model type can be thought of as "zero-slope" since surface heat flux forcing remained steady throughout each run. High-slope, linearly increasing models started with an initial surface cooling with the magnitude of outgoing longwave flux linearly increasing with time. High-slope, linearly increasing models were divided into two subtypes, those that started with sea ice covering the model domain and

43

those without. The low-slope, linearly increasing models were initialized and run as the steady models until a predetermined point in time. After this time, surface heat flux forcing was increased linearly with time, but at a slower rate as compared to the high-slope models. These low-slope, linearly increasing models were developed after analyzing initial steady and high-slope runs and the rationale behind their inclusion in this study will be discussed in more detail below. Seasonal model surface heat flux forcing varied during each model year according to idealized monthly values. Two subtypes of seasonal models were employed, one in which the time-integral of net surface heat flux remained constant during each year and another that experienced a linear increase in the time-integral as the model integrated forward. In all cases, the surface of the entire domain was uniformly forced by the prescribed heat flux at any given time.

The third main set of differences between models, and perhaps the most important for our study, involves the presence or absence of both turbulent diffusivity and double-diffusive mixing. Given these two dichotomies, four types of models naturally suggested themselves: (1) no turbulent diffusivity and no double-diffusion, (2) no turbulent diffusivity with double-diffusion, (3) non-zero turbulent diffusivity without double-diffusion, and (4) non-zero turbulent diffusivity with double-diffusion. The first case is hardly interesting and would yield no useful information for this investigation, so it was not considered. The remaining cases offered three distinct environments for vertical mixing. The first is a purely double-diffusive regime while the second is a purely turbulent one. These two choices represent idealized cases in which differences between the two could, perhaps, be brought into stark contrast. The third, hybrid, case more closely models the region studied and promised to be the most illustrative (even if possibly producing more ambiguous or subtle results). In the end, all three cases were used, with the results of the first two cases framing those of the last.

These model differences in overall surface heat flux forcing formulation, time-dependent surface heat flux variation, and vertical mixing parameterization, including the subtypes mentioned above, define the 45 distinct models used in this study. All specific model formulations are numbered and these designations are summarized in Table 3.1. In

addition, a letter following each numbered model designation denotes which of the three turbulent/double-diffusive cases was used for that model.

C.   MODEL RESULTS AND OBSERVATIONS

What follows is a systematic description of model results. First, the model characteristics common to all runs are detailed. After this, each model type is explored, steady, high-slope, low-slope, and seasonal. Within each section covering type, results will be compared between fixed and free runs and between runs varying in turbulent/double-diffusive parameterization.

1.   General Model Characteristics at Steady State

A base model of this area must approximate conditions of the eastern Weddell Sea in the vicinity of Maud Rise as closely as possible if useful information is to be gained. Marginal water column stability is a prevalent, defining feature of the region. The model also needs to represent the basic elements of the thermal barrier processes (Martinson 1990), which maintain thin ice conditions over a range of internal and surface forcing. Characteristics common to all models in the series form the dynamic and thermodynamic basis upon which variables in model ocean physics can be explored. General model characteristics must conform to these observed conditions, even if a full simulation is not used. In this way, a high-resolution model of intermediate complexity can yield insights without having the peculiarities of the region overwhelm the key processes being investigated.

To provide examples of general model characteristics, Model 24A will be used. This model has free, steady surface cooling and zero turbulent diffusivity with double-diffusive mixing parameterization included (Table 3.1 lists all models with keyword designations). The particular choice of model is not important as the characteristics covered in this section are exhibited by all other models as well.

After initialization, the model reaches tracer and momentum equilibrium quickly, as shown in Figure 3.7 and Figure 3.8. For these plots, a location near the seamount was avoided as this location is extremely dynamic and would not be representative of the

45

overall ambient conditions found elsewhere. The time-progression of tracer and momentum values in areas of near-constant bathymetry are better indicators that the model has equilibrated. For this reason, equilibrium model diagnostics at each year of the model run were based on mean values that were located well away from the seamount.

Although the entire domain is forced with a zonal, westward flow, the current pattern develops meridional components near the seamount. Figure 3.9 illustrates surface currents at year 10 of Model 24A. Velocities north of the seamount peak at values of up to $0.2\,ms^{-1}$, three times the mean velocity of surface current (as predicted by Chapman and Haidvogel 1992). Magnitudes of velocities to the south are higher as well, reaching approximately double the domain mean. Magnitudes of velocity approach zero directly over the seamount; this feature represents the Taylor cap that persists over Maud Rise (Muench et al. 2001, McPhee et al. 2006, De Steur et al. 2007, Shaw and Stanton 2014). Relative vorticity due to both curvature and shear of the surface current field further highlights the area of the seamount (Figure 3.10). Finally, a meridional cross-section of zonal velocity (Figure 3.11) shows that these surface features are also represented at all depths.

Representative cross-sections of salinity, potential temperature, and potential density along the same meridian at year 10 of Model 24A are depicted in Figure 3.12, Figure 3.13, and Figure 3.14, respectively. These figures illustrate some important qualitative similarities in all models but are not meant to infer that these particular values or specific features appear across every model run. It can be seen that the halocline, thermocline, and pycnocline are very well-defined, with strong gradients, outside of the vicinity of the seamount. Salinity, temperature, and potential density values in these locations illustrate the "Ambient" conditions discussed in Shaw and Stanton (2014). Conditions over the seamount are more in keeping with "Halo" or Taylor cap conditions (De Steur et al. 2007, Shaw and Stanton 2014). Figure 3.15 displays three potential density profiles, one well south of the seamount, another directly over the peak, and a third between these two. Differences in potential density across the pycnocline vary from

approximately $0.03\,kg\ m^{-3}$ directly over the seamount to $0.1\,kg\ m^{-3}$ in waters representing Ambient conditions.

But why this is so? The early years of model integration are marked by a cooling-induced increase of sea ice concentration and thickness throughout the domain with corresponding brine rejection. Background flow is unimpeded in the Ambient region of the domain, enhanced north of the seamount, and brought to a near-standstill over the seamount (Figure 3.9 and Figure 3.11). With these conditions, we would expect salinity to increase at a rate faster than the increases in the Ambient region (while salinities would be less north of the seamount). Figure 3.16 illustrates surface salinity for Model 24A at year 10 and shows this to be the case. Higher salinities above the seamount produce higher densities with a correspondingly weaker pycnocline above the representation of Maud Rise. Thus, modeled potential density differences across the pycnocline in Ambient and Taylor cap areas are comparable to observed values in the region (De Steur et al., 2007; Shaw and Stanton, 2014).

Stability regimes classified by Turner angle (Ruddick 1983) are shown in Figure 3.17. A meridional cross-section of Model 24A at year 10 (Figure 3.18) depicts the locations of these stability regimes relative to the seamount. As with the previous cross-sections of salinity, temperature, and potential density, this plot highlights some qualitative observations about the model series in general. Initial temperature and salinity profiles produce a mixed layer to $76m$, an upper region of diffusive convection, and a lower region of stability with an interface at approximately $500m$. As each model integrates forward, the volume above the seamount and downstream from it experiences more dynamic changes in stability when compared to other areas in the domain with near-constant seafloor depth. As can be seen in this figure, a volume of marginal stability has developed above the seamount.

Models in the series equilibrate quickly, settle into expected current patterns, and exhibit observed variations in salinity, temperature, and potential density gradient by region. These characteristics are common to all models and provide the foundation upon which a systematic exploration of the effects of double-diffusive mixing on column

47

stability and sea ice cover in the vicinity of Maud Rise can be conducted. The following sections are organized by the type of surface heat flux forcing used (Table 3.1), starting with the basic case of a steady surface cooling, ending with the most complex—a seasonally varying surface heat flux with a linearly increasing time-integral of net cooling.

2.   Constant Surface Heat Flux Forcing

The first cases to examine are also the simplest in terms of the time-domain variation in surface heat flux forcing. Models 17, 18, 24, and 25 have steady surface cooling with Models 17 and 18 having the "fixed" surface heat flux condition and Models 24 and 25 having a prescribed, zero-slope cooling with sensible, latent, and net longwave heat flux that freely varied as conditions warranted.

The fixed and free models will be examined in turn.

a.   *Fixed Surface Heat Flux*

Time series of sea ice concentration, sea ice thickness, and the mean potential density at two depths are given by Figure 3.19 for Model 17A. Each times series was produced by taking the mean of the 121 values found within five grid points in both horizontal directions at $(189,112)$, which marks the summit of the Gaussian seamount representing Maud Rise (at 65 S, 2.5 E). This "summit areal mean" is used for all time-series plots to follow. Sea ice concentrations are given as a percentage while sea ice thickness is in meters. Mean potential densities at $10m$ and approximately $1000m$ are shown as well. The difference between these mean potential densities serves as a proxy to determine when convection over the seamount has initiated. The criterion used to make the determination of convection is

$$\Delta \rho_{conv} = \overline{\rho}_{1000} - \overline{\rho}_{10} < 0.005 \; kg \; m^{-3} \tag{3.5}$$

with the overbar notation denoting the mean described above and subscripts indicating the depth in meters of that particular calculation of the mean. The value of $0.005 \; kg \; m^{-3}$ was chosen as it is significantly smaller than the smallest typical potential density

difference across the pycnocline in this region ($\sim 0.02 \, kg \, m^{-3}$), but not so small as to make this determination impossible (due to intrinsic variability). Figure 3.20 compares this measure of convection onset time with the expected increase in temperature and salt diffusivities and vertical velocities for Model 25C. Similar comparisons for other models (not shown) indicates that our criterion correctly captures the onset of deep convection. Thus, the layout of Figure 3.19 allows for a quick identification of polynya formation and the initiation of convection over the seamount and this layout will be used when analyzing the models to follow.

The fixed, steady models (17 and 18) are characterized by a rapid equilibration followed by near-stasis in sea ice concentration, sea ice thickness, and mean potential densities. Convection did not occur in the domain of interest, either over the seamount or elsewhere. These results are summarized in Figure 3.19 through Figure 3.23. Although these fixed, steady surface flux forcing models did not produce convection over the seamount, they were important to illustrate that an overall equilibrium could be reached by the model.

However, one important and significant feature appearing in all six models of this series is a region of thin sea ice situated directly over the horizontal area above the model's version of Maud Rise. Figure 3.24 and Figure 3.25 illustrate this feature at year 14 for Model 18A as it is reflected in sea ice concentration and sea ice thickness, respectively. The Ambient area (as described in Shaw and Stanton 2014) experiences sea ice concentrations of greater than 85% and sea ice thicknesses of 0.4m to 0.6m. The Ambient area has a near-constant bathymetry with depths of $5500 \pm 200m$ (see Figure 3.4). However, in the vicinity of the seamount, where bathymetry is varied, reduced sea ice concentrations and thicknesses are evident (cf., Lindsay et al. 2004, De Steur et al. 2007, and Lindsay et al. 2008) and markedly lower when compared to the Ambient region. Within the Taylor cap, sea ice concentrations diminish to approximately 30–60% while thicknesses are only 0.01-0.07m.

These model results may indicate that the thermal barrier feedback mechanisms in the Ambient region are better able to balance the densification brought on by surface

cooling with subsurface thermal and haline density fluxes across the pycnocline. Model sea ice thicknesses in the Ambient region match observations and are steady. However, in the Taylor cap region above the seamount there are several indicators that the thermal barrier effects may not be able to prevent an eventual melting of sea ice and subsequent onset of convection indefinitely. Temperature and salt diffusivities in the water column above the summit are significantly higher than those found in the Ambient region (Figure 3.26). Low density ratios (Figure 3.27) and layers exhibiting convection (Figure 3.28) are further indicators. Thin sea ice above the seamount in this model could be interpreted as either the product of a balance distinct from that of the Ambient region or the foreshadowing of polynya formation.

b. *Free Surface Heat Flux*

Unlike the fixed models, the free models (24 and 25) go ice-free over the seamount early into each run. The onset of convection in each model, however, does not necessarily occur in conjunction with this event (or ever).

The time series for Models 24 (A, B, and C) begin with Figure 3.29. As a "free" model, Model 24 had non-zero coefficients for sensible (3.2), latent (3.3), and net longwave (3.4) heat fluxes along with an additional prescribed cooling (Q_{pr}) in the form of longwave radiation at a rate of $1\,Wm^{-2}$. Model 24A produced a polynya over the seamount, which persisted for the entire run. Figure 3.29 shows that the summit areal means of sea ice concentration and thickness went to zero by year 4. However, there was no onset of convection as $\Delta\rho_{conv}$ settled at $\sim 0.04\,kg\,m^{-3}$ by year 10. Similarly, Models 24B and 24C produced ice-free areas above the seamount, but the extent and duration of these polynyas were sporadic. Figure 3.30 shows that the sea ice thickness varied between 0 to $0.01m$ with corresponding sea ice concentrations. Model 24A and 24B both have double-diffusive mixing parameterization and $\Delta\rho_{conv} = 0.04\,kg\,m^{-3}$ in Model 24B (just as in 24A). Model 24B also shows similarities to the results of Model 24C, with both having a non-zero turbulent diffusivity. Model 24C (Figure 3.31) first goes ice-free above the seamount at year 10, but has a greater occurrence of zero sea ice concentration

and thickness compared to 24B. The difference in potential densities at depths $10m$ and $1000m$, $\langle \Delta \rho_{conv} \rangle = 0.035 \; kg \; m^{-3}$, is slightly lower than both 24A and 24B sometimes going as low as $0.025 \; kg \; m^{-3}$. It is interesting to note that Models 24A, 24B, and 24C all mirror the observed potential density differences across the pycnocline in the Maud Rise Taylor cap (Shaw and Stanton, 2014).

Sea ice concentration (Figure 3.32) and sea ice thickness (Figure 3.33) at year 14 of Model 24B's run shows three distinct regions characterized by differences in these parameters. Overall, Ambient ocean conditions produce sea ice having a concentration of 100% and thicknesses of $0.4m$ to $0.6m$. A central area, directly above the seamount contains a polynya and this is encircled by a halo of intermediate sea ice concentration (~50%) and thicknesses (better shown by Figure 3.33b). Curiously, the double-diffusion-only model (24A) and the turbulent diffusion-only model (24C) do not produce this intermediate area (it is simply part of a larger polynya).

Note that the three runs that constituted Model 24 have an integration time of 40+ years (whereas all other steady runs discussed in this section are 17–19 years long). The run time on these models was extended to preclude the possibility that a short run time was responsible for the lack of convection. However, even with this increase in model integration time, Model 24 did not go convective.

The same cannot be said for Model 25. Each run in Model 25, with a higher prescribed longwave cooling $(Q_{pr} = 5 \; Wm^{-2})$ along with sensible, latent, and net longwave fluxes, went convective by year 4. The higher values of surface heat flux to the atmosphere in this model led to more rapid sea ice formation, brine rejection, and a faster rate of surface densification. This increased magnitude of external forcing, led to a breakdown of the thermal barrier (discussed in Section A), resulting in the onset of convection. Figure 3.34 displays the time series for Model 25A. This run began like the previous steady runs, but instead of settling into a near-constant, non-zero $\Delta \rho_{conv}$, the potential densities converge by year 4. This, of course, is the unmistakable onset of deep convection in the column over our Maud Rise simulacrum. Model 25B displays a similar

pattern (Figure 3.35). In both cases, sea ice concentration and thickness reach zero by year 3 with convection occurring a year later. By contrast, Model 25C (Figure 3.36) sees polynya formation and deep convection occur during the same year. Temperature and potential density profiles for Model 25C both before and after the initiation of convection illustrate the significant loss of deep heat and reduction of the cross-pycnocline density difference to negligible values over the seamount (Figure 3.37).

c. Summary of Steady Forcing Models

Equation (3.4) gives two terms for surface heat flux forcing. Regarding the first term, half of the steadily forced models (17 and 24) are cooled with $Q_{pres} = 1\,Wm^{-2}$ while the other half (18 and 25) experience $Q_{pres} = 5\,Wm^{-2}$. Also, surface cooling in fixed models (with $c_f = 0$) is less than that of free models $(c_f = 0.03)$, as the second term is non-zero for free models. Model 25 $(Q_{pres} = 5\,Wm^{-2}, c_f = 0.03)$ alone saw the onset of convection over the seamount indicating that the lower magnitudes of steady cooling were not sufficient to bring about the densification required to initiate deep convection. Figure 3.38 shows the surface heat flux entering the atmosphere for each steady model out to year 14 for comparison.

Noteworthy within the three runs of Model 25 is the fact that both models having double-diffusion parameterization experienced an onset of this convection approximately one year later than the first ice-free year. Model 25C, a model without double-diffusion, had an ice-free ocean and deep convection above the seamount occur at the same time (Table 3.2). Could double-diffusion be delaying the onset of convection? To further investigate this possibility, the next series of model runs incorporated a linearly increasing Q_{pr} while keeping the same "fixed" and "free" distinctions defined by the coefficients in the surface heat flux equations given in Section B.2.

3. High-Slope, Linearly Increasing Surface Heat Flux Forcing

As set forth in Section B.2, high-slope, linearly increasing models were of the fixed and free variety and further divided on the basis of models with initial sea-ice and

those without. These four possibilities, with each having one of three mixing schemes, gives us another 12 models with which to investigate the effects of a linearly increasing cooling on the onset of convection during polynya events.

Models initialized with sea ice started with 100% concentration and a thickness of 0.5m. This concentration and thickness is typical of the Ambient areas of the steady-forcing models previously detailed. Models initialized without sea ice had zero concentration and thickness, naturally. These two starting conditions will be referred to as "icy start" and "ice-free start" below. All models in this section experienced an initial cooling (through Q_{pr}) of 1Wm^{-2} with a linearly increasing cooling of +1$Wm^{-2}yr^{-1}$.

Referring to Table 3.1, Models 14 and 20 had fixed flux with an ice-free and icy start, respectively. The free flux models were Models 26 (ice-free) and 27 (icy). As in the previous section, fixed flux model results will be detailed before free flux model results.

a.   Fixed Surface Heat Flux

The linearly increasing, fixed surface heat flux models (i.e., those models without sensible, latent, and the additional net longwave heat fluxes) produced results that further substantiate the claim that diffusive convection form of double-diffusion may be effective in delaying the onset of deep convection in areas of marginal column stability. Models 14 and 20 saw the two double-diffusive models (A and B of the three) delay this convection. Delays manifest as a "lag time" in the onset of deep convection after polynya formation and also in overall model integration time required for the onset of convection over the seamount.

Model 14A, a purely double-diffusive model without turbulent diffusivity, first went ice-free above the seamount representing Maud Rise by year 5 (Figure 3.39). Our indicator for convection, $\Delta\rho_{conv}$, slowly decreases over the course of the model run, even after polynya formation. This occurs due to the combined effects of the increased upward heat flux in conjunction with the negative density flux caused by double-diffusion. Mean sea ice concentration and thickness becomes non-zero through years 7 to 13, but even after resuming ice-free conditions, the onset of convection does not occur until year 16

53

(when $\Delta\rho_{conv}$ goes below the threshold). Model 14B (Figure 3.40) displays similar behavior. Model 14B shares the double-diffusive parameterization of 14A, but has turbulent diffusivity ($\kappa_{turb} = 2\cdot10^{-5}\,m^2s^{-1}$), unlike 14A. The area above the seamount is ice-free by year 4 and experiences convection by year 16. By contrast, Model 14C (Figure 3.41), with turbulent diffusivity only, behaves in a significantly different fashion from its double-diffusive counterparts (14A and 14B). Sea ice continues to thicken until year 12, when the drop-off of sea ice concentration, thickness, and $\Delta\rho_{conv}$ occur simultaneously.

To summarize, Models 14A and 14B go ice-free early (years 5 and 4, respectively), experience an intervening period (the "lag time" mentioned above) of 11 and 12 years of variable sea ice conditions before going convective at year 16. Model 14C, on the other hand, experiences sea ice thickness increases during this same time and experiences no lag time between a zeroing out of sea ice concentration, thickness, and $\Delta\rho_{conv}$. Model 14C goes convective two years earlier overall as well, as compared to Models 14A and 14B.

Model 20 (icy start) differs from Model 14 (ice-free start) but still exhibits the same trends of previous models. In Model 20A (Figure 3.42), sea ice steadily diminishes and is gone by year 10. However, the $\Delta\rho_{conv}$ threshold of $0.005\,kg\ m^{-3}$, signifying convection, is reached between years 14 and 15. Model 20B (Figure 3.43) is very similar with sea ice concentration and thickness also reaching zero at year 10. Convection begins five years later as well. As expected, Model 20C (Figure 3.44), does not go ice-free at year 10, but instead experiences a slight thickening of sea ice starting at year 8, which lasts until year 12. The onset of convection and the elimination of sea ice both occur by year 14.

Qualitatively similar to Model 14, the Model 20 double-diffusive runs (A and B) experience an ice-free surface earlier than the purely turbulent run (C). The period of time between ice-free conditions and the onset of convection is five years in the icy-start cases (about half the time of ice-free start models). Like its ice-free start counterpart,

Model 20C has no lag time, going convective as sea ice simultaneously disappears. Model 20C also experiences convection earlier overall than Models 20A and 20B (albeit slightly earlier).

b.   *Free Surface Heat Flux*

Similar to the steady forcing "free" models (Section 2.b), these models go ice-free over the seamount early into each run. Unlike the steady cases, the initiation of convection is always nearly coincident to the area above the seamount going ice-free.

All three variations of Model 26 (ice-free start) go convective at year 5. In the case of the double-diffusive models (Figure 3.45 and Figure 3.46), a polynya forms one year prior. Convection coincides with this event for Model 26C (Figure 3.47). Model 27 (icy start) sees open ocean above the seamount at the same time convection commences for all three models by year 8 (Figure 3.48 to Figure 3.50).

c.   *Summary of High-Slope, Linearly Increasing Heat Flux Forcing Models*

Models 14A and 14B (with double-diffusion) are effective in transporting heat upward to prevent or eliminate sea ice (Figure 3.39 and Figure 3.40) but have a delayed onset of deep convection. In the case of Model 14C (no double-diffusion) sea ice grows in both extent and thickness (Figure 3.41) as the model integrates forward. Only after convection is initiated does sea ice concentration and thickness quickly fall to zero. Model 20 follows these results yielding similar observations.

Sensible, latent, and net longwave heat fluxes in free models consistently add up to an additional 10 Wm^{-2} to Q_{pr} resulting in significantly higher values of surface cooling. Figure 3.51 plots the increasing surface heat flux to the atmosphere for the four linearly increasing models using the A case in each model as the example. Heat fluxes are not significantly different for the B and C cases, so this one figure represents both results.

The rapid onset of convection is most likely attributed to the larger values of surface cooling in the free models. Model 26 saw this even occur at year 5 while Model 27 at year 7 (for A) and 8 (B and C). Surface cooling was less in Model 27 for the first

six years of the model run; this may account for the onset of convection occurring two to three years later. There were little significant differences between double-diffusive and turbulent-only runs in these models with larger cooling. These observations led to the development of the next series of models. In the following section, a steady-starting, linearly increasing surface heat flux model with a smaller slope will be used to augment the results from the previous two types of models. It was hoped that this model, with its initially steady forcing and smaller slope, would be better able to capture any differences in polynya formation and convection initiation that might be due to double-diffusive convection.

The model results for this section are given in Table 3.3.

4.   Low-Slope, Linearly Increasing Surface Heat Flux Forcing

The designation of low-slope, linearly increasing is a bit of a misnomer, as it does not fully describe how surface heat flux forcing was implemented in this set of model runs. Each of these six runs (21A/B/C and 30A/B/C) were initialized with $1\,Wm^{-2}$ and no sea ice cover. All models were integrated forward for 15 years, with this surface heat flux forcing held constant (as in the "steady" cases in section C.2). After year 15, surface heat flux was increased by $0.25\,Wm^{-2}yr^{-1}$. Model 21 is the fixed surface flux forcing model of the set, while Model 30 was forced with sensible, latent, and net longwave fluxes above those prescribed.

a.   The Fixed Surface Heat Flux Model

The fixed flux model required exceptionally long integration times before the onset of convection. Figure 3.52 shows the three familiar time series for Model 21A. Sea ice thickness grew during the first 15, steady, years of the run while concentration remained approximately 50%. After cooling began its yearly climb, mean thickness diminished, finally reaching zero at year 29, indicating open ocean above the seamount. The density difference in the column steadily lowered until year 70, when the potential density time series converged. Model 21A produced the longest lag time (i.e., time between zero ice and convection) of any model in this study. Models 21B (Figure 3.53)

and 21C (Figure 3.54) were dissimilar to Model 21A, but similar to each other. These two models maintained sea ice cover for much longer than 21A, a total of 65 years for 21B and 64 years for 21C. Convection occurred six years after for 21B and only two years after open ocean conditions for 21C.

b.   The Free Surface Heat Flux Models

Whereas Model 21 produced the longest lag time, Model 30 produced the most surprising and anomalous results. The plots for Model 30A (Figure 3.55) are comparable to those of 21A. Sea ice cover is completely gone early, by year 3 and convection follows at year 19, giving, once again, a long lag time. Model 30B (Figure 3.56), with both double-diffusion and a non-zero turbulent diffusivity, sees sea ice concentrations reach zero at years 8 and 14 with the first multi-year period of open ocean starting year 19. Sea ice thickness from year 8 on hovers slightly above zero as concentration fluctuates to year 19. The model reaches the definition of convection ($\Delta\rho_{conv} < 0.005\ kg\ m^{-3}$) at year 21. If the open ocean year can be said to be year 8, this yields a 13 year lag time for this model.

Model 30C defied all expectations. As Figure 3.57 documents, open ocean occurs at year 9, but convection is initiated at year 21, giving an unprecedented 12 year lag time for models of this type. All models without double-diffusion, up to this point, have seen convection occur no more than two years after a polynya is formed, and in most cases immediately after. Model 30C provides an anomalous case of a turbulent-only model experiencing the early onset of a polynya without the column over the seamount quickly moving into a convective state.

The perplexing results of Model 30 prompted a further investigation into the low-slope, linearly increasing cooling conditions for the free model types. Model 31 was designed to be an intermediate model between the low, steady surface flux forcing case, Model 24, and Model 30, the linearly increasing case. The increasing surface cooling was prescribed to be $0.125\ Wm^{-2}yr^{-1}$, halfway between the no-slope and low-slope of surface cooling. The no-slope, steady version never went convective in any case (Model 24), while all three went convective in the low-slope case (Model 30). All six, however, went

ice-free early in the model run between years 4 and 10. Model 31 began with an ice-free start, an initial cooling of $1\,Wm^{-2}$ with the aforementioned increase of $0.125\,Wm^{-2}yr^{-1}$.

Figure 3.58 shows results for Model 31A, the purely double-diffusive model with zero turbulent diffusivity. Polynya formation occurs early, just as in Model 30A, by year 4. Model 31A comes close to meeting the chosen threshold criterion of $\Delta\rho_{conv} < 0.005\,kg\,m^{-3}$ but maintains a difference in potential densities at 10m and 1000m of 0.006 to 0.01 $kg\,m^{-3}$ until model termination. However, if we consider the "bottleneck" at year 9 in Figure 3.58 to be the point of convection, then this model has a lag time of five years between an ice-free surface and the onset of convection. If we rigidly enforce our chosen definition, however, the model never goes convective.

Models 31B and 31C are similar to each other. Model 31B (Figure 3.59) experiences its first ice free year after nine years of model integration. Unlike Model 31A, the threshold is reached, and this model experiences convection in the column above the seamount by year 12. Model 31C, like 31B, is ice-free above the seamount at year 9. The criterion for convection is met by year 12, but by year 13, the difference in potential density rises slightly higher than the maximum allowed.

Model 31 produces slightly less ambiguous results. If we relax the condition for convection, then Model 31A had a lag time of five years, while Models 31B and 31C had three years between ice opening and convection occurring. This offers additional evidence, admittedly weak in the case of these particular models, that double-diffusion does act to offset convection after polynya formation.

c.   *Summary of Low-Slope, Linearly Increasing Surface Heat Flux Models*

Table 3.4 provides the model results of Models 21, 30, and 31. Comparison of Models 21 and 30 further emphasizes the differences between the models with prescribed cooling only (fixed) and those with other forms of surface heat fluxes (free). Examining Figure 3.38, Figure 3.51, and Figure 3.61, one can see that adding in sensible, latent, and additional longwave surface heat fluxes causes little variation in cooling, but adds a substantial amount of net cooling over the models having prescribed heat flux only.

Adding sensible, latent, and an additional net longwave heat flux simply increases the overall cooling at the surface, with no substantial change in the prescribed slope of that cooling. This would seem to indicate that these models do not necessarily require other forms of surface heat flux and prescribing higher values of cooling could have the same effect. The thermal flywheel (McPhee et al. 1999) and thermal barrier (Martinson 1990) negative feedback mechanisms are well-represented in the every model up to this point, evidenced by how well the basic model formulation handles the large changes in both magnitude and variability of surface heat fluxes in the series.

More cooling, however, does tend to bring on convection on faster, perhaps so fast that no discernable difference can be detected between models with double-diffusion parameterization and those without. The ramifications of these onset times and overall energy lost to the atmosphere will be discussed in Section D.

d.   *From Cooling-Only to Seasonal Variation*

All models up to this point have experienced surface cooling at all points in time as the model integrated forward. The models in the next section had a significantly different surface heat flux prescription scheme than the previous models. Because the Weddell Sea polynya was a multi-year phenomenon, a seasonally varying surface heat flux (with both heating and cooling) based on an idealized climatology was developed to investigate how sea ice cover varies seasonally and how this seasonal variation might affect the onset of deep convection.

5.   Seasonally Varying Surface Heat Flux Forcing

Up until this point, simplified cooling schemes have been used to stimulate sea ice formation and enhance densification of surface water. Model runs in the previous three sections have been forced with relatively low values of heat flux over extremely long times in an effort to determine the differences in onset times for both polynya formation and open ocean deep convection. This section describes the results from the final series of model runs (16, 19, 28, and 29) in which a monthly varying surface heat flux forcing was used. This monthly forcing was based on monthly mean heat flux to the atmosphere over a fully ice-covered ocean between 60S and 70S (from Gordon 1981) with time and

amplitude set such that overall net annual surface heat flux was equal to $0\,Wm^{-2}$. This baseline forcing is shown in Figure 3.62.

The values in Figure 3.62 represent a monthly varying form of Q_{pr} in Equation (3.4). Model 16 uses this as its sole heat flux forcing. To this, Model 19 adds $+1\,Wm^{-2}yr^{-1}$. Model 28 adds $0.03\varepsilon\sigma T_{surf}^4$ longwave radiation loss to this baseline and Model 29 adds both $+1\,Wm^{-2}yr^{-1}$ and $0.03\varepsilon\sigma T_{surf}^4$. Adding the additional net longwave flux term results in surface cooling that is typically $10\,Wm^{-2}$ higher at any given month.

a.   *Steady Annual Mean Surface Heat Flux*

The seasonal heat flux models with a steady annual mean surface heat flux provide the baseline results for comparison against later models that experience a surface cooling that increases yearly. As a fixed model, Model 16 was forced with the cyclical heating and cooling shown in Figure 3.62 and had a mean annual heat flux of $0\,Wm^{-2}$. Its free model counterpart, Model 28, had a mean annual cooling of approximately $10\,Wm^{-2}$ due to additional sensible, latent, and longwave heat fluxes.

In the first of the seasonally varying surface heat flux runs, Model 16A (double-diffusive with no turbulent diffusivity) experiences a near-constant $\Delta\rho_{conv}$ even though surface heat flux forcing ranges from -32 to +24 Wm^{-2} during each year (Figure 3.63). Sea ice concentration and thickness vary over the seamount according to expected patterns with no multi-year polynyas occurring. Model 16B (Figure 3.64), which has both turbulent and double-diffusive mixing, causes $\Delta\rho_{conv}$ to vary quite significantly during each year. Mean sea ice concentration and thickness still follow monthly variations in surface heat flux. Model 16C is the purely turbulent case in the Model 16 series (Figure 3.65). With no double-diffusive mixing parameterization, the variation in $\Delta\rho_{conv}$ in 16C is slightly greater throughout the year, as compared to 16B. The most likely reason for this difference is the greater brine rejection associated with sea ice formation in the turbulent-only model (16C) when compared to 16B since 16C sees thicker sea ice during the winter.

60

Model 28A is identical to Model 16A, but with the inclusion of sensible, latent, and additional net longwave radiation. Figure 3.66 shows the model experiences a slow decline in seasonal sea ice cover with a corresponding breakdown of $\Delta\rho_{conv}$ even though there is no increase in annual net cooling. There is, however, a constant mean annual cooling of $10\,Wm^{-2}$. Starting at year 11, $\Delta\rho_{conv}$ almost reaches the convection criterion of 0.005 $kg\ m^{-3}$ and each year after. Conversely, Model 28B (Figure 3.67) maintains consistent sea ice concentration, thickness, and $\Delta\rho_{conv}$ from year to year, unlike 28A. And very similar to 28B, Model 28C (Figure 3.68) sees no decrease in overall sea ice concentration, thickness, or potential density differences as the model integrates.

b.   *Linearly Increasing Annual Mean Surface Heat Flux*

By increasing net annual cooling each year, convection is eventually reached in each of the seasonal models. The fixed surface flux model, 19, starting at a net annual cooling of $0\,Wm^{-2}$ and increasing this cooling by $+1\,Wm^{-2}yr^{-1}$, experiences less cooling overall than its free model counterpart, 29, which begins with $\sim 10\,Wm^{-2}$. Consequently, Model 19 runs have convection initiated after a longer period of time. The presence of convection, however, is no guarantor of the production of a multi-year polynya.

Model 19A (Figure 3.69) experienced the first sign of convection in the column over the seamount before year 15. However, mean sea ice concentration and thickness still reach non-zero values in the austral winter. A multi-year polynya never forms. Models with turbulent diffusivity undergo a different progression. Model 19B, having both double-diffusion and non-zero turbulent diffusivity, sees an onset of convection immediately before year 17 (Figure 3.70). By year 18, a multi-year polynya has formed, evidenced by zero summit areal mean sea ice concentration and thickness from that point forward. Similarly, the turbulent-only model, 19C (Figure 3.71) achieves convection and a subsequent zeroing of sea ice concentration and thickness. However, the onset of convection is earlier, right before year 16 and the multi-year polynya begins at year 17. The model with double-diffusion manages to hold off convection and polynya formation for an additional year, as compared to the model without.

Due to additional surface heat fluxes, Model 29 experiences a net annual mean cooling of $10\,Wm^{-2}$ along with an increase of $+1\,Wm^{-2}yr^{-1}$. Even with this large amount of net cooling, the purely double-diffusive model (Figure 3.72) still fails to produce a multi-year polynya (but just barely fails). Convection occurs first at year 4. With an onset of deep convection at year 5, Model 29B (Figure 3.73) goes ice free immediately and maintains a multi-year polynya throughout the remainder of the run. Model 29C, with purely turbulent diffusivity and no double-diffusion, experiences convection over Maud Rise at year 4, one year earlier than the model identical in every way, except for double-diffusion (i.e., Model 29B). The multi-year polynya begins at this time as well (Figure 3.74).

c.   *Summary of Seasonally Varying Heat Flux Forcing Models*

The results of the seasonally varying models are summarized in Table 3.5 and Table 3.6. Model 16 results illustrate that with a net annual heat flux of zero and no change in this annual integral of heat flux, each of the three models reach a stable annual cycle quickly (clearly by year 5 in all cases). Model 28 has a positive net annual heat flux (surface cooling) and reaches a stable cycle in the models having a non-zero turbulent diffusivity. However, the purely double-diffusive case, as shown by Model 28A, does experience convection starting at year 11. This marked difference in the double-diffusive model, when no convection is expected, might indicate that the seasonally forced models require turbulent diffusivity to achieve cyclical stability. This result makes it important to carefully evaluate the other purely double-diffusive models (19A and 29A) in light of the results from Model 28A.

Models 19 and 29 give further evidence that double-diffusion may play a role in delaying the onset of convection in a column experiencing densification over a Maud Rise-like seamount, even if we discount the "A" cases (which would be highly supportive of this assertion). Both Models 19B and 29B, with double-diffusion, saw a later onset of convection with a concurrent initiation of a multi-year polynya when compared to 19C and 29C (turbulent-only).

6.   Summary of Model Results

The models in this study use surface boundary heat flux forcing as the primary upper layer densification mechanism to explore the breakdown in the thermal barrier in this region of marginal water column stability. This method was chosen to take advantage of observed thermal flywheel feedback effects. Other forcing options would require the relaxation of interior conditions; surface heat flux forcing also provides the least intrusive mechanism. Models with steady surface forcing (having no time-dependent increase in cooling) provided a baseline upon which to evaluate later, more complicated forcings. Linearly increasing, higher-slope surface cooling schemes further bracketed the problem by providing the upper boundaries on the magnitude of surface cooling. Models with the linearly increasing, lower-slope cooling formulation explored surface heat flux forcings between these two extremes. Finally, seasonally forced models allowed an examination of the system's response to both surface heating and cooling in an effort to draw conclusions on the role of double-diffusion in polynya formation and convection onset in the eastern Weddell Sea.

The fixed, steady models (Table 3.2) never experienced an onset of convection or a multi-year open ocean period above the seamount. Even though all Models of 24 went ice-free, only Model 25, subjected to the highest amounts of surface cooling, saw initiation of convection in the column.

Models in the high-slope, linearly increasing series (Table 3.3) were particularly illuminating with three consistent results and one anomaly. For the first three models (14, 20, 26), cases with double-diffusion (A and B) had polynya formation earlier in the run than the turbulent-only case (C). Furthermore, open ocean above the seamount coincided with the onset of convection in the turbulent-only case, but not in the double-diffusive cases. A lag time between these two events on the order of years characterized the double-diffusive runs. Model 27, which started with total sea ice cover in the domain, saw simultaneous sea ice melting and convection. These three cases were all similar. The combination of initial sea ice cover with large fluxes due to the addition of sensible, latent, and net longwave radiation led to convection first, with sea ice melt as the natural consequence.

The double-diffusive models in the low-slope, linearly increasing series (Table 3.4) all consistently have earlier polynya formation times than the models with non-zero turbulent diffusivity. Lag time is significantly greater as well with 41, 16, and infinite for Models 21A, 30A, and 31A. If the criterion for the onset of convection is relaxed somewhat, Model 31A would have a lag time of five years as convection could be said to occur at year 9. By comparison, open ocean appears much later in the B and C models with convection occurring more quickly after this event.

As for the seasonally varying models (Table 3.5 and Table 3.6), Model 16, with a net annual mean heat flux of zero, forms the baseline for the seasonally varying model series. All cases of this model settle into a cyclical and stable configuration leading to no polynya formation or convection in the column over the seamount. Model 28 experiences net inter-annual cooling overall, even as seasonal variations produce alternating heating and cooling at the surface during any given year. A repeated pattern of sea ice formation occurs for Model 28B and 28C, but not for 28A, the purely double-diffusive case. The remaining double-diffusive models are noteworthy as ice cover never completely recedes in Models 19A and 29A. Both convection and polynyas appear later in the double-diffusive/turbulent cases (19B and 29B) than the turbulent-only cases (19C and 29C) further bolstering the idea that double-diffusive mixing could delay the onset of deep convection in columns of marginal water stability in the Weddell Sea near Maud Rise.

D.   ANALYSIS AND DISCUSSION

Heretofore, the model results have simply hinted at a possible relationship between double-diffusive mixing and a delay in the onset of deep convection in the volume of water above a seamount representing an idealized Maud Rise. The 45 models used in this study were mainly differentiated by the magnitude, sign, and both interannual and seasonal variability of surface heat flux forcing. Armed with this extensive body of results, we are well-positioned to determine if a "double-diffusive delay" is actually the case. However, the challenge in analyzing such a large number of models is in the development of objective methods to compare models with seemingly disparate surface heat flux formulations.

What follows is a method to analyze the majority of the data available to come to sensible conclusions. This method analyzes onset times in terms of energy lost by the surface over the seamount. This method shifts focus from the actual onset times themselves (in years) to the quantifiable amount of energy lost by the system prior to the onset of polynya formation and deep convection (in Jm^{-2}).

1. Methodology

Common to all runs is some form of surface heat flux forcing. Surface cooling drives the densification of the surface levels, eventually leading to instability in the column and convection over the seamount. Three quantities will be considered for the models that produced them—the time-integral of the mean of surface heat flux to the atmosphere from start to (1) the polynya formation time and (2) the onset of deep convection with (3) the lag time, defined as the difference between (1) and (2). Polynya formation time is defined as the first year of a multi-year period of completely ice-free conditions marked by zero values for the summit areal means of sea ice concentration and thickness. Convection onset time is defined as the first model output having $\Delta\rho_{conv} = \overline{\rho}_{1000} - \overline{\rho}_{10} < 0.005 \ kg \ m^{-3}$. $\overline{Q}_{atm}$ is the summit areal mean of surface heat flux to the atmosphere. The first quantity is

$$\int_0^{t_p} \overline{Q}_{atm}(t) \ dt \tag{3.6}$$

where t_p is the polynya formation time. The total energy lost to the atmosphere per unit area, until the onset of convection is

$$\int_0^{t_c} \overline{Q}_{atm}(t) \ dt \tag{3.7}$$

where t_c is the convection onset time. Finally, the difference between the two is simply

$$\int_{t_p}^{t_c} \overline{Q}_{atm}(t) \ dt \ . \tag{3.8}$$

Of the models that were not seasonally forced, eight sets out of 11 formed polynyas and experienced convection. One additional set (Model 24) had polynya

formation, but no convection. These nine sets, with three models each, are included in this analysis of surface cooling. Table 3.7 gives the values of energy calculated with (3.6) , (3.7), and (3.8) in the columns labeled (1), (2), and (3), respectively. However, it is the differences in these values that determine what effect, if any, double-diffusion has on the additional cooling required to initiate polynya formation and convection.

Each energy benchmark (polynya, convection, and lag) was investigated in turn. Five values were calculated for each set of models. First, the mean of the values from Table 3.7 for the pair of double-diffusive runs (A and B) was calculated and the value for the purely turbulent run (C) was subtracted from this. This gives the difference in energy between the double-diffusive runs and the turbulent-only run, with the double-diffusive runs equally weighted. Next, the same procedure was followed for the turbulent runs. The mean of the values for the runs with non-zero turbulent diffusivity (B and C) were calculated and subtracted from the purely double-diffusive case (A). This gives the difference between the purely double-diffusive runs and the turbulent runs with these runs being equally weighted. Finally, three remaining possibilities for differences between model runs were calculated (A–C, B–C, and A–B). These five values for each model form the basis for each of the three analyses below.

2.   Analysis of Net Energy Loss Before Polynya Formation

The differences in the time-integrals of surface heat flux to the atmosphere from model initiation to polynya formation time are shown in Table 3.8. What is striking is the prevalence of negative values, indicating that models with double-diffusive mixing generally require less cooling, and therefore less surface densification, before a polynya forms. It is important to note that this opening in the sea ice does not necessarily lead to convection. Even with the averaging of the double-diffusive/turbulent runs (B) with the purely turbulent runs (C), the "A–Turb." calculations are uniformly negative. The results of the differences between unaveraged runs provide further evidence. Only two differences, those for Models 21 and 31 in the "B–C" calculation, provide counter examples.

Mean values across all model runs are negative and the range of values in the 95% confidence interval are all negative as well, with the sole exception of the upper value ($0.411\,GJm^{-2}$) for the difference between purely double-diffusive runs (A) and double-diffusive/turbulent runs (B), which requires 88.4%. This would seem to indicate that, on the whole, double-diffusion's ability to transport heat upward is an important contributor to the observed multi-year sea ice thinning in the vicinity of Maud Rise (Drinkwater 1996, Lindsay et al. 2004) and may even provide the impetus for polynya formation in the presence of appropriate pre-conditioning (Carsey 1980, Timmermann et al. 1999). However, these results do not necessarily mean that double-diffusion plays a role in multi-year polynyas occurring from heat loss due to prior deep convection.

3.   Analysis of Net Energy Loss Leading Up to Convection

The differences in the total amount of energy transferred to the atmosphere up until the point of convection are given in Table 3.9. In most cases, models with double-diffusive mixing required more heat loss before convection was initiated than the turbulent cases. Models 25, 14, 20, 26, and 21 underwent more cooling before initiation while Models 27, 30, and 31 did not. Column means look promising, with positive values for the three means corresponding to the double-diffusive/turbulent-only differences. The 95% confidence interval ranges are not as convincing as in the polynya analysis above, however. If the confidence intervals are reduced until both the lower and upper bounds are positive, the "DD–C" case requires 72.6%, the "A–C" case 28.9%, and the "B–C" case 94.5%. The "B–C" case is the strongest while "A–C" the weakest. Given these results it is likely that double-diffusive mixing is responsible for delaying the onset time of convection in these model runs. The "B" cases contain parameterizations that more closely represent actual ocean physics, through the inclusion of both turbulent and double-diffusive diffusivities. On the other hand, these results could be interpreted to mean that the measurement of energy lost to the atmosphere from model initiation to convection onset is not a good indicator of the effects (if any) of double-diffusion on the system and that measuring from polynya formation time (rather than model initiation) is a more sound approach.

4.   **Analysis of the Additional Energy Loss Required to Initiate Convection after Polynya Formation**

If we consider the energy lost at the surface to the atmosphere starting from the polynya formation time and ending with the onset of convection, as in Table 3.10, the results become more compelling. Examining these results, we see that all double-diffusive runs require more cooling after polynya formation before convection is initiated as compared to the turbulent-only runs, with only one exception, Model 31B. All mean values of energy per unit area are positive. The lower and upper boundaries at the 95% confidence interval are positive for the "DD–C" and "B–C" comparisons. The boundaries for the "A -C" difference frame positive values at the 94.2% confidence interval. The "A–Turb." and "A–B" values, which consider differences between double-diffusive runs, show that the purely double-diffusive case requires more energy loss than the "B" case.

5.   **Discussion**

In the Ambient areas outside of the vicinity of the seamount, sea ice concentrations and thicknesses hold constant near to or at 100% and 0.4 to 0.6m, respectively. It is only in the area of close proximity to the seamount that these values reach zero at varying times between model runs. It is clear that dynamic effects contribute to the creation of open-ocean conditions in an otherwise ice-covered Weddell Sea (Holland 2001). Flow fields around and over the Gaussian seamount conform to expected values (Chapman and Haidvogel 1992) with steady-state flow over the seamount reduced to negligible velocities. This makes the water column above the seamount extremely susceptible to densification forcings, which would otherwise be unable to occur in the Ambient region, with its stronger background flow. However, the variability in interannual sea ice thinning and the existence of sporadic polynya events point to additional, thermodynamic, factors involved in these phenomena. The presence of Maud Rise alone cannot be the sole cause, otherwise the Weddell Sea Polynya would be a permanent fixture in the Southern Ocean. The introduction (Section A) recounts the development of the theories explaining the transient nature of the WP, most of which rely on thermodynamic causes relating to its onset and maintenance.

Analysis of this series of models in terms of net energy lost to the atmosphere provides an objective way to determine if double-diffusion is in fact a contributor to multi-year sea ice thinning and polynya events in the Weddell Sea near Maud Rise and to examine the role of double-diffusion in delaying the onset of convection. Table 3.11 gives a summary of the confidence levels of the three hypotheses presented in this analysis, namely that (*a*) double-diffusion cases cause a polynya to form earlier than the case without double-diffusion (Earlier Polynya), (*b*) cases with double-diffusion see a delay in the onset of convection compared to the turbulent-only case (Later Convection), and (*c*) double-diffusive cases experience a delay in the onset of convection after polynya formation when compared to the non-double-diffusive case (Greater Lag).

The confidence levels for Earlier Polynya are all greater than 95%. Later Convection confidence levels are extremely low, with only that for the "B–C" case approaching 95%. The levels for Greater Lag are better, with two above 95%. Given these confidence levels, there is strong evidence that double-diffusion contributes to greater sea ice thinning and increases the chance of polynya formation. There is fairly strong evidence that double-diffusion also delays the onset of convection after polynya formation.

The results from this analysis make the argument that double-diffusion has a dual effect of hastening the formation of polynyas as well as delaying the onset of convection in marginal water columns in open-ocean conditions. The analysis conducted in this study implies that double-diffusion could play a larger role in sea ice thinning and multi-year polynya events than previously thought. High latitude models containing sea ice should take double-diffusion into account, as ice melt rates may be underpredicted by models using only turbulent diffusivity and the initiation of deep convection may occur earlier.

E. CONCLUSIONS AND SUMMARY

A comprehensive high resolution numerical modeling study of an area mirroring the dynamic and thermodynamic properties of the eastern Weddell Sea in the vicinity of Maud Rise was conducted. Persistent sea ice thinning and the appearance of a multi-year

polynya highlights the marginal nature of water column stability above and near Maud Rise. Multi-year polynya formation is not necessarily coincident with an onset of deep convection. Many theories have been developed to explain the mechanisms leading to areas of thin sea ice and the sporadic appearance of polynyas. Although these phenomena are well-studied, no previous attempts have been made to investigate the possible role of double-diffusion in the onset and maintenance of deep convection near Maud Rise.

Extensive modeling in the form of 45 distinct cases forms the basis of this study. Surface heat flux forcing was used as the primary densification mechanism. Various surface cooling schemes were employed to stimulate initial sea ice growth to baseline values matching observations from the region. A thermal barrier effect (Martinson 1990) effectively kept sea ice concentrations and thicknesses stable outside the vicinity of the seamount. This Ambient region (Shaw and Stanton 2014) experienced minute variations in sea ice thickness due to a robust system of negative feedback. However, in the Taylor cap region these negative feedback mechanisms, though present, were more susceptible to the thermal barrier breakdown processes described in Martinson et al., 1990 due to negligible flow. Above the seamount, this dynamic preconditioning provided the proper milieu for differences in thermodynamic mixing types to be explored as various types of surface heat flux forcing were applied. Models with purely turbulent, purely double-diffusive, and dual turbulent/double-diffusive mixing parameterizations exhibited differences in polynya formation and convection onset times.

In an attempt to objectively compare models with significantly different surface heat flux forcing schemes, polynya formation and convection onset times were restated in terms of the total energy lost to the atmosphere in an area above the summit of the seamount. The differences in these energy amounts between similar models across the three mixing parameterizations were then analyzed in terms of confidence levels. Standard practice in using confidence levels is that a null hypothesis can be rejected if the range of values at the 95% confidence level is such that it supports the proposed hypothesis. The null hypothesis in each of our comparisons is that the presence of double-diffusive convection has no effect on the polynya formation or convection onset times.

In the case of polynya formation, we can reject the null hypothesis. Comparisons between model types with and without double-diffusion indicate earlier formation times above a 95% confidence level. This provides strong evidence that these outcomes are not the result of random differences between models. In light of this, it seems reasonable to conclude that double-diffusion plays a role in the persistent area of thin sea ice in the Weddell Sea near Maud Rise and may even contribute to polynya formation when conducive preconditioning occurs.

As far as convection onset time from model initiation is concerned, results are mixed. Comparing the dual turbulent/double-diffusive cases with the turbulent-only cases, the confidence level is 94.5%. However, when comparing the pure double-diffusive cases with the turbulent-only cases, upper and lower boundaries at the 95% confidence level include a range of both positive and negative values. This result does not allow a rejection of the null hypothesis in this case.

Comparing convection onset time differences from the reference point of polynya formation time (rather than model initiation) provides an overall mean confidence level of 96.9%. This is, once again, strong evidence that the variations in "lag time" (i.e., the difference between convection onset and polynya formation times in the model) are not the result of random variations. Taken with the previous results, it is likely that double-diffusion has the effect of delaying the onset of deep convection over Maud Rise.

The model results and analysis in this study support the initial "thought experiment" regarding the fundamental difference between turbulence and diffusive convection regimes in relation to the magnitudes of the thermal and haline contributions to density flux above the pycnocline. In the turbulent regime, the haline contribution is larger, resulting in a water column that becomes more susceptible to reaching static instability over time. In the diffusive convection regime, the thermal contribution is larger, meaning that static stability is promoted over time, making convection less likely as compared to the turbulent regime. Furthermore, with comparable values for diffusivity and identical temperature and salinity profiles, upward heat fluxes under conditions of double-diffusion are larger than those in turbulent regimes, making double-diffusion more effective in limiting sea ice thicknesses. The overall result of double-diffusion is the

promotion of conditions favorable to polynya formation and production of a water column better able to weather changes in surface density, thus delaying the onset of deep convection. It is in this way that double-diffusion, perhaps, prevents us from enjoying the Weddell Sea Polynya as a permanent winter time phenomenon in the Southern Ocean.

IV.   SUMMARY

Double-diffusive convection is a mixing process characterized by the presence of density-determining constituents that diffuse at significantly different rates. Seawater potential density is determined by temperature and salinity, with the diffusion of heat being 100 times faster than that of salinity. This difference in diffusion rates, coupled with the existence of an unstable vertical gradient in one of these constituents, leads to a mixing process that promotes increased static stability in a seawater column. There are two forms of double-diffusion: salt fingering and diffusive convection. Salt fingering occurs in the subtropical ocean where both temperature and salinity have positive vertical gradients (values decrease with depth). Salinity, the slow diffuser, provides the unstable gradient in the salt fingering regime. Diffusive convection, on the other hand, occurs in environments where the temperature and salinity gradients in the vertical are both negative (values increase with depth). In this case, the fast diffuser has the unstable gradient. This work provided two studies, one for each regime, as contributions to the ongoing study of double-diffusion and its effects on ocean physical processes across the spectrum of scales.

The first study challenged the classical view of thermohaline circulation by examining constraints imposed on diapycnal velocity by double-diffusion in the subtropical thermocline. A series of numerical models exploring double-diffusive and turbulent mixing parameterization along a continuum framed by the singular presence of these two extremes was conducted. It was found that the equal diffusivities provided by the turbulent mixing parameterization offered no constraint on diapycnal velocities. However, as the double-diffusive contribution to overall vertical mixing increased, constraints on diapycnal velocity tightened as the fraction of mixing attributed to double-diffusion increased, with the most severe constraints imposed in the cases containing the double-diffusive mixing parameterization only. It is commonly assumed that the increase in diapycnal diffusion of temperature and salinity necessarily amplifies the diabatic component of overturning (e.g., Bryan 1987). This study presents a peculiar counter-example of this tendency by showing that mixing can have an adverse impact on

overturning. In essence, double-diffusion acts to "seal" the thermocline by preventing the leakage of seawater (both upward and downward) across the isopycnal surfaces on which double-diffusion is a dominant mixing process. Furthermore, the values of diapycnal velocity present in the cases that most closely resembled the observed mid-latitude diffusivities were comparable to current estimates. This provides further evidence that double-diffusion may play an important role in the selection of diapycnal velocity, potentially requiring a modification of the classical views of thermohaline circulation.

The second study constituted the first comprehensive numerical modeling study of the role of double-diffusion in the onset and maintenance of deep convection during Weddell Sea polynya and persistent interannual sea ice thinning events. A series of high resolution numerical models compared cases experiencing three distinct regimes for vertical mixing–purely double-diffusive, purely turbulent, and dual turbulent/double-diffusive while being forced with an extensively varied suite of surface heat flux prescriptions. The data were analyzed in terms of an energy-loss proxy to find correlations in the differences in polynya formation and convection onset times between the three mixing schemes modeled. It was concluded that the fundamental differences in thermal and haline contributions to density flux between turbulent and double-diffusive regimes, supported by extensive model results, indicate double-diffusion could play an important role in delaying the onset of deep convection, definitely influences the persistence of thin sea ice in the Weddell Sea near Maud Rise, and may even contribute to polynya formation under propitious conditions.

It is important to note that the results presented in this work represent only a starting point for the fuller treatment of the subjects investigated. As far as the study of diapycnal velocity is concerned, the information presented in this thesis would be complemented greatly by a further testing of the theory. Chapter II presents results in terms of a regime dominated by salt fingering. Although it is believed that these results will hold in the presence of diffusive convection, this may be a fruitful area for study. Another possible investigation could involve testing diapycnal velocity constraints in the presence of basin-wide upwelling. And with regard to the Weddell Sea study, modeling of additional densification mechanisms, or combinations thereof, can supplement the

results here. Modeling of seasonal air temperatures, interannual precipitation anomalies, and long-term variations in runoff could provide additional insights into the role that double-diffusion plays in determining the thermodynamic properties of the seawater in that region.

A common misconception is that double-diffusion is similar to turbulence and can be represented in numerical models in a similar fashion. The two studies comprising this work illustrate the dramatic differences between the two forms of double-diffusion (salt fingering and diffusive convection) and turbulent mixing and underscore the urgency of including formulations of double-diffusive mixing in all large-scale climate models.

THIS PAGE INTENTIONALLY LEFT BLANK

V. TABLES

Type	Q_{surf}	Fixed	Free
Steady, Low	1 Wm^{-2} + 0 Wm^{-2}yr^{-1}	17	24
Steady, High	5 Wm^{-2} + 0 Wm^{-2}yr^{-1}	18	25
High Slope, No Ice	1 Wm^{-2} + 1 Wm^{-2}yr^{-1}	14	26
High Slope, Ice	1 Wm^{-2} + 1 Wm^{-2}yr^{-1}	20	27
Low Slope	1 Wm^{-2} + $^1/_4$ Wm^{-2}yr^{-1}	21	30
Very Low Slope	1 Wm^{-2} + $^1/_8$ Wm^{-2}yr^{-1}	--	31
Seasonal, Steady	Monthly + 0 Wm^{-2}yr^{-1}	16	28
Seasonal, Increasing	Monthly + 1 Wm^{-2}yr^{-1}	19	29

Table 3.1. Number designations of all models run. Each model run has either fixed or variable surface heat flux forcing and is further differentiated by the type of surface heat flux forcing. Each combination consists of three model runs, one with (*a*) no turbulent diffusivity with double-diffusion, (*b*) a turbulent diffusivity of $2 \cdot 10^{-5} m^2 s^{-1}$ with double-diffusion, and (*c*) turbulent diffusivity ($2 \cdot 10^{-5} m^2 s^{-1}$) without double-diffusion. These three cases are denoted A, B, or C. Thus, model 17B is a model with completely prescribed flux forcing ("fixed"), that forcing being a constant $1 Wm^{-2}$ throughout the run ("steady, low"), with non-zero turbulent diffusivity and double-diffusion parameterization included ("B").

Model	Time Series Figure	Length of Run (yr)	Start of Multiyear Ice-Free (yr)	Onset of Convection (yr)
17A	Figure 3.19	19	Never	Never
17B	(not shown)	20	Never	Never
17C	Figure 3.21	18	Never	Never
18A	Figure 3.22	19	Never	Never
18B	Figure 3.23	17	Never	Never
18C	(not shown)	17	Never	Never
24A	Figure 3.29	42	4	Never
24B	Figure 3.30	48	8	Never
24C	Figure 3.31	46	10	Never
25A	Figure 3.34	14	3	4
25B	Figure 3.35	14	3	4
25C	Figure 3.36	14	4	4

Table 3.2. Summary of model results (steady). Fixed, steady models never experienced an onset of convection or a multi-year open ocean period above the seamount. Even though all Models of 24 went ice-free, only Model 25, subjected to the highest amounts of surface cooling, saw initiation of convection in the column.

Model	Time Series Figure	Length of Run (yr)	Start of Multiyear Ice-Free (yr)	Onset of Convection (yr)
14A	Figure 3.39	16	5	16
14B	Figure 3.40	16	4	16
14C	Figure 3.41	15	14	14
20A	Figure 3.42	19	10	15
20B	Figure 3.43	16	10	15
20C	Figure 3.44	18	14	14
26A	Figure 3.45	13	4	5
26B	Figure 3.46	14	4	6
26C	Figure 3.47	13	5	5
27A	Figure 3.48	14	7	7
27B	Figure 3.49	14	8	8
27C	Figure 3.50	14	8	8

Table 3.3.   Summary of model results (high-slope, linearly increasing). Models in this series were particularly illuminating with three consistent results and one anomaly. For the first three models (14, 20, 26), cases with double-diffusion (A and B) had polynya formation earlier in the run than the turbulent-only case (C). Furthermore, open ocean above the seamount coincided with the onset of convection in the turbulent-only case, but not in the double-diffusive cases. A lag time between these two events on the order of years characterized the double-diffusive runs. Model 27, which started with total sea ice cover in the domain, saw simultaneous sea ice melting and convection. These three cases were all similar. The combination of initial sea ice cover with large fluxes due to the addition of sensible, latent, and net longwave radiation led to convection first, with sea ice melt as the natural consequence.

Model	Time Series Figure	Length of Run (yr)	Start of Multiyear Ice-Free (yr)	Onset of Convection (yr)
21A	Figure 3.52	77	29	70
21B	Figure 3.53	80	65	71
21C	Figure 3.54	75	64	66
30A	Figure 3.55	25	3	19
30B	Figure 3.56	26	(8) 18	21
30C	Figure 3.57	25	9	21
31A	Figure 3.58	18	4	Never (9)
31B	Figure 3.59	19	9	12
31C	Figure 3.60	19	9	12

Table 3.4.   Summary of model results (low-slope, linearly increasing). The double-diffusive models in these series all consistently have earlier polynya formation times than the models with non-zero turbulent diffusivity. Lag time is significantly greater as well with 41, 16, and infinite for Models 21A, 30A, and 31A. If the criterion for the onset of convection is relaxed somewhat, Model 31A would have a lag time of five years as convection occurs at year 9. By comparison, open ocean appears much later in the B and C models with convection occurring more quickly after this event.

Model	Time Series Figure	Length of Run (yr)	Start of Multiyear Ice-Free (yr)	Onset of Convection (yr)
16A	Figure 3.63	$18\,^{5}/_{12}$	Never	Never
16B	Figure 3.64	$17\,^{11}/_{12}$	Never	Never
16C	Figure 3.65	$16\,^{5}/_{12}$	Never	Never
28A	Figure 3.66	$16\,^{2}/_{12}$	Never	11
28B	Figure 3.67	$12\,^{7}/_{12}$	Never	Never
28C	Figure 3.68	$14\,^{1}/_{12}$	Never	Never

Table 3.5.   Summary of model results (seasonally varying, steady). Model 16, with a net annual mean heat flux of zero, forms the baseline for the seasonally varying model series. All cases of this model settle into a cyclical and stable configuration leading to no polynya formation or convection in the column over the seamount. Model 28 experiences net interannual cooling overall, even as seasonal variations produce alternating heating and cooling at the surface during any given year. A repeated pattern of sea ice formation occurs for Model 28B and 28C, but not for 28A, the purely double-diffusive case.

Model	Time Series Figure	Length of Run (yr)	Start of Multiyear Ice-Free (yr)	Onset of Convection (yr)
19A	Figure 3.69	$19 \, {}^{11}/_{12}$	Never	15
19B	Figure 3.70	$19 \, {}^{11}/_{12}$	18	17
19C	Figure 3.71	$19 \, {}^{11}/_{12}$	17	16
29A	Figure 3.72	$11 \, {}^{11}/_{12}$	Never	4
29B	Figure 3.73	13	5	5
29C	Figure 3.74	$13 \, {}^{1}/_{12}$	4	4

Table 3.6.   Summary of model results (seasonally varying, linearly increasing annual mean). Ice cover never completely recedes with the double-diffusive cases of Models 19 and 29. Both convection and polynyas appear later in the double-diffusive/turbulent cases (B) than the turbulent-only cases (C).

Model	Polynya (1)	Convection (2)	Lag (3)
24A	1.033	--	--
24B	2.384	--	--
24C	3.052	--	--
25A	0.931	1.408	0.477
25B	0.922	1.395	0.473
25C	1.390	1.390	0.000
14A	0.436	4.199	3.764
14B	0.280	4.199	3.919
14C	3.235	3.235	0.000
20A	1.680	3.701	2.021
20B	1.680	3.701	2.021
20C	3.235	3.235	0.000
26A	1.217	1.695	0.478
26B	1.194	2.179	0.985
26C	1.663	1.663	0.000
27A	2.523	2.523	0.000
27B	2.997	2.997	0.000
27C	3.015	3.015	0.000
21A	1.580	13.700	12.120
21B	11.520	14.150	2.630
21C	11.110	11.940	0.830
30A	0.686	6.367	5.681
30B	2.384	7.052	4.668
30C	2.705	7.035	4.330
31A	1.055	2.933	1.878
31B	2.874	4.048	1.174
31C	2.860	4.042	1.182

Table 3.7.   Mean surface heat energy to atmosphere (GJm^{-2}). For models with polynya formation and convection onset times, the total cooling is shown. The differences between these two appear in the last column as "Lag." For the purposes of this calculation, Model 31A is considered to have had a convection onset time of nine years (as explained in Section III.C.4.b).

Model	DD–C	A–Turb.	A–C	B–C	A–B
24	-1.344	-1.685	-2.019	-0.668	-1.351
25	-0.464	-0.225	-0.459	-0.468	0.009
14	-2.877	-1.322	-2.800	-2.955	0.156
20	-1.555	-0.778	-1.555	-1.555	0.000
26	-0.458	-0.213	-0.446	-0.469	0.023
27	-0.255	-0.483	-0.492	-0.018	-0.474
21	-4.560	-9.735	-9.530	0.410	-9.940
30	-1.170	-1.858	-2.019	-0.321	-1.698
31	-0.896	-1.812	-1.805	0.014	-1.819
Mean	-1.509	-2.012	-2.347	-0.670	-1.677
St Dev	1.391	2.970	2.819	1.017	3.197
Low	-2.417	-3.953	-4.189	-1.334	-3.766
High	-0.600	-0.071	-0.506	-0.006	0.411

Table 3.8.   Differences in mean surface heat energy to the atmosphere up to polynya formation time (GJm^{-2}). The differences in the time-integrals of surface heat flux to the atmosphere from model initiation to polynya formation time are shown. The first column, "DD–C," gives the mean values for double-diffusive runs (A and B) minus the value for the corresponding turbulent-only run. The second column, "A–Turb." gives the value when the mean of the turbulent runs (B and C) are subtracted from the purely double-diffusive run (A). The remaining three columns give the differences shown. "A" indicates the purely double-diffusive run, "B" the double-diffusive run with non-zero turbulent diffusivity, and "C" is the turbulent-only run. With the exception of two cases (21B and 31B), all double-diffusive runs required less cooling energy before polynya formation.

Model	DD–C	A–Turb.	A–C	B–C	A–B
24	--	--	--	--	--
25	0.012	0.016	0.018	0.005	0.013
14	0.964	0.482	0.964	0.964	0.000
20	0.466	0.233	0.466	0.466	0.000
26	0.274	-0.226	0.032	0.516	-0.484
27	-0.255	-0.483	-0.492	-0.018	-0.474
21	1.985	0.655	1.760	2.210	-0.450
30	-0.326	-0.677	-0.668	0.017	-0.685
31	-0.552	-1.112	-1.109	0.006	-1.115
Mean	0.321	-0.139	0.121	0.521	-0.399
St Dev	0.829	0.602	0.929	0.768	0.396
Low	-0.253	-0.556	-0.523	-0.011	-0.674
High	0.896	0.278	0.765	1.053	-0.125

Table 3.9.   Differences in mean surface heat energy to the atmosphere up to convection onset time (GJm^{-2}). The differences in the time-integrals of surface heat flux to the atmosphere from model initiation to convection onset time are shown. In most cases, double-diffusive runs required more cooling before the onset of convection. The mean, standard deviation, lower and upper boundaries for the 95% confidence interval are shown for each column.

Model	DD–C	A–Turb.	A–C	B–C	A–B
24	--	--	--	--	--
25	0.475	0.241	0.477	0.473	0.004
14	3.841	1.804	3.764	3.919	-0.156
20	2.021	1.011	2.021	2.021	0.000
26	0.732	-0.015	0.478	0.985	-0.507
27	0.000	0.000	0.000	0.000	0.000
21	6.545	10.390	11.290	1.800	9.490
30	0.844	1.182	1.351	0.338	1.013
31	0.344	0.700	0.696	-0.008	0.704
Mean	1.850	1.914	2.510	1.191	1.319
St Dev	2.264	3.482	3.743	1.344	3.337
Low	0.281	-0.499	-0.084	0.260	-0.944
High	3.419	4.327	5.104	2.122	3.631

Table 3.10. Differences in mean surface heat energy to the atmosphere between polynya formation and convection onset times (GJm^{-2}). The differences in the time-integrals of surface heat flux to the atmosphere from polynya formation time to convection onset time are shown. With one exception (31), all double-diffusive runs require more cooling after polynya formation before convection is initiated as compared to the turbulent-only runs.

Hypothesis	DD–C	A–C	B–C
Earlier Polynya	99.8%	98.7%	95.2%
Later Convection	72.6%	28.9%	94.5%
Greater Lag	97.9%	94.2%	98.7%

Table 3.11.   Confidence levels of the role of double-diffusion in polynya formation and the onset of convection. The confidence levels of three hypotheses are given, (*a*) double-diffusion cases cause a polynya to form earlier than the case without double-diffusion (Earlier Polynya), (*b*) cases with double-diffusion see a delay in the onset of convection compared to the turbulent-only case (Later Convection), and (*c*) double-diffusive cases experience a delay in the onset of convection after polynya formation when compared to the non-double-diffusive case (Greater Lag). Given these confidence levels, there is strong evidence that double-diffusion contributes to greater sea ice thinning and increases the chance of polynya formation.

THIS PAGE INTENTIONALLY LEFT BLANK

VI. FIGURES
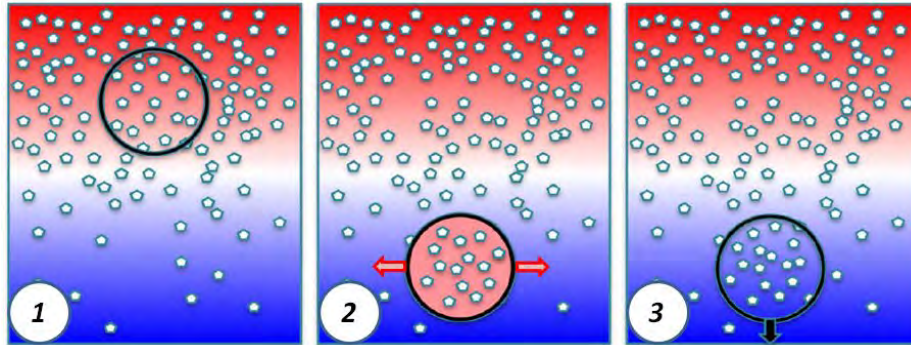
Figure 1.1.   Salt fingering. Consider a parcel in warmer, saltier seawater that overlies cooler, fresher seawater (*1*). Due to some perturbation, this parcel is displaced downward across the interface (*2*). The diffusivity of temperature is greater than that of salinity, so the parcel loses heat faster than it loses salt. Once the parcel's temperature has equilibrated to its surroundings, it is denser due to its higher salinity, therefore the parcel continues to sink (*3*).
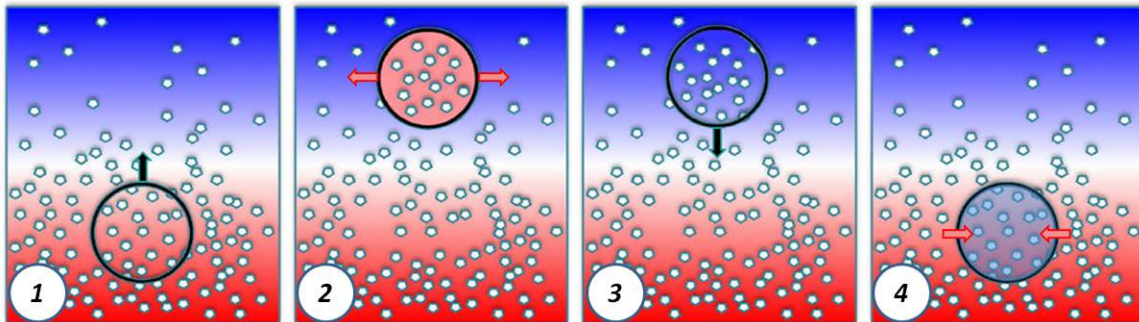
Figure 1.2.   Diffusive convection. A parcel resides near an interface where cooler, fresher seawater overlies warmer, saltier seawater (*1*). A perturbation displaces this parcel upward across the interface (*2*). Heat diffuses faster than salt, so the parcel's density becomes greater than the density of its surroundings (*3*) and the parcel sinks. Crossing the interface once more, heat diffuses into the relatively cooler parcel (*4*).
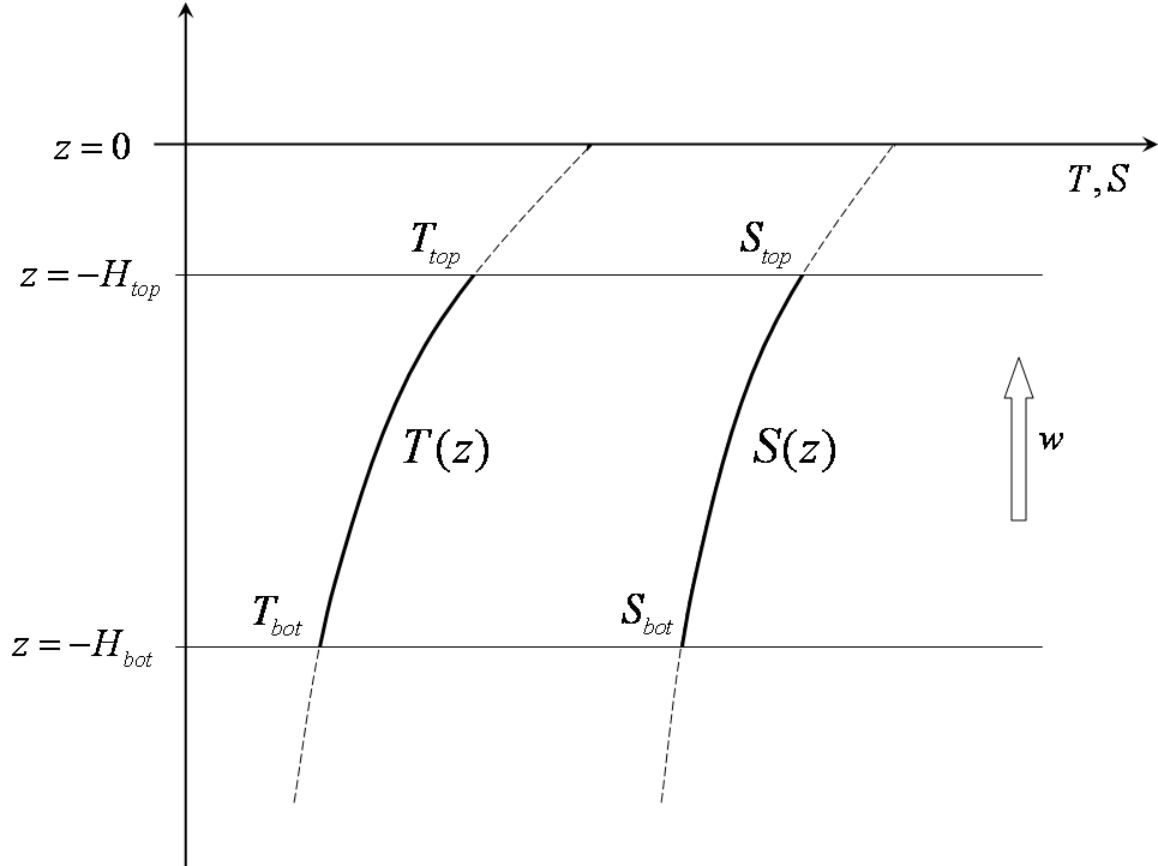
Figure 2.1. One dimensional model. We search for the temperature and salinity profiles $T(z)$ and $S(z)$ satisfying the vertical advection-diffusion equations for given vertical velocity (w) and boundary conditions at the ends of the mixing zone $(-H_{bot} < z < -H_{top})$..
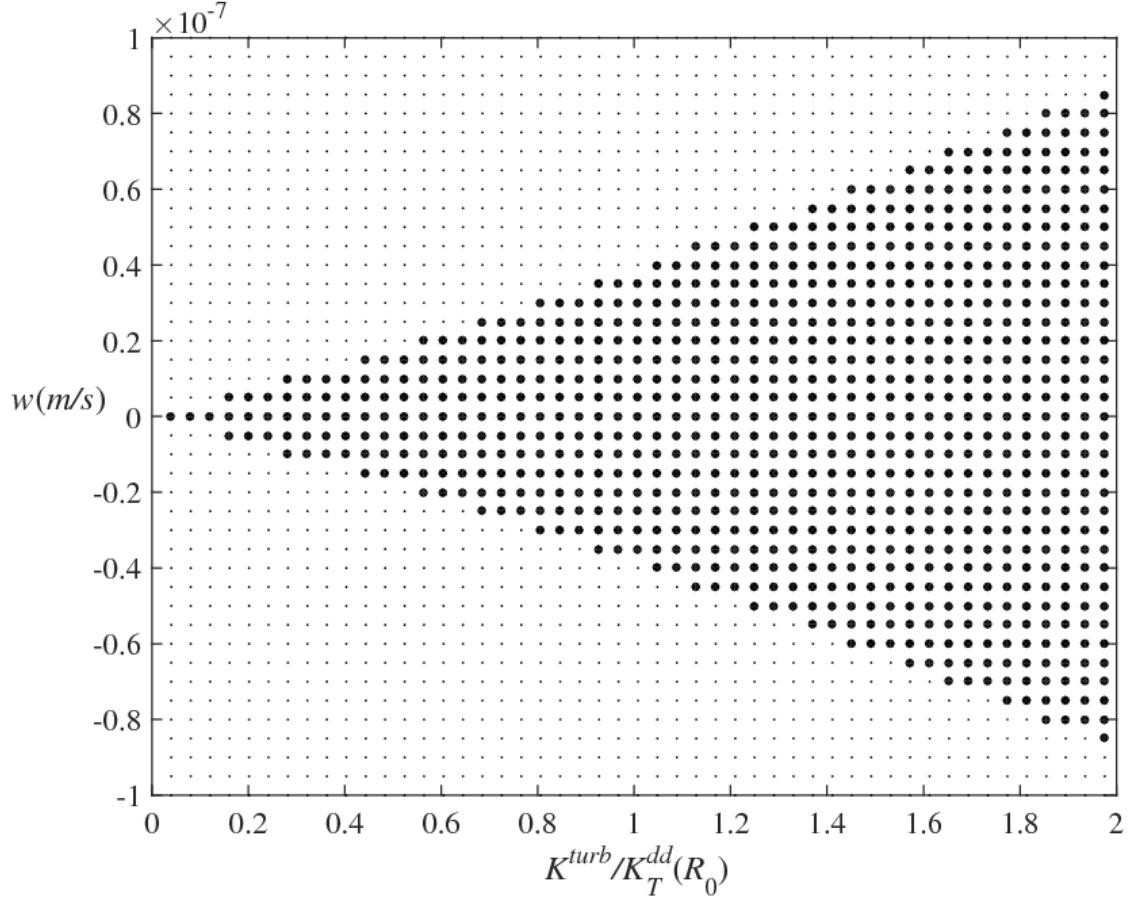
Figure 2.2. The range of diapycnal velocities permitted in the hybrid model, which includes both double-diffusive and turbulent mixing. Parameter $K^{turb}/K_T^{dd}(R_0)$ measures the relative contributions from turbulence and double-diffusion to the net mixing. Numerical calculations resulting in regular solutions are indicated by heavy dots and light dots represent conditions under which no solutions were found.
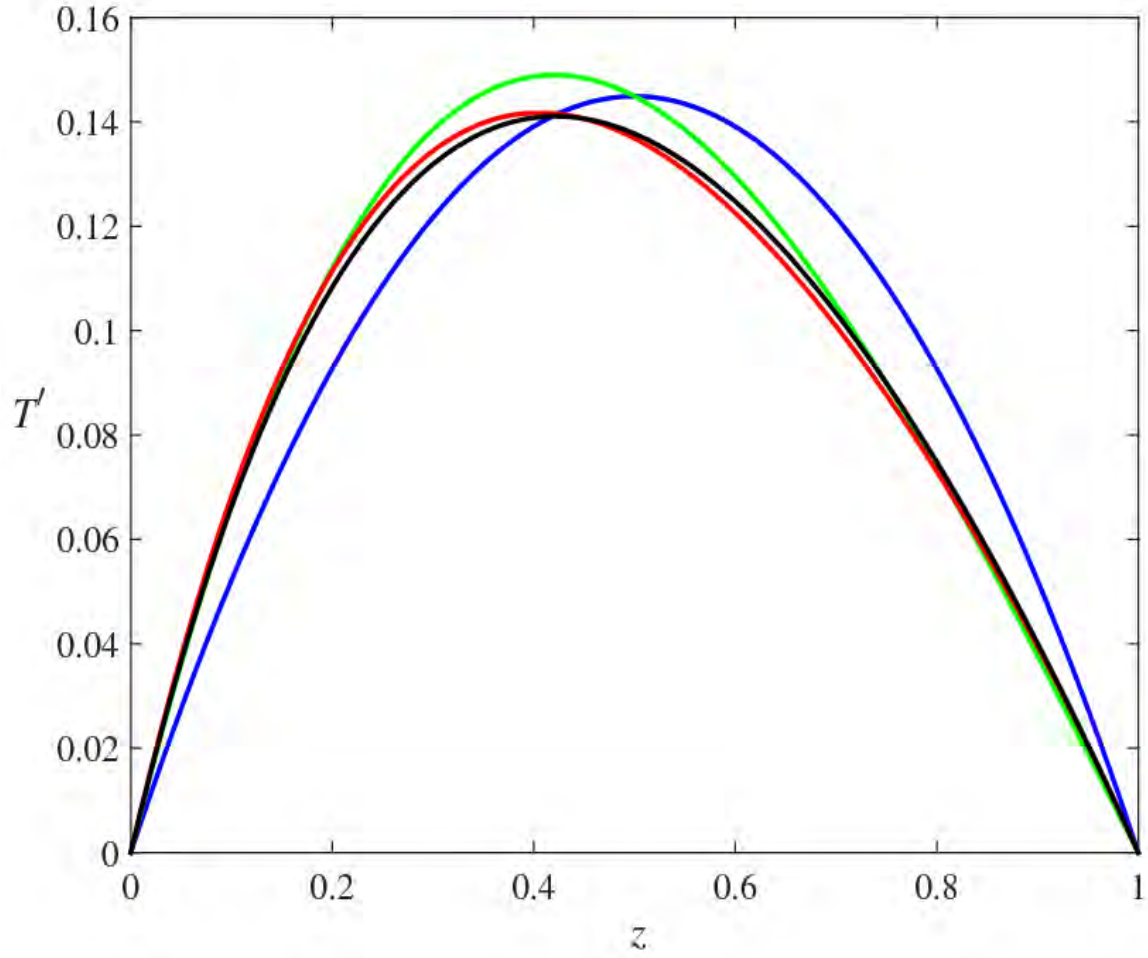
Figure 2.3.   The non-dimensional departure of temperature from the linear gradient $T'(z) = T(z) - z$. T' is computed numerically (black curve) and compared with the calculation based on the asymptotic expansion in ε truncated at the first, second, and third orders (blue, green, and red curves respectively). For $\varepsilon = 0.32$ $(\delta = 0.1)$, the numerical result is almost indistinguishable from the third order asymptotic prediction.
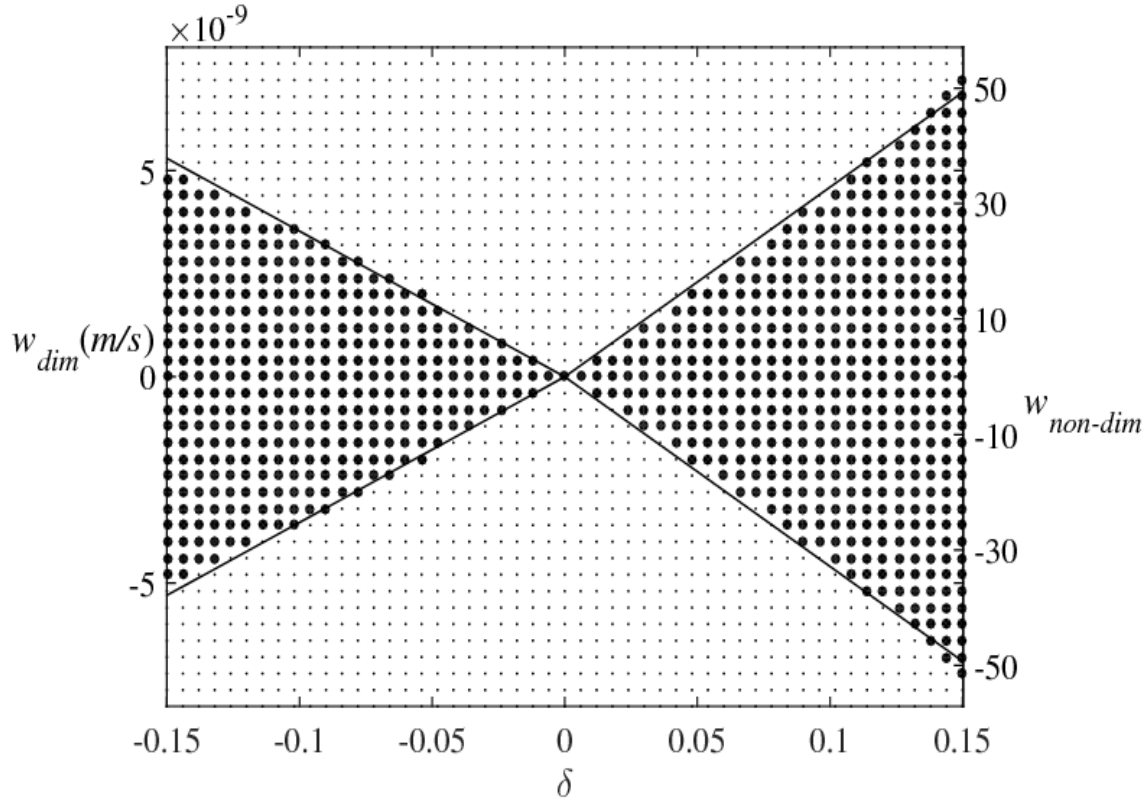
Figure 2.4.   The range of diapycnal velocities permitted in the one-dimensional model with variable flux ratio (γ). Parameter δ measures the extent of variation in γ, with positive (negative) values corresponding to the increasing (decreasing) $\gamma(R_\rho)$ relation. Numerical calculations resulting in regular solutions are indicated by heavy dots and light dots represent conditions under which no solutions were found.
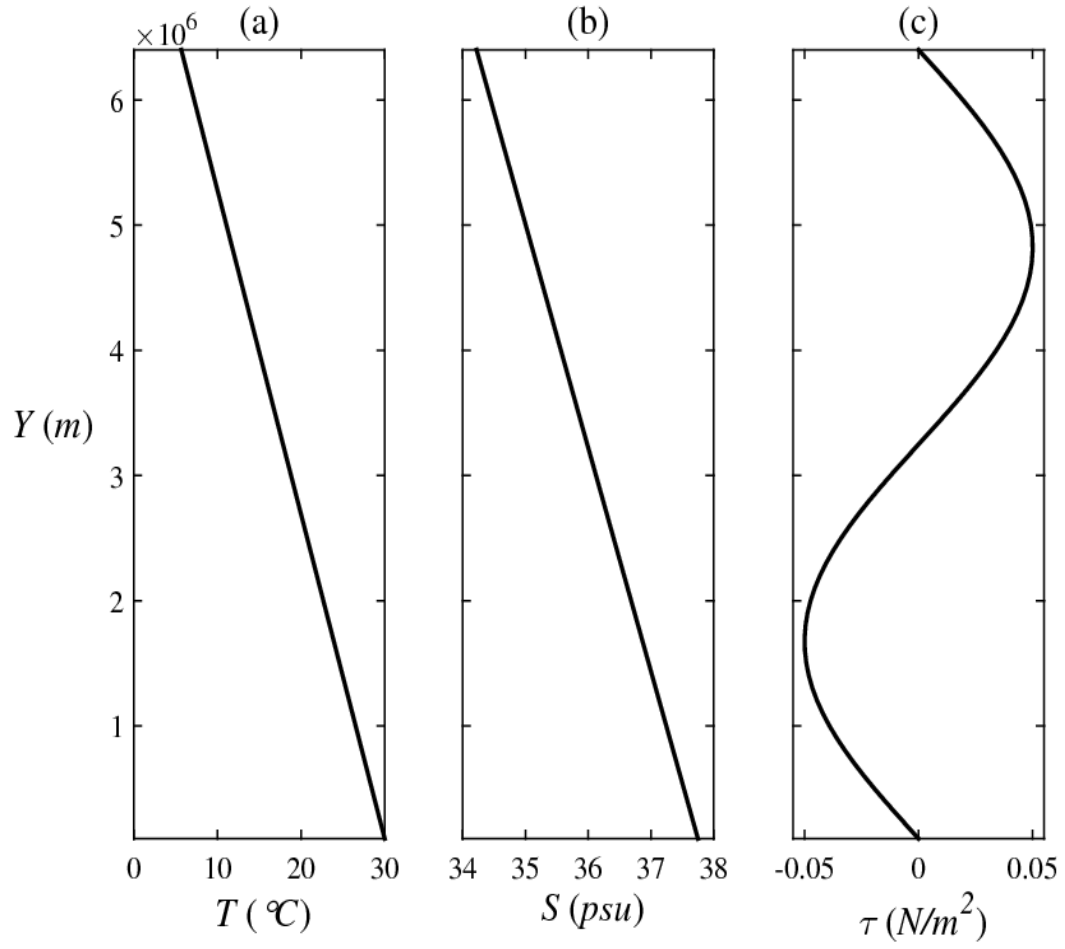
Figure 2.5.   The meridional patterns of the model forcing fields. Thermohaline forcing is applied by relaxing the surface temperature and salinity to the target patterns shown in (*a*) and (*b*) respectively. The wind stress is shown in (*c*). All forcing fields are zonally uniform.
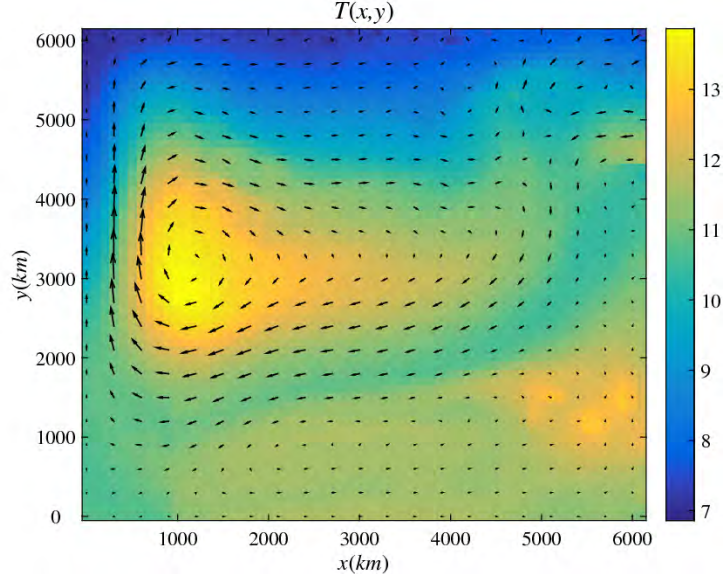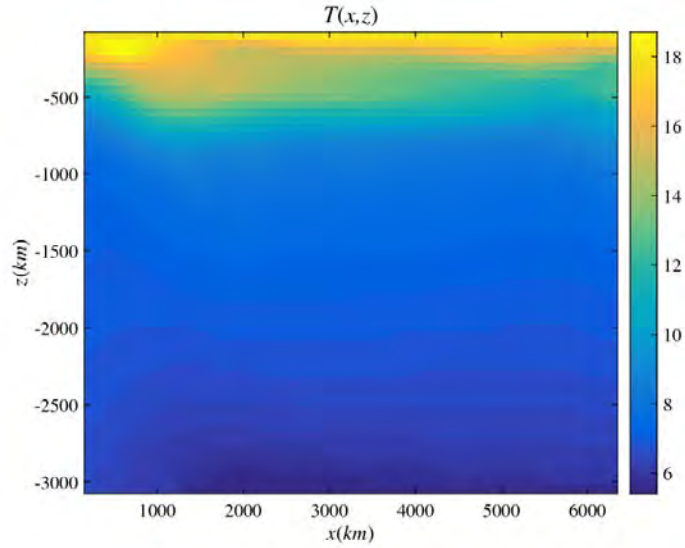
Figure 2.6. The final state $(t = 200\,yr)$ realized in the numerical experiments with double-diffusive mixing (the constant flux ratio case). (a) The horizontal temperature distribution and velocity pattern at $z = -500m$. (b) The zonal section of temperature at $y = 0.5L_y$. Clearly visible is a well-defined thermocline with relatively warm water extending several hundred meters downward from the surface.

95
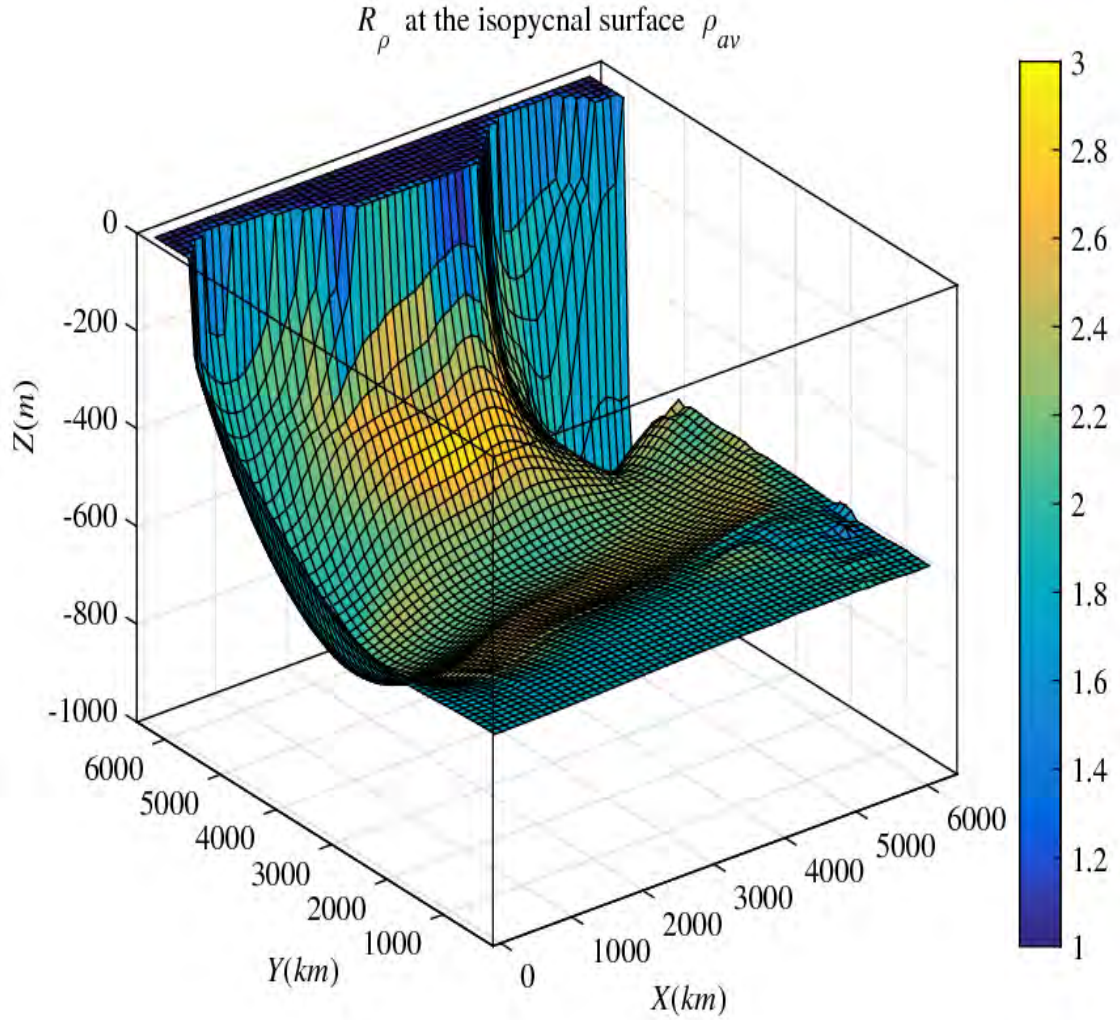
Figure 2.7.   Three-dimensional view of the average isopycnal surface $\rho = \rho_{av}$ defined in (2.43). Color coding represents the density ratio distribution on this isopycnal. The observed range of density ratios $1 < R_\rho < 3$ indicates that salt fingering is active and that its intensity is relatively high.
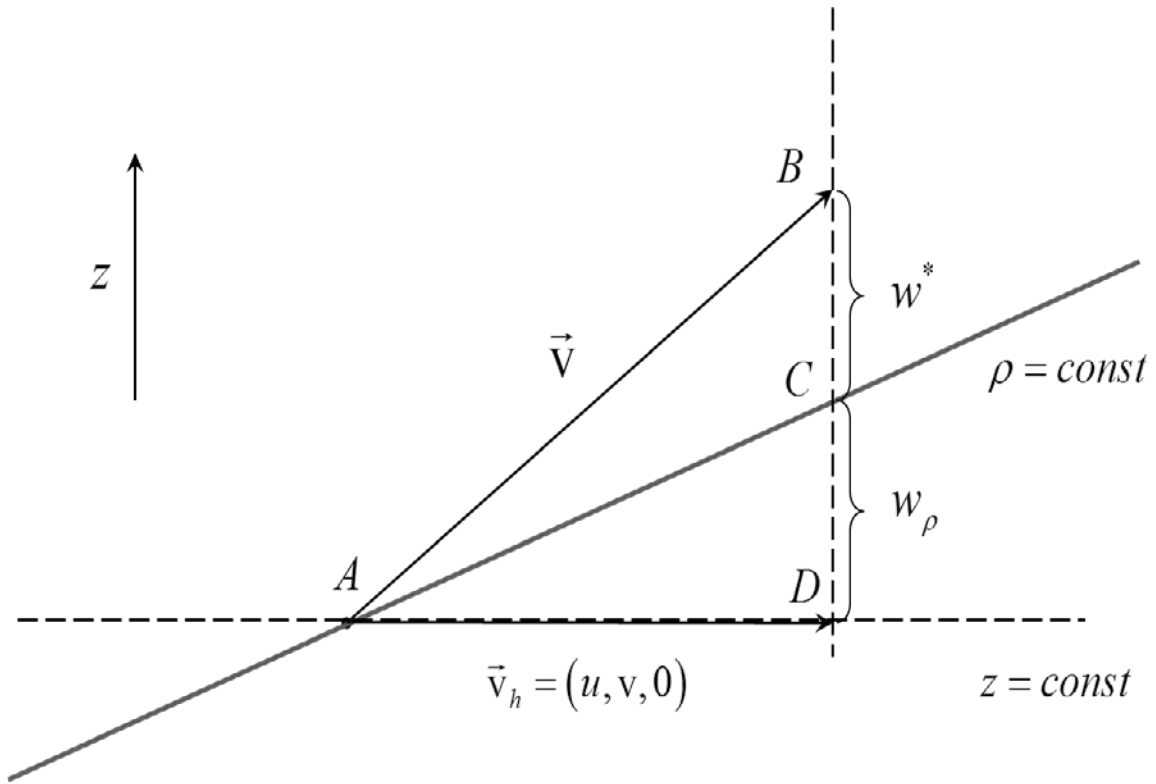
Figure 2.8.   Physical interpretation of diapycnal velocity. A Lagrangian particle initially located on a motionless tilted isopycnal surface is advected from A to B by a cross-isopycnal flow. Point C is the vertical projection of B onto the isopycnal surface. Diapycnal velocity represents the rate of the increase in vertical separation of the Lagrangian point from the isopycnal surface.
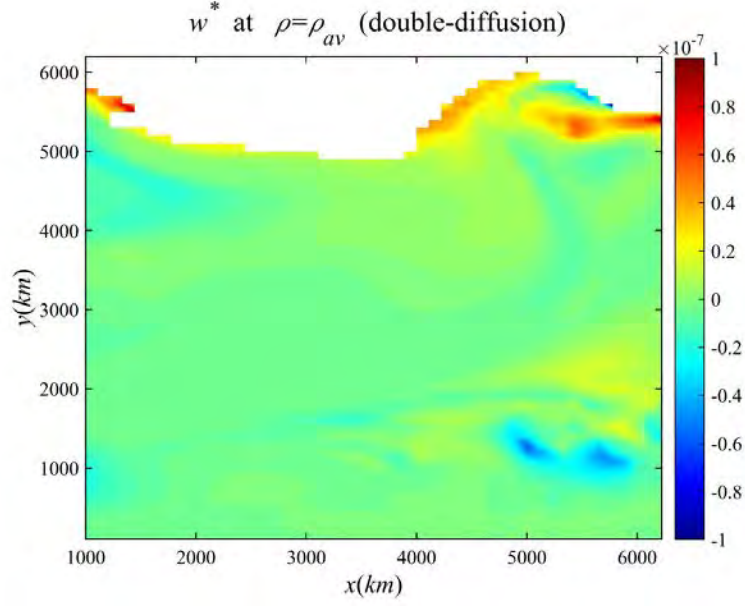
(a)
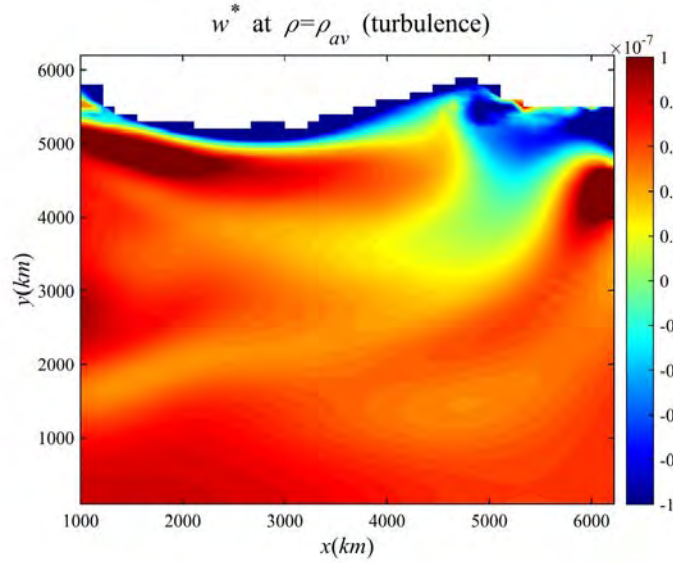
(b)

Figure 2.9.   Diapycnal transport in the double-diffusive and turbulent oceans. Diapycnal velocity (w^*) is evaluated at the average isopycnal surface $\rho = \rho_{av}$ in the ocean interior $(x > L_{int})$ and shown for the double-diffusive (a) and turbulent (b) experiments. In the double-diffusive case, typical values of w^* are on the order of $\sim 5 \cdot 10^{-9} \, m/s$ or less with both positive and negative values observed. In the turbulent experiment, diapycnal velocities are mostly positive and larger by at least an order of magnitude $(\sim 5 \cdot 10^{-8} \, m/s)$.
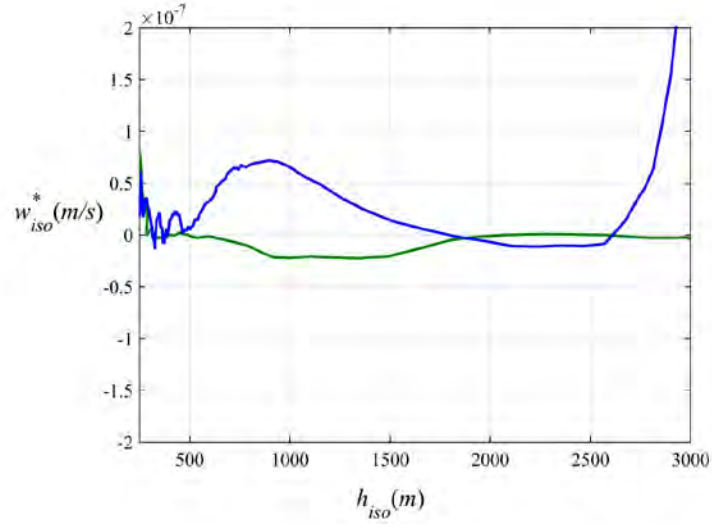
(a)
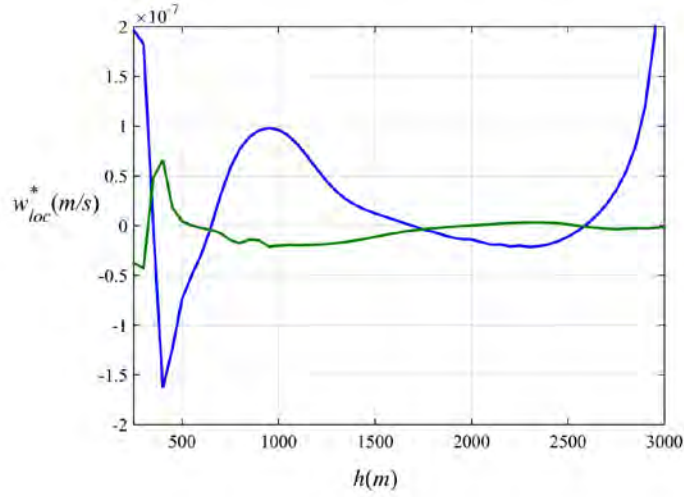
(b)

Figure 2.10.   The vertical distribution of diapycnal transport. (*a*) The mean diapycnal velocity evaluated at various isopycnals (w_{iso}^*) and plotted as a function of the average depth of those surfaces. (*b*) The local vertical profile of diapycnal velocity (w_{loc}^*) at $(x,y)=(0.5L_x,0.5L_y)$. Both diagnostics indicate that diapycnal velocity in the turbulent case (indicated by the blue curves) substantially exceeds that in the double-diffusive ocean (green curves). The patterns of w_{iso}^* and w_{loc}^* are qualitatively similar.
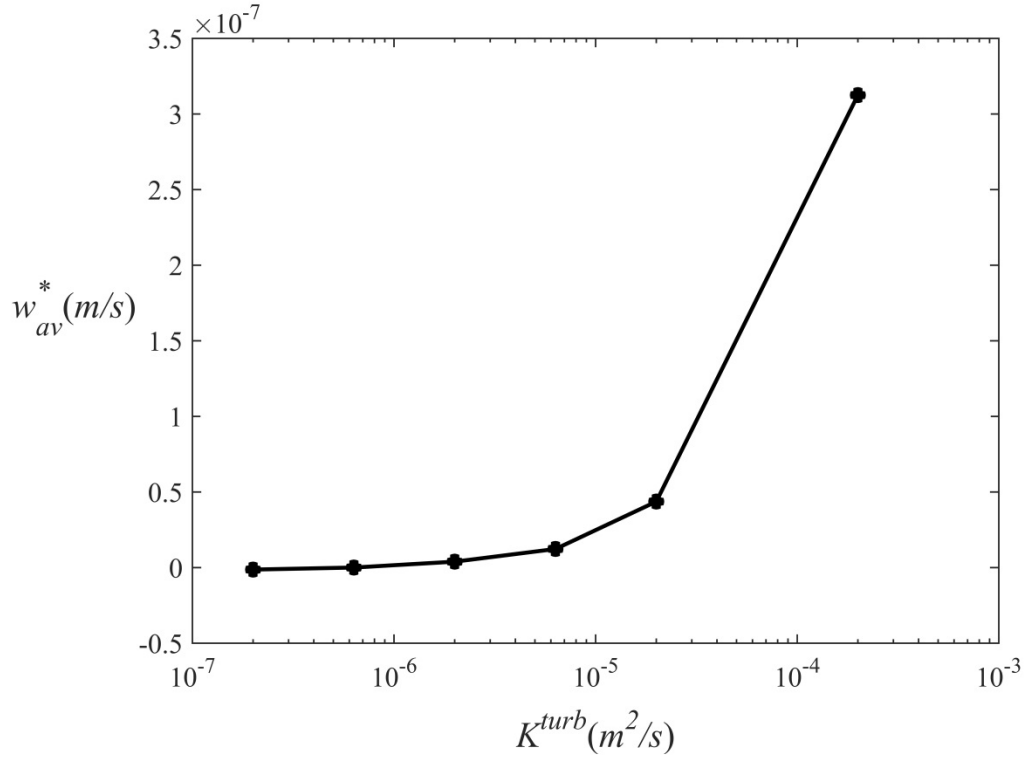
Figure 2.11.   The variation of the mean diapycnal velocity at the density surface $\rho = \rho_{av}$ (w^*_{av}) as a function of K^{turb}. The diagnostics are based on a series of simulations that incorporate both double-diffusive and turbulent mixing. Note the monotonic increase in w^*_{av} with increasing K^{turb}.
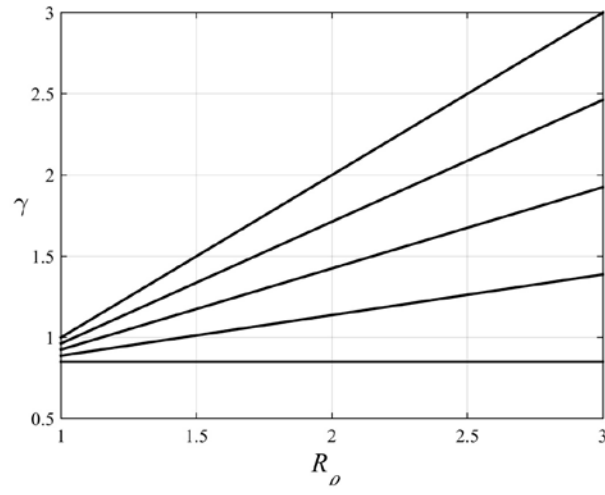
(a)
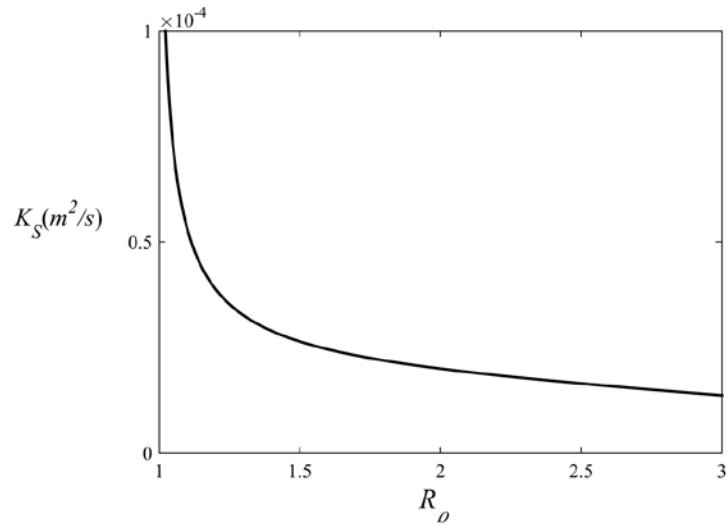
(b)

Figure 2.12. The assumed patterns of the flux ratio (*a*) and salt diffusivity (*b*) used for parameterization of double-diffusion in the numerical simulations.

101
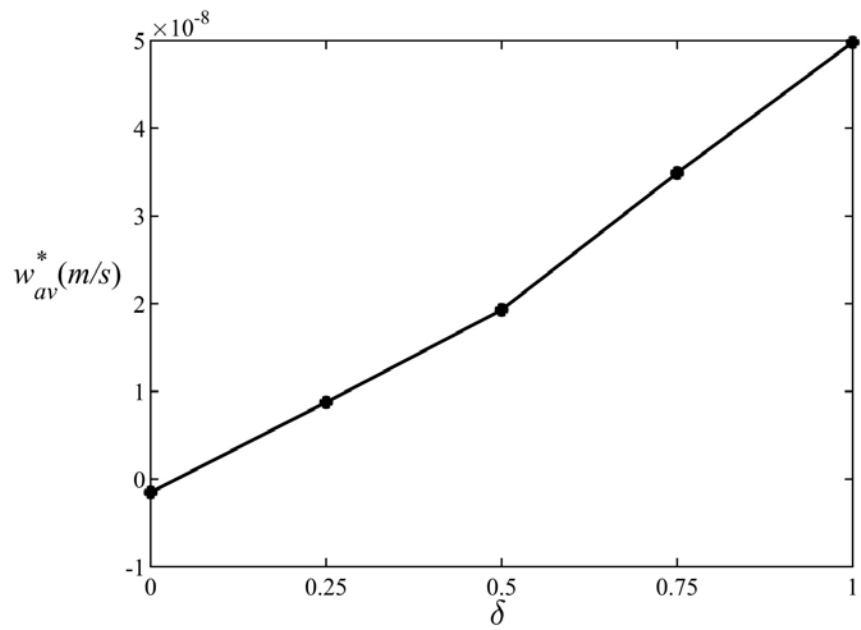
Figure 2.13.   A series of large-scale simulations in which the variation in the flux ratio (as measured by the parameter δ) is systematically increased. For each experiment, the mean diapycnal velocity (w^*_{av}) at the average isopycnal surface ρ_{av} is plotted as a function of δ. Note the monotonic—nearly linear—increase in w^*_{av} with δ.
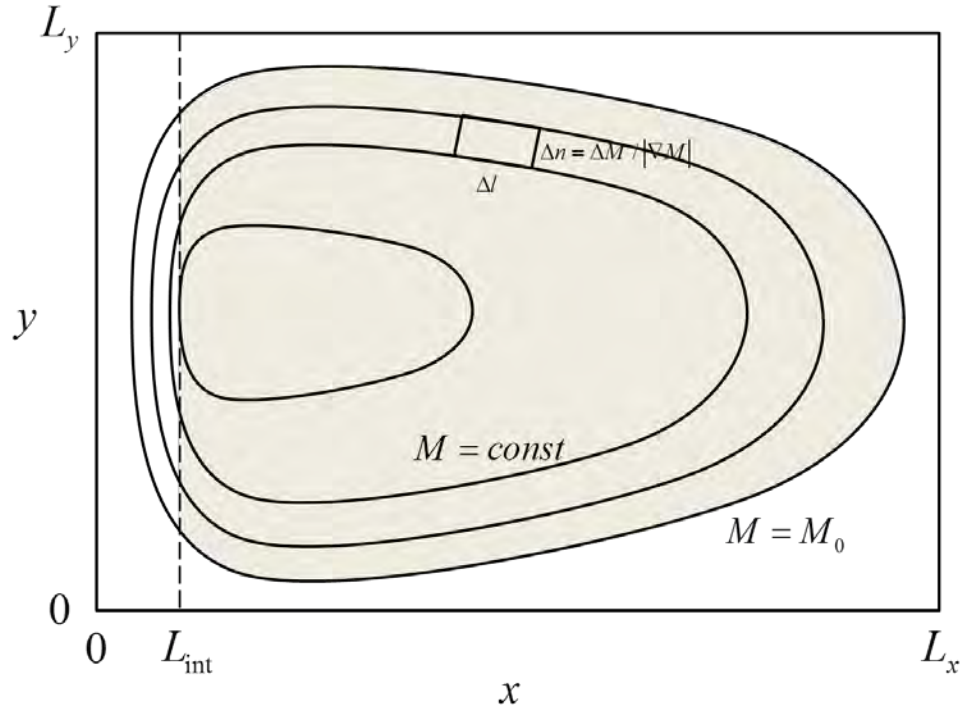
Figure 2.14. Schematic diagram illustrating the analytical model of double-diffusive insulation. The model suggests that the average diapycnal velocity in the regions bounded by closed streamlines on the density surfaces in the ocean interior (indicated by grey shading) is zero if vertical mixing is double-diffusive but can be finite in the presence of mechanically generated turbulence.
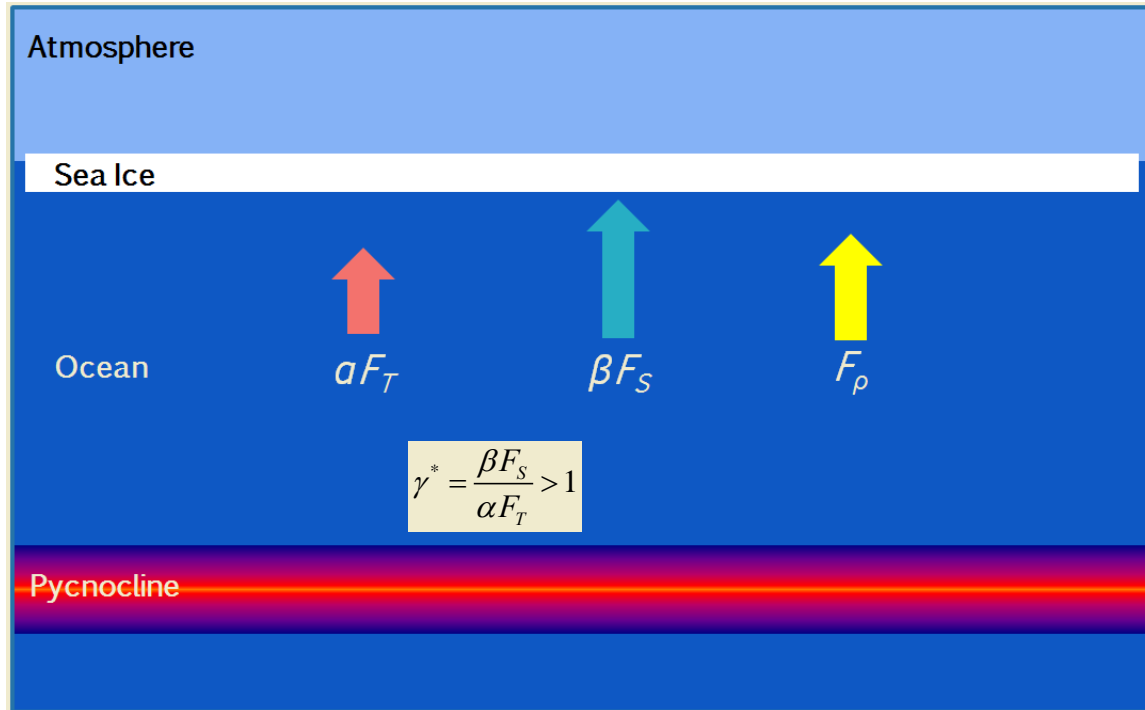
Figure 3.1.   Thermal and haline contributions to density flux: Turbulent case. In a column dominated by turbulence, $\gamma^* > 1$. The haline contribution to density flux is greater than the thermal contribution. As a consequence, overall density flux (the sum of both contributions) is positive, leading to increased water column instability as density near the surface increases.
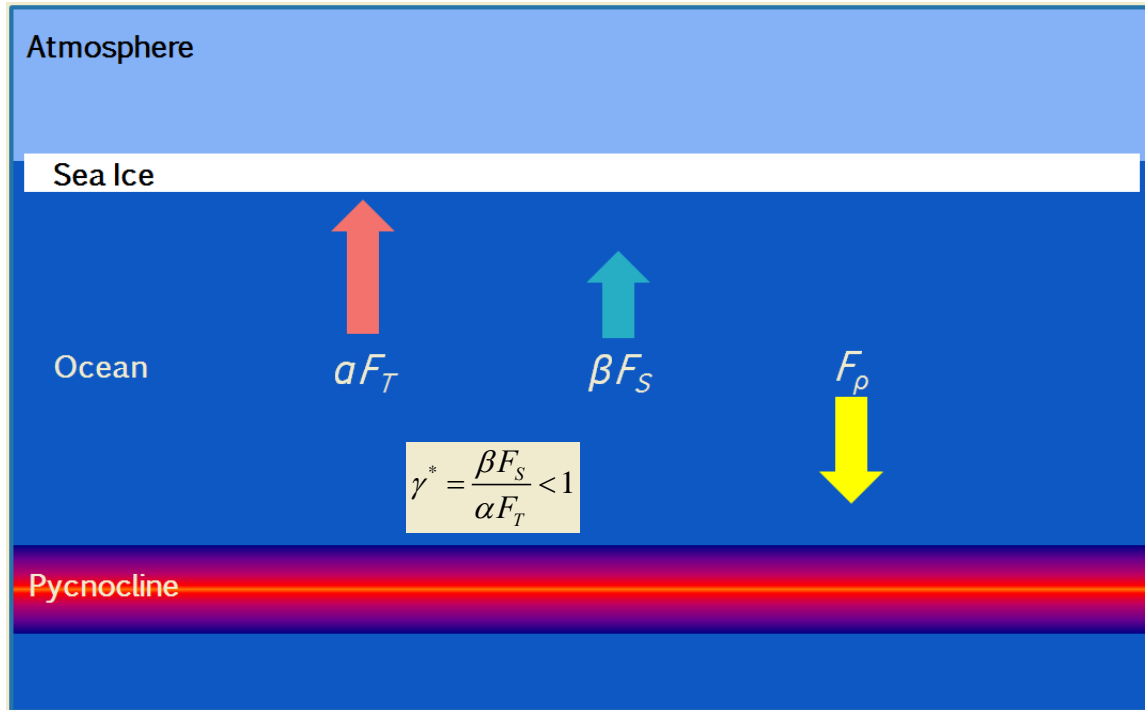
Figure 3.2.   Thermal and haline contributions to density flux: Double-diffusive case. When the water column experiences conditions favorable for diffusive convection, $\gamma^* < 1$. In this case, the thermal contribution to density flux is greater than the haline contribution. Double-diffusion acts to stabilize the water column through a negative density flux, causing density to decrease at the surface.
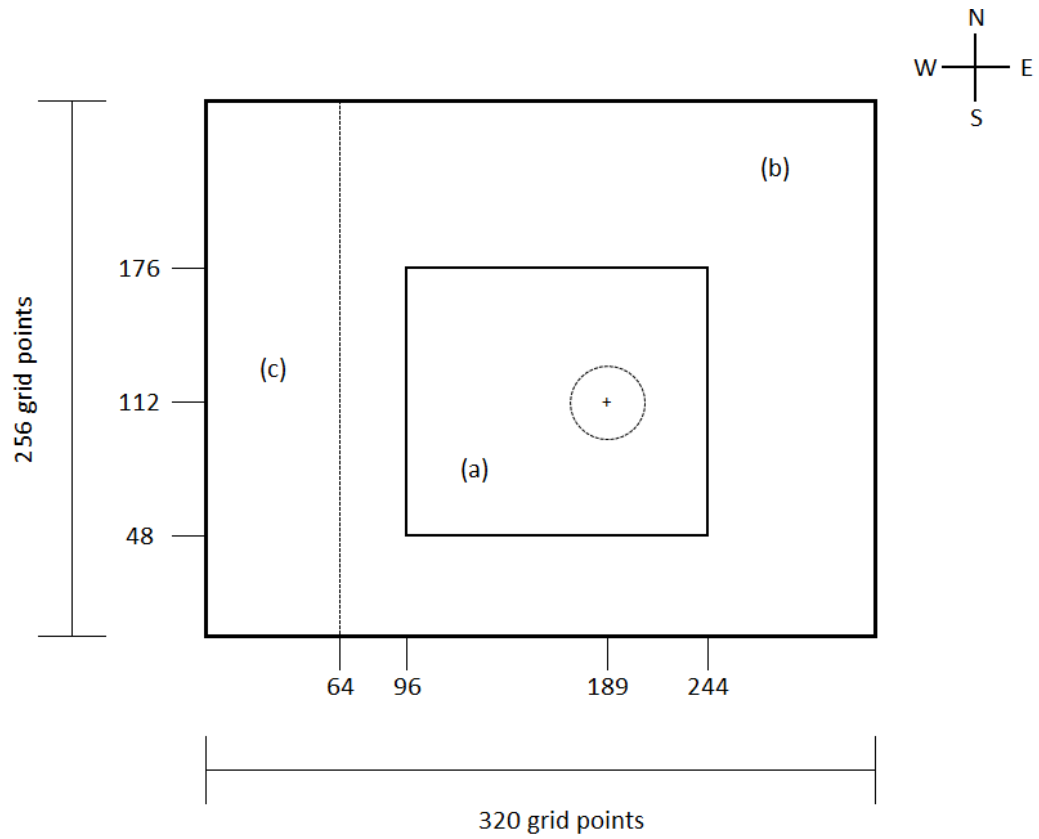
Figure 3.3.   The model domain. To eliminate open boundary edge effects, the domain of interest (*a*) is contained within a larger domain (*b*). Zonal grid spacing increases exponentially in the western region to ensure consistent background flow through the domain at all times (*c*). The seamount (*circle, representing 4500m isobath*) is placed far enough from the eastern boundary to keep in-flow advection from dominating the conditions in the domain of interest.
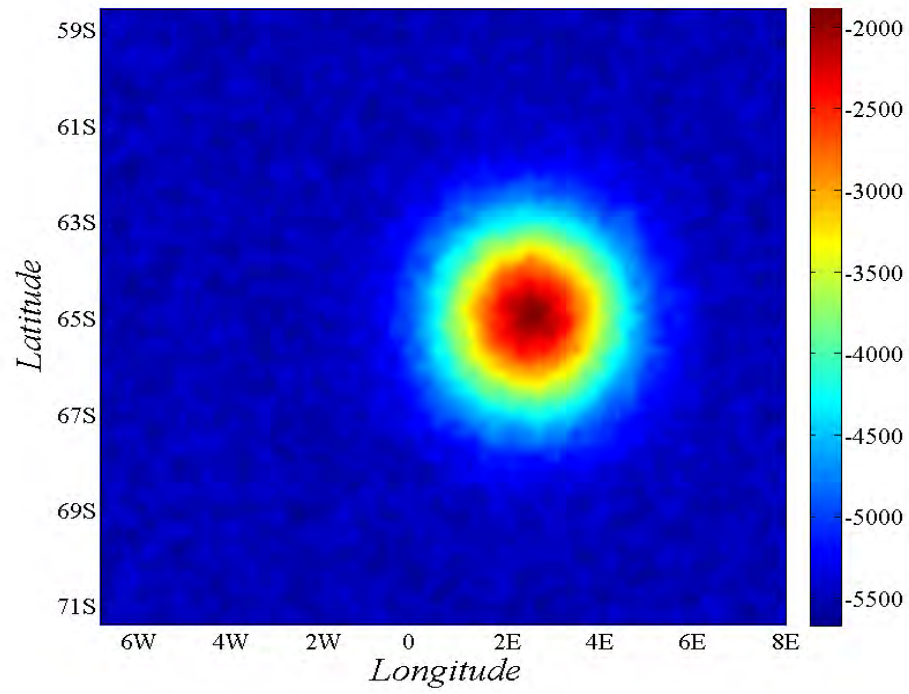
(a)
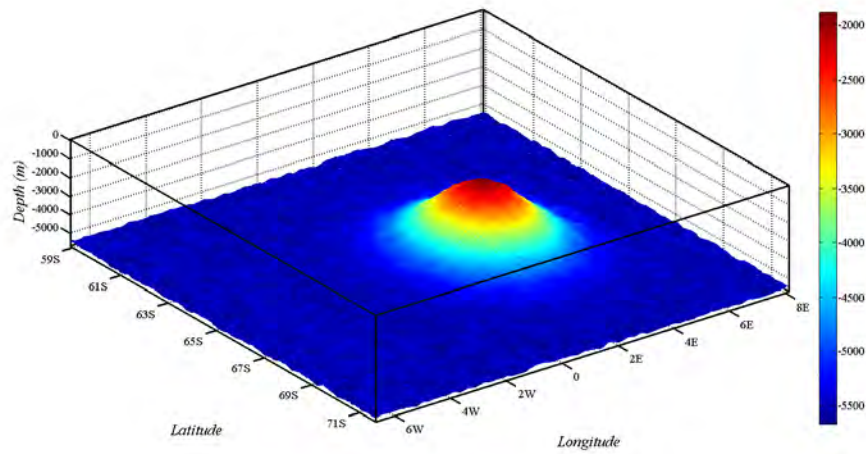
(b)

Figure 3.4.   High   resolution   model   bathymetry.   The   idealized   seamount represents Maud Rise in the eastern Weddell Sea and depths are randomized throughout the domain to simulate a rough bottom
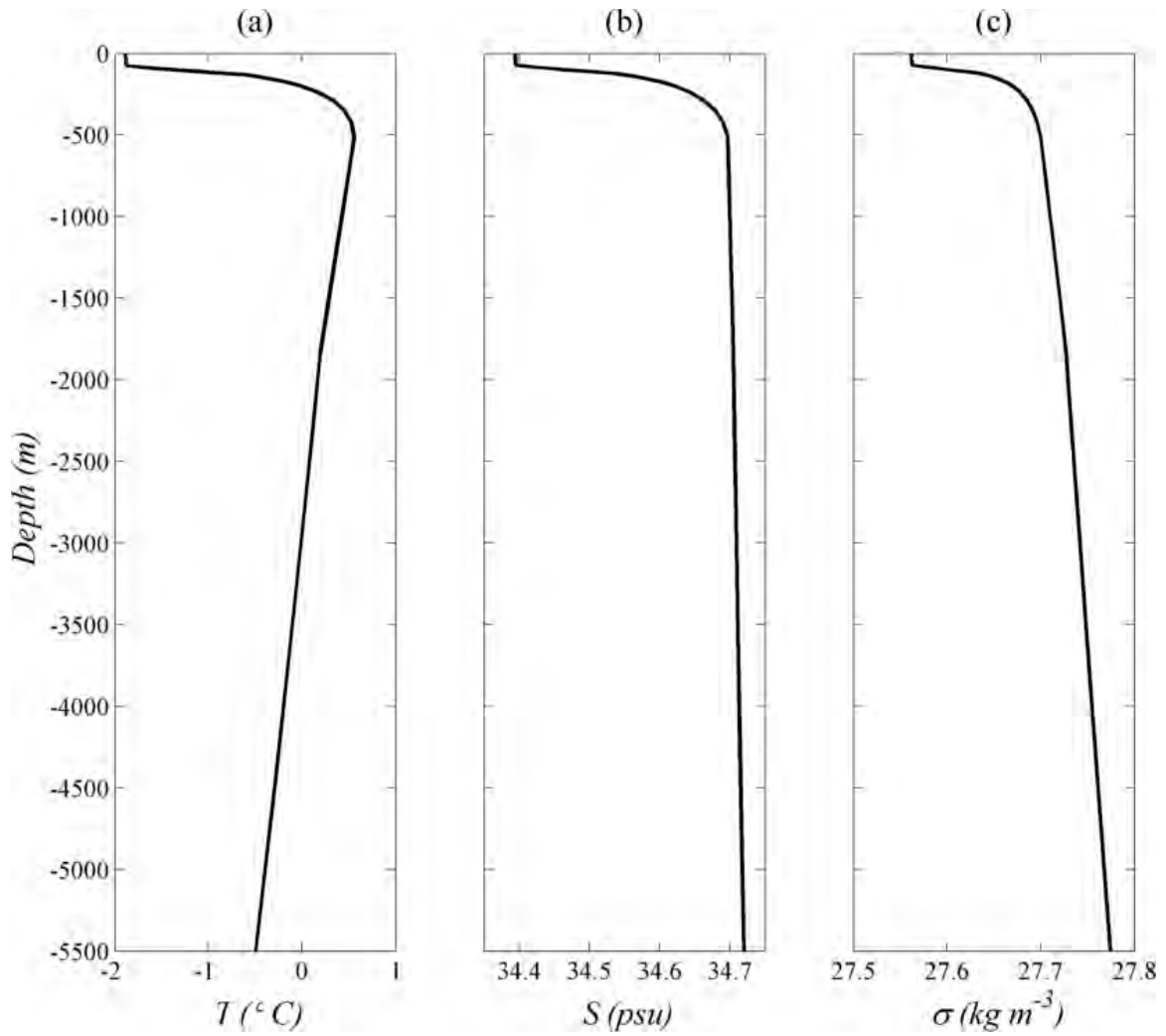
Figure 3.5. Vertical profiles of (*a*) temperature, (*b*) salinity, and (*c*) potential density anomaly at model initialization. Mixed layer depth is $76m$. The diffusive convection regime dominates below the mixed layer to approximately $500m$.
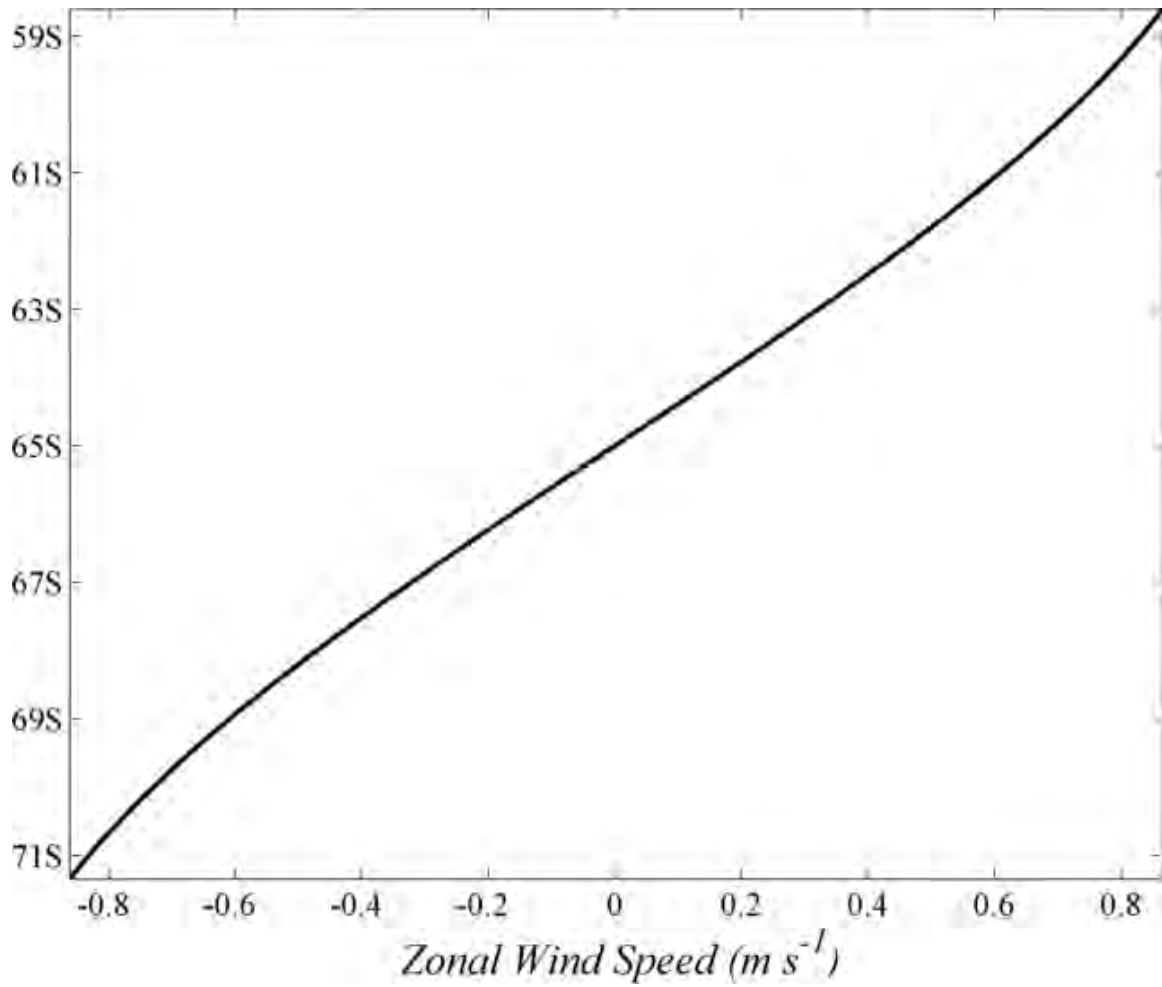
Figure 3.6.   Zonal wind forcing. Wind forcing mirrors climatological mean wind speeds by latitude and remains zonally and temporally constant throughout model runs.
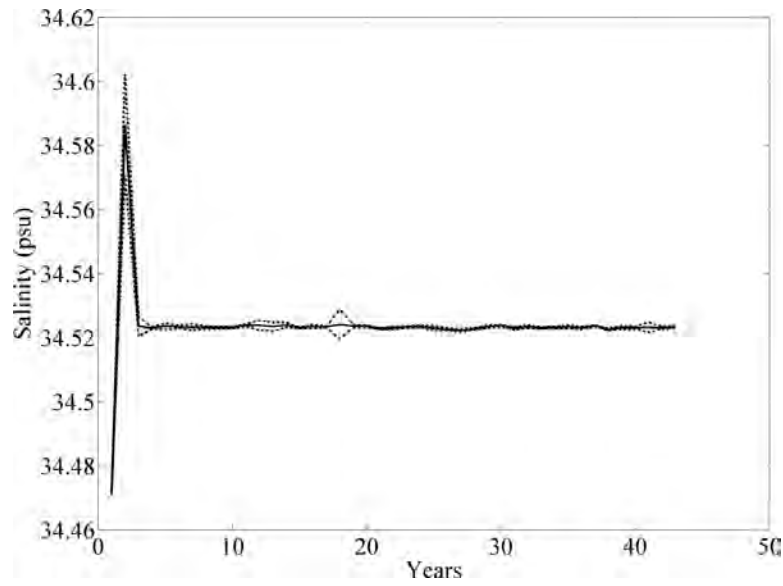
(a)
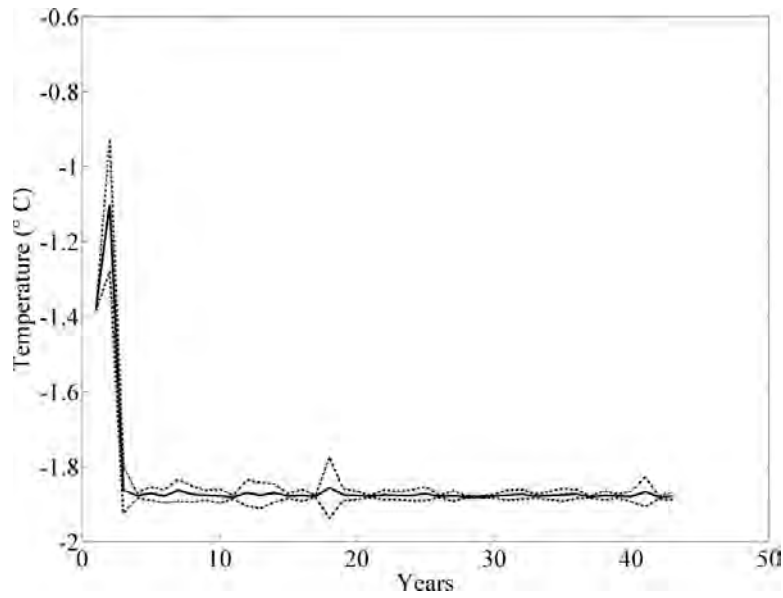
(b)

Figure 3.7.   Tracer equilibration: Mean (*a*) salinity and (*b*) temperature centered at 60 S, 4 W (averaged over grid points $124 \pm 5, 160 \pm 5, 10$), at a $100m$ depth. Mean (*solid*) and one standard deviation (*dotted*) illustrate how quickly the model equilibrates.

(a)

(b)
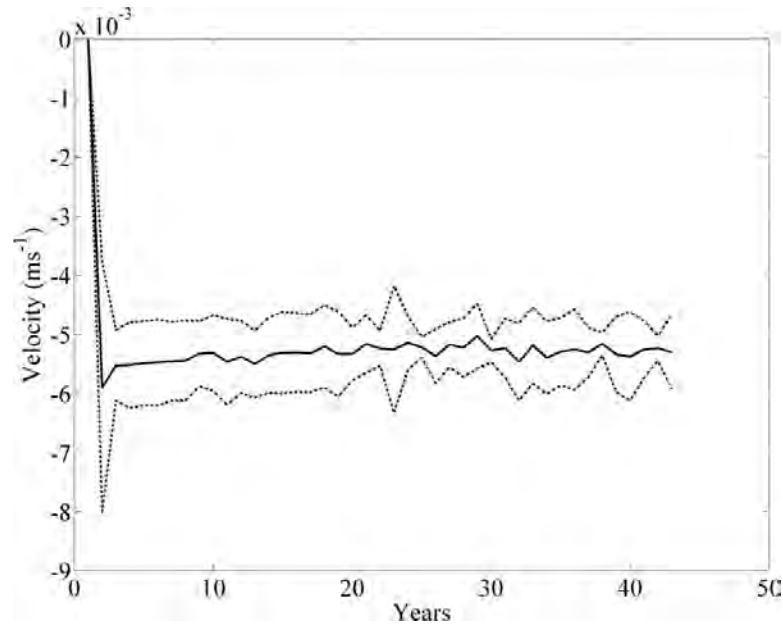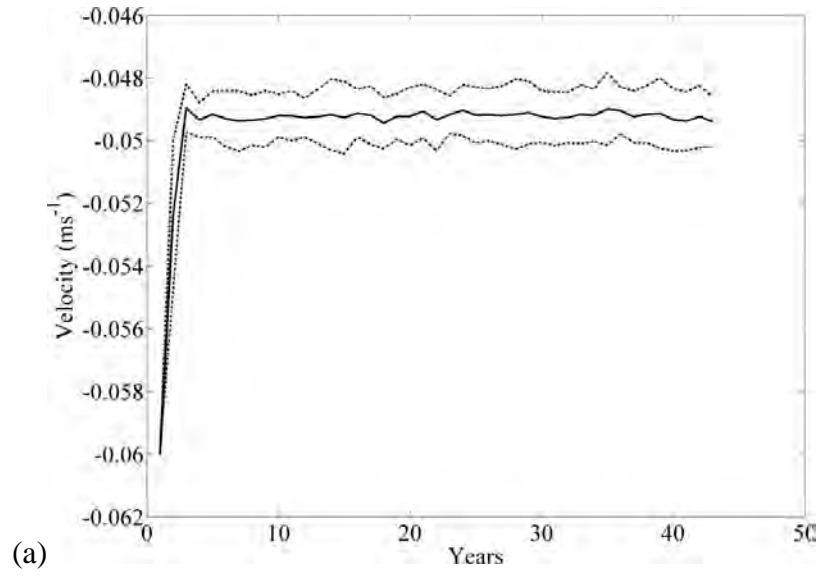
Figure 3.8.   Momentum equilibration: Mean (*a*) zonal velocity and (*b*) meridional velocity centered at 60 S, 4 W (averaged over grid points $124 \pm 5, 160 \pm 5, 10$), at a 100*m* depth. Equilibration of momentum parameters occurs quickly. Mean (*solid*) and one standard deviation (*dotted*).
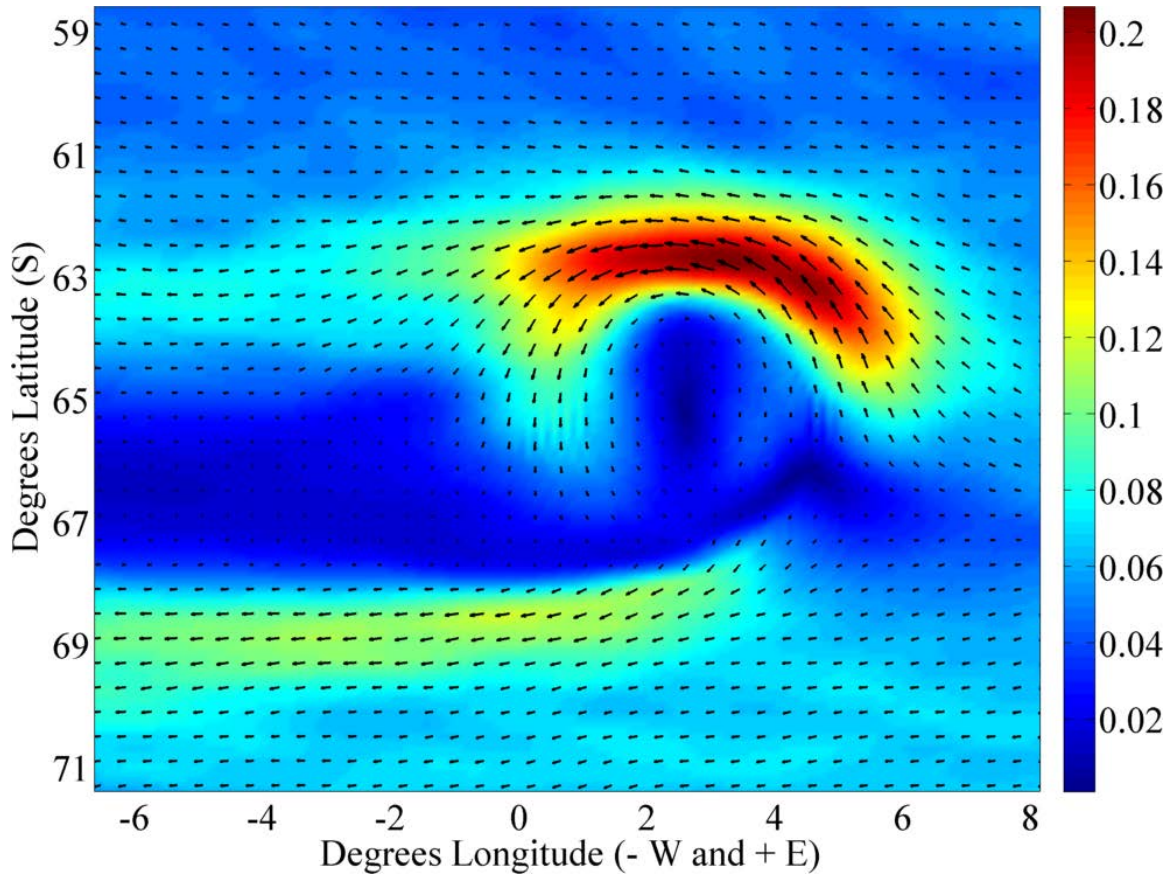
Figure 3.9.   Steady-state surface velocity field for Model 24A at Year 10 (ms^{-1}). This represents the typical surface current field for all models. The idealized Maud Rise centered at 65 S, 2.5 E. Although induced flow in the model is $0.06\,ms^{-1}$ magnitudes reach $0.2\,ms^{-1}$ north of the seamount and come to a near stand-still directly over the seamount, correctly modeling the Taylor cap found in the same area of the Weddell Sea.
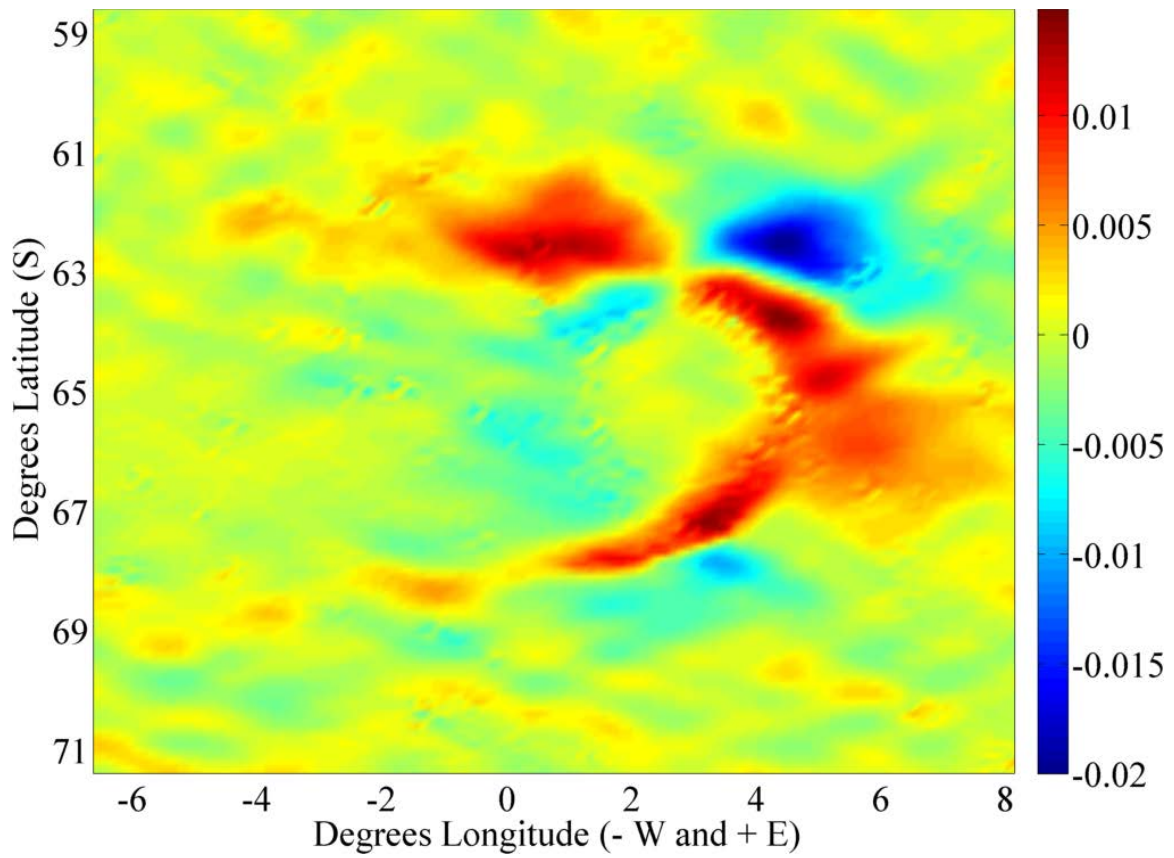
Figure 3.10.   Relative vorticity at the surface for Model 24A at Year 10 (s^{-1}). The surface above the seamount is clearly visible as an area of low vorticity.
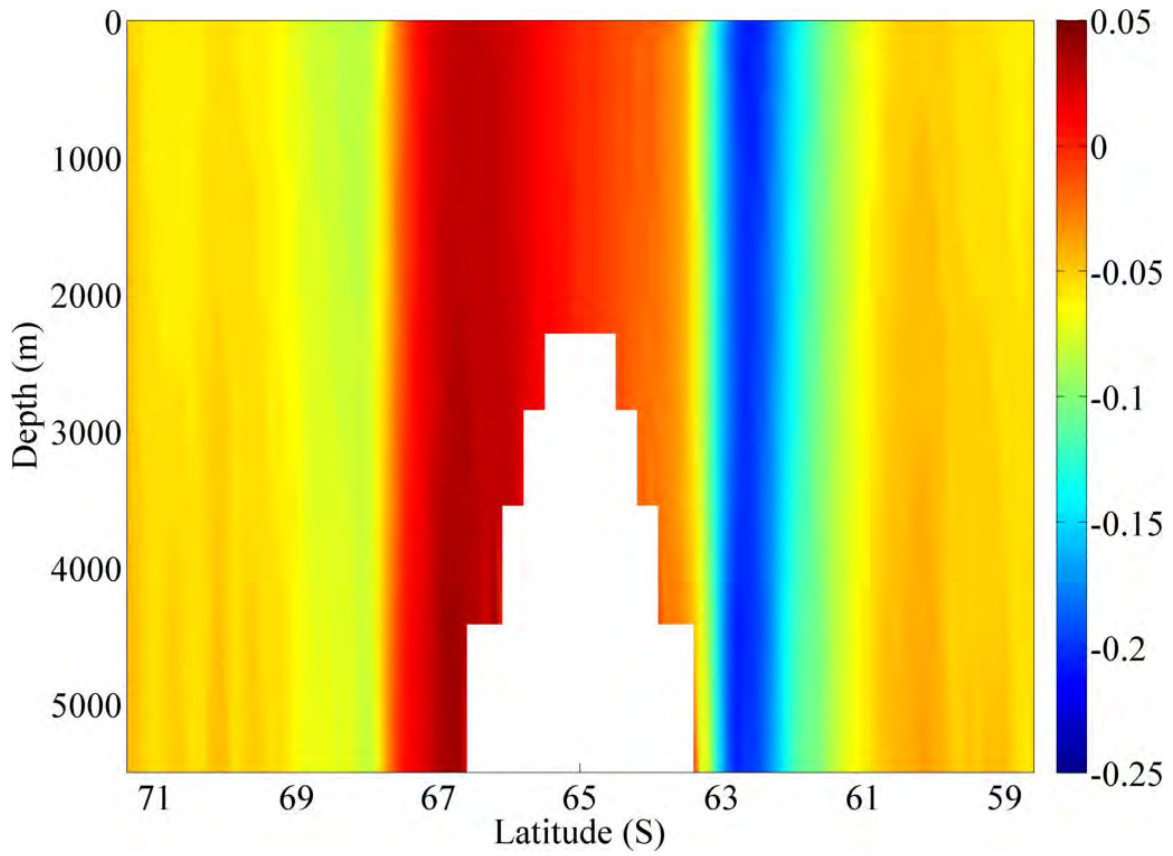
Figure 3.11.   Zonal velocity for Model 24A at Year 10 (ms^{-1}). This meridional cross-section at 2.5 E illustrates the vertical extent of the Taylor cap situated over the seamount. Also note the heightened westward zonal velocity between 62 and 63 S.
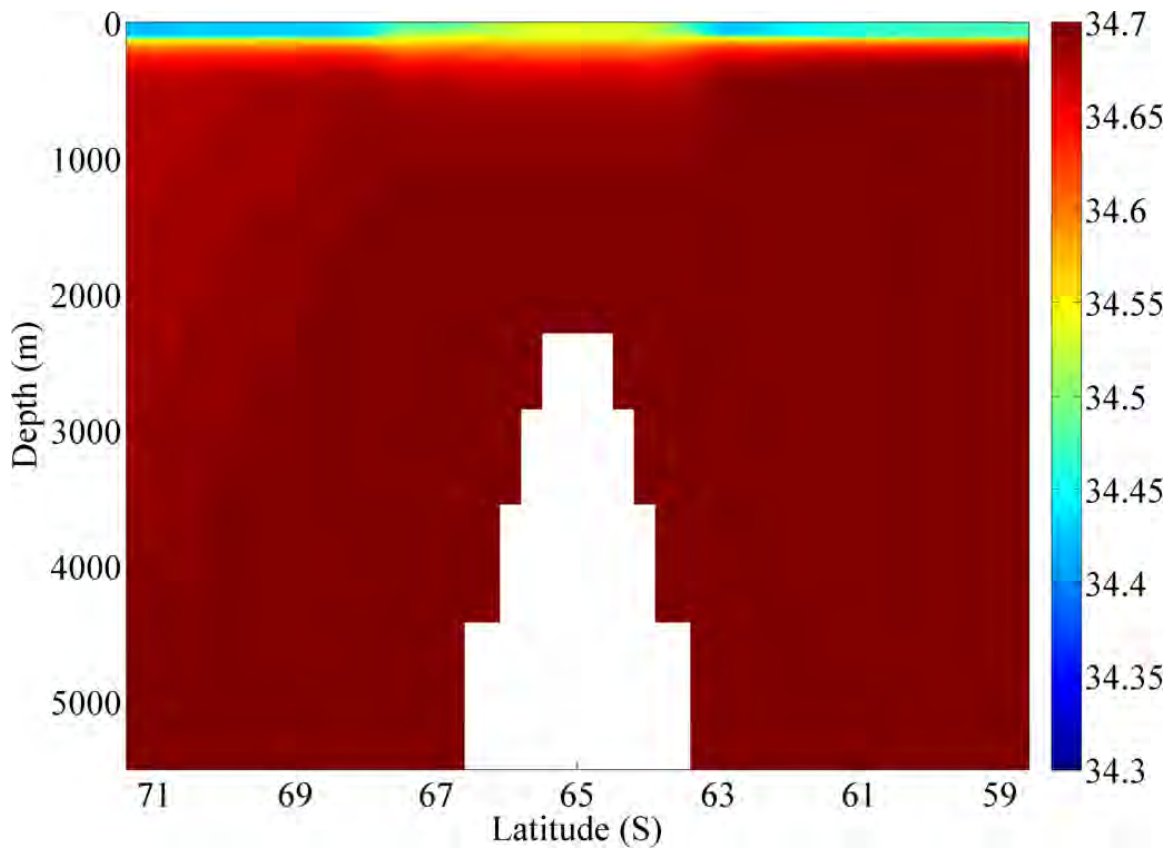
Figure 3.12. Representative meridional cross-section (2.5E) of salinity (psu) for Model 24A at Year 10. The halocline is clearly visible at a depth of approximately $125m$ outside the vicinity of the seamount. Over the seamount, this salinity gradient is smaller.
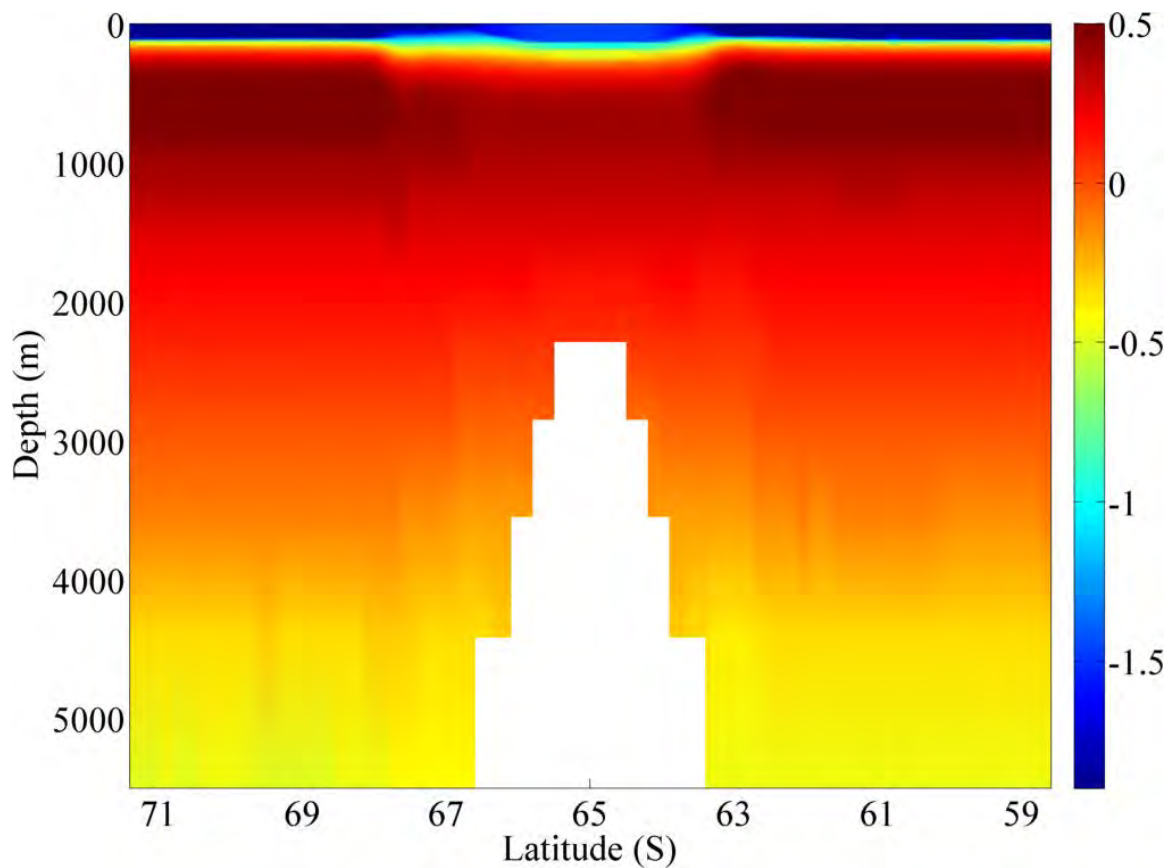
Figure 3.13.   Representative meridional cross-section (2.5E) of temperature $(^{\circ}C)$ for Model 24A at Year 10. The thermocline appears at a depth of about $125m$ to the north and south of the seamount. Surface temperatures are higher over the seamount while temperatures at depth over the seamount are lower.
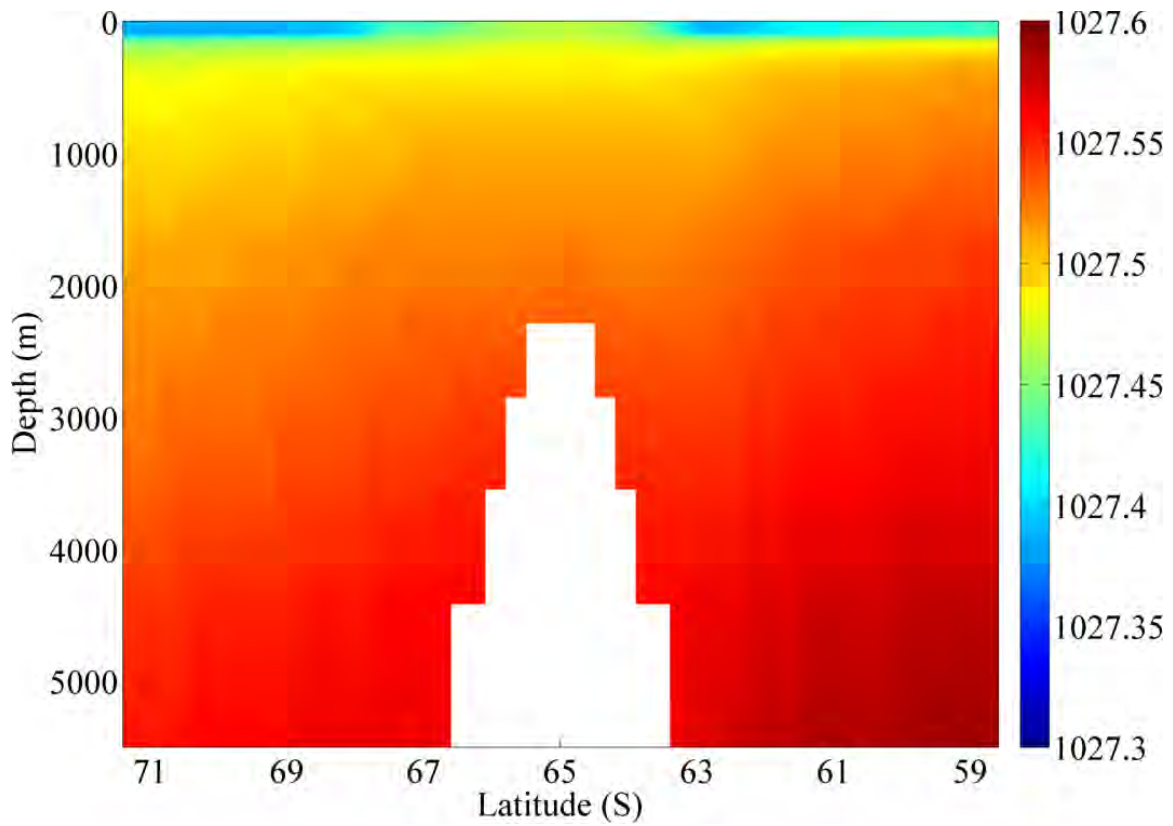
Figure 3.14. Representative meridional cross-section (2.5E) of potential density ($kg\ m^{-3}$) for Model 24A at Year 10. The combined effects of salinity (Figure 3.12) and temperature (Figure 3.13) produce a well-defined pycnocline away from the seamount. However, isopycnal shoaling at the periphery of the area above the seamount marks the transition to an area of weak pycnocline directly over the seamount.
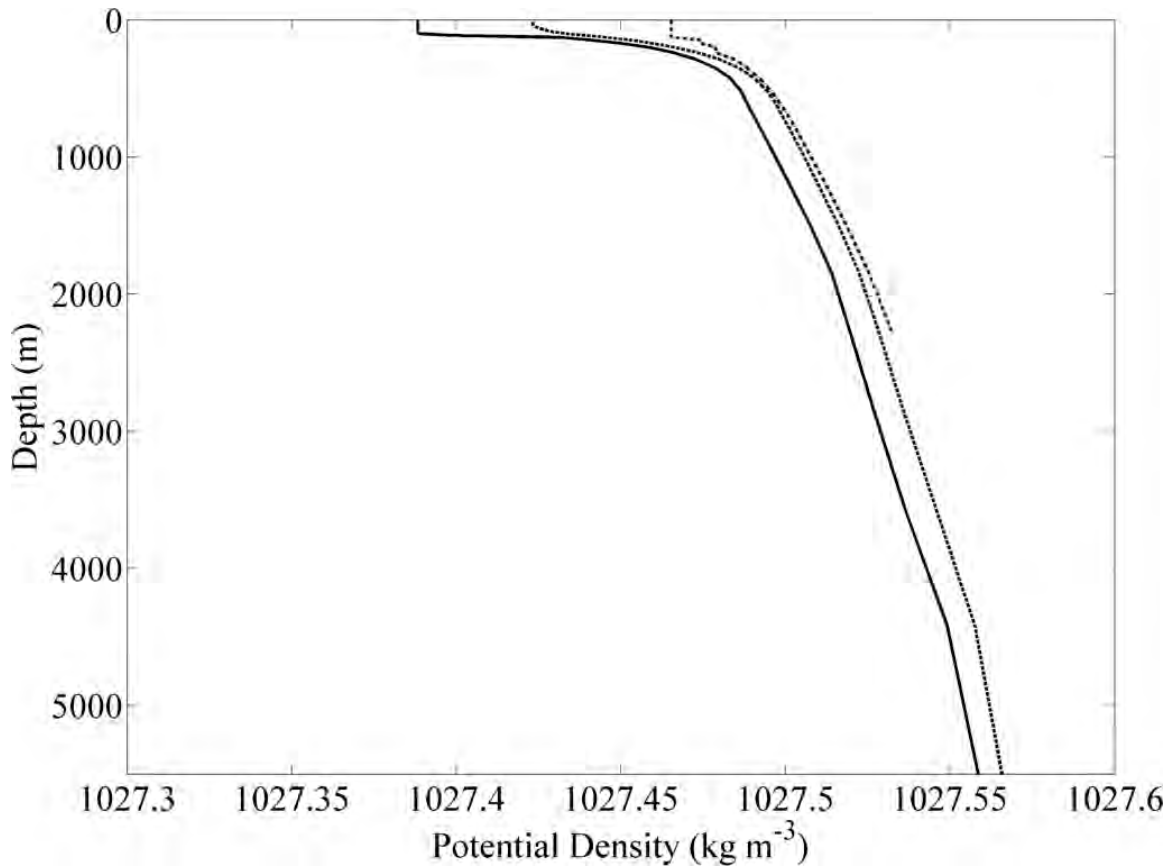
Figure 3.15.   Profiles of potential density. Potential density is shown for locations representing "Ambient" conditions (*solid*), transition conditions (*dashed*), and Taylor cap conditions (*dotted*). These profiles are from Model 24A, Year 10, along the 2.5 E meridian at 71.5 S, 69 S, and 65 S. Potential density differences across each pycnocline is 0.1, 0.07, and 0.03 $kg\ m^{-3}$, respectively. These values are comparable to observed values near Maud Rise in the Weddell Sea at the same locations.
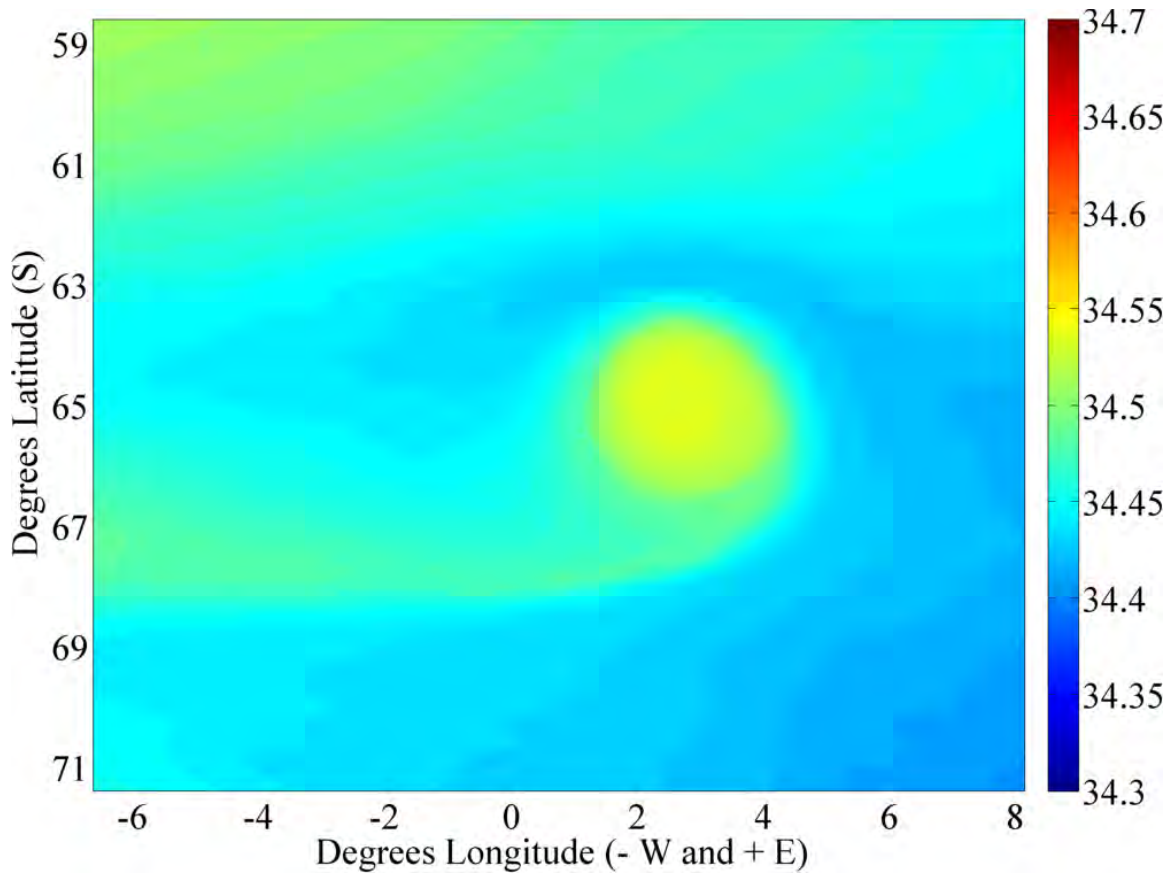
Figure 3.16. Surface salinity (*psu*) for Model 24A at Year 10. Reduced flow (see Figure 3.9 and Figure 3.11) over the seamount leads to heightened salinity at the surface above, higher densities, and a correspondingly weaker pycnocline (Figure 3.15).
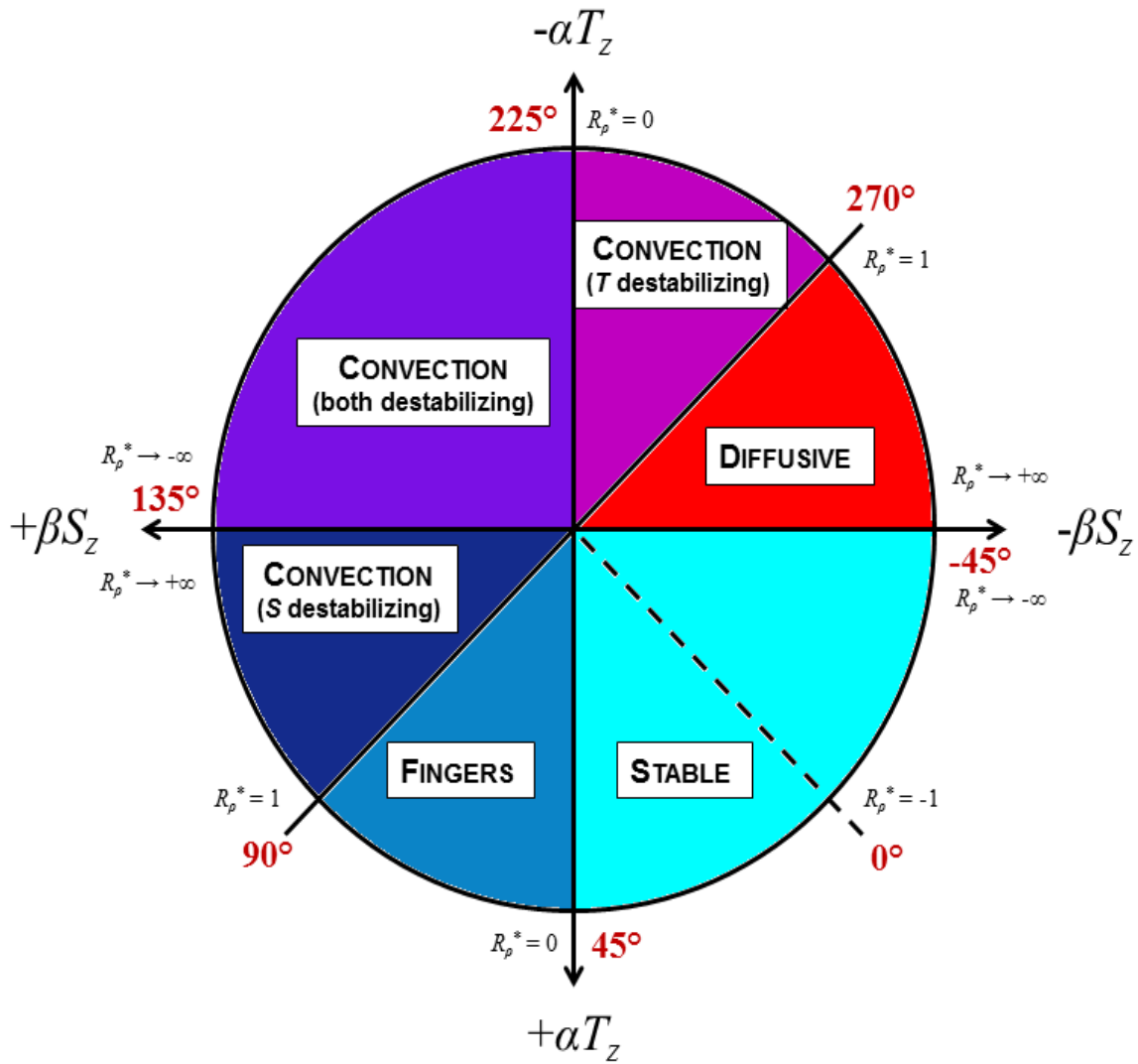
Figure 3.17. Schematic diagram of the Turner angle. Turner angles with associated diffusive density ratios are shown. Turner angle ranges delineate four main stability regimes: stable, salt fingering, convection, and diffusive convection. After Ruddick (1983) and Radko (2013).
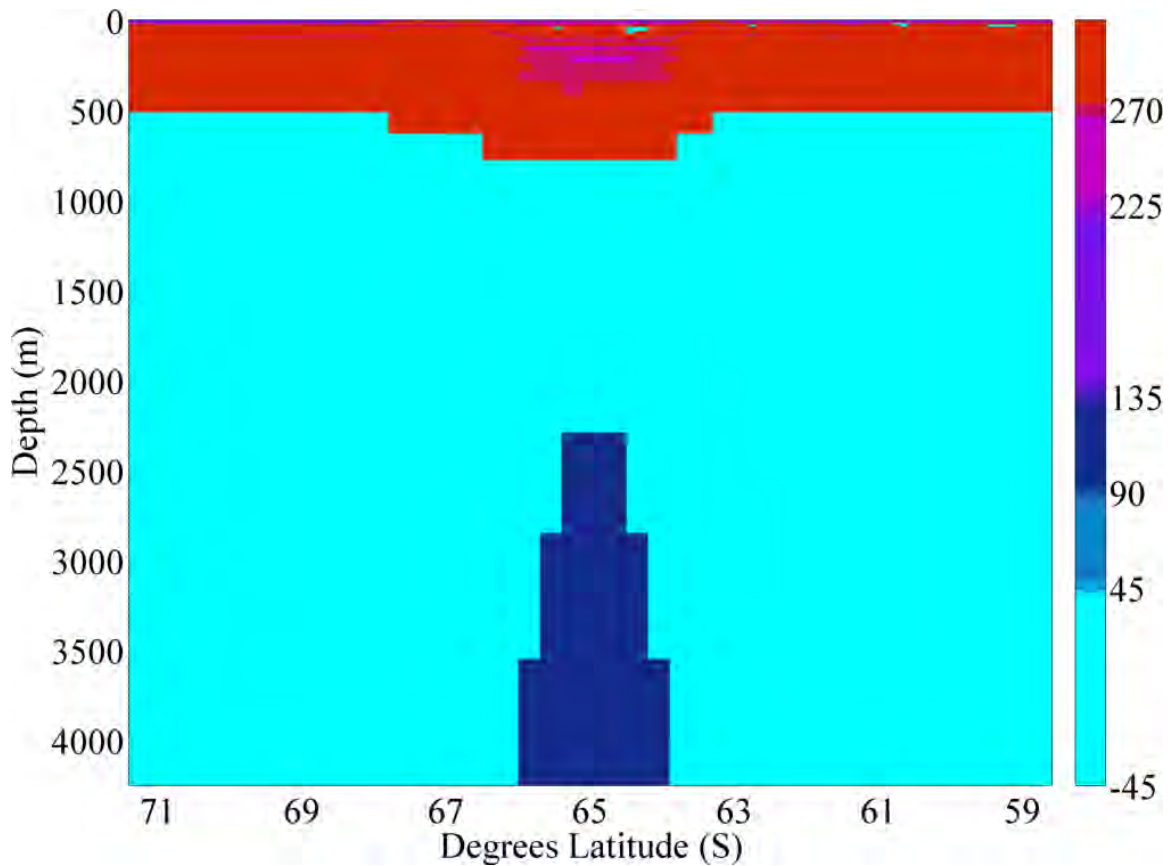
Figure 3.18. A representative cross-section of Turner angle (Tu) from Model 24A at Year 10. Plot color indicates dominant conditions based on the Turner angle. Stable portions of the column (*cyan*) and diffusive convection (*red*) are typical. The gravitationally unstable regime occurs from $Tu = 90°$ to $Tu = 270°$ and occurs when (*a*) the salinity gradient is destabilizing and its magnitude is greater than that of temperature (*indigo*), (*b*) both salinity and temperature gradients are destabilizing (*purple*), or (*c*) the temperature gradient is destabilizing and its magnitude is greater than that of salinity (*magenta*). Finally, salt fingering (*blue*) occurs when $45° < Tu < 90°$, but such conditions would be rare in this region. Corresponding Turner angles are shown with the color bar for reference (see Figure 3.17). The seamount is shown in blue.

Model 17A: Fixed, Steady (1 *Wm⁻²*), *K_{turb}* = 0, with Double-Diffusion
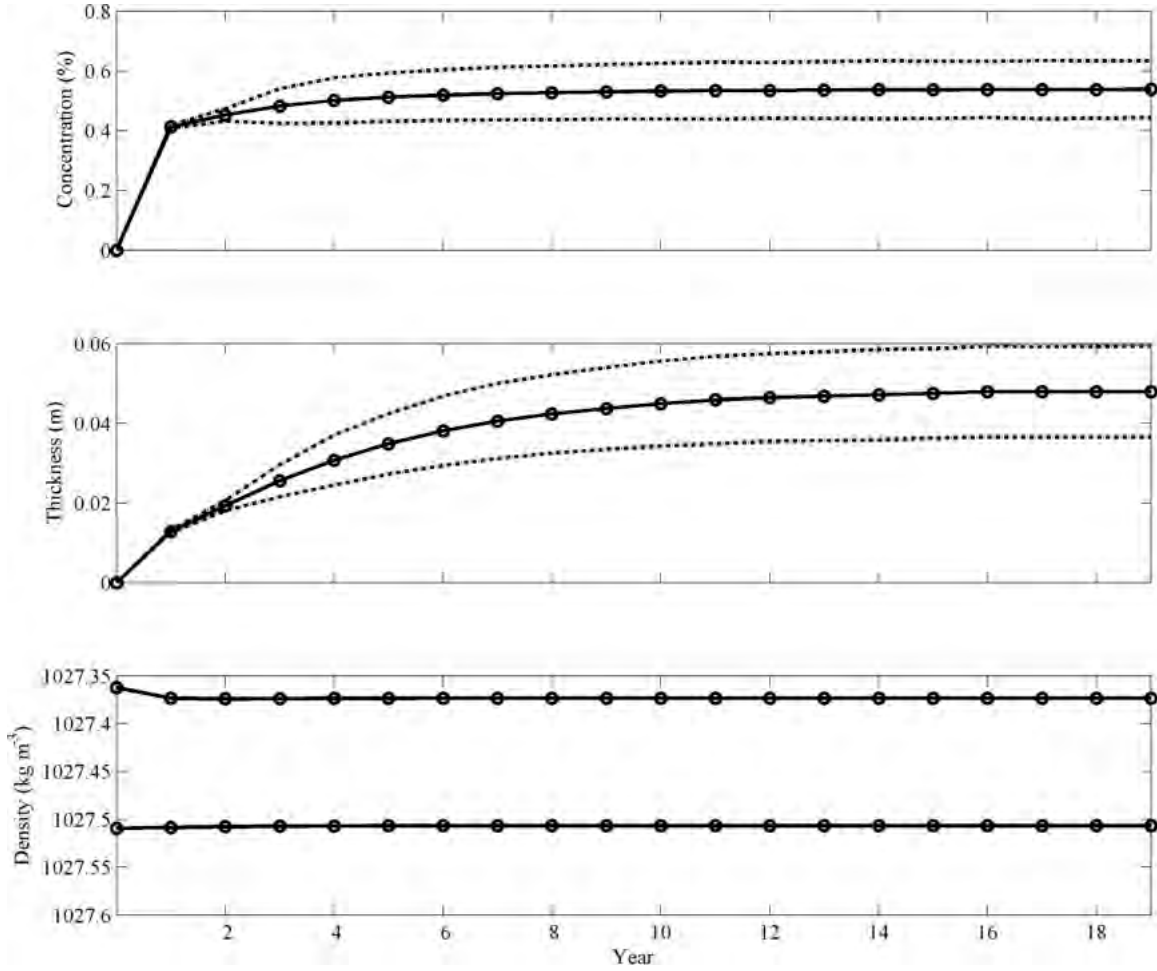
Figure 3.19. Model 17A, Time Series. Mean sea ice concentration, mean thickness and potential density. The time evolution of sea ice concentration (*upper*) and thickness (*middle*) shows initial growth and then leveling off for this model with a steady cooling of $1 Wm^{-2}$. These means have been averaged over 121 grid points centered above the seamount peak $(189 \pm 5, 112 \pm 5)$. Dashed lines indicate one standard deviation. Mean potential density (*lower*) at two locations, one at a depth of 10m (*upper curve*) and the other at a depth of approximately 1000m (*lower curve*) serves as a proxy to indicate whether convection has initiated. In this case, no convection occurs at any point during the run. Note that potential density values on the ordinate have been inverted to follow the proper direction for a stable gradient.
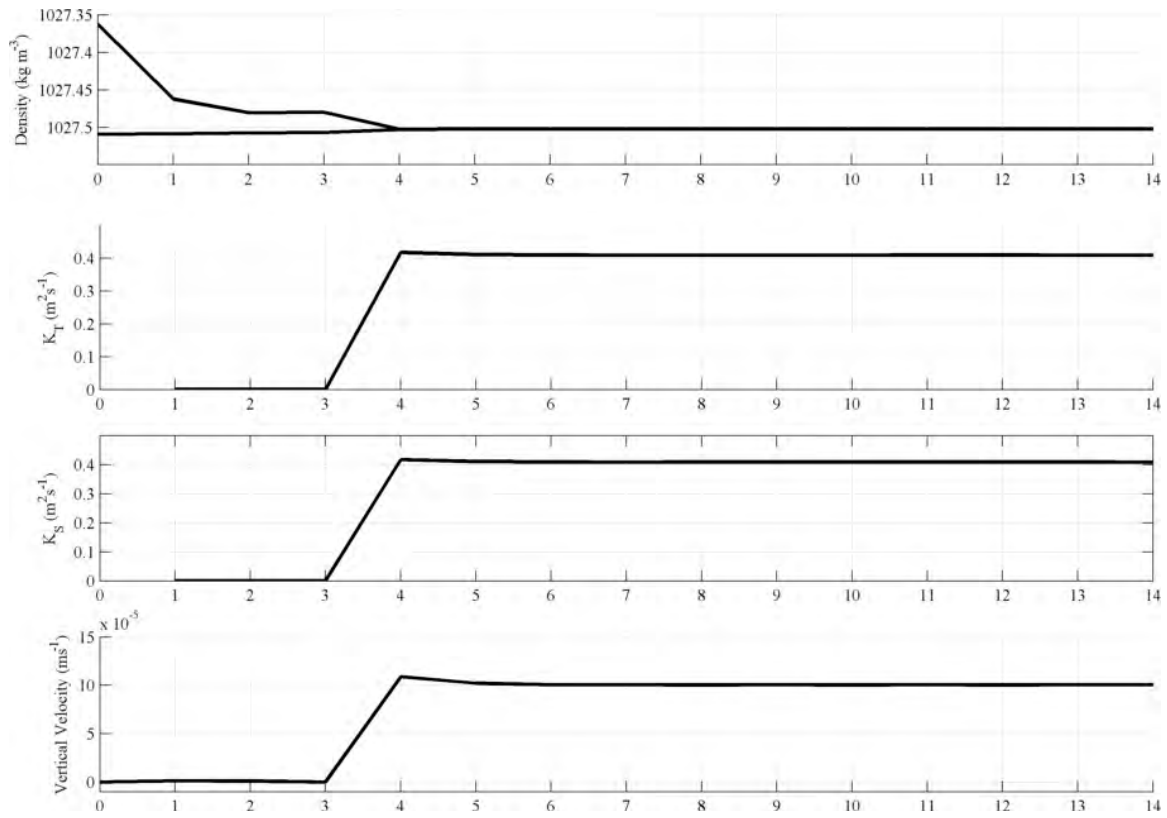
Figure 3.20. Comparing Measures of Convection. Time-series of summit areal means of potential densities $(10m$ and $1000m)$, temperature and salt diffusivities, and vertical velocities all indicate the onset of convection prior to year 4 (Model 25C).

Model 17C: Fixed, Steady (1 Wm^{-2}), K_{turb} = 2•10^{-5}, No Double-Diffusion
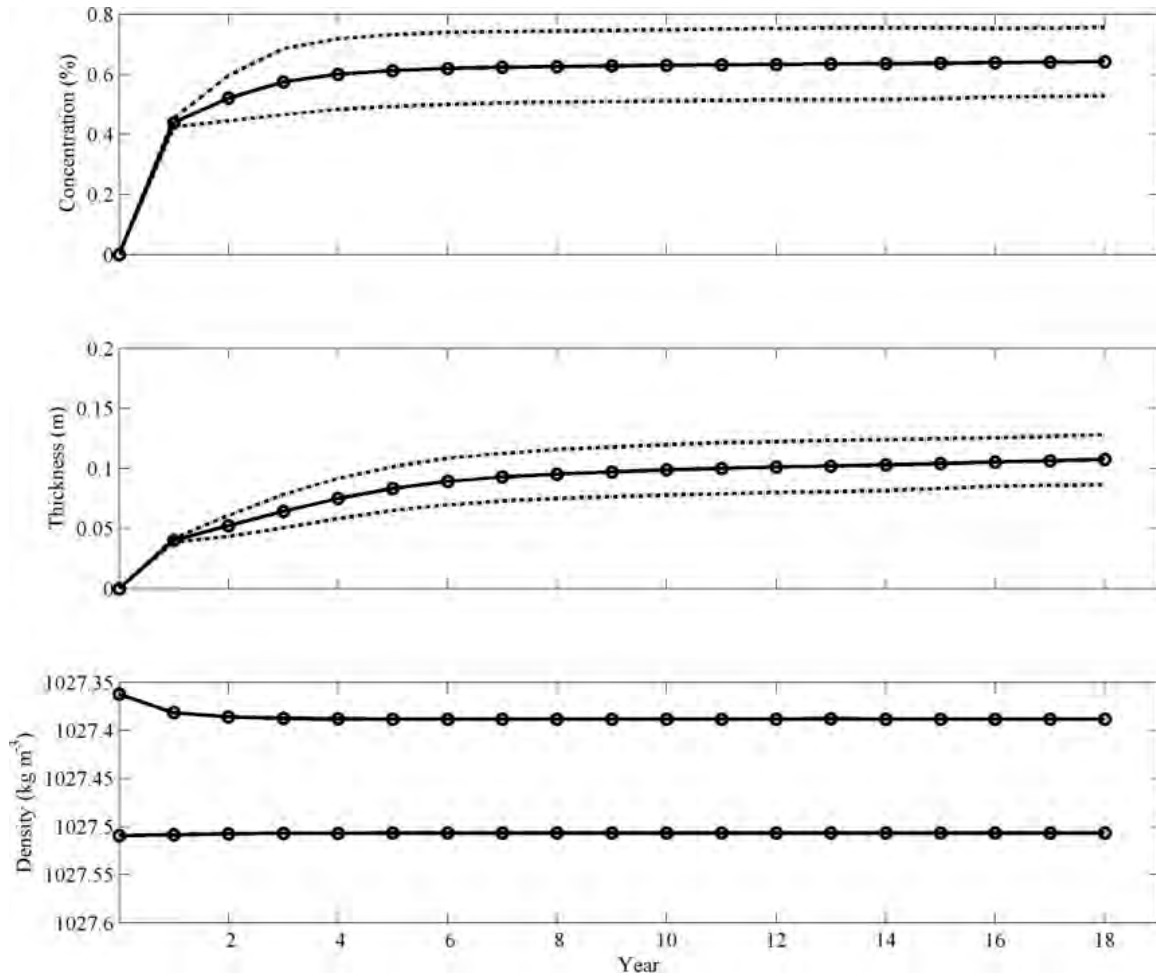
Figure 3.21.   Model 17C, Time Series. Mean sea ice concentration, thickness, and potential density. This model is identical to 17A, save there is no double-diffusive parameterization and the turbulent diffusivity is non-zero. As with 17A (*previous*) and 17B (*not shown*), no convection occurs over the seamount during this run. A model equilibrium was reached in these three cases.

Model 18A: Fixed, Steady (5 Wm^{-2}), K_{turb} = 0, with Double-Diffusion
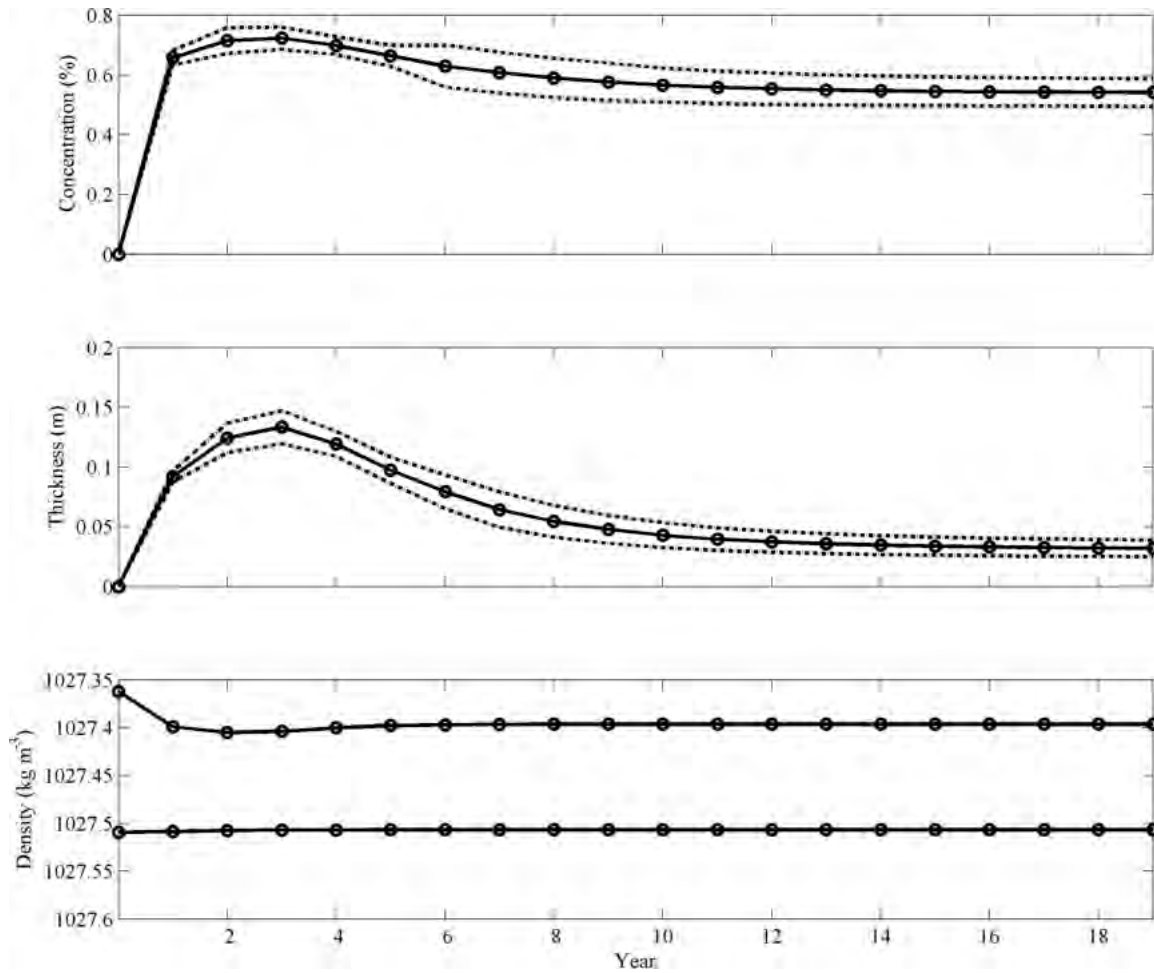
Figure 3.22.   Model 18A, Time Series. Mean sea ice concentration, thickness, and potential density. These series are from the fixed, steady, higher surface flux forcing ($5\,Wm^{-2}$) run with zero turbulent diffusivity and double-diffusion. As with Model 17A, no convection occurs and the model reaches an equilibrium state.

Model 18B: Fixed, Steady (5 Wm^{-2}), K_{turb} = $2 \cdot 10^{-5}$, with Double-Diffusion
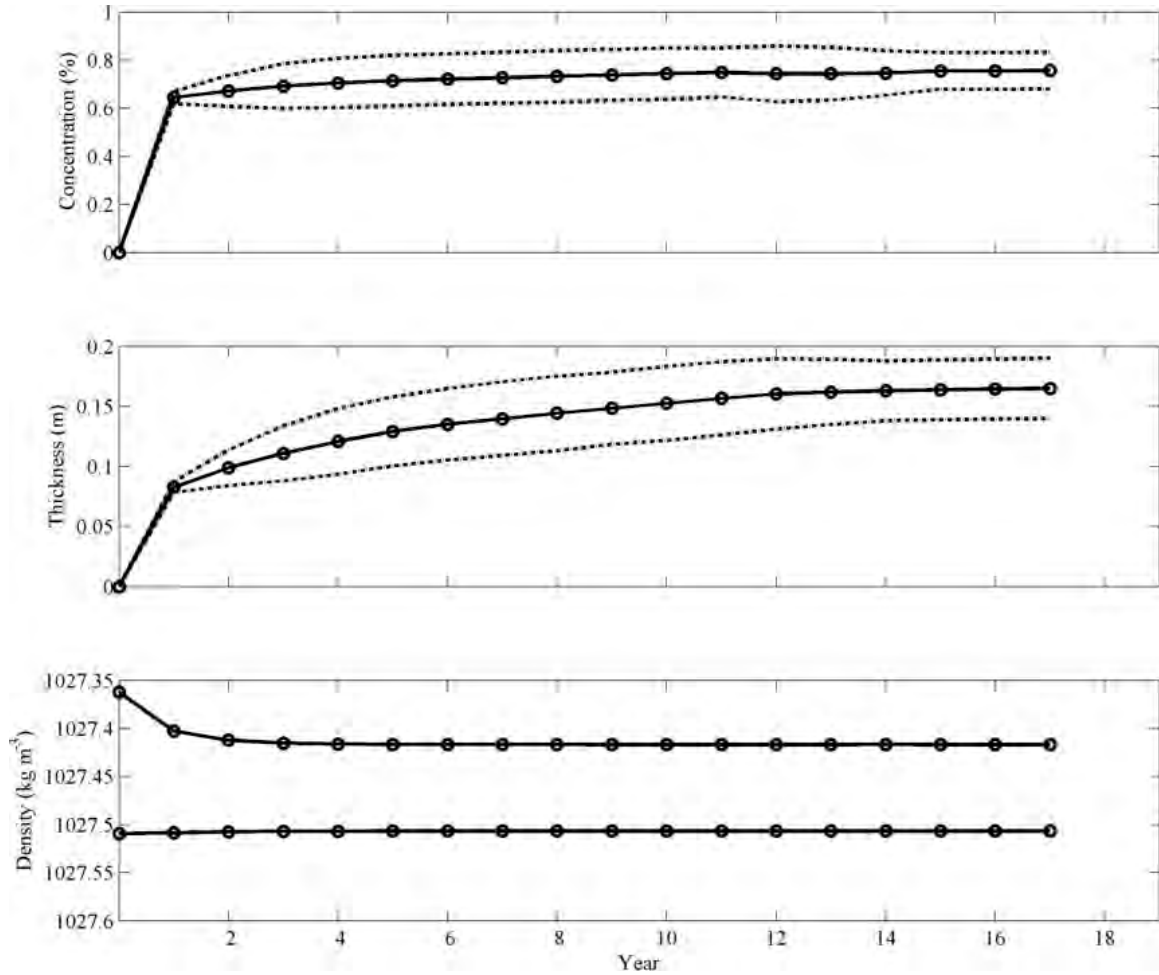
Figure 3.23.   Model 18B, Time Series. Mean sea ice concentration, thickness, and potential density. Plots for Model 18C are similar (*not shown*). The fixed, steady surface flux forcing models did not produce convection over the seamount, but were important to illustrate that an overall equilibrium could be reached.

Model 18A: Fixed, Steady (5 *Wm^{-2}*), *K$_{turb}$* = 0, with Double-Diffusion
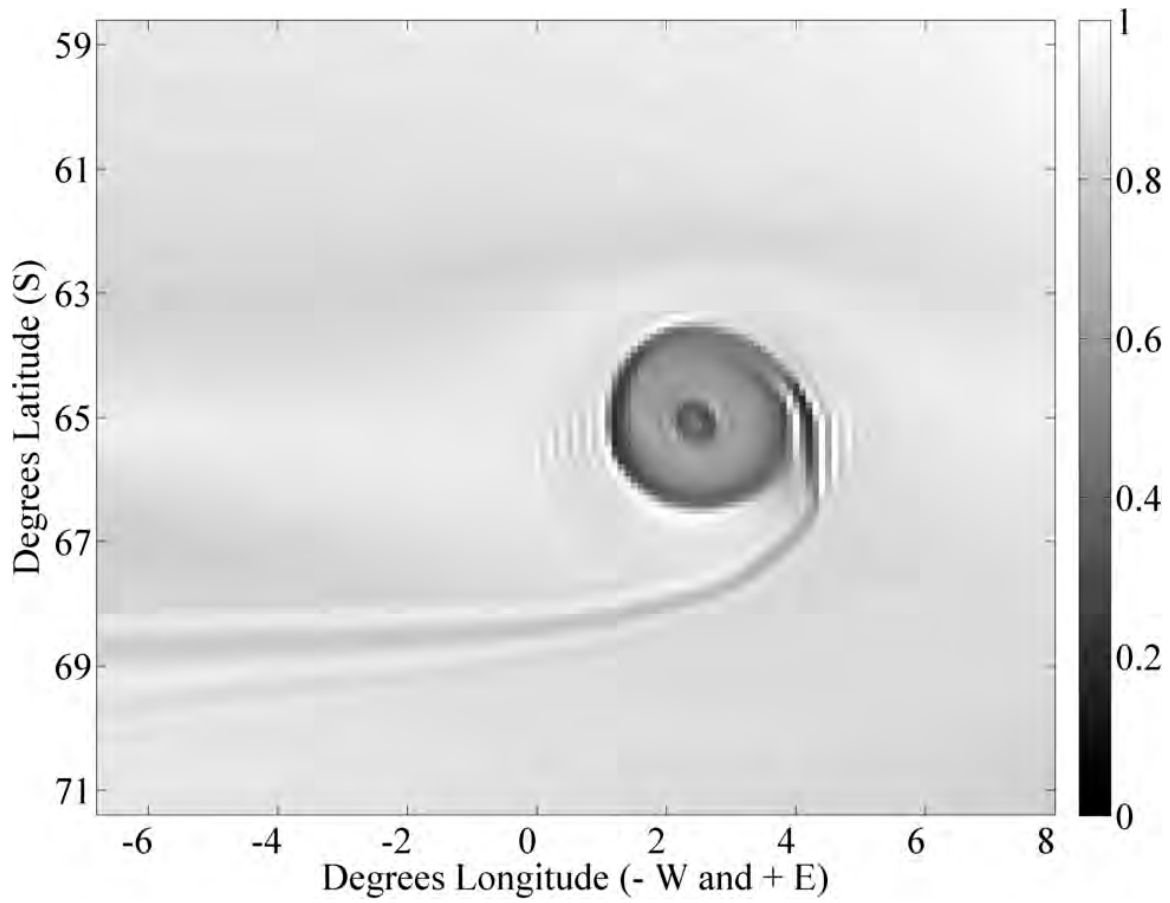
Figure 3.24.   Model 18A, Year 14, Sea ice concentration (%). Sea ice concentration is reduced over the area above the seamount representing Maud Rise.

Model 18A: Fixed, Steady (5 Wm^{-2}), K_{turb} = 0, with Double-Diffusion
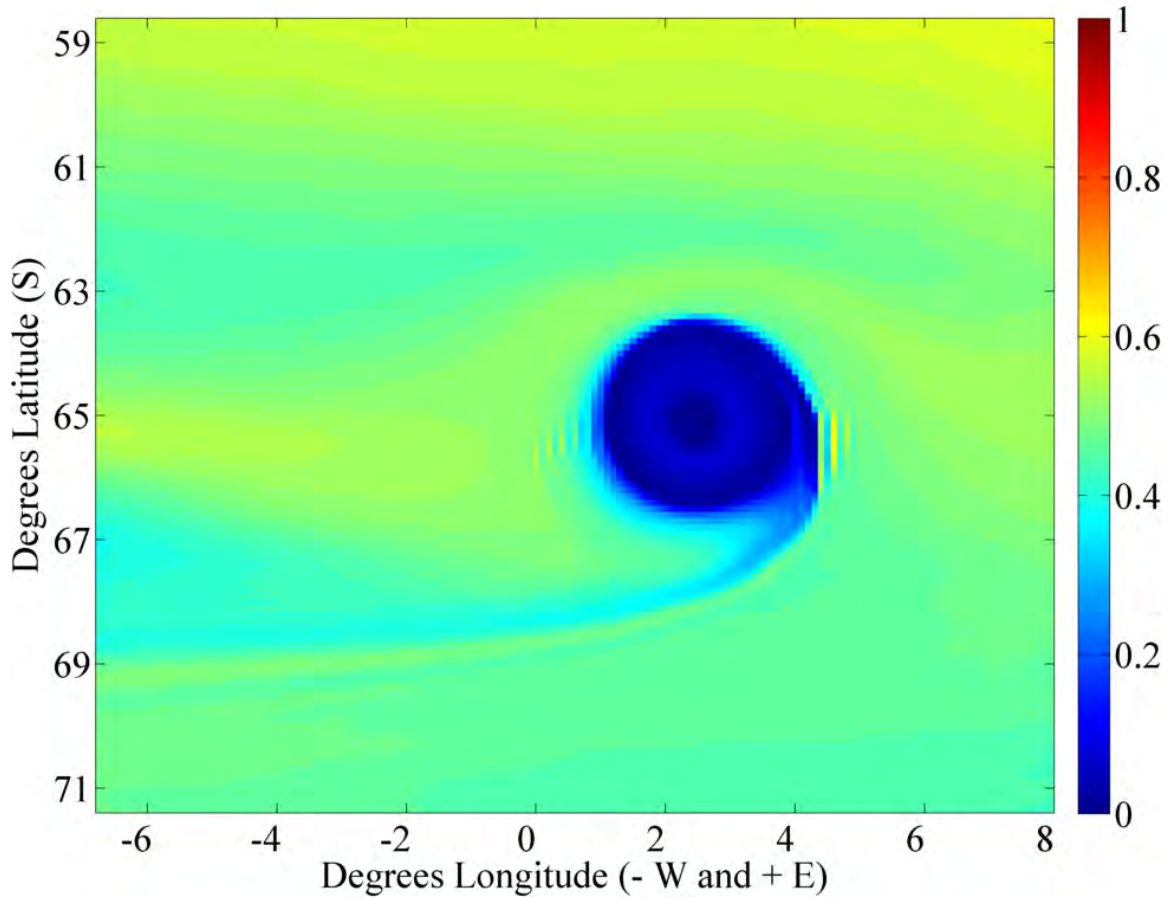
Figure 3.25.   Model 18A, Year 14, Sea ice thickness (*m*). Sea ice is much thinner directly over the seamount with a mean less than 0.1 *m*. Outward, in the Ambient region, sea ice thickness is consistently greater than 0.4 *m*.
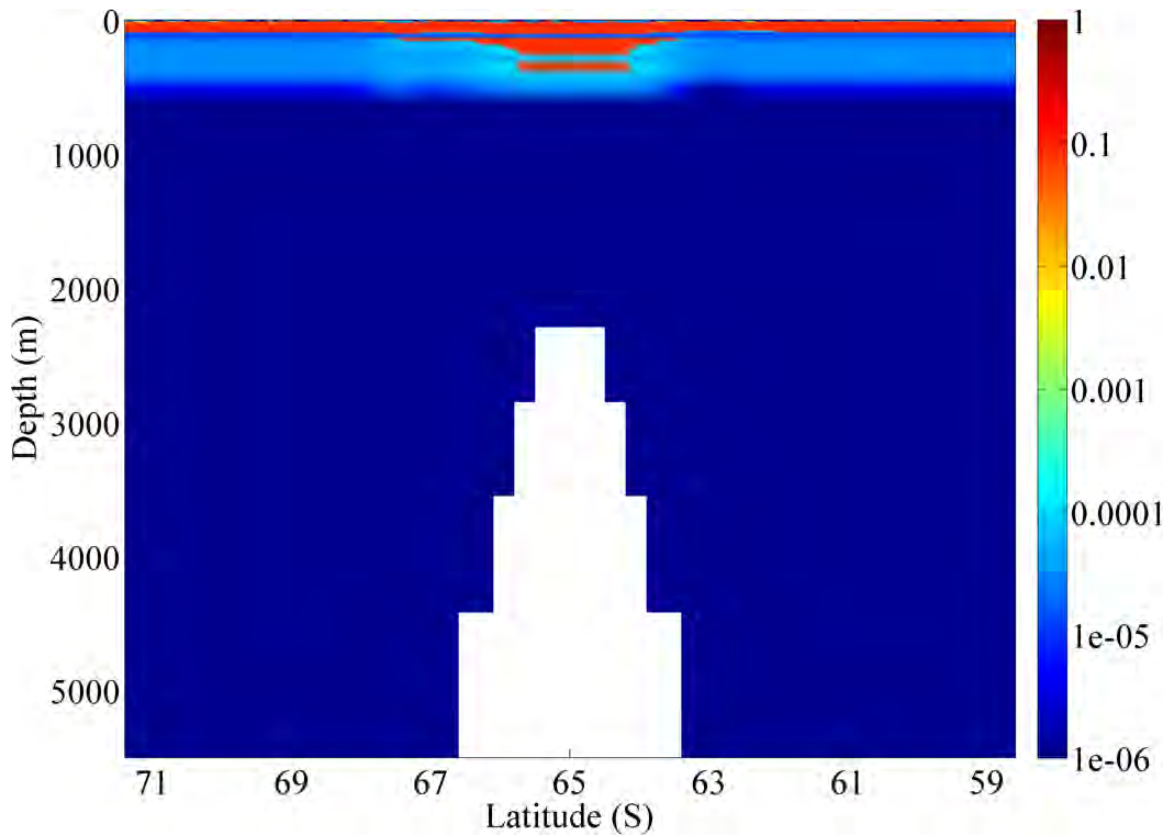
Figure 3.26.   Model 18A, Year 14, Temperature Diffusivity $(m^2 s^{-1})$. Enhanced diffusivity above the seamount is an indicator of the beginning breakdown of the thermal barrier. The cross-section of salt diffusivity (*not shown*) is similar.
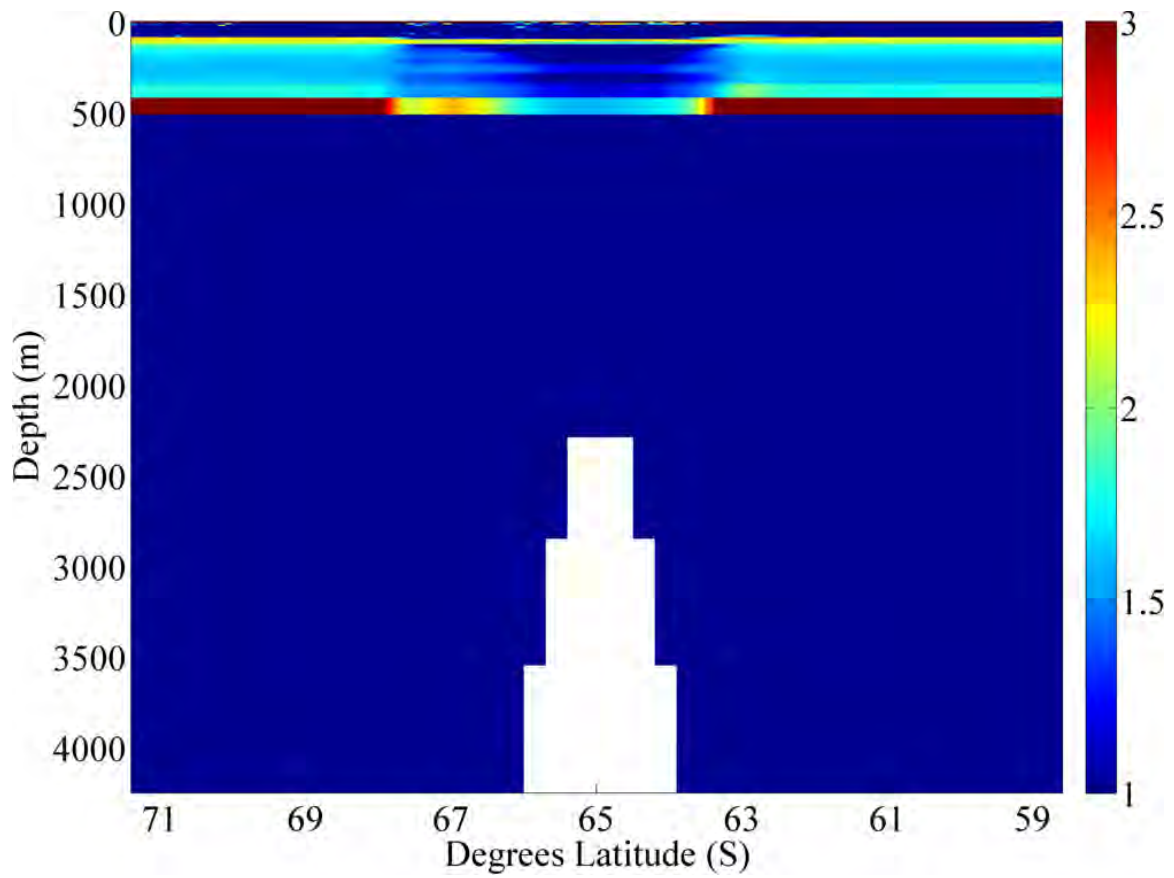
Figure 3.27.   Model 18A, Year 14, Density ratio (R_ρ). Density ratios indicate the marginal nature of stability above the seamount.
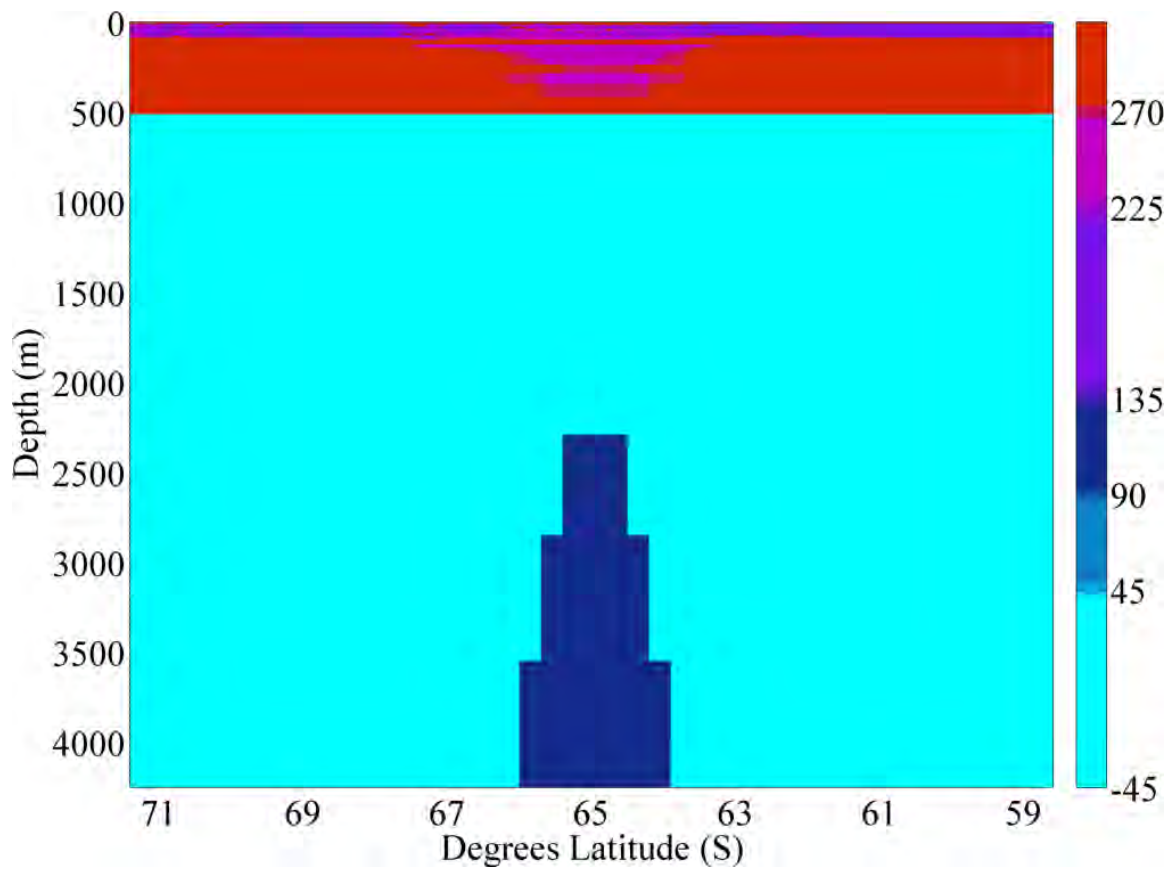
Figure 3.28.   Model 18A, Year 14, Turner angle (Tu). Almost convective, the water column above the seamount approaches $Tu = 270°$.

Model 24A: Free, Steady (1 Wm^{-2}), K_{turb} = 0, with Double-Diffusion
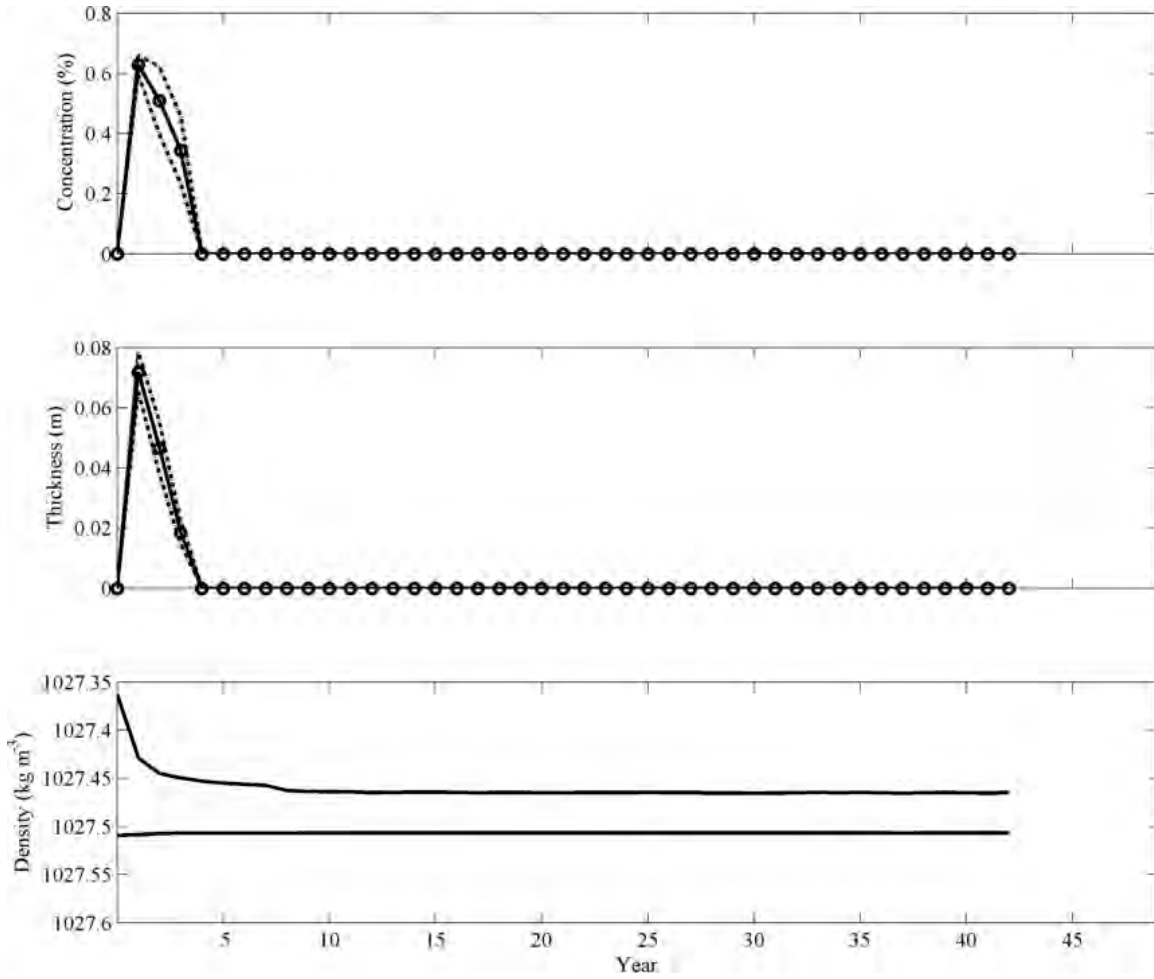
Figure 3.29. Model 24A, Time Series. Even though ice free starting at Year 4, no convection occurs over the seamount for the entirety of this extended model run. The potential density difference, $\Delta\rho_{conv}$ from (3.5), equals ~ 0.04 $kg\ m^{-3}$ at all times after $t = 10\ years$.

Model 24B: Free, Steady (1 Wm^{-2}), K_{turb} = 2•10⁻⁵, with Double-Diffusion
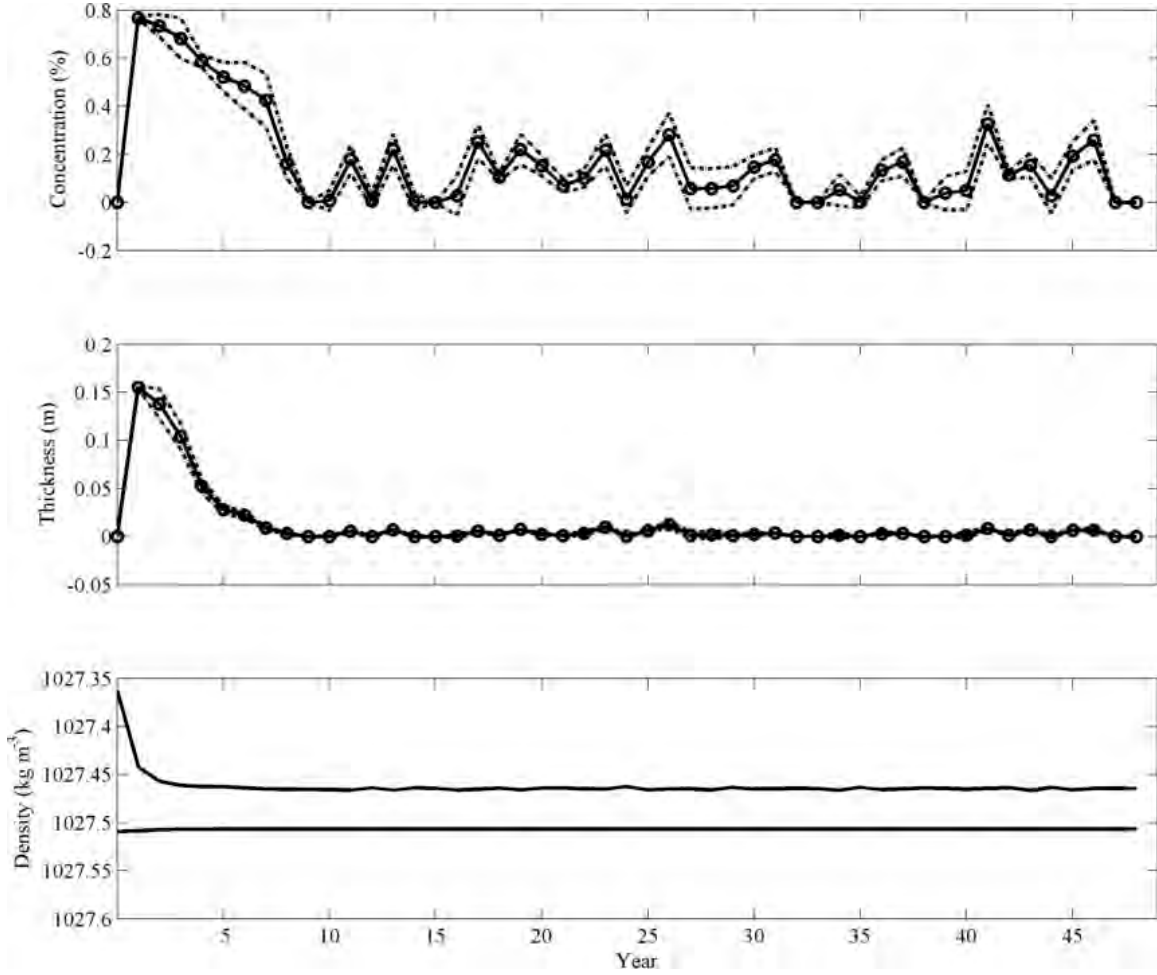
Figure 3.30.   Model 24B, Time Series. After Year 8, ice thicknesses are mere millimeters, the choice of lead closing parameter (Hibler 1979, Smedsrud and Martin 2015) making all the difference in sea ice concentration as it fluctuates between 0% and 30%. There is no onset of convection for the first 48 years of the model run, and not likely to be even after, as $\langle \Delta \rho_{conv} \rangle = 0.04$ kg m^{-3} for the majority of the time.

Model 24C: Free, Steady (1 Wm^{-2}), K_{turb} = 2•10^{-5}, No Double-Diffusion
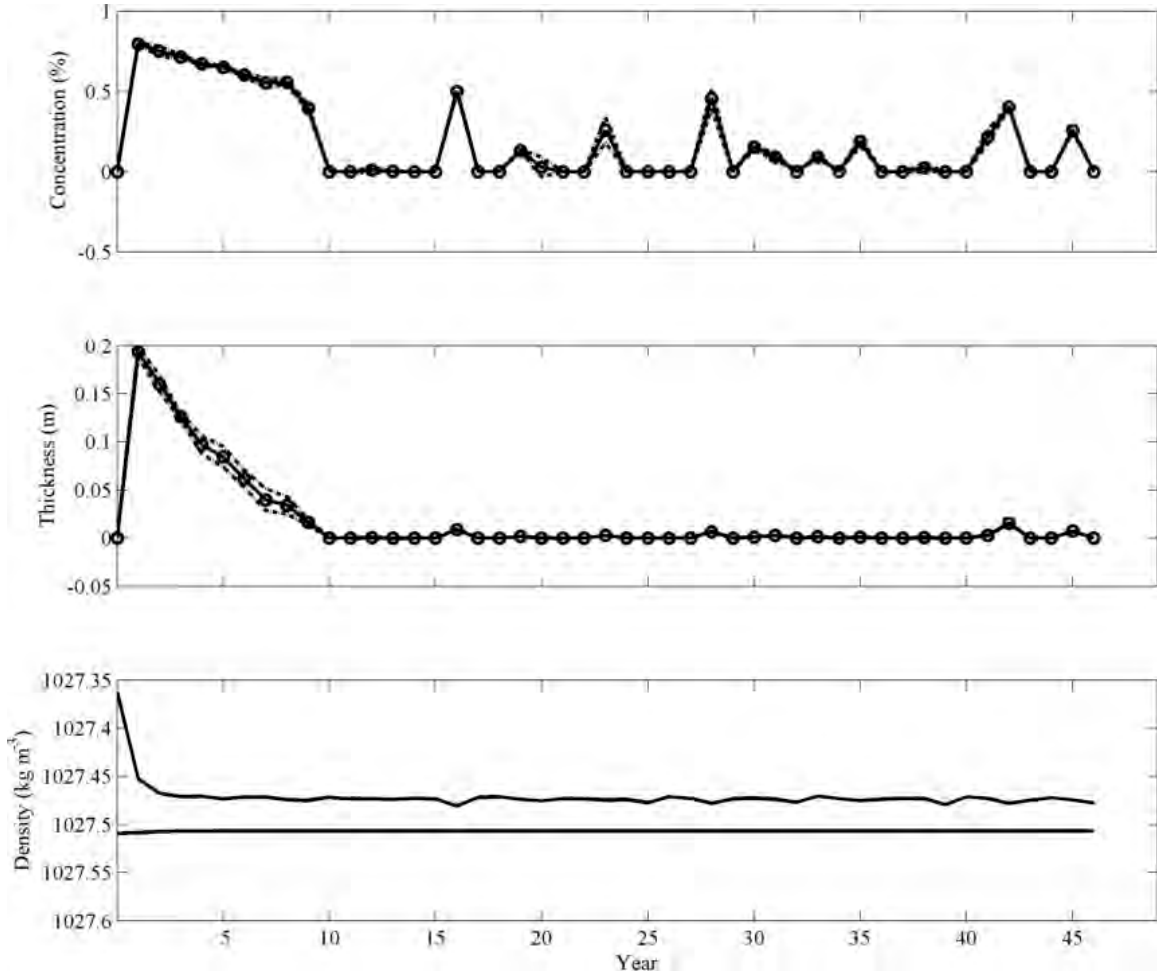
Figure 3.31.   Model 24C, Time Series. Sea ice thickness is effectively zero starting at Year 10. No convection for this run; $\Delta\rho_{conv}$ reaches ~ 0.025 $kg\ m^{-3}$ at its lowest points and $\langle\Delta\rho_{conv}\rangle = 0.035\ kg\ m^{-3}$. Models 24A, 24B, and 24C all mirror the observed potential density differences across the pycnocline in the Maud Rise Taylor cap (Shaw and Stanton 2014).

Model 24B: Free, Steady (1 *Wm*$^{-2}$), *K$_{turb}$* = 2•10^{-5}, with Double-Diffusion
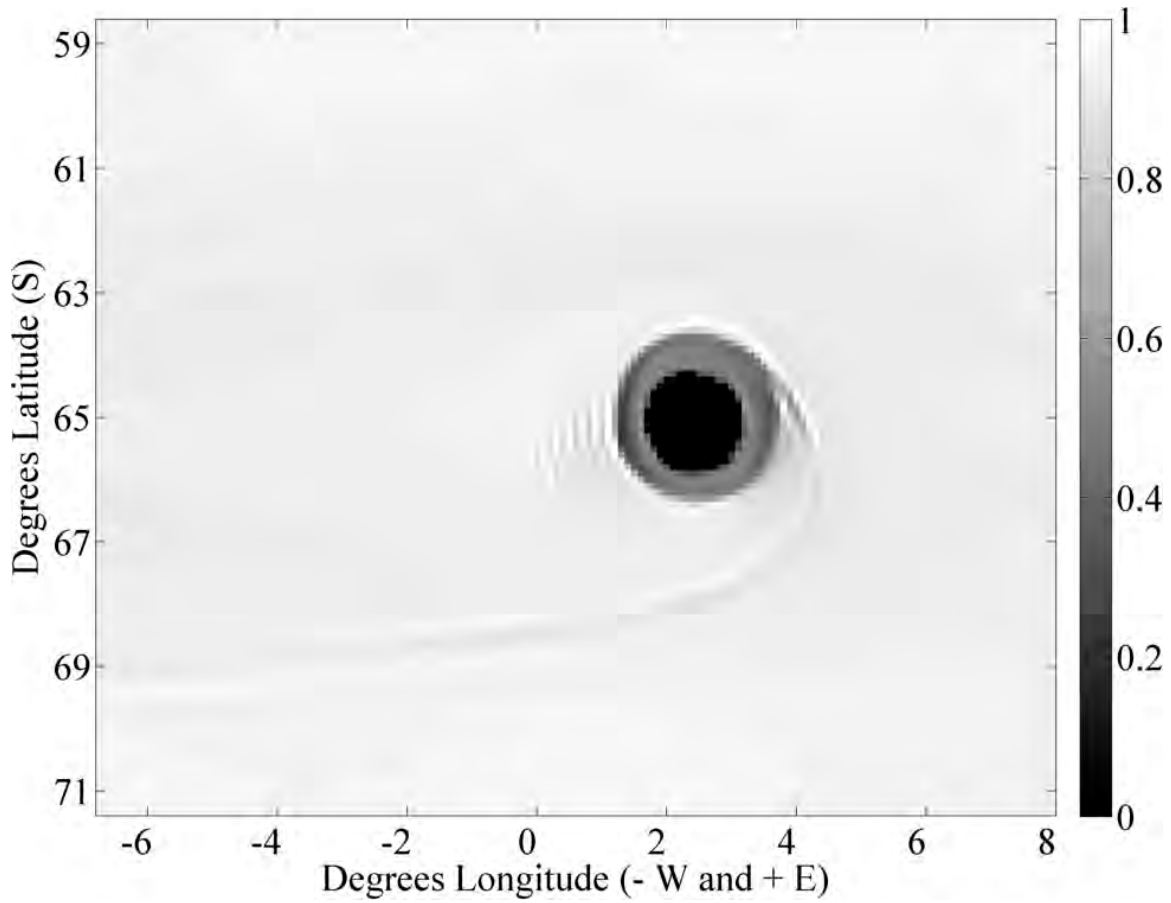
Figure 3.32. Model 24B, Year 14, Sea ice concentration (%). Three distinct regions of sea ice concentration are present in Model 24B at Year 14. Ambient conditions produce a 100% concentration. Over the seamount, a halo of 50% concentration encircles a polynya.

Model 24B: Free, Steady (1 *Wm⁻²*), *K_{turb}* = 2•10⁻⁵, with Double-Diffusion
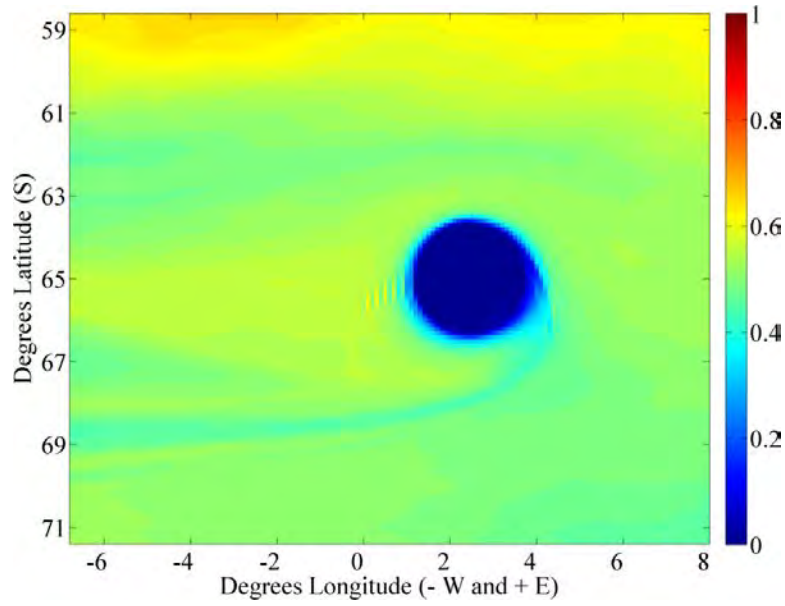
(a)
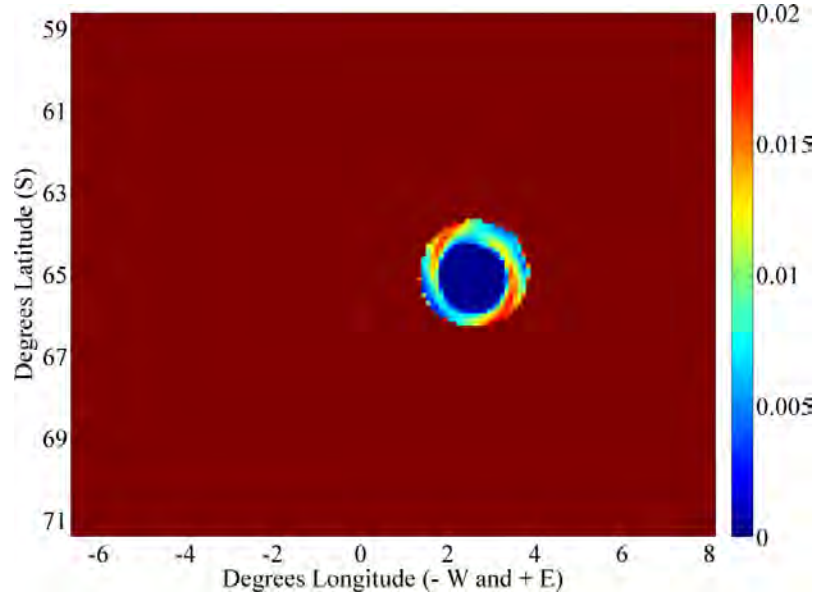
(b)

Figure 3.33.   Model 24B, Year 14, Sea ice thickness (*m*). Ambient sea ice thickness (*a*) is 0.4*m* to 0.6*m*. Over the seamount (*b*), sea ice thickness is 0.005*m* to 0.02*m*, where sea ice concentration is 50% in Figure 3.32. The center has no ice, and thickness is zero.

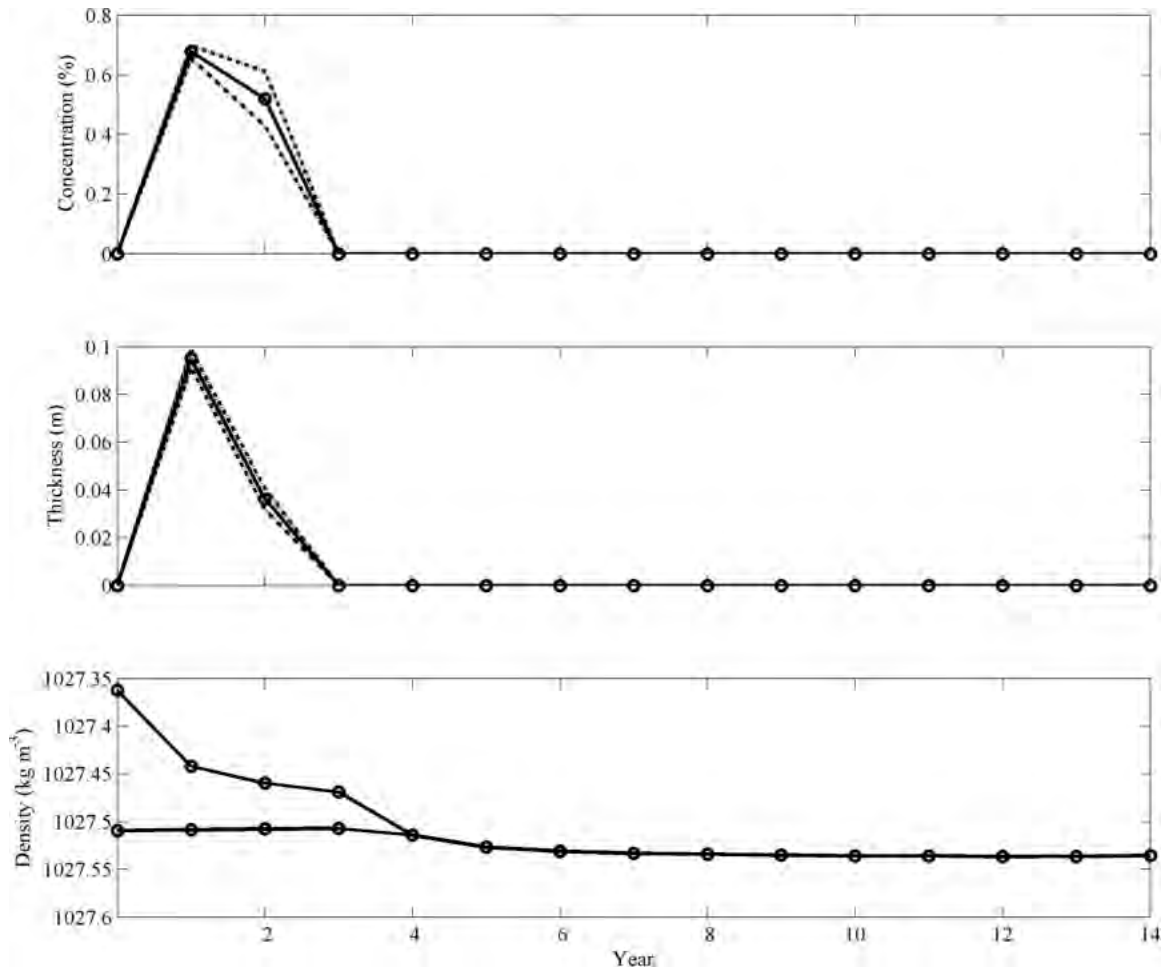**Model 25A: Free, Steady (5 Wm^{-2}), K_{turb} = 0, with Double-Diffusion**

Figure 3.34. Model 25A, Time Series. The surface over the seamount summit is completely ice-free by Year 3. Whereas Model 24A (Figure 3.29) never goes convective after ice-free conditions commence, the mean potential density series for 25A converge by Year 4, indicating convection over the seamount. Surface cooling for 24A was 1 Wm^{-2} while 25A was forced with 5 Wm^{-2}.

Model 25B: Free, Steady (5 Wm^{-2}), K_{turb} = 2•10^{-5}, with Double-Diffusion
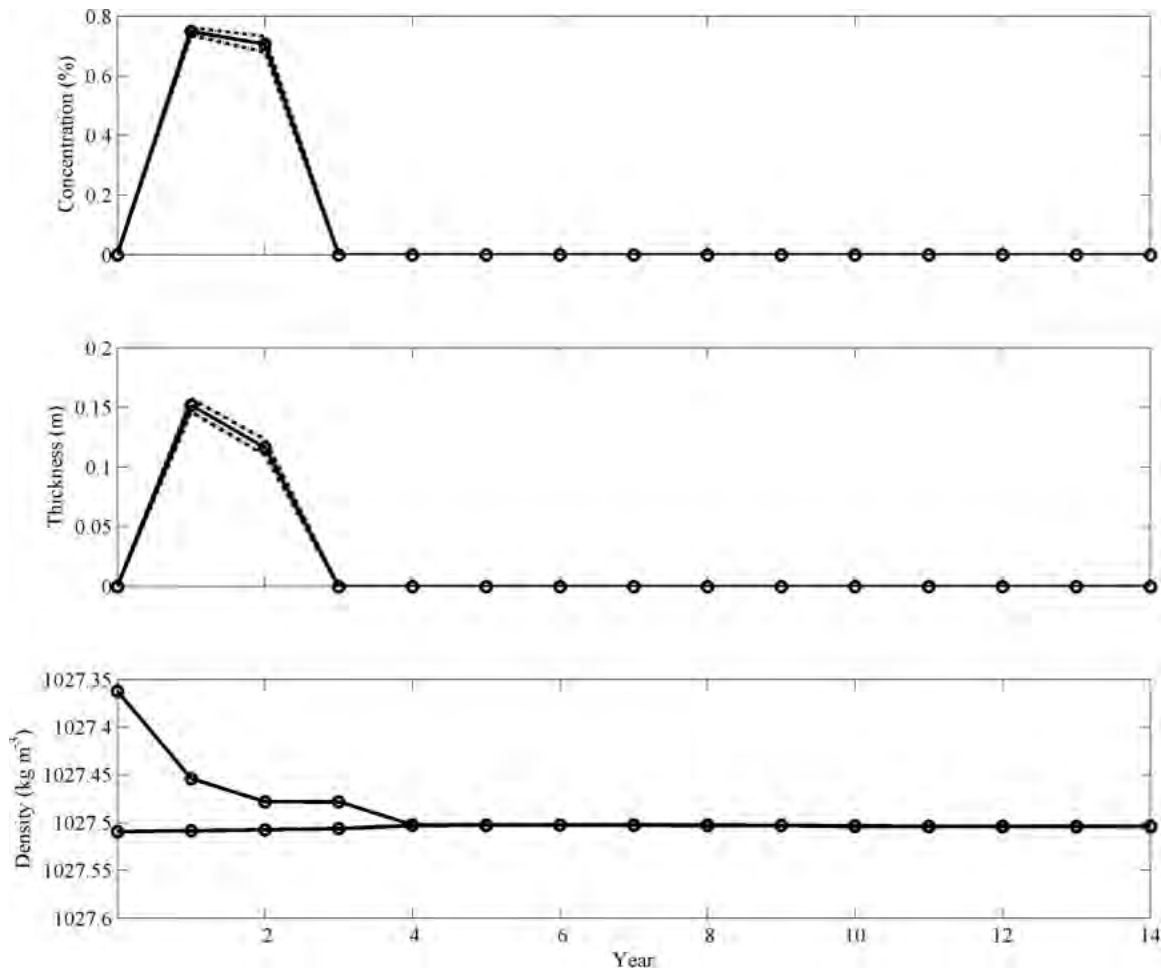
Figure 3.35.   Model 25B, Time Series. Similar to Model 25A (Figure 3.34), Model 25B went ice-free at Year 3 and convective at Year 4, one year later. This model has a non-zero turbulent diffusivity and double-diffusive mixing parameterization.

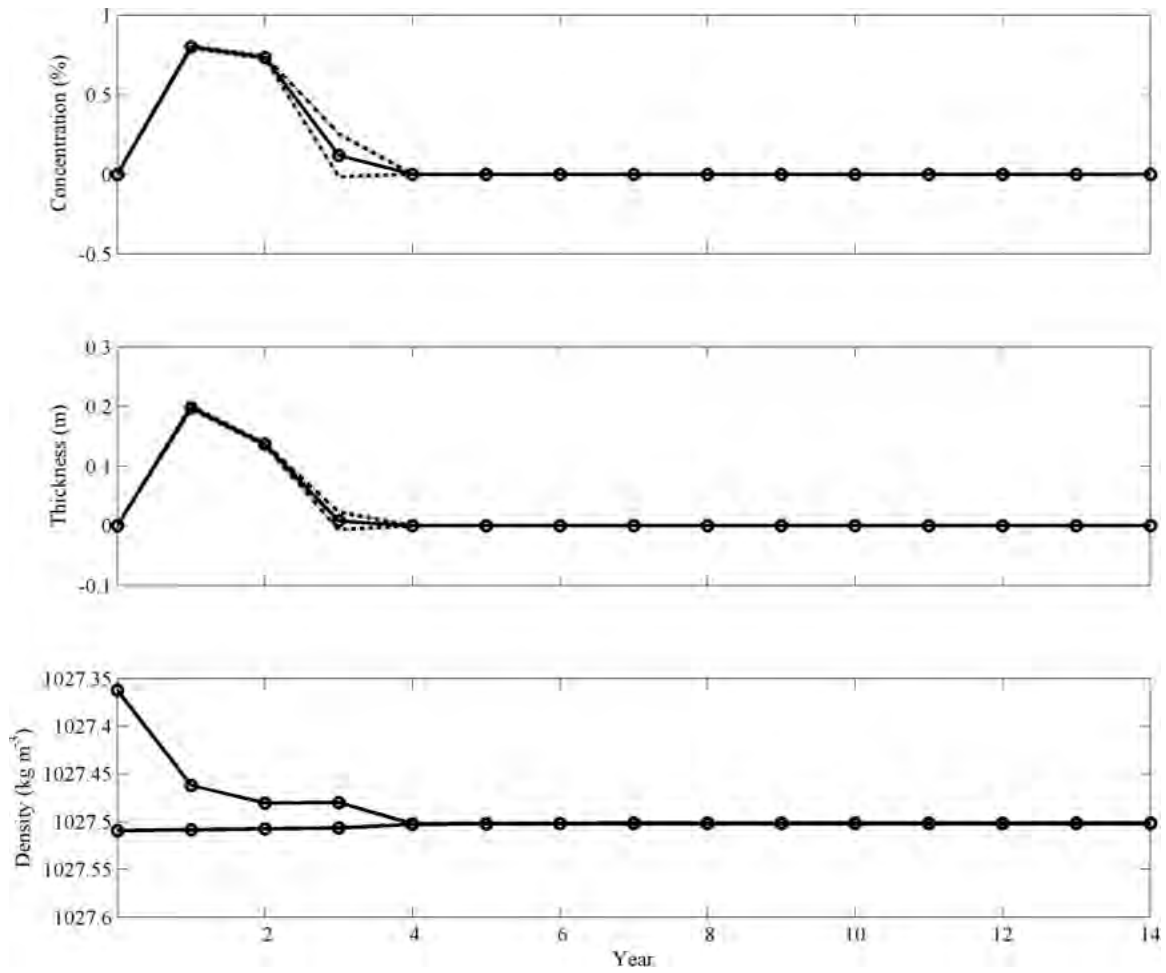**Model 25C: Free, Steady (5 Wm^{-2}), $K_{turb} = 2 \cdot 10^{-5}$, No Double-Diffusion**

Figure 3.36.   Model 25C, Time Series. Unlike either Model 25A or 25B, Model 25C goes ice-free and convective at the same time, Year 4. Model 25C does not have double-diffusion.
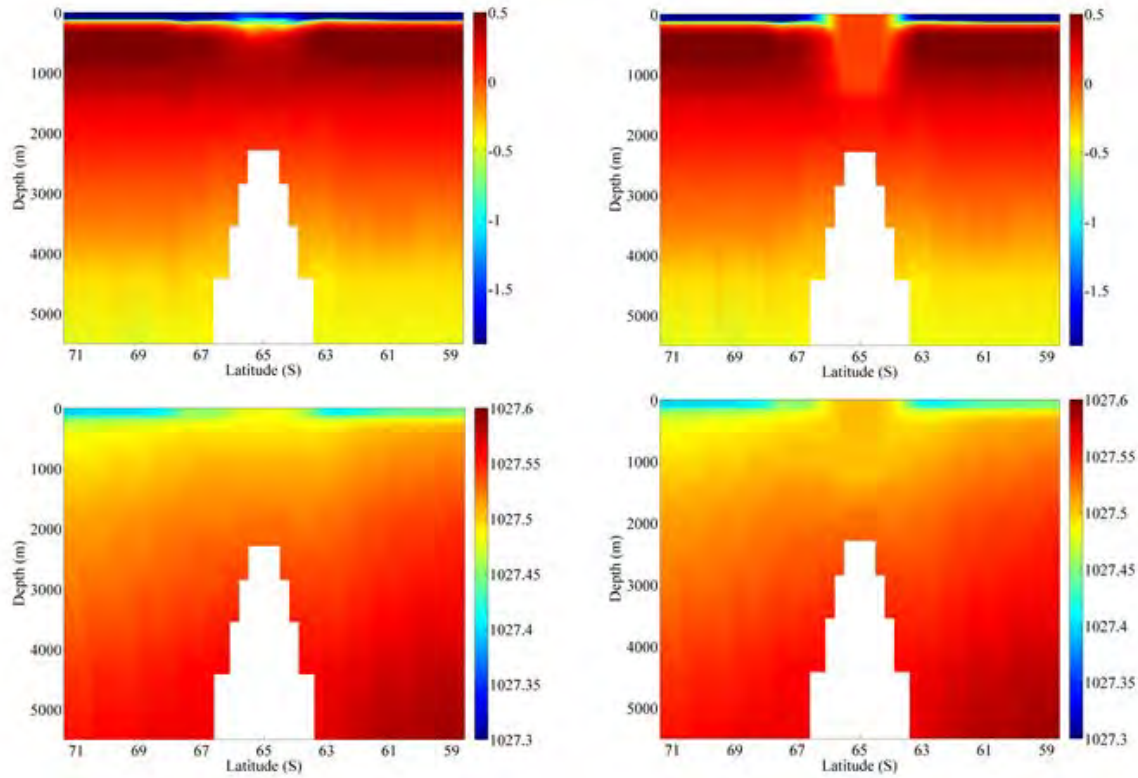
Figure 3.37. Model 25C, Onset of Convection. Meridional cross-sections of temperature (*upper*) and potential density (*lower*) shown for Model 25C, before convection at year 3 (*left*) and after the onset of convection at year 4 (*right*). The water column above the seamount experiences a significant loss of deep heat and the potential density difference across the pycnocline becomes negligible.
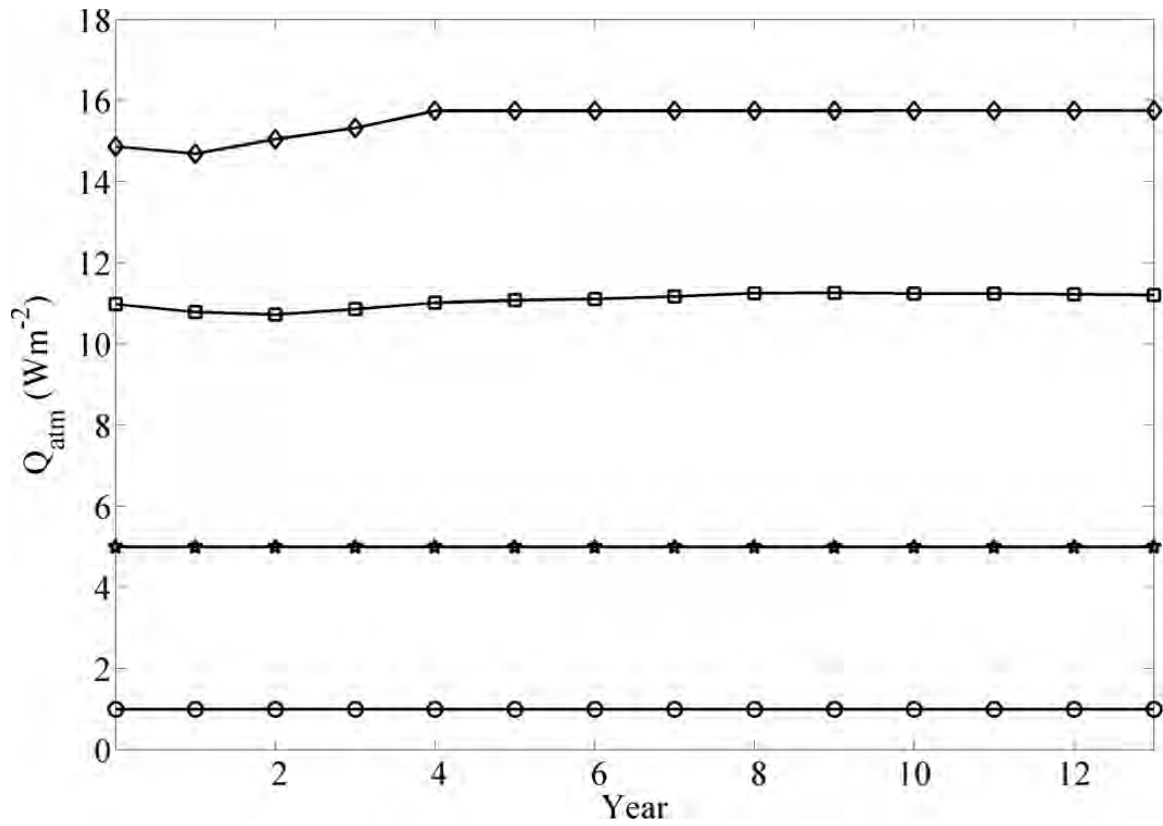
Figure 3.38.   Steady models: Mean surface heat flux to the atmosphere (Wm^{-2}). These means are the average of the 121 grid points centered above the seamount peak ($189 \pm 5, 112 \pm 5$) taken from Model 17B (*circle*), 18B (*star*), 24B (*square*), and 25B (*diamond*).

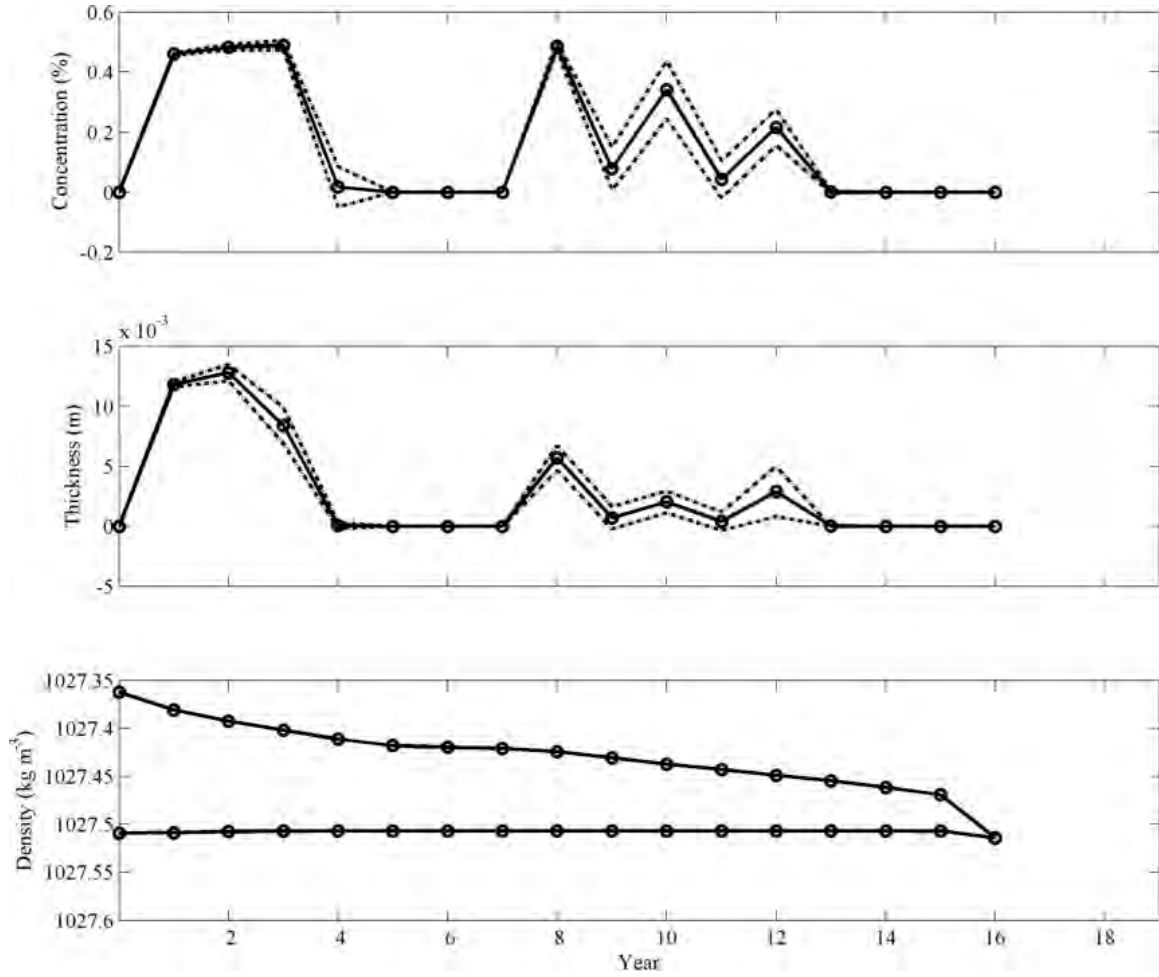**Model 14A: Fixed, Linear, Ice-Free Start, K_{turb} = 0, with Double-Diffusion**

Figure 3.39.   Model 14A, Time Series. By year 5, the area above the seamount is ice-free but $\Delta\rho_{conv}$ slowly decreases even as mean sea ice concentration and thickness oscillates. Convection occurs at year 16.

Model 14B: Fixed, Linear, Ice-Free Start, $K_{turb} = 2 \cdot 10^{-5}$, with Double-Diffusion
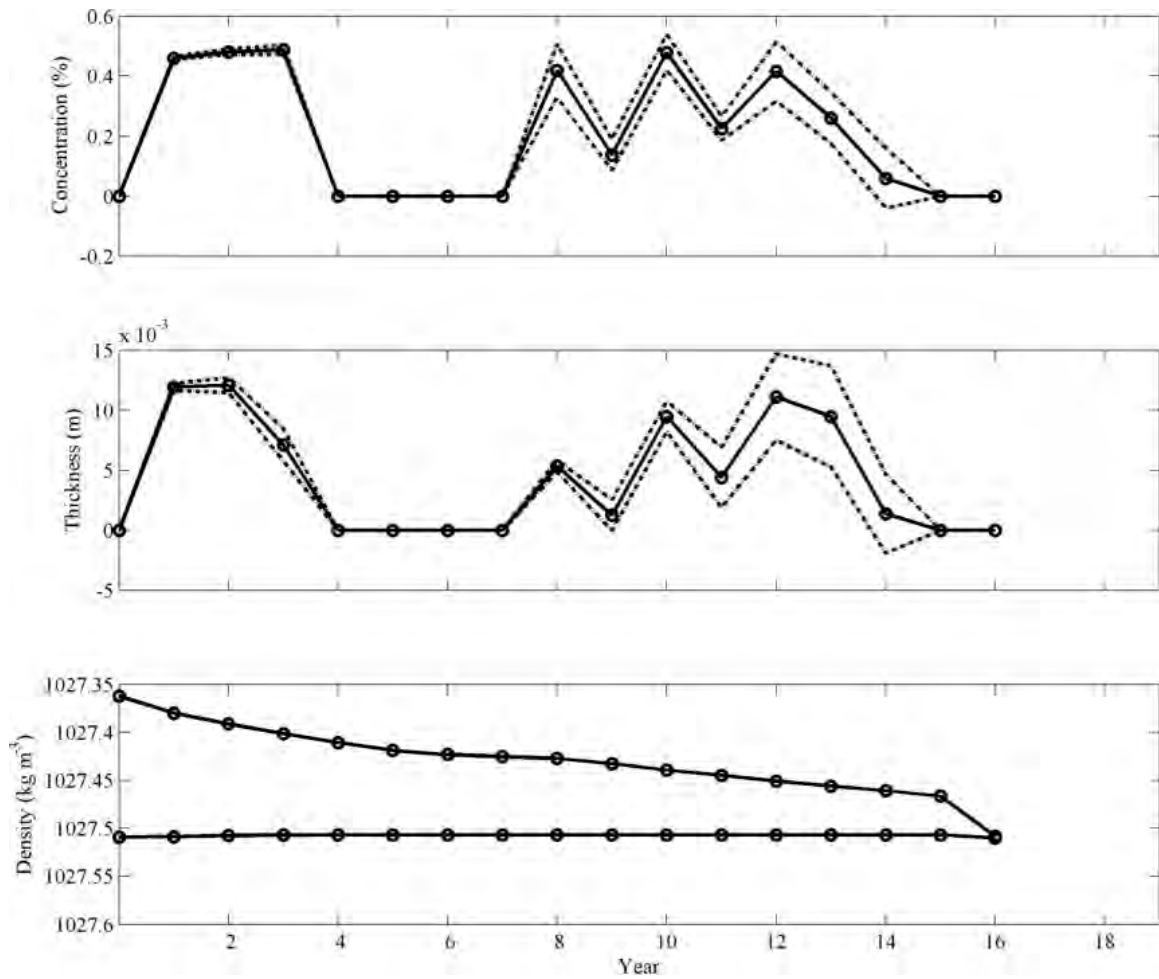

Figure 3.40.   Model 14B, Time Series. This run, identical to Model 14A, except with a non-zero turbulent diffusivity, displays similar behavior. A polynya opens by year 4, but it takes another 12 years for deep convection to initiate over the seamount.

Model 14C: Fixed, Linear, Ice-Free Start, $K_{turb} = 2 \cdot 10^{-5}$, No Double-Diffusion
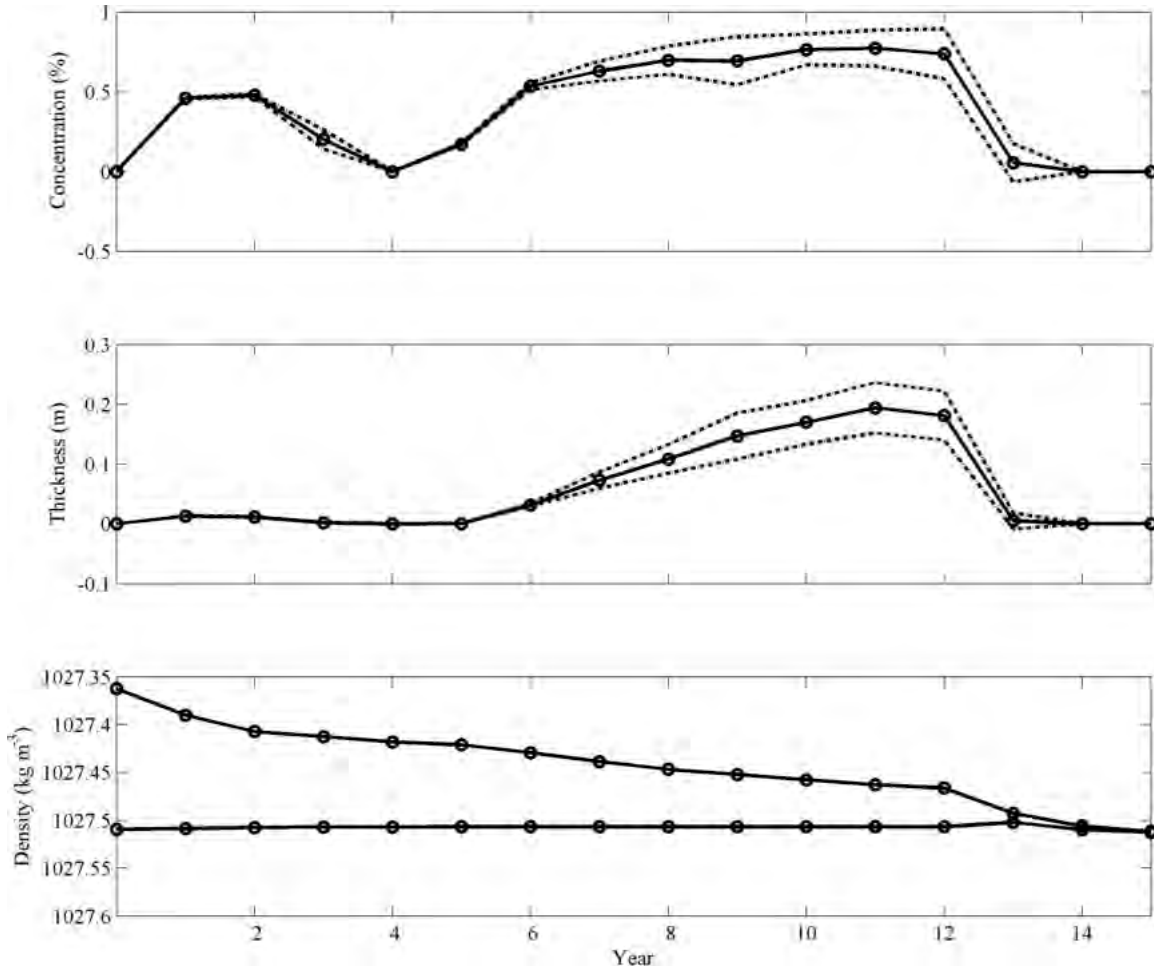

Figure 3.41.   Model 14C, Time Series. Without double-diffusion, Model 14C behaves in a significantly different fashion from its double-diffusive counterparts. Sea ice continues to thicken until year 12, when a drop-off of sea ice concentration, thickness, and $\Delta\rho_{conv}$ occurs simultaneously.

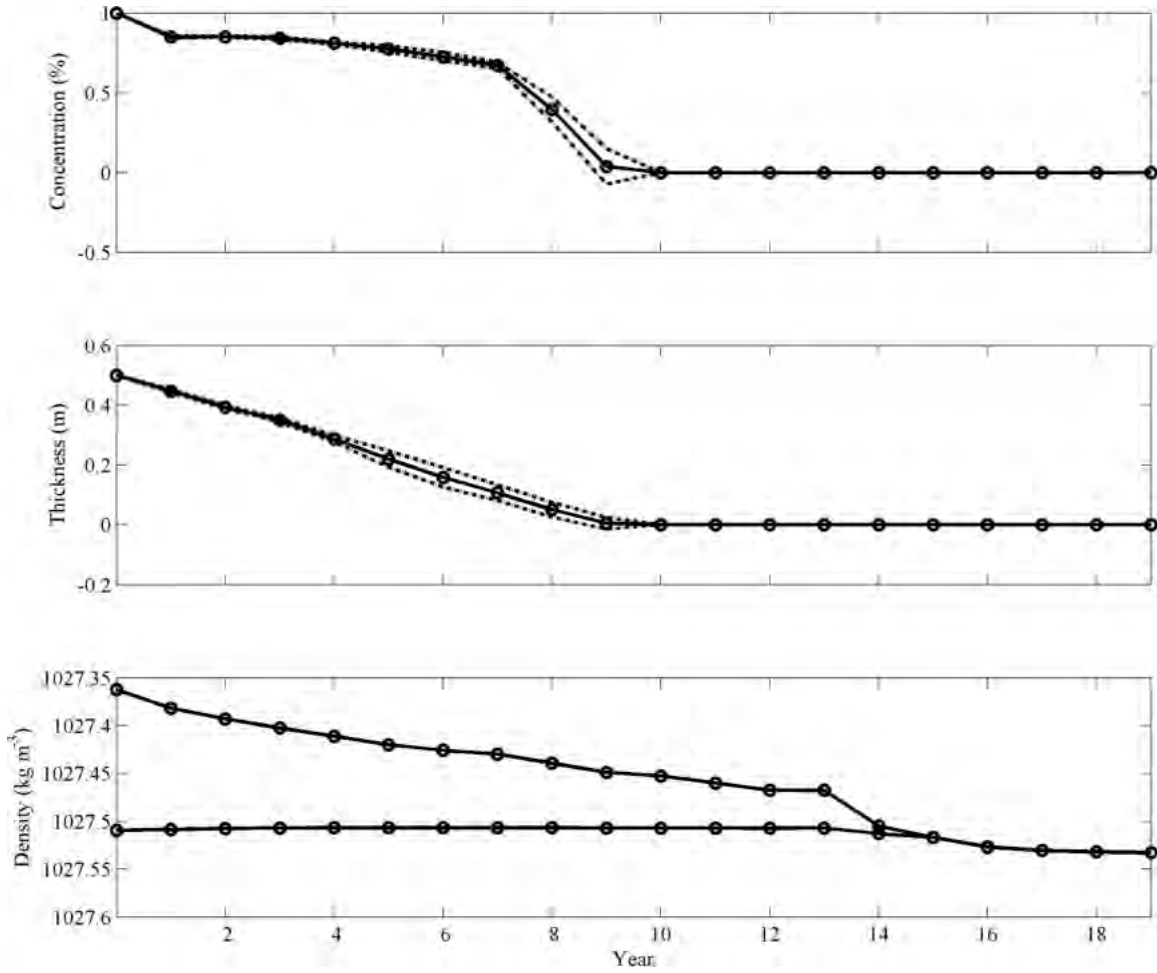**Model 20A: Fixed, Linear, Icy Start, $K_{turb} = 0$, with Double-Diffusion**

Figure 3.42. Model 20A, Time Series. The Model 20 series is identical to the Model 14 series, with one change—Model 20 starts with a sea ice-covered surface. Sea ice steadily diminishes and is gone by year 10. The $\Delta\rho_{conv}$ threshold of 0.005 $kg\ m^{-3}$ signifying convection is reached between years 14 and 15.

Model 20B: Fixed, Linear, Icy Start, $K_{turb} = 2 \cdot 10^{-5}$, with Double-Diffusion
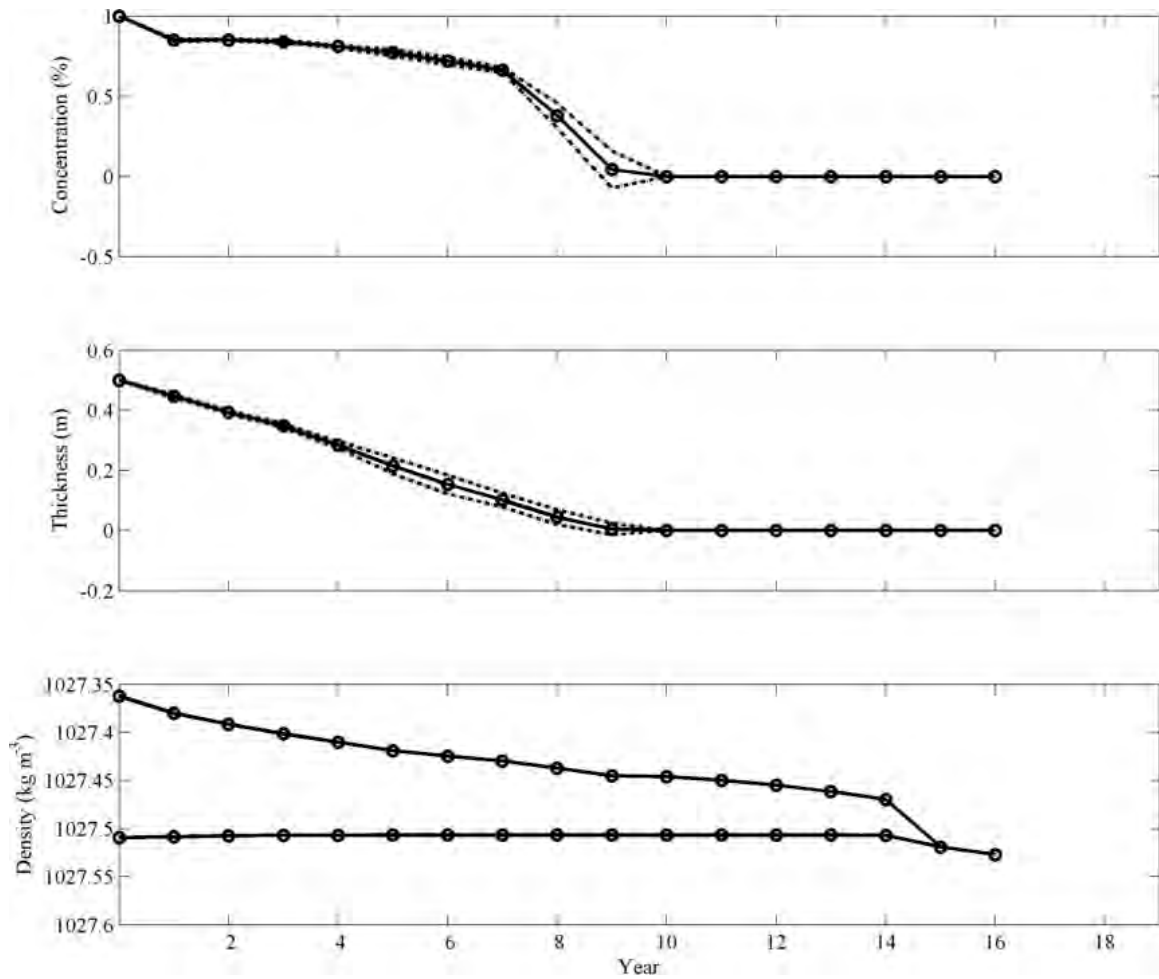

Figure 3.43. Model 20B, Time Series. Very similar to Model 20A, sea ice concentration and thickness reaches zero at year 10. Convection begins five years later.

Model 20C: Fixed, Linear, Ice-Free Start, K_{turb} = 2•10^{-5}, No Double-Diffusion
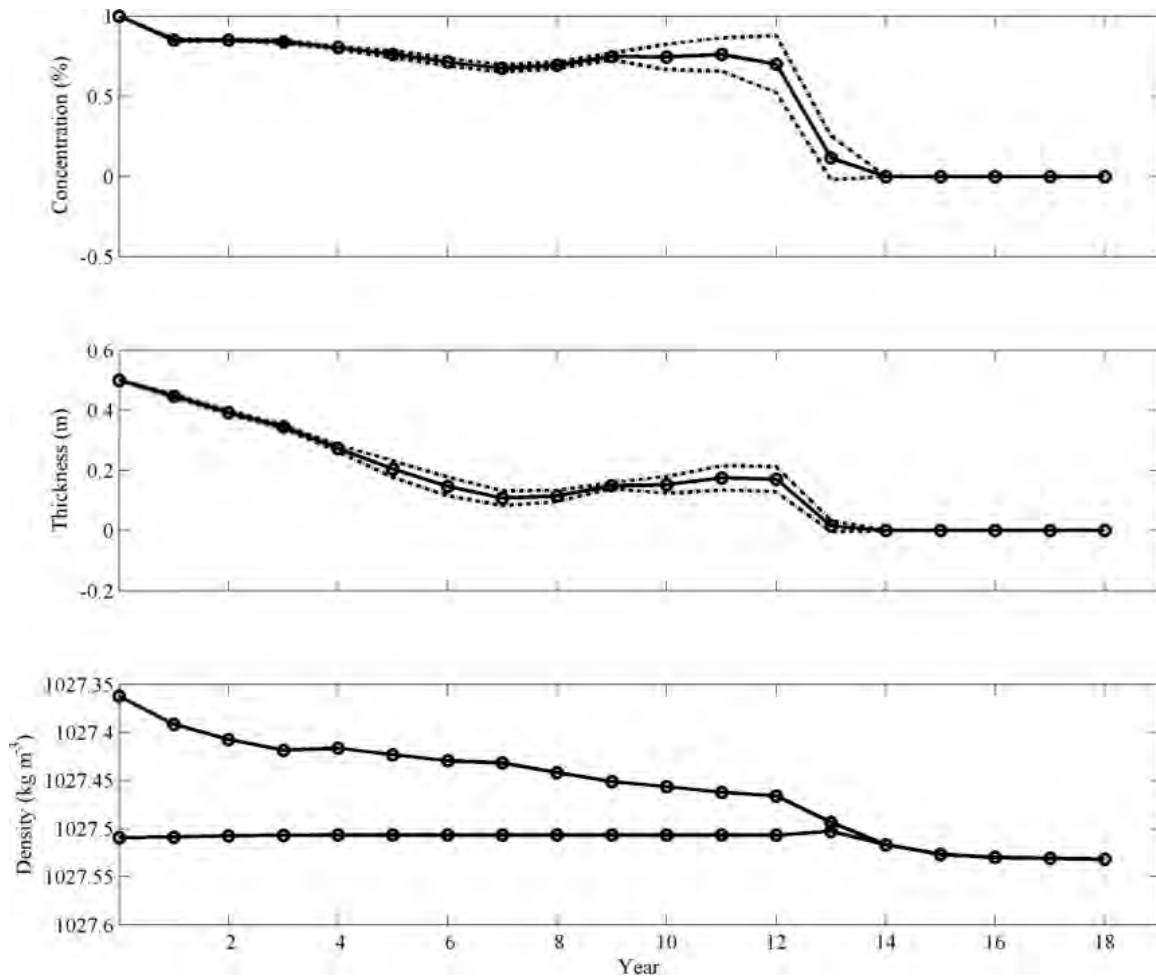

Figure 3.44.   Model 20C, Time Series. As expected, this model without double-diffusion does not go ice-free at year 10, but experiences slight thickening starting year 8 lasting until year 12. The onset of convection and elimination of sea ice occur during the same year (13-14).

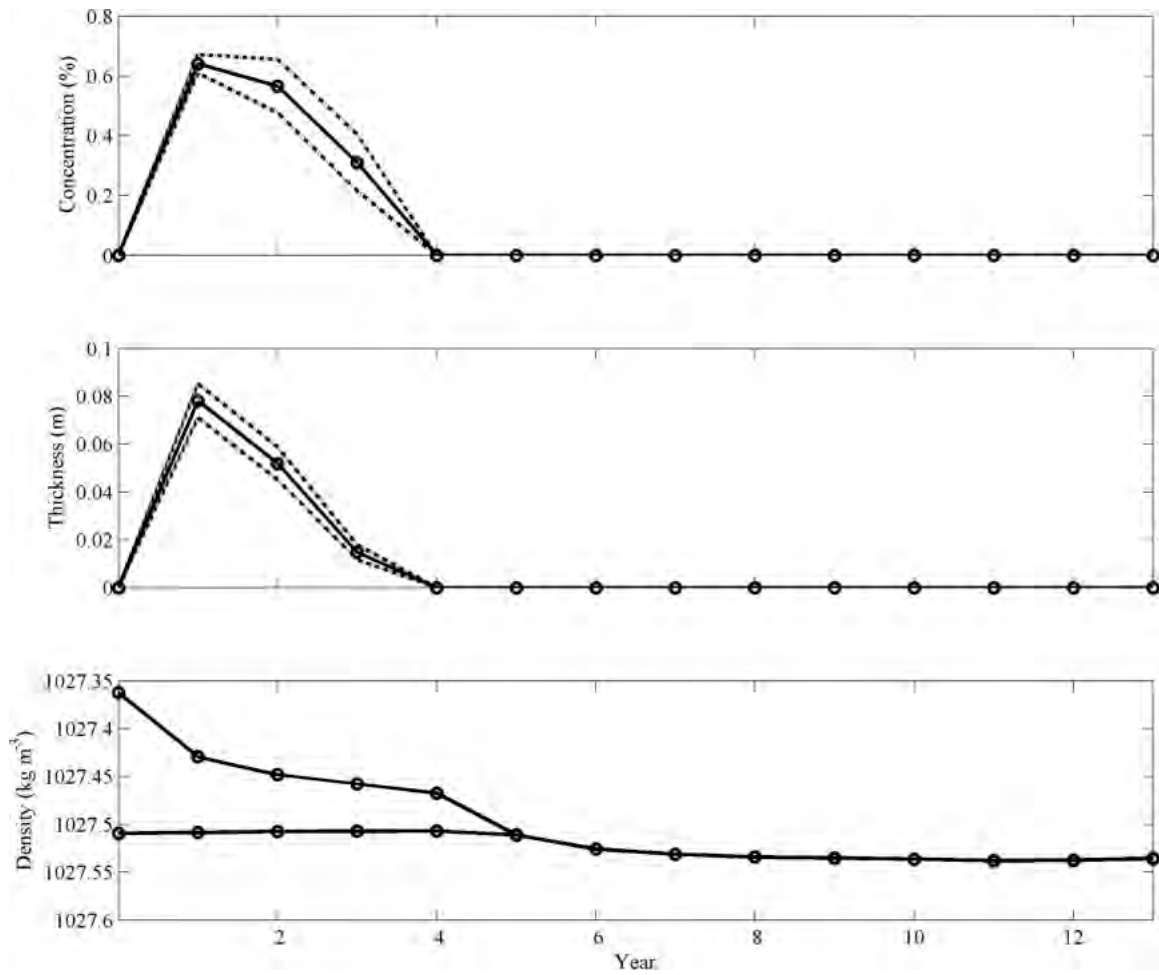**Model 26A: Free, Linear, Ice-Free Start, K_{turb} = 0, with Double-Diffusion**

Figure 3.45.   Model 26A, Time Series. Sensible, latent, and net longwave heat fluxes in "free" models consistently add up to and additional $10Wm^{-2}$ to Q_{pr} resulting in significantly higher values of surface cooling. This is evidenced by shorter convection onset times when compared to "fixed" models (cf. Figure 3.39).

Model 26B: Free, Linear, Ice-Free Start, K_{turb} = 2•10^{-5}, with Double-Diffusion
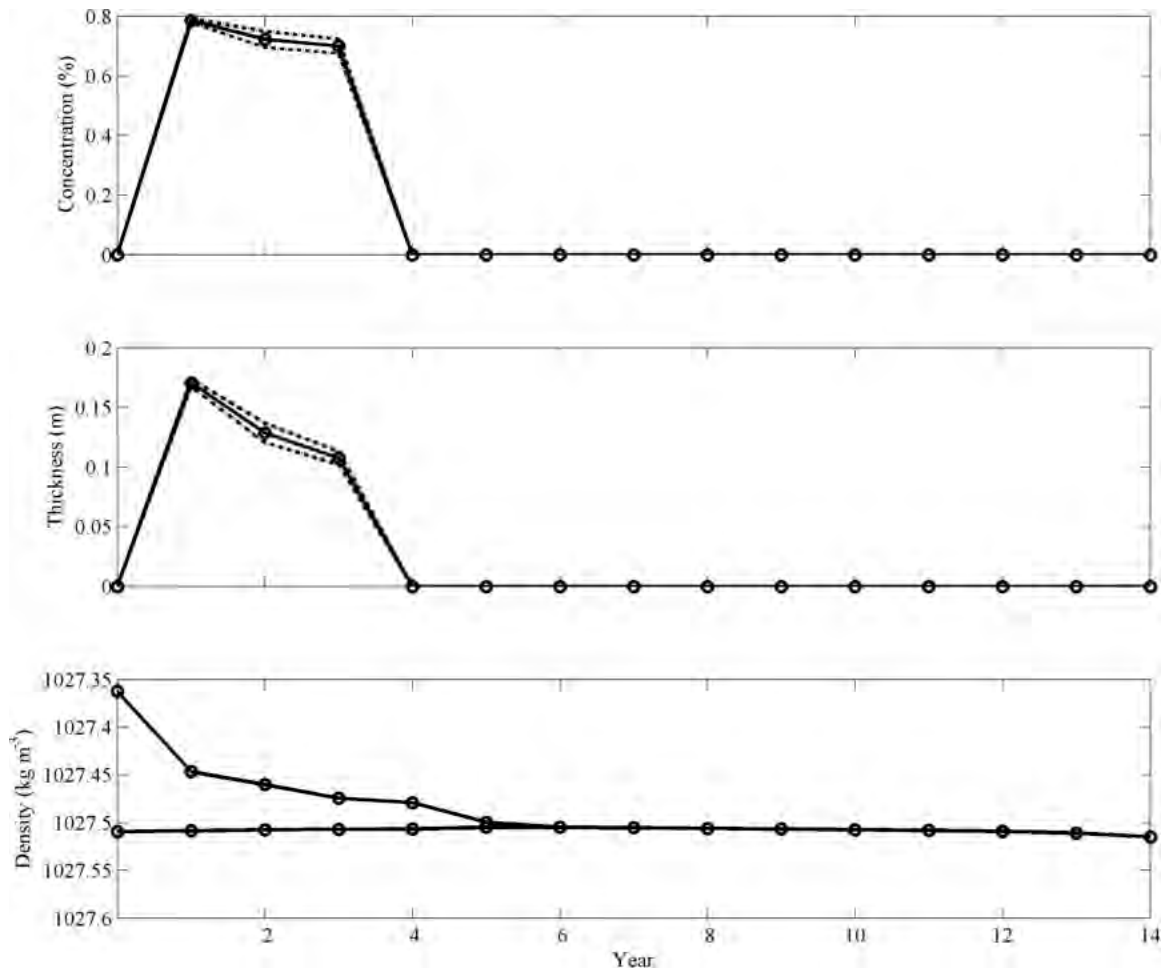

Figure 3.46.   Model 26B, Time Series. Like Model 26A (Figure 3.45), convection occurs at year 5 with the model going ice-free only one year earlier.

Model 26C: Free, Linear, Ice-Free Start, K_{turb} = 2•10^{-5}, No Double-Diffusion
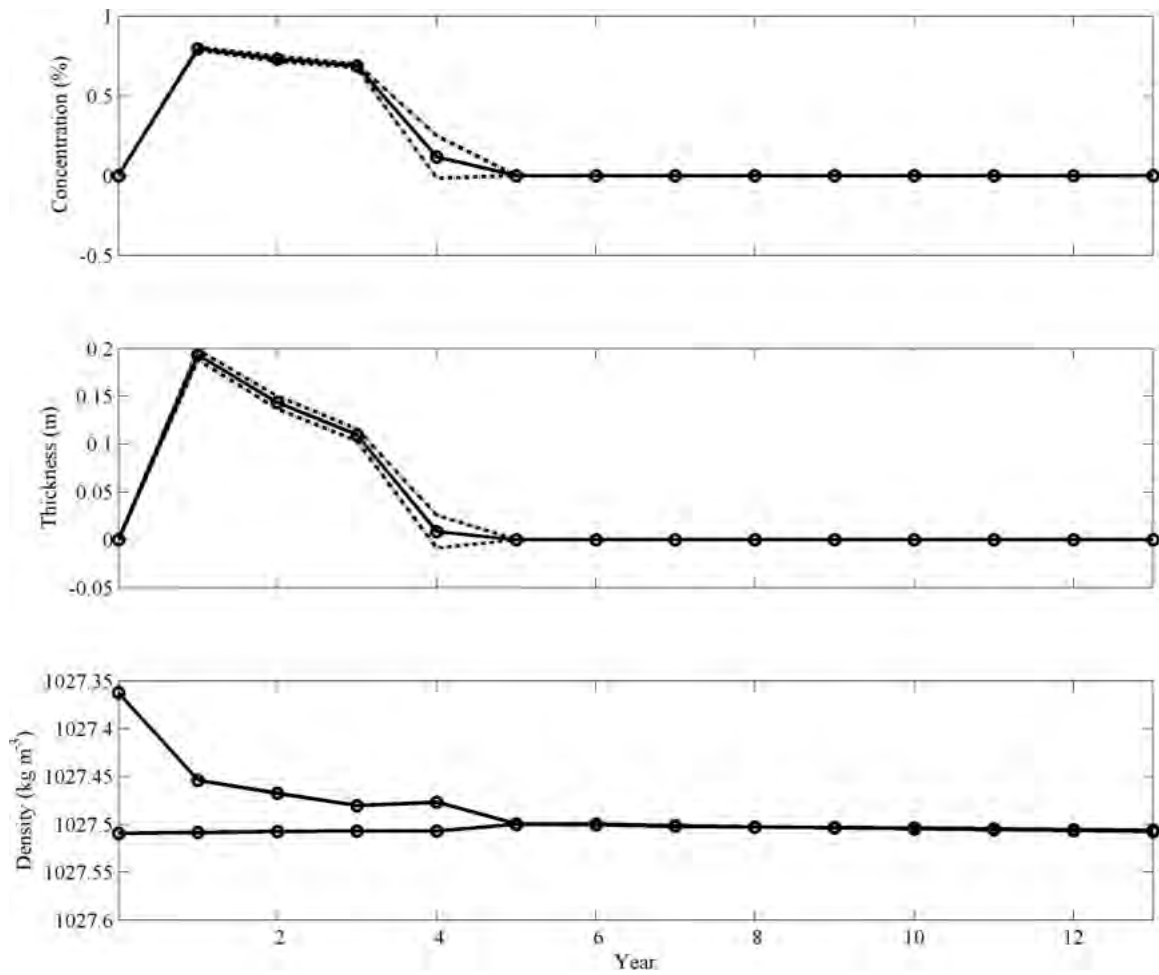

Figure 3.47.   Model 26C, Time Series. Like all models in the Model 26 series, the turbulent-only model experiences convection at year 5. However, there is no lag time, as sea ice has disappeared by this time as well.

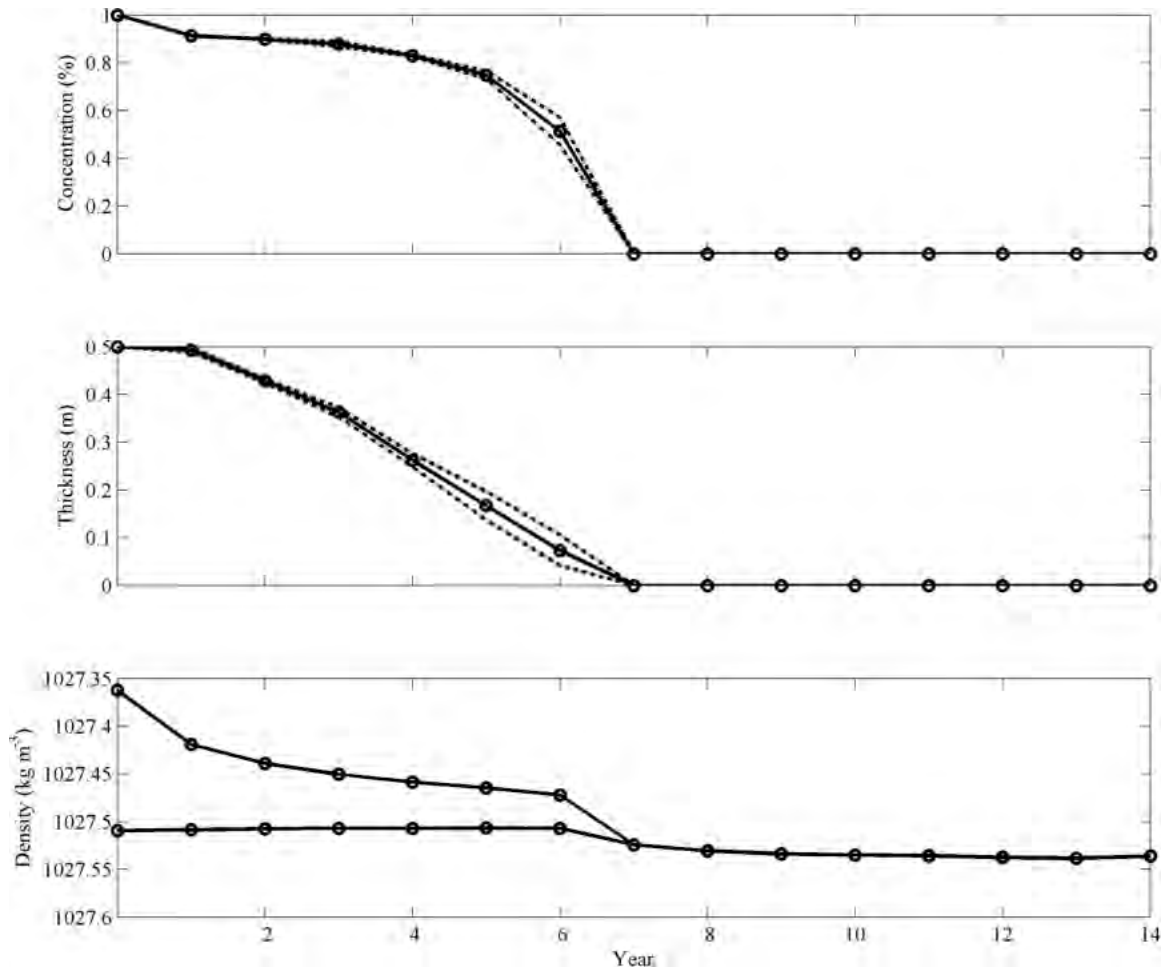**Model 27A: Free, Linear, Icy Start, $K_{turb} = 0$, with Double-Diffusion**

Figure 3.48.   Model 27A, Time Series. Sea ice concentration, thickness, and $\Delta\rho_{conv}$ all go to zero at year 7.

Model 27B: Free, Linear, Icy Start, $K_{turb} = 2 \cdot 10^{-5}$, with Double-Diffusion
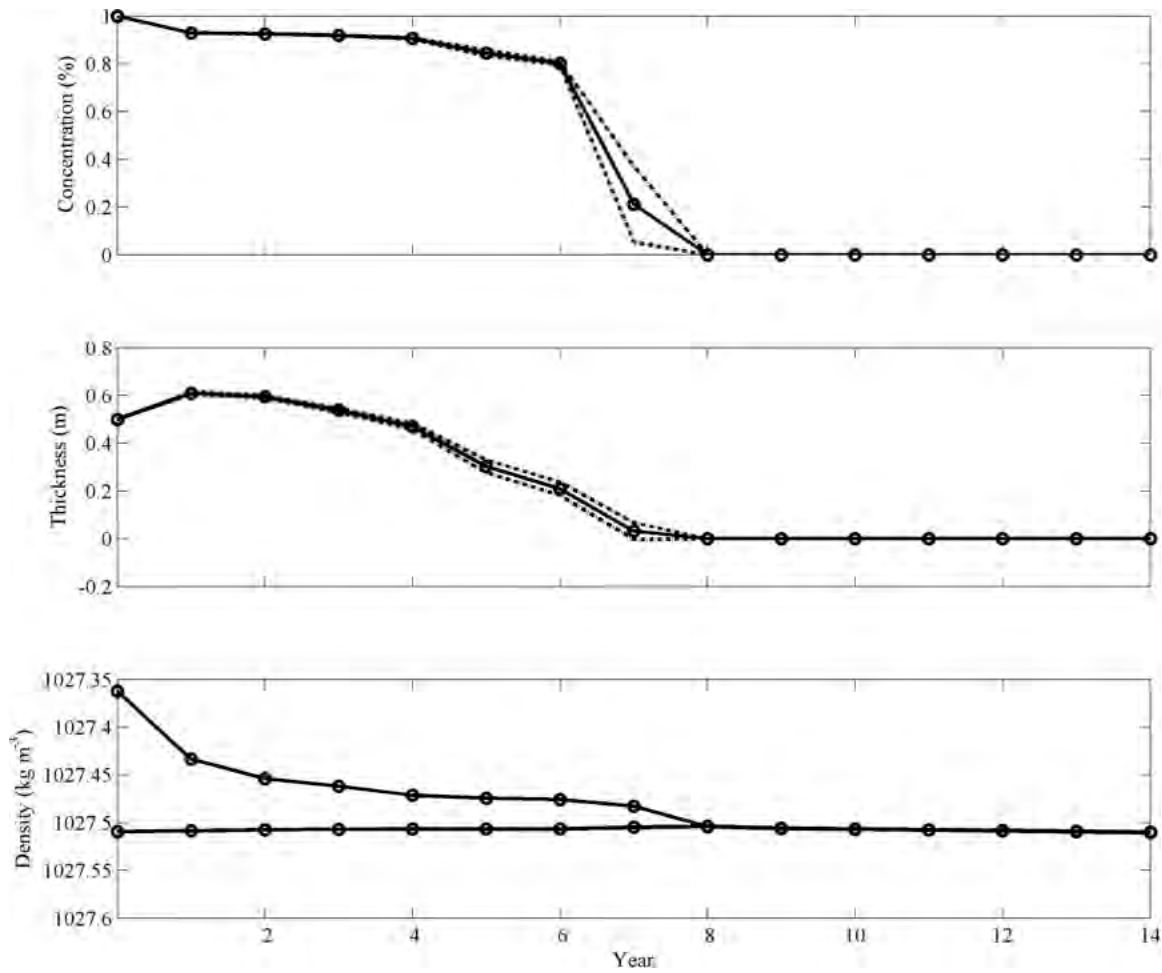

Figure 3.49. Model 27B, Time Series. Sea ice concentration, thickness, and $\Delta\rho_{conv}$ all go to zero at year 8.

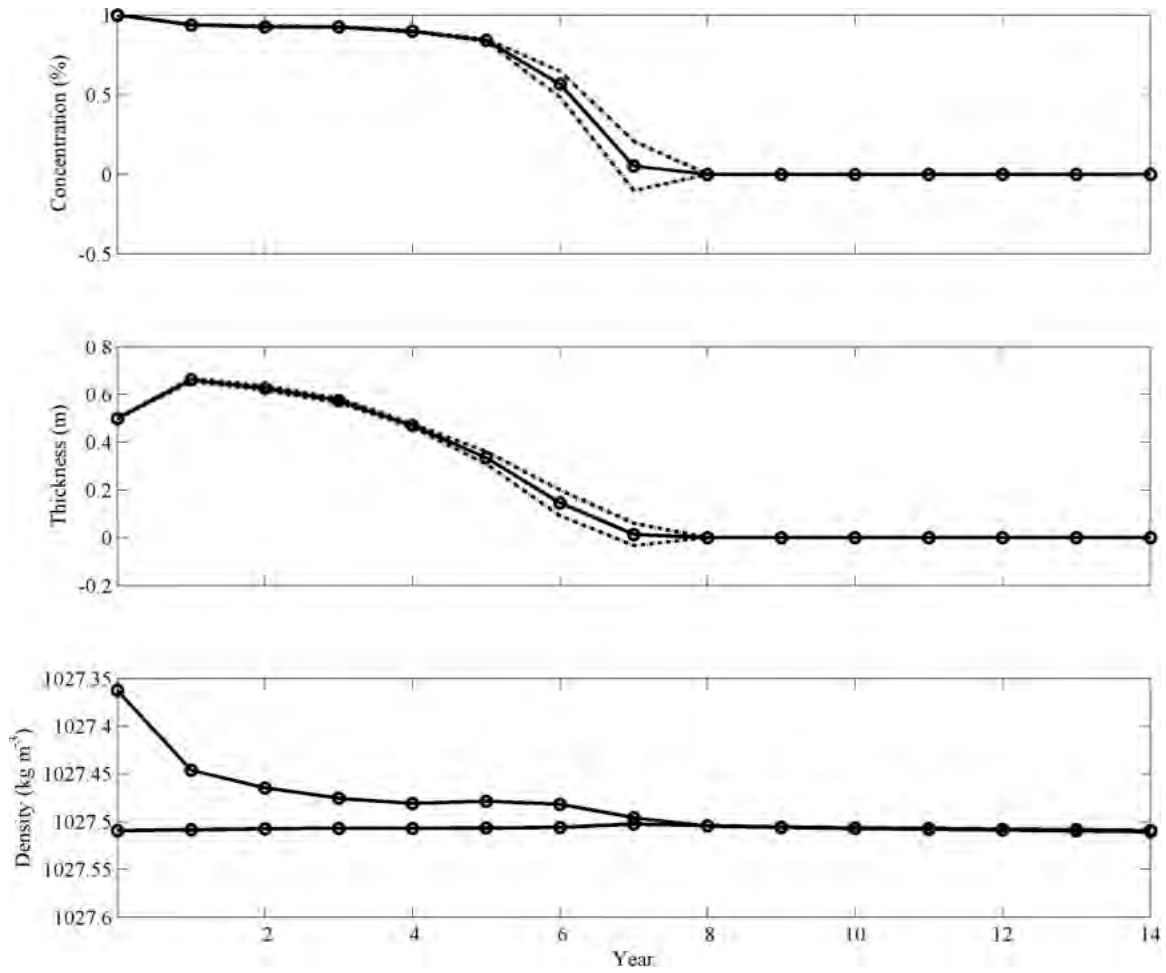**Model 27C: Free, Linear, Icy Start, $K_{turb} = 2 \cdot 10^{-5}$, No Double-Diffusion**

Figure 3.50.   Model 27C, Time Series. Like the previous two models, sea ice concentration, thickness, and $\Delta \rho_{conv}$ all go to zero by the same year.
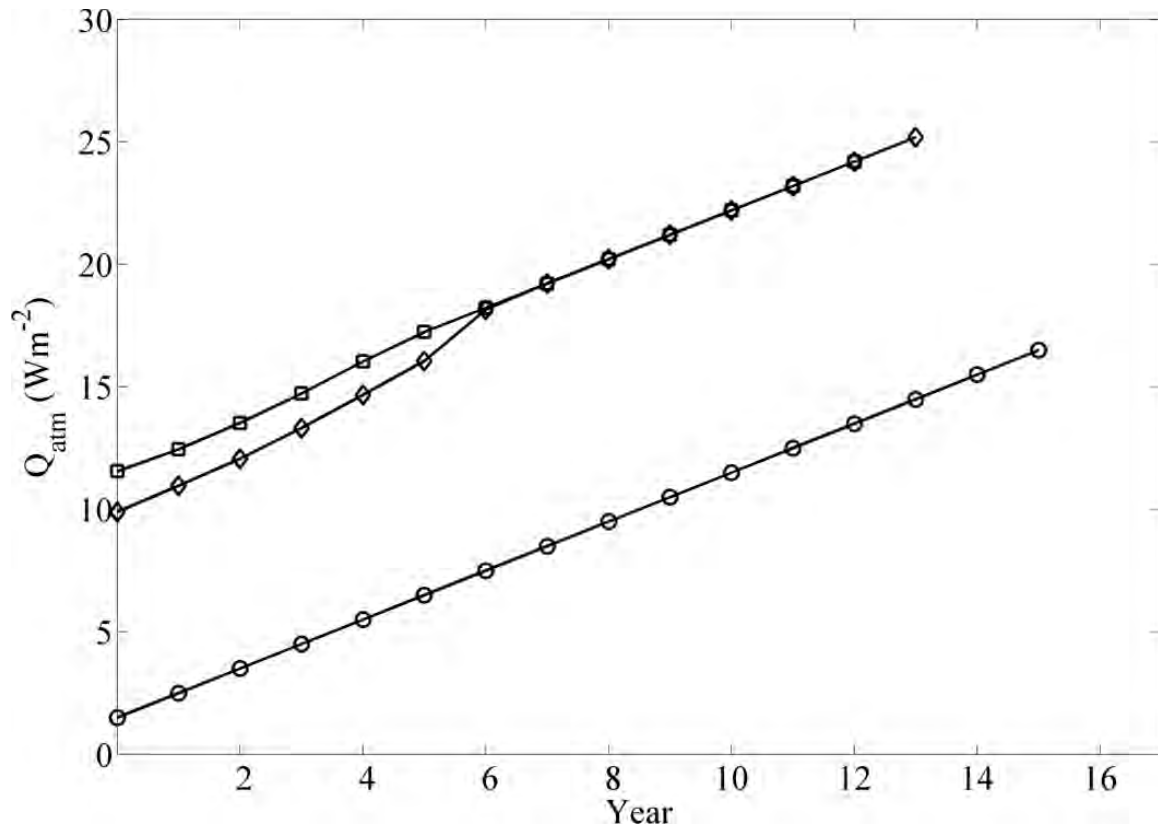
Figure 3.51. High-slope, linearly increasing surface heat flux models: Mean surface heat flux to the atmosphere (Wm^{-2}). These means are the average of the 121 grid points centered above the seamount peak $(189\pm5,112\pm5)$ taken from Model 14A and 20A (*circle*), 26A (*square*), and 27A (*diamond*).

Model 21A: Fixed, Low-Slope Linear, K_{turb} = 0, with Double-Diffusion

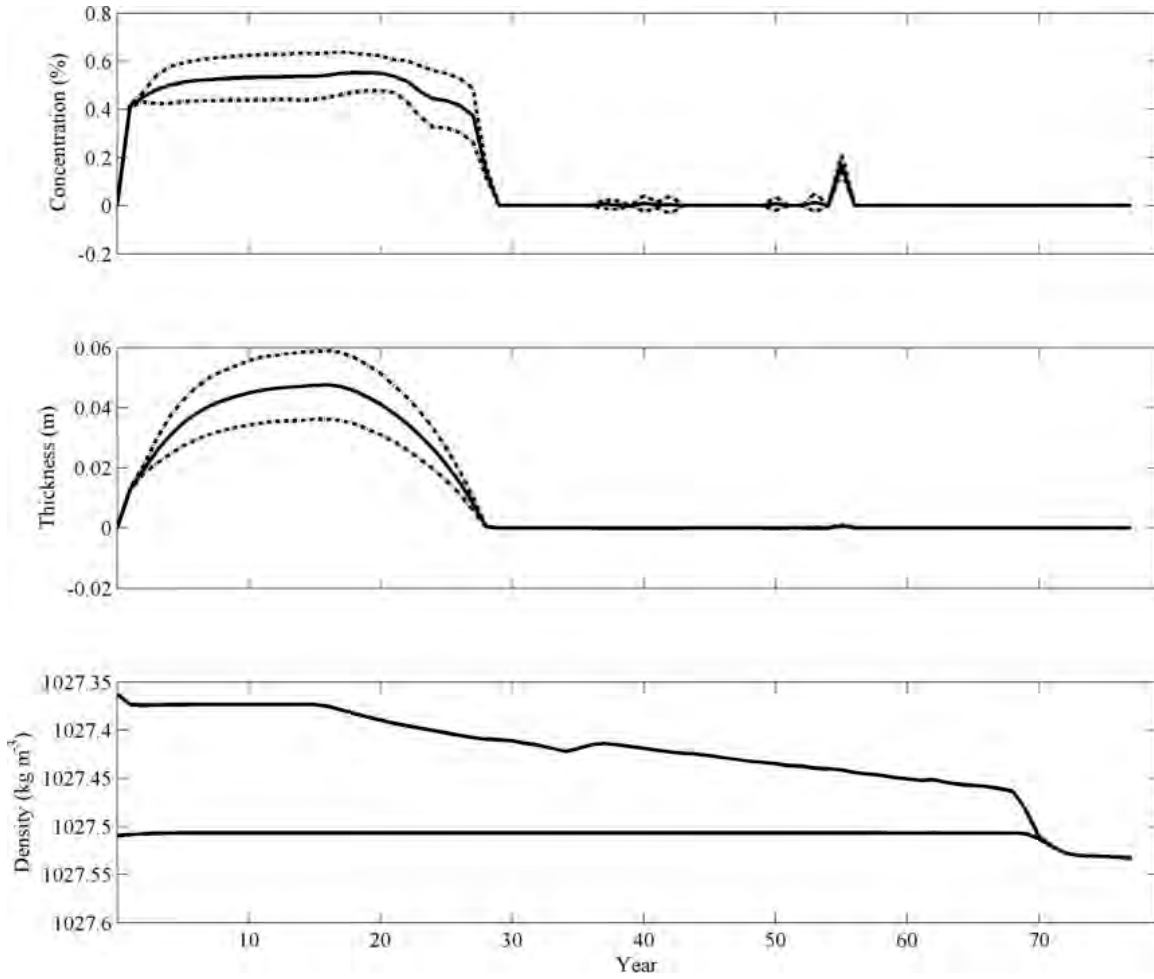Figure 3.52.   Model 21A, Time Series. The first 15 years of this, and all other runs in 21 and 30, experienced a $1\,Wm^{-2}$ steady cooling. After 15 years, prescribed cooling increased at a rate of $0.25\,Wm^{-2}yr^{-1}$. Mean sea ice concentration and thickness were effectively zero starting at year 29. However, an exceptionally long run was required before the model reached a convective state (at year 70).

Model 21B: Fixed, Low-Slope Linear, $K_{turb} = 2 \cdot 10^{-5}$, with Double-Diffusion
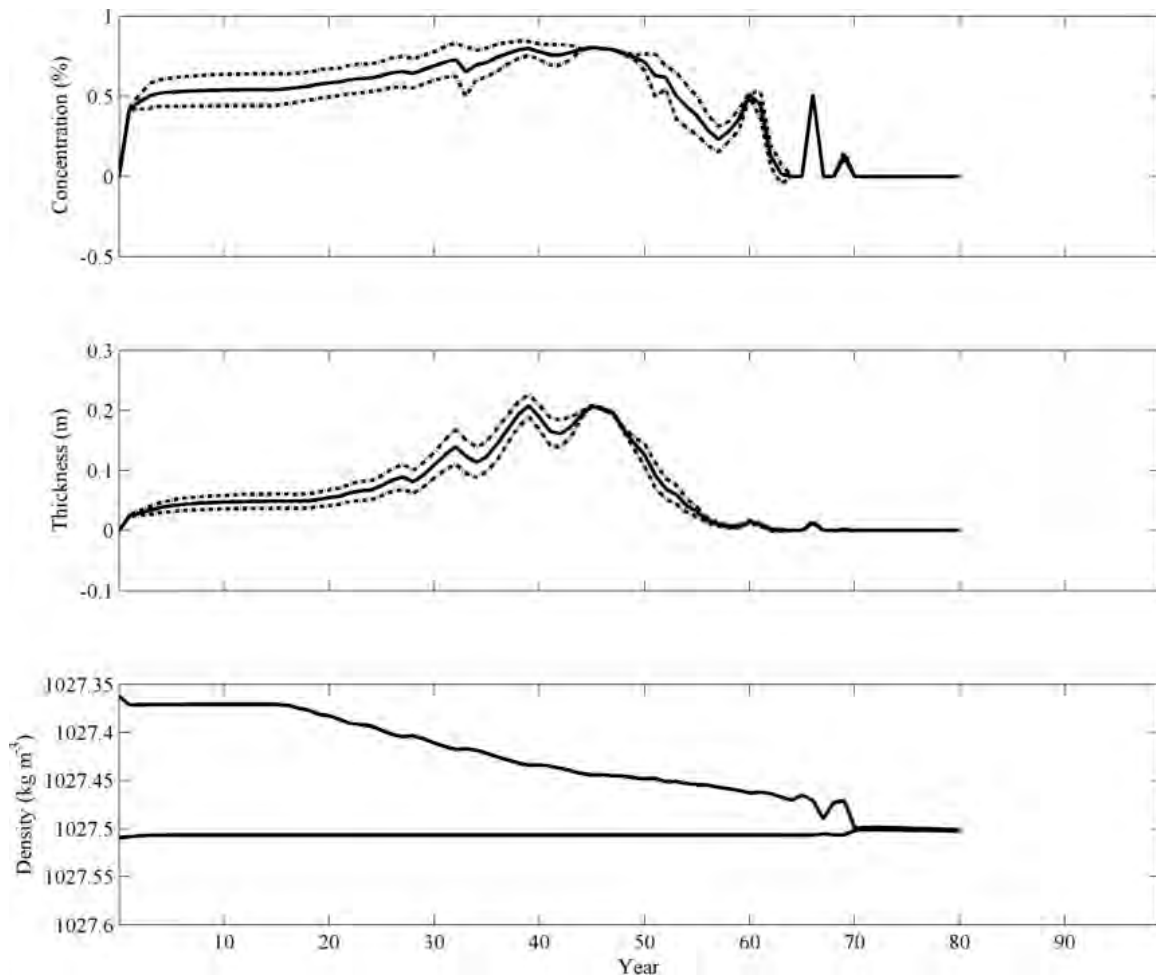
Figure 3.53.   Model 21B, Time Series. Sea ice completely disappears in the area immediately over the seamount summit at year 65, with convection occurring six years later.

Model 21C: Fixed, Low-Slope Linear, K_{turb} = 2•10^{-5}, No Double-Diffusion

Figure 3.54.   Model 21C, Time Series. Convection occurs two years after sea ice completely melts away at year 64.

Model 30A: Free, Low-Slope Linear, K_{turb} = 0, with Double-Diffusion
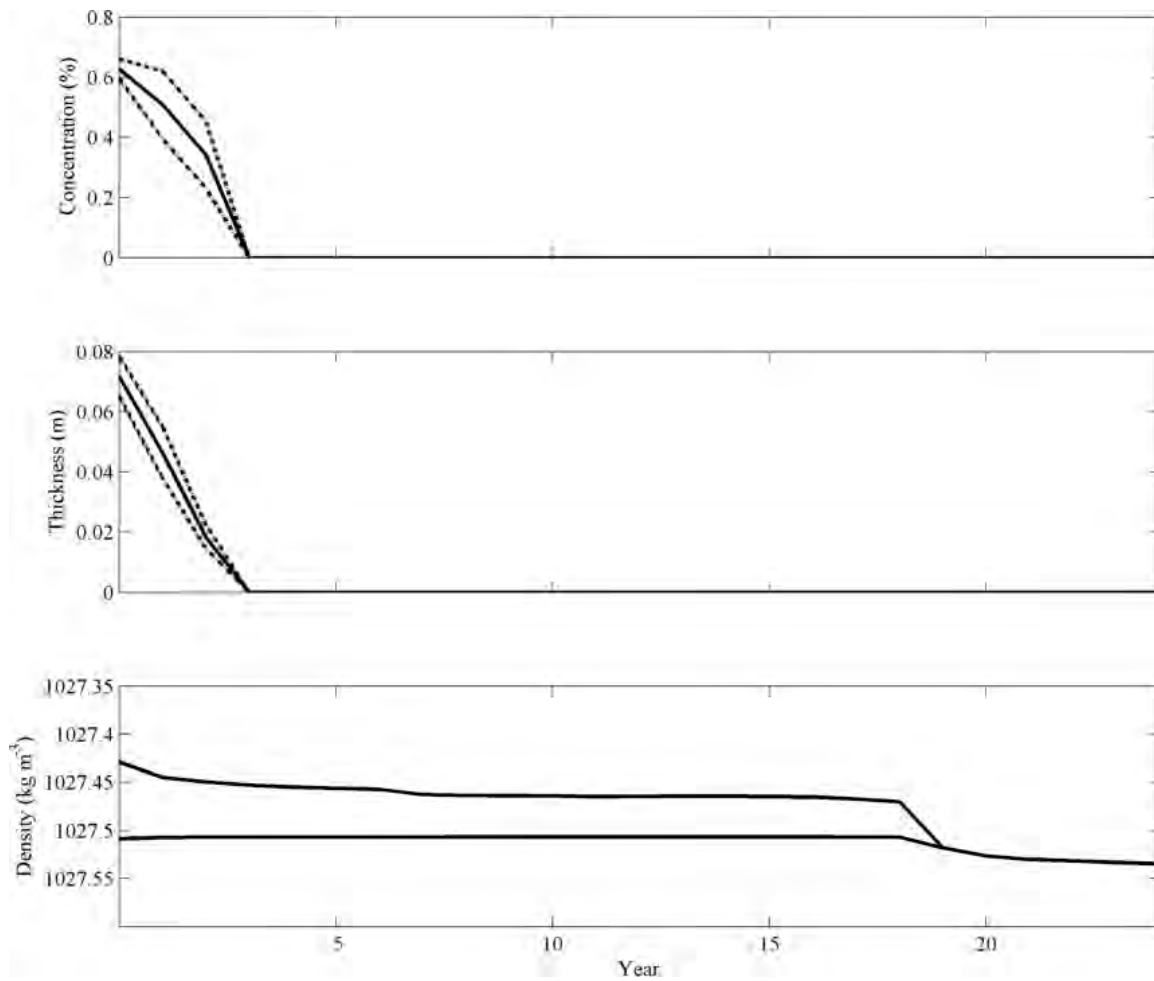
Figure 3.55. Model 30A, Time Series. Much like Model 21A, sea ice cover is completely gone early, at year 3. Convection follows at year 19, sixteen years later.

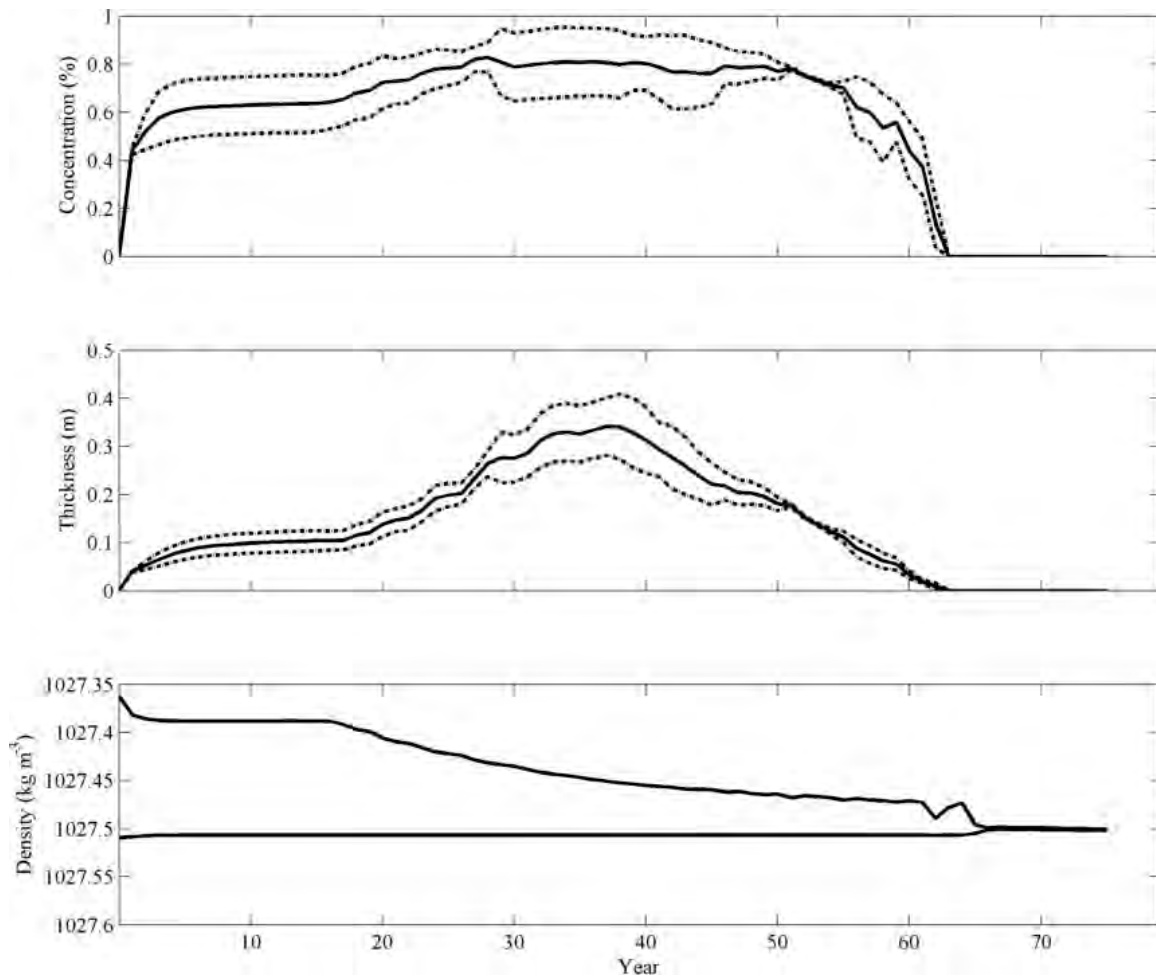**Model 30B: Free, Low-Slope Linear, K_{turb} = 2•10^{-5}, with Double-Diffusion**
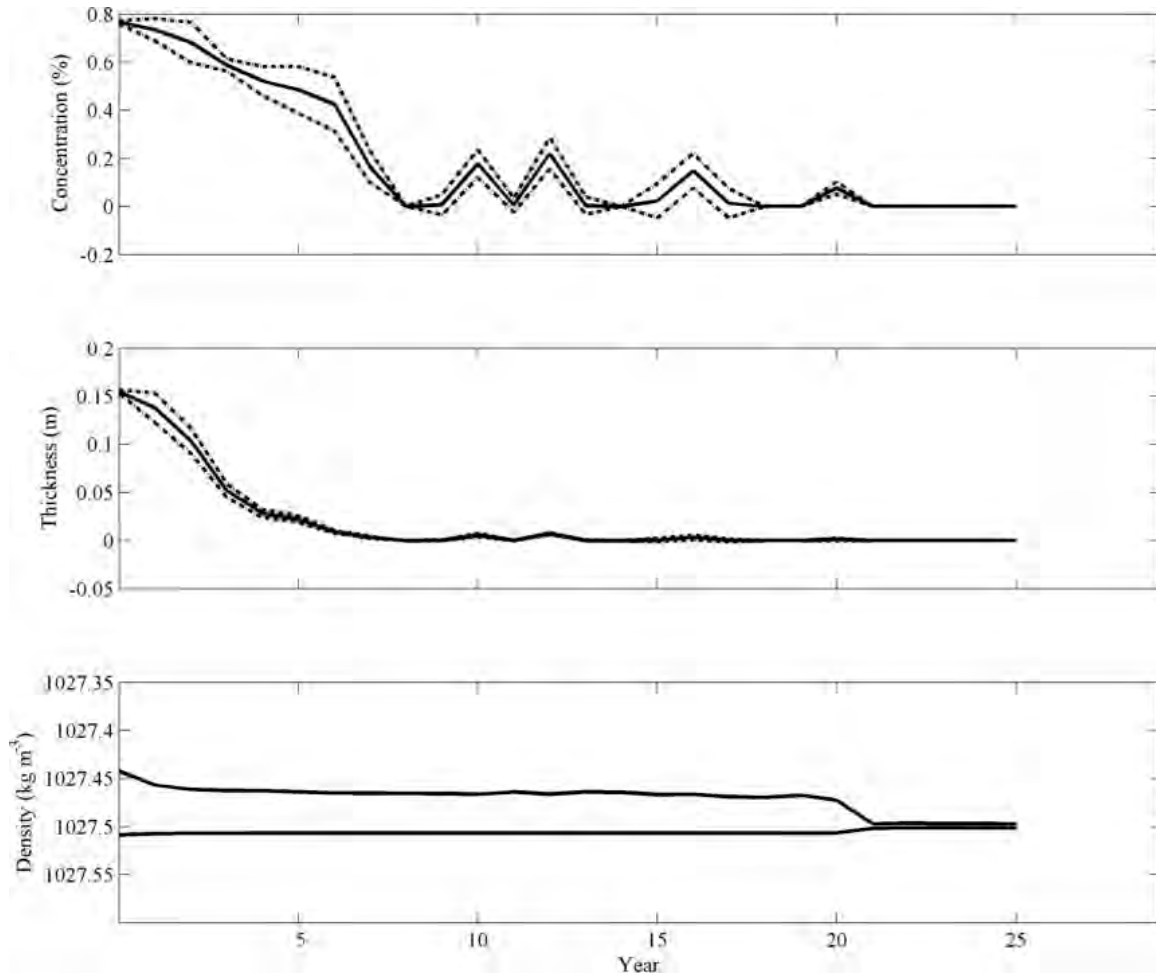
Figure 3.56.   Model 30B, Time Series. Sea ice concentrations reaches zero at year 8 and year 14, but the first year of a multi-year period of open ocean occurs at year 18. Sea ice thickness after year 8 hovers slightly above zero. The model reaches our definition of convection $(\Delta\rho_{conv} < 0.005 \; kg \; m^{-3})$ at year 21.

Model 30C: Free, Low-Slope Linear, K_{turb} = 2•10⁻⁵, No Double-Diffusion
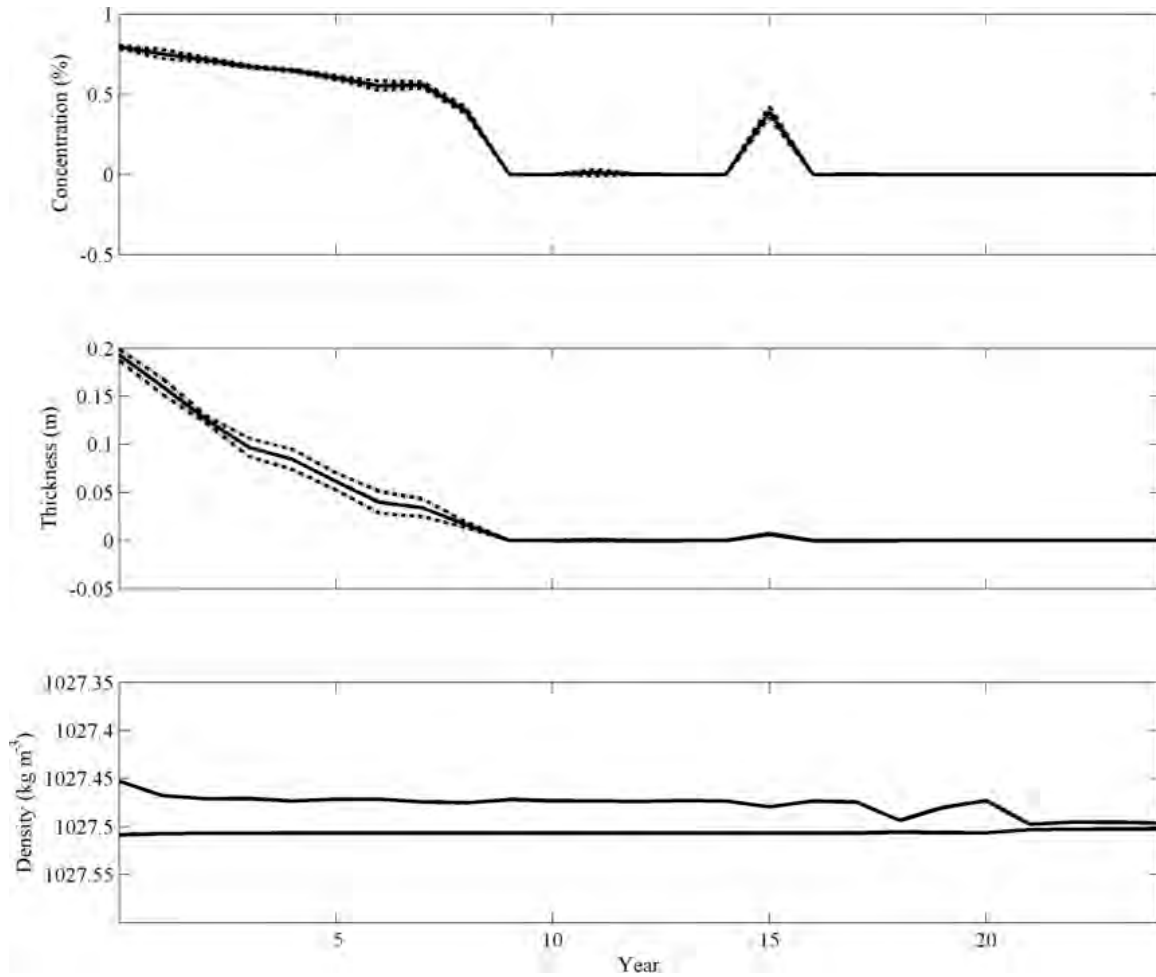
Figure 3.57.   Model 30C, Time Series. Model 30C provides an anomalous case of a turbulent-only model experiencing the early onset of a polynya without quickly moving into convection. Open ocean occurs at year 9, but convection occurs at year 21, similar to Model 30A and 30B.

Model 31A: Free, Very Low-Slope Linear, K_{turb} = 0, with Double-Diffusion
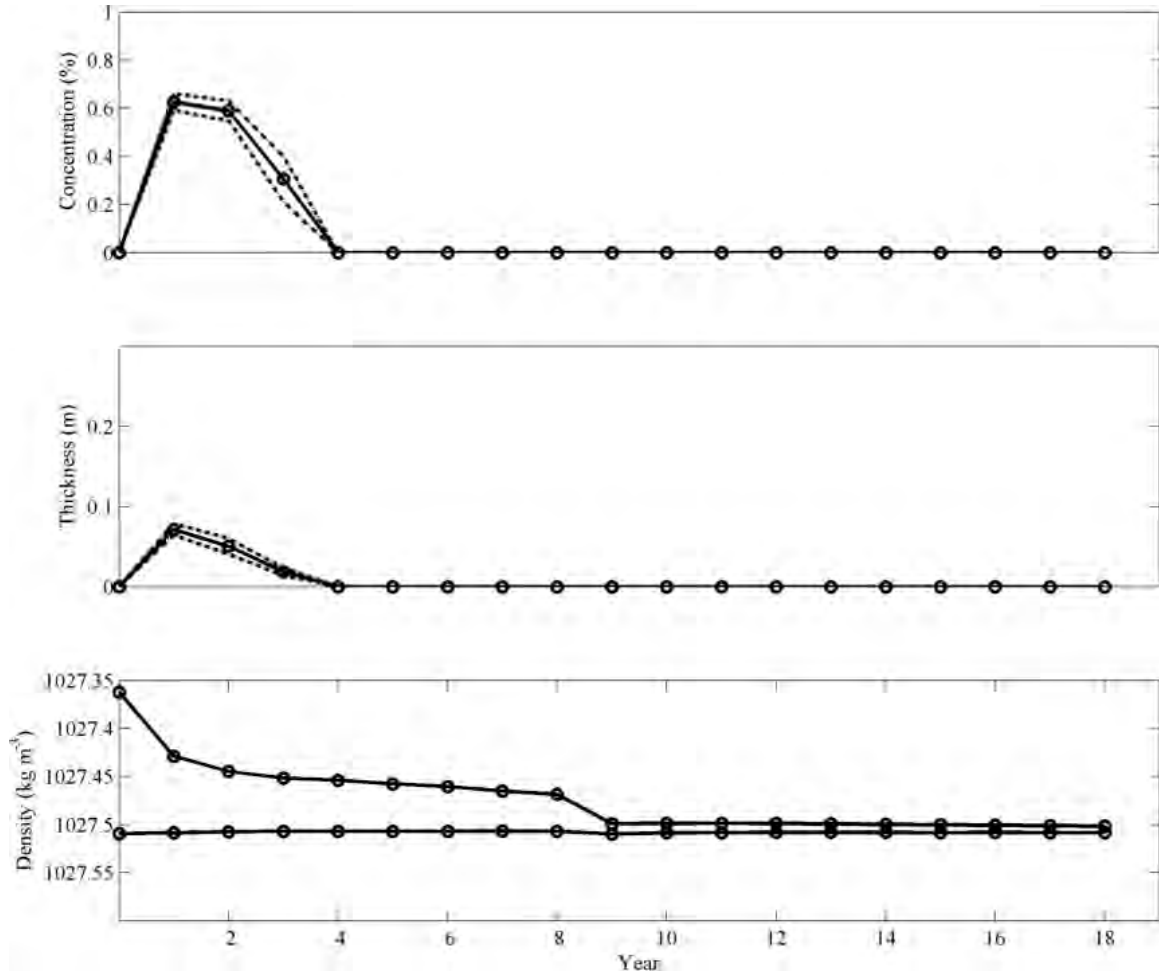
Figure 3.58.   Model 31A, Time Series. Ice-free by year 4, this purely double-diffusive model comes close to the threshold of convection by year 9, but maintains $\Delta\rho_{conv}$ greater than the required $\Delta\rho_{conv} < 0.005\ kg\ m^{-3}$.

161

Model 31B: Free, Very Low-Slope Linear, $K_{turb} = 2 \cdot 10^{-5}$, with Double-Diffusion
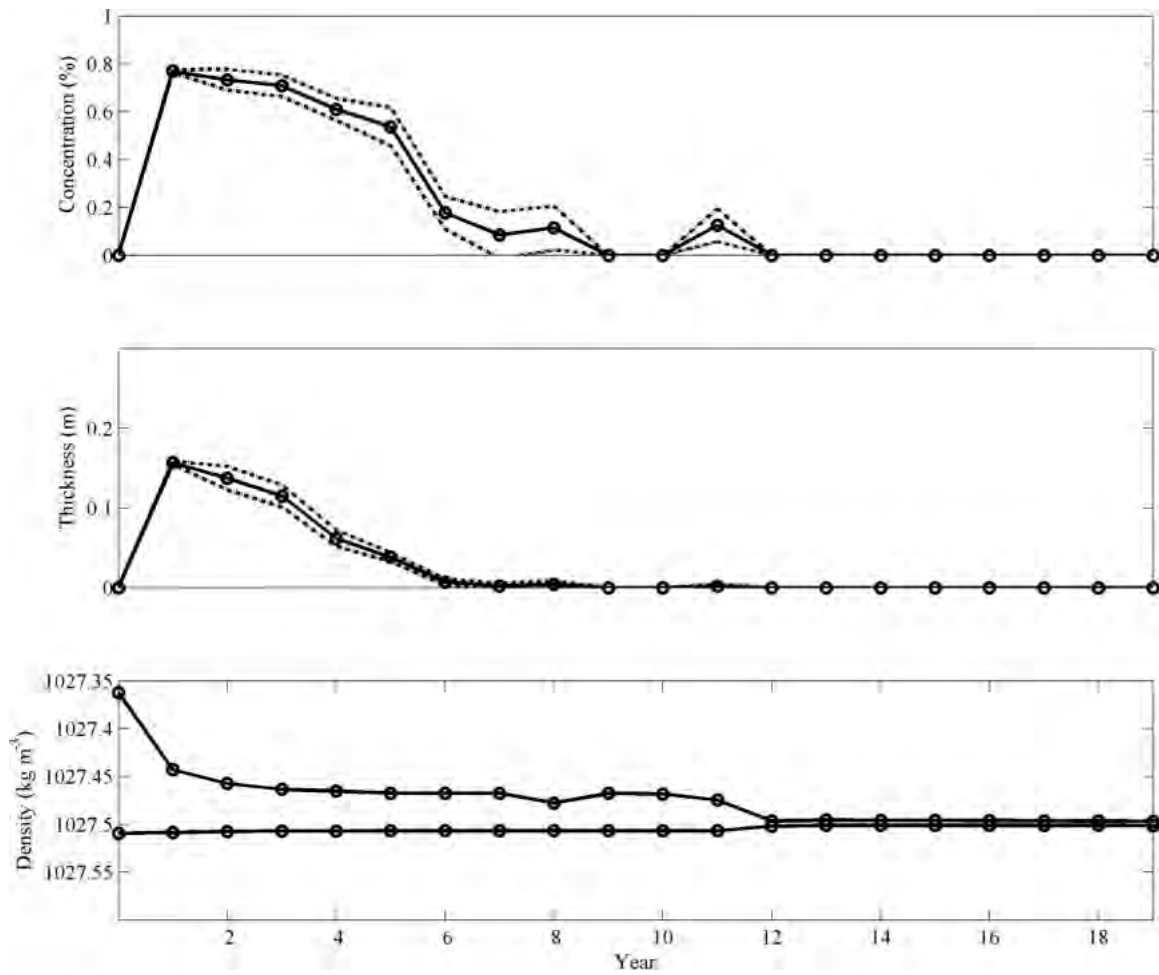
Figure 3.59.   Model 31B, Time Series. The first year of total open ocean in the averaged area occurs at year 9. Even though a promising bottleneck occurs in the potential density plots at year 8, convection initiates by year 12.

162

Model 31C: Free, Very Low-Slope Linear, $K_{turb} = 2 \cdot 10^{-5}$, No Double-Diffusion
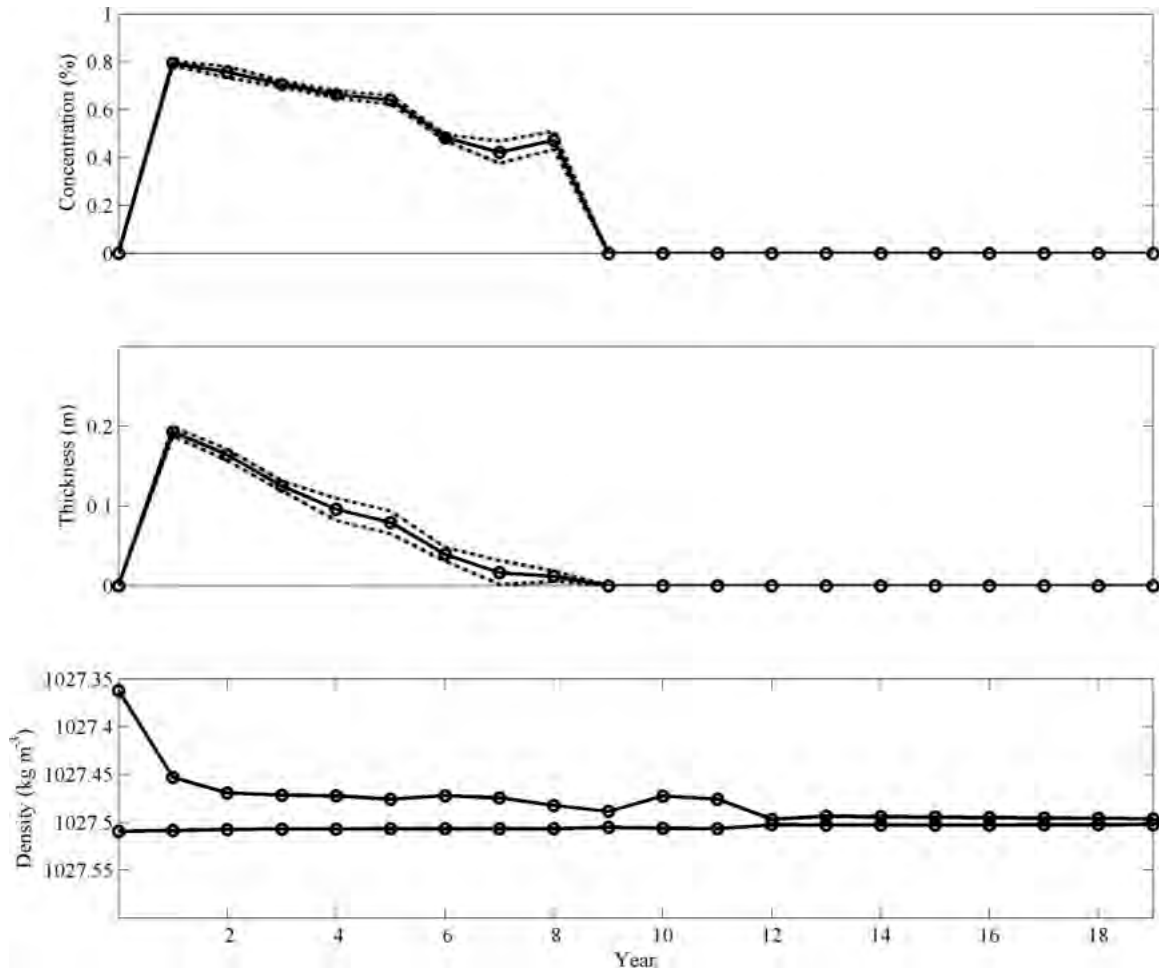
Figure 3.60.   Model 31C, Time Series. Like 31B, the ocean above the seamount is ice-free at year 9, with a dip in the difference in potential density occurring that same year. The criterion for convection is met by year 12, but by year 13 $\Delta\rho_{conv}$ has increased to a value slightly over 0.005 $kg\ m^{-3}$.
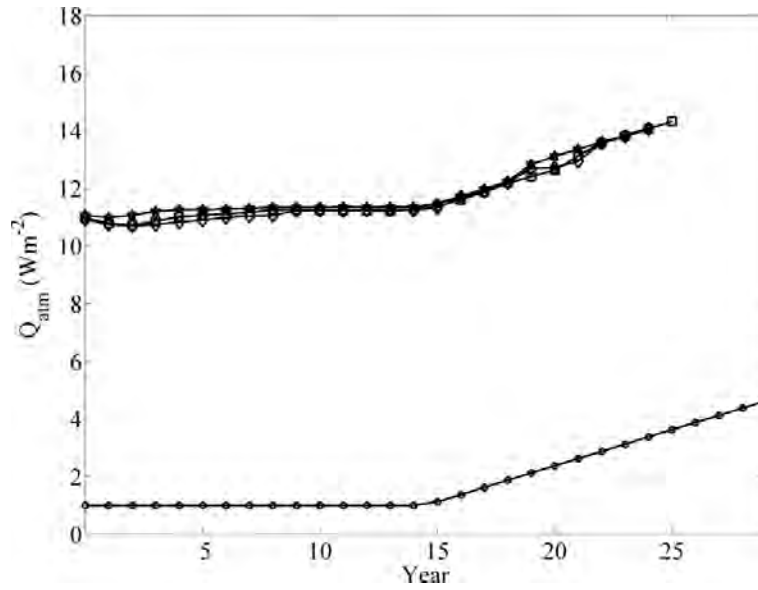
(a)
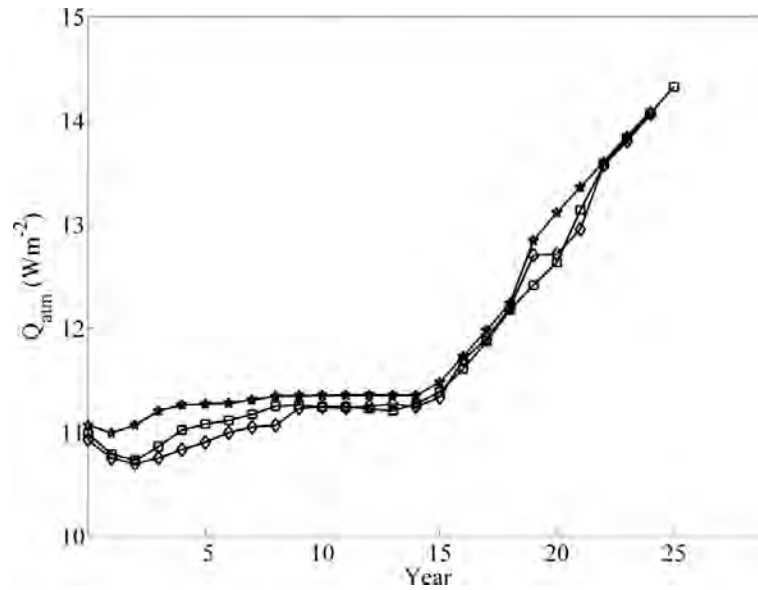
(b)

Figure 3.61. Low-slope, linearly increasing surface heat flux models: Mean surface heat flux to the atmosphere (Wm^{-2}). Plots show (*a*) Model 21A (*circle*), 30A (*star*), 30B (*square*), and 30 C (*diamond*) and (*b*) a close-up on Model 30 runs. Adding in sensible, latent, and additional longwave surface heat fluxes causes little variation in cooling, but adds a substantial amount of net cooling over the models having prescribed heat flux only.
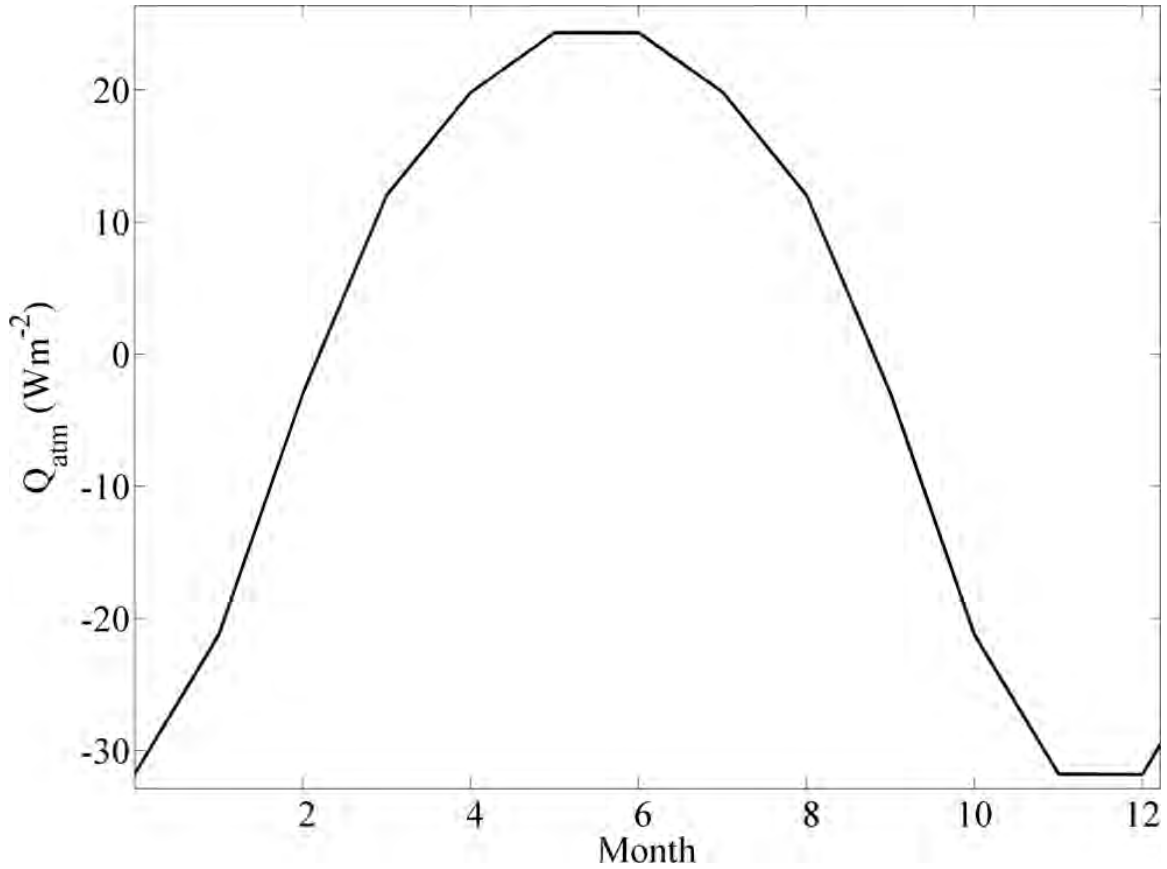
Figure 3.62. Cyclical baseline surface heat flux forcing for seasonal models. These values represent a monthly varying form of Q_{pr} from Equation (3.4). Model 16 uses this as its sole heat flux forcing. To this, Model 19 adds $+1\,Wm^{-2}yr^{-1}$. Model 28 adds $0.03\varepsilon\sigma T_{surf}^4$ to this baseline and Model 29 adds both $+1\,Wm^{-2}yr^{-1}$ and $0.03\varepsilon\sigma T_{surf}^4$. Adding the additional net longwave flux term results in surface cooling that is typically $10\,Wm^{-2}$ higher at any given month. The time-domain integral of this baseline forcing is $0\,Wm^{-2}$. Positive heat flux represents loss from the ocean to the atmosphere.

Model 16A: Fixed, Seasonal (+0 $Wm^{-2}yr^{-1}$), K_{turb} = 0, with Double-Diffusion
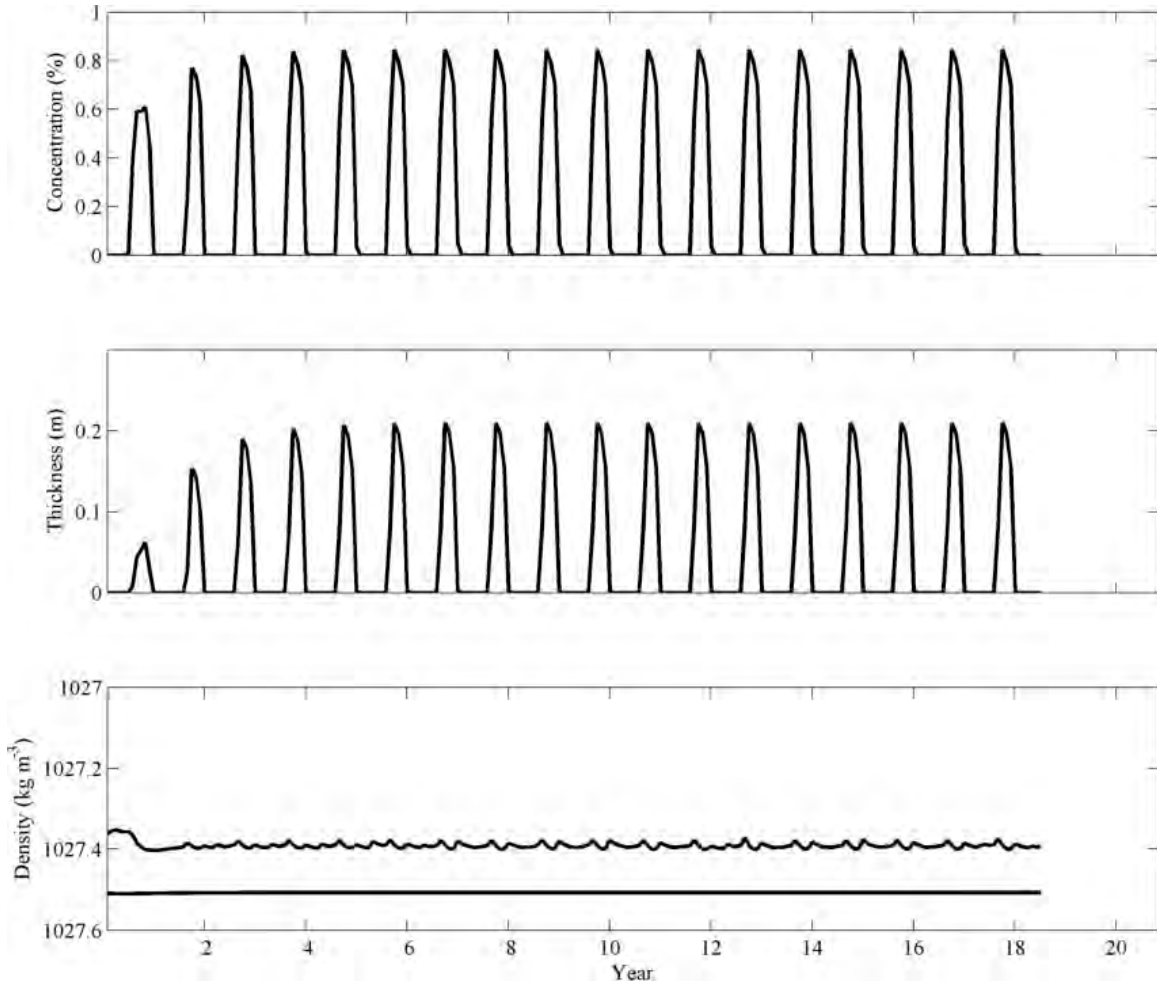
Figure 3.63. Model 16A, Time Series. In the first of the seasonally varying surface heat flux runs, Model 16A, double-diffusive with no turbulent diffusivity, experiences a near-constant $\Delta\rho_{conv}$ even though surface heat flux forcing ranges from -32 to +24 Wm^{-2} during each year. Sea ice concentration and thickness vary over the seamount according to expected patterns with no multi-year polynyas occurring.

Model 16B: Fixed, Seasonal (+0 *Wm^{-2}yr^{-1}*), *K$_{turb}$* = 2•10^{-5}, with Double-Diffusion
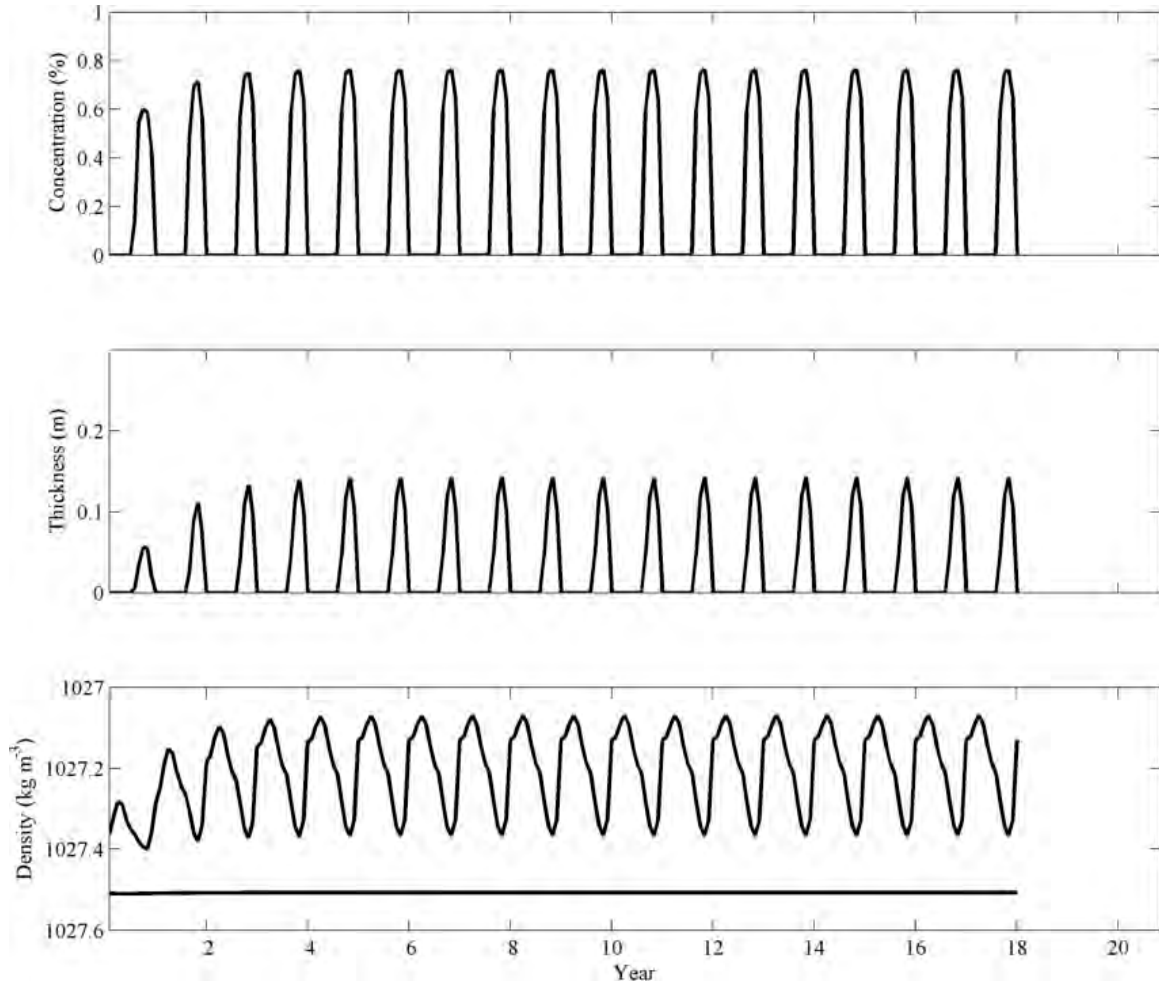
Figure 3.64.   Model 16B, Time Series. Adding turbulent diffusivity to a double-diffusive run causes $\Delta\rho_{conv}$ to vary quite significantly during each year. Mean sea ice concentration and thickness still follow monthly variations in surface heat flux.

Model 16C: Fixed, Seasonal (+0 *Wm⁻²yr⁻¹*), K_{turb} = 2•10⁻⁵, No Double-Diffusion
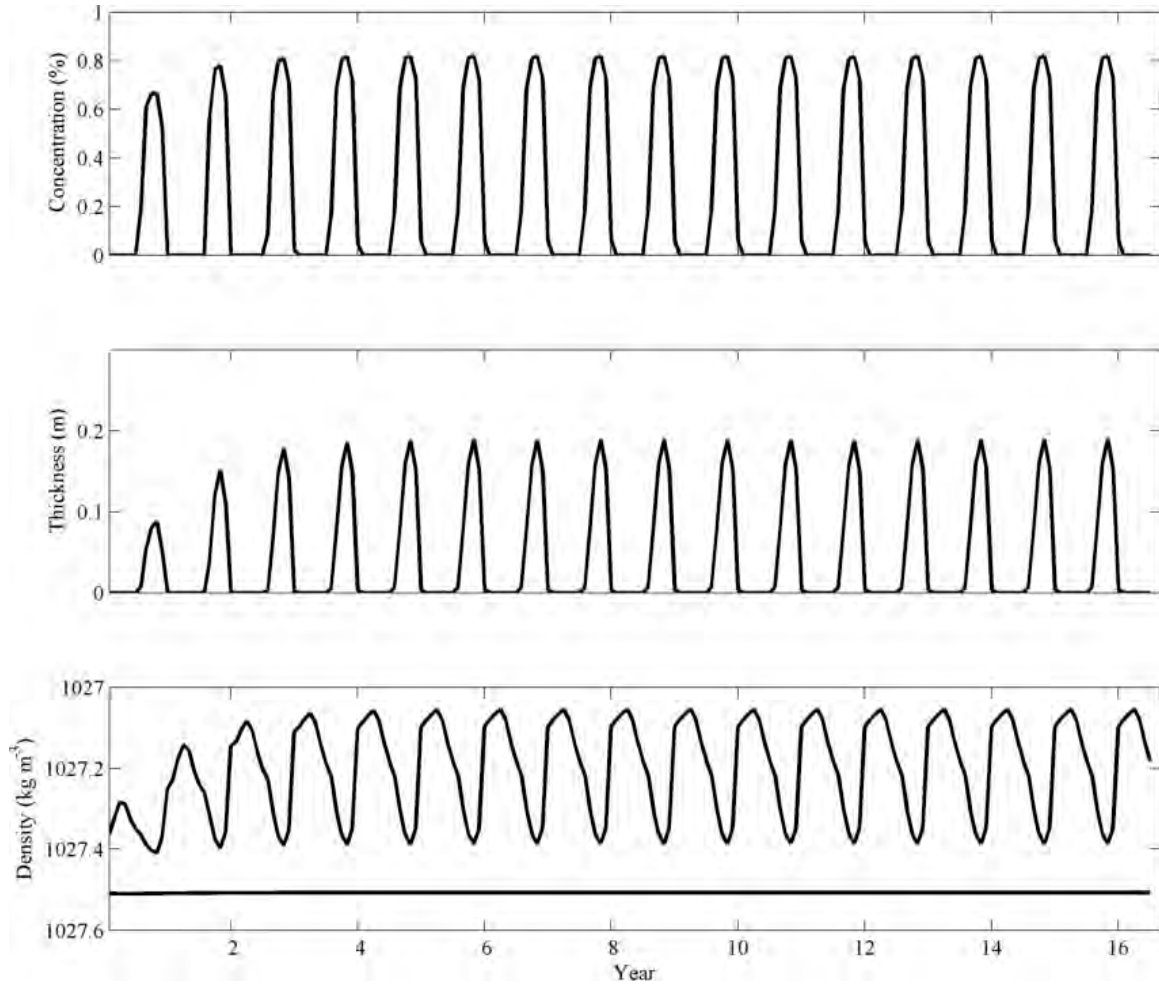
Figure 3.65. Model 16C, Time Series. Model 16C is the purely turbulent case in the Model 16 series. With no double-diffusive mixing parameterization, the variation in $\Delta\rho_{conv}$ is slightly greater throughout the year, as compared to 16B.

Model 28A: Free, Seasonal (+0 $Wm^{-2}yr^{-1}$), K_{turb} = 0, with Double-Diffusion
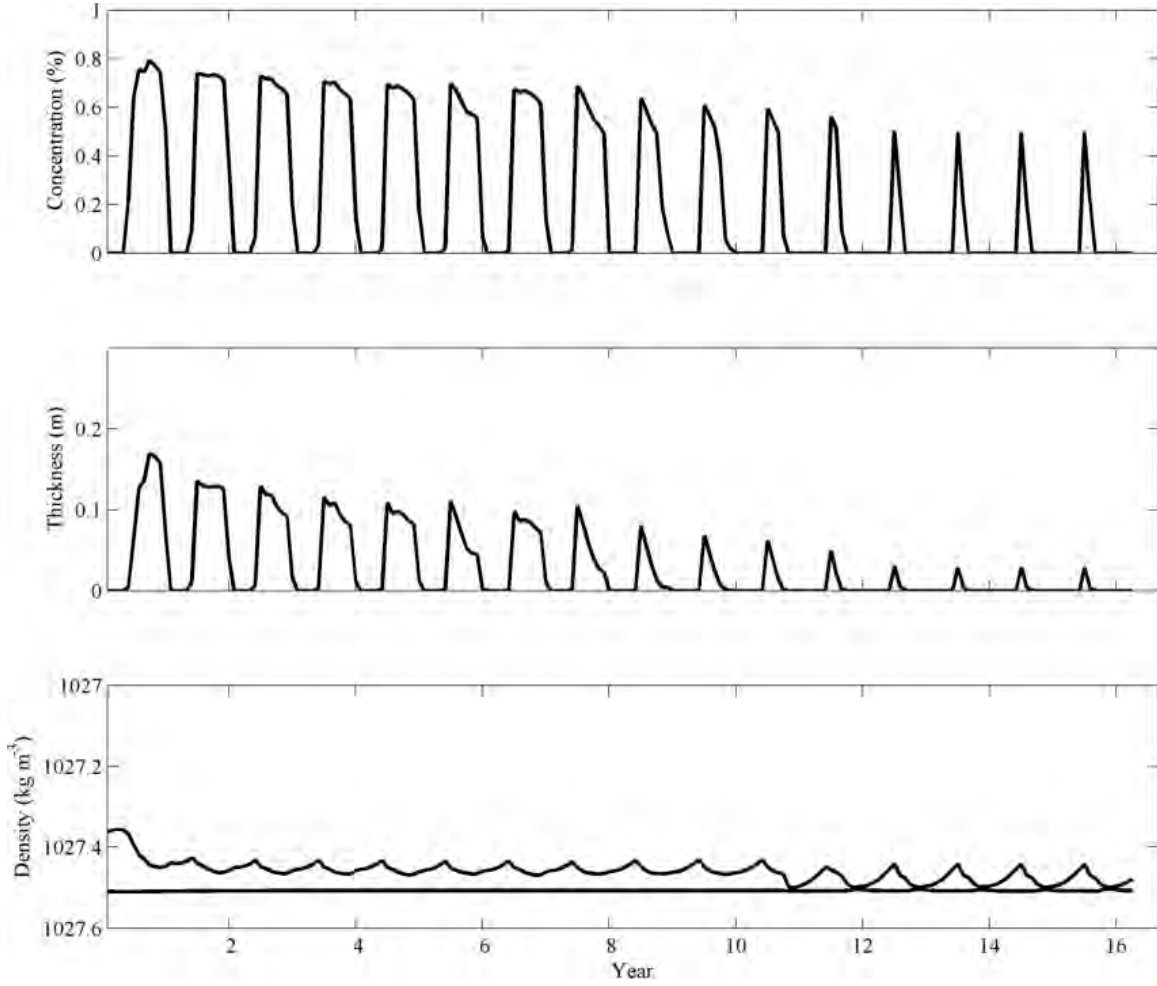
Figure 3.66. Model 28A, Time Series. Identical to Model 16A, but with the inclusion of sensible, latent, and additional net longwave radiation, Model 28A experiences a slow decline in seasonal sea ice cover with a corresponding breakdown of $\Delta\rho_{conv}$ even though there is no increase in annual net cooling. Starting at year 11, $\Delta\rho_{conv}$ almost reaches the convection criterion of 0.005 $kg\ m^{-3}$ and each year after.

Model 28B: Free, Seasonal (+0 $Wm^{-2}yr^{-1}$), K_{turb} = 2•10^{-5}, with Double-Diffusion
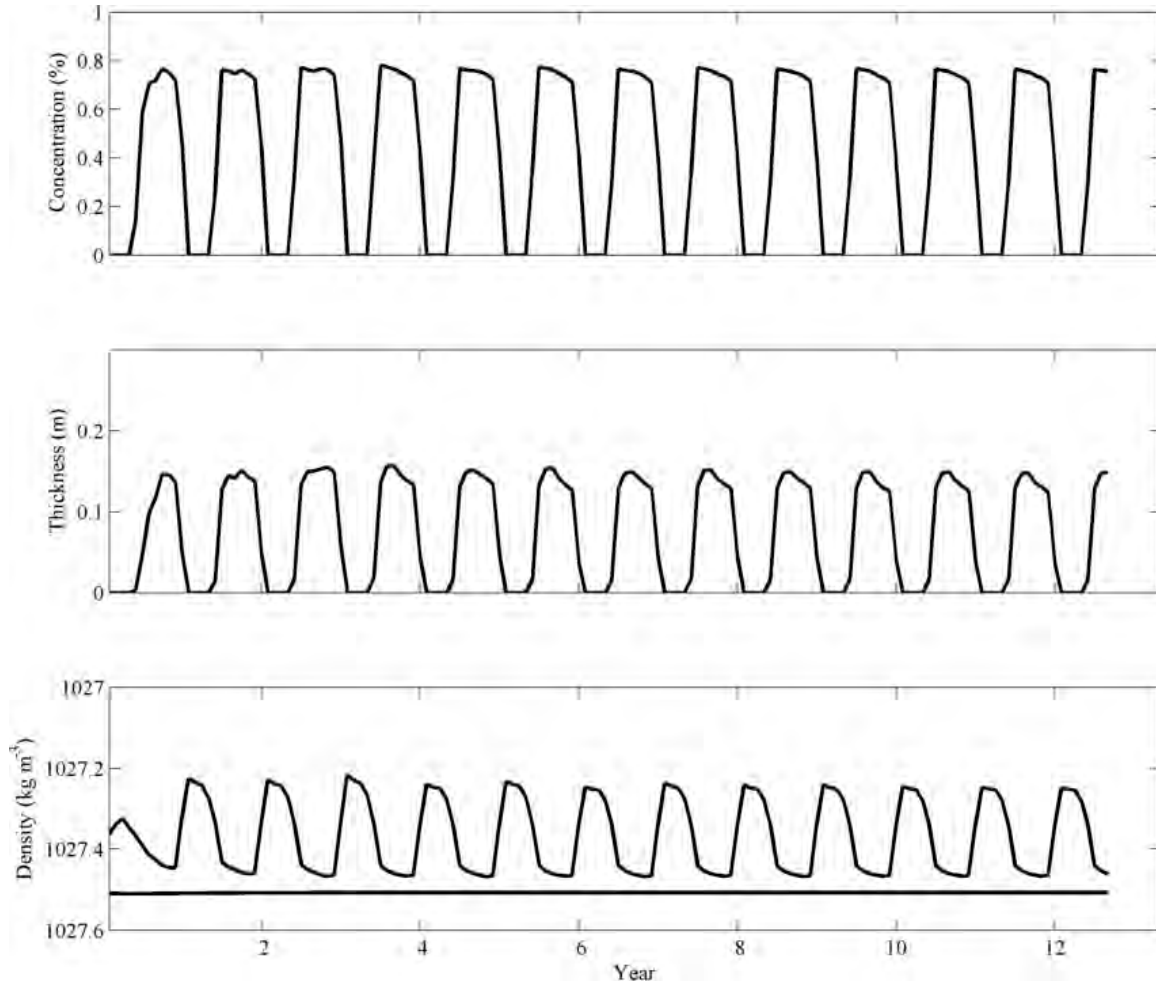
Figure 3.67.   Model 28B, Time Series. Although all three cases of Model 28 experience no increase in mean annual cooling, Model 28B maintains consistent sea ice concentration, thickness, and $\Delta\rho_{conv}$ from year to year, unlike 28A. Purely double-diffusive cases seem to be more sensitive to the higher monthly forcing variations of the "free" models.

Model 28C: Free, Seasonal (+0 *Wm⁻²yr⁻¹*), *K_turb* = 2•10⁻⁵, No Double-Diffusion
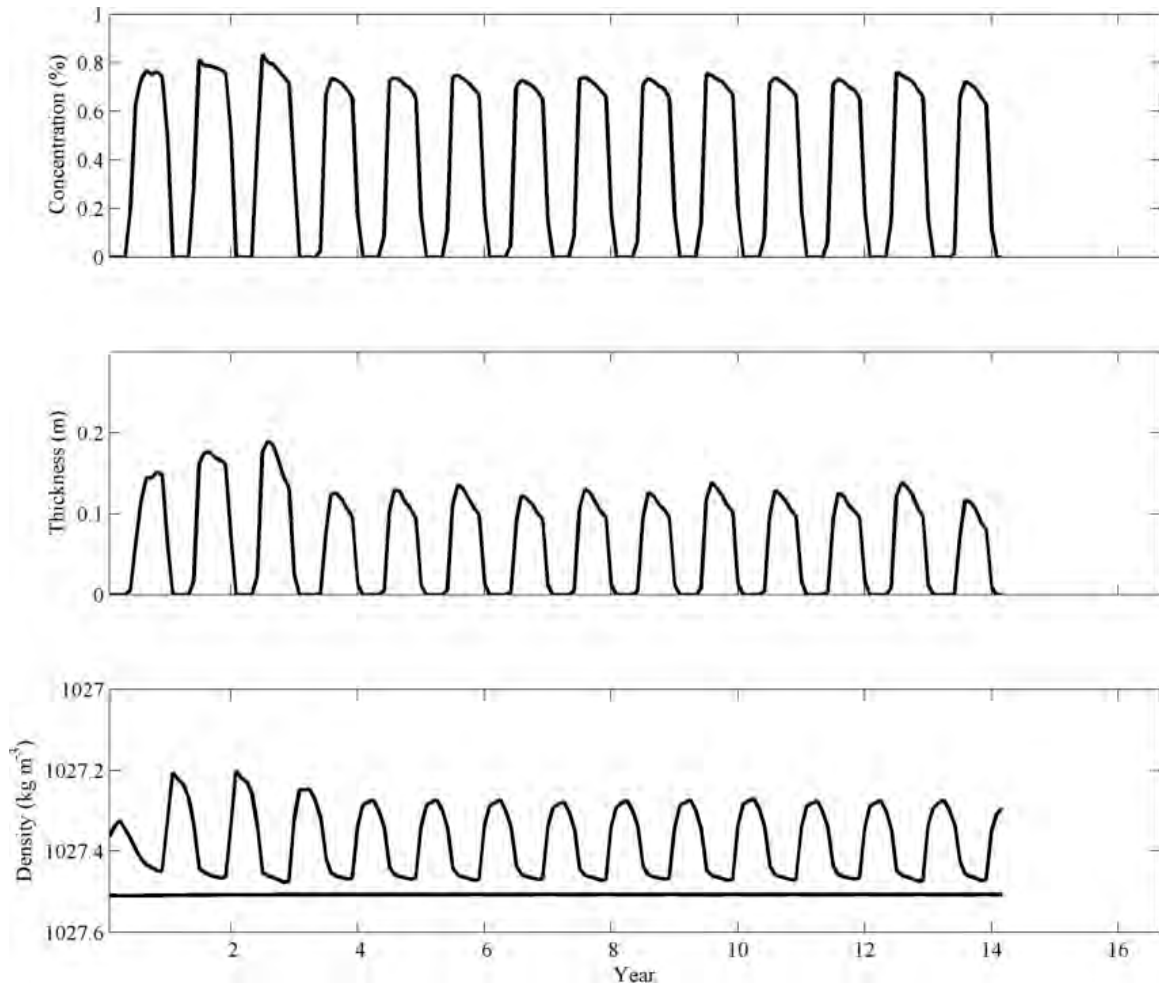
Figure 3.68.   Model 28C, Time Series. Very similar to 28B, Model 28C sees no decrease in overall sea ice concentration, thickness, or potential density differences as the model integrates.

171

Model 19A: Fixed, Seasonal (+1 $Wm^{-2}yr^{-1}$), K_{turb} = 0, with Double-Diffusion
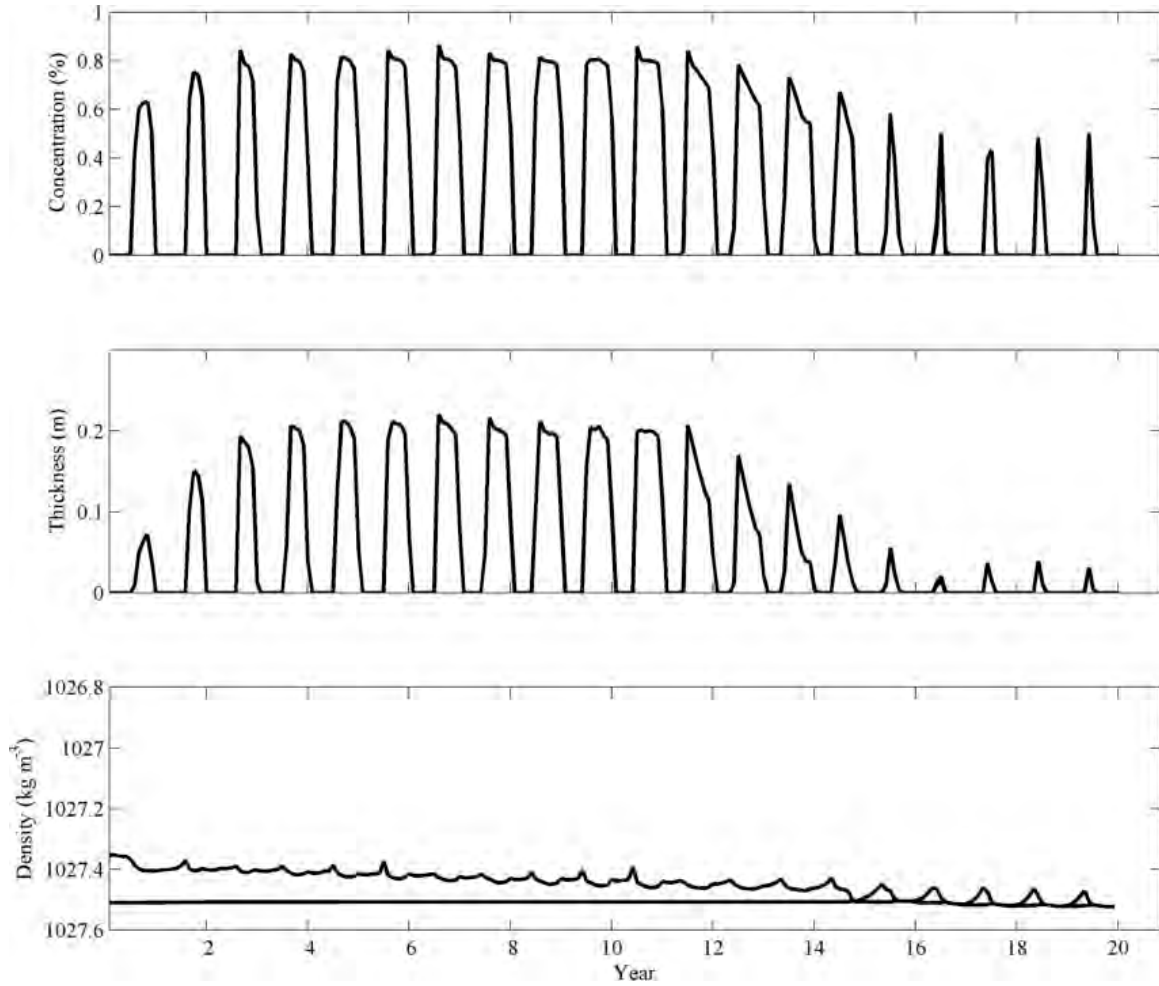
Figure 3.69.   Model 19A, Time Series. The first sign of convection in the column over the seamount occurs at year 15. However, mean sea ice concentration and thickness still reach non-zero values in the austral winter. A multi-year polynya never forms.

Model 19B: Fixed, Seasonal (+1 $Wm^{-2}yr^{-1}$), $K_{turb} = 2 \cdot 10^{-5}$, with Double-Diffusion
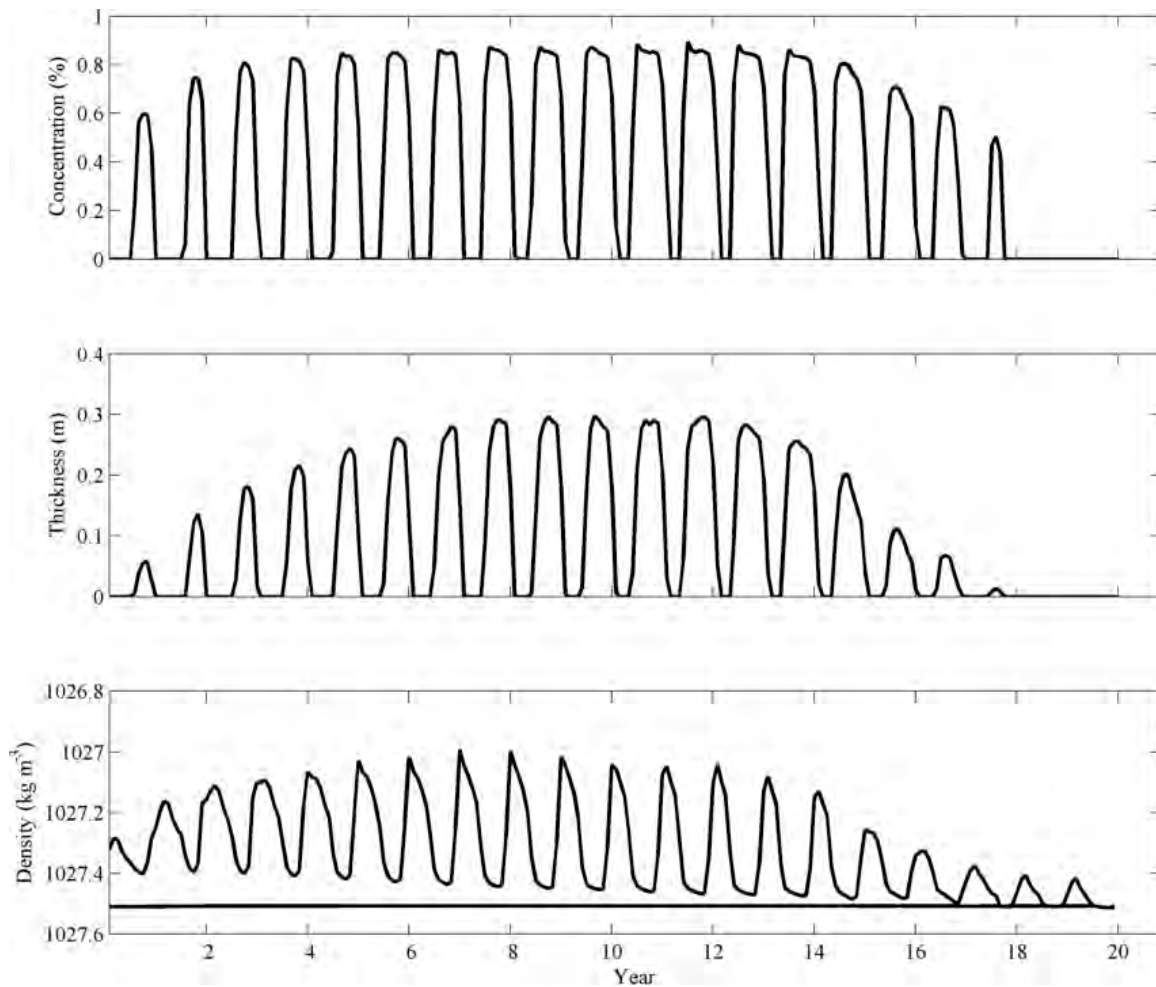
Figure 3.70.   Model 19B, Time Series. This model, having both double-diffusion and turbulent diffusivity included sees an onset of convection immediately before year 17. By year 18, a multi-year polynya has formed, evidenced by zero mean sea ice concentration and thickness from that point forward.

Model 19C: Fixed, Seasonal (+1 $Wm^{-2}yr^{-1}$), K_{turb} = 2•10⁻⁵, No Double-Diffusion
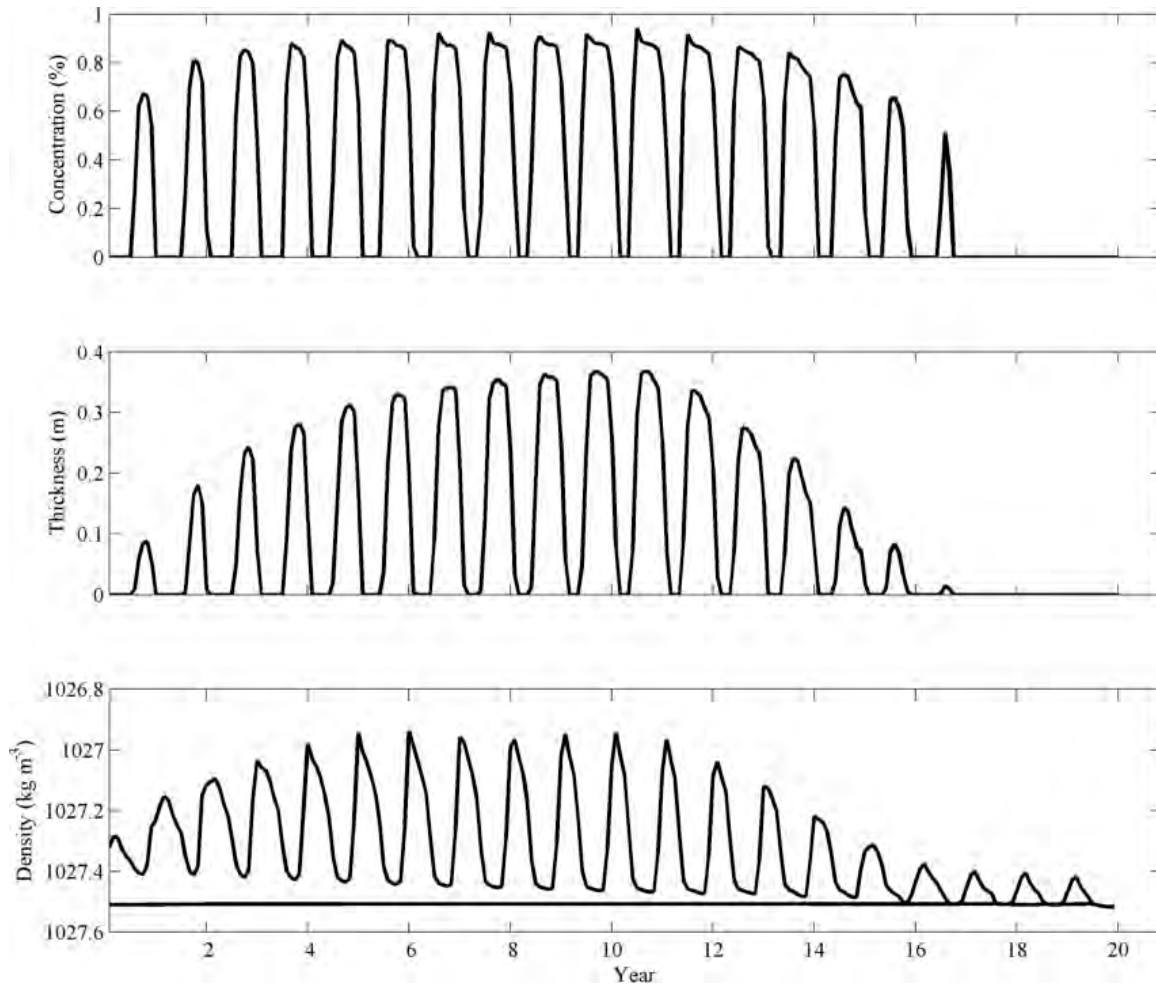
Figure 3.71.   Model 19C, Time Series. Much like 19B, the model achieves convection and a subsequent zeroing of sea ice concentration and thickness. However, the onset of convection is earlier, right before year 16 and the multi-year polynya begins at year 17.

Model 29A: Free, Seasonal (+1 $Wm^{-2}yr^{-1}$), K_{turb} = 0, with Double-Diffusion
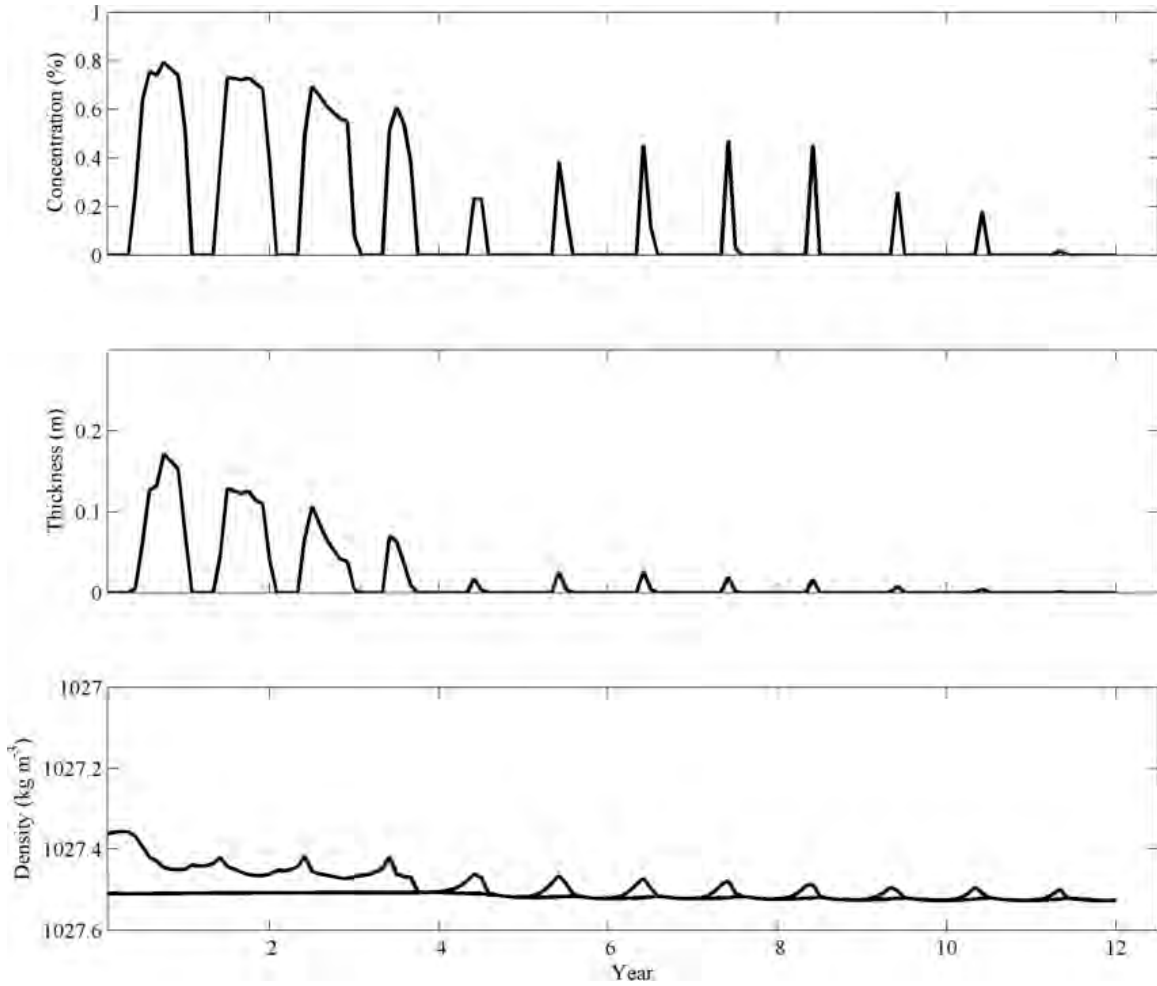
Figure 3.72. Model 29A, Time Series. Due to additional surface heat fluxes, Model 29 experiences a net annual mean cooling of $10\,Wm^{-2}$ along with an increase of $+1\,Wm^{-2}yr^{-1}$. Even with this large amount of net cooling, the purely double-diffusive model still fails to produce a multi-year polynya (but just barely). Convection occurs first at year 4.

Model 29B: Free, Seasonal (+1 $Wm^{-2}yr^{-1}$), $K_{turb} = 2 \cdot 10^{-5}$, with Double-Diffusion
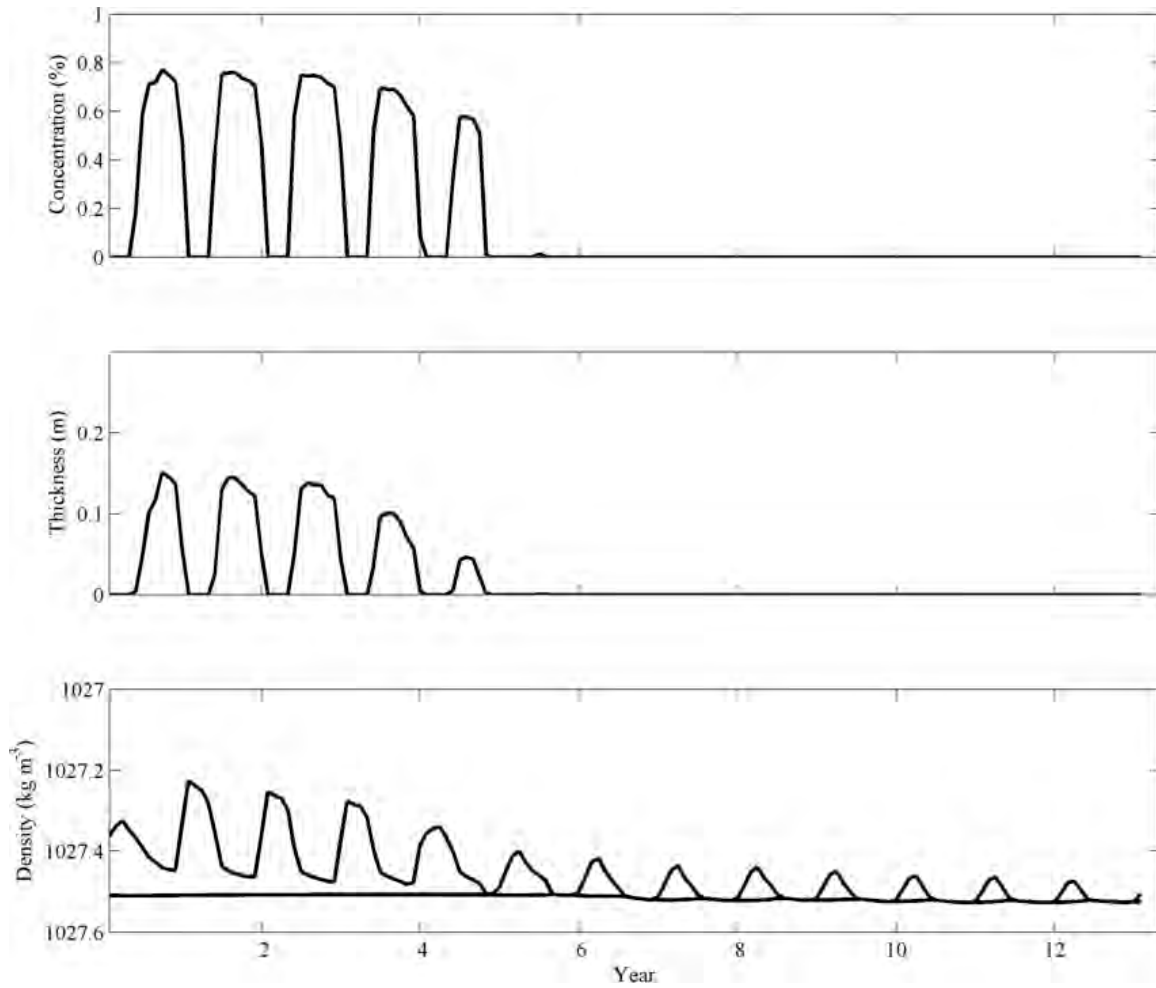
Figure 3.73.   Model 29B, Time Series. With an onset of deep convection at year 5, this model goes ice free immediately and maintains a multi-year polynya throughout the remainder of the run.

Model 29C: Free, Seasonal (+1 $Wm^{-2}yr^{-1}$), K_{turb} = 2•10^{-5}, No Double-Diffusion
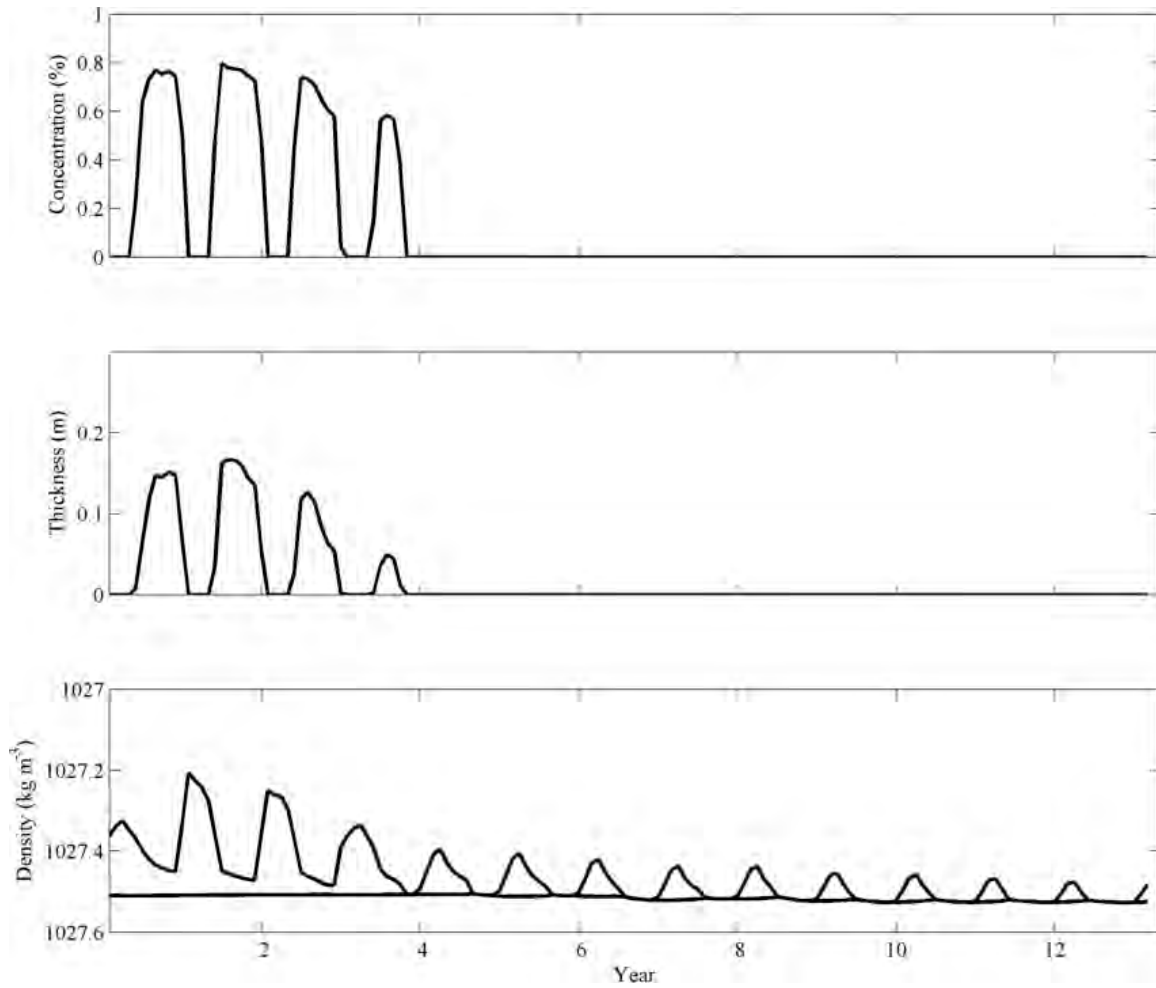
Figure 3.74.   Model 29C, Time Series. This model, with purely turbulent diffusivity and no double-diffusion, experiences convection over Maud Rise at year 4, one year earlier than the model identical in every way, except for double-diffusion (29B). The multi-year polynya begins at this time as well.

THIS PAGE INTENTIONALLY LEFT BLANK

LIST OF REFERENCES

Batteen, M. L., 2015: *Exploring Ocean Physics*. Blackwell-Wiley, Inc., 576 pp.

Bryan, F., 1987: Parameter sensitivity of primitive equation ocean general circulation models. *J. Phys. Oceanogr.*, **17**, 970–985.

Carsey, F. D., 1980: Microwave observation of the Weddell polynya. *Mon. Wea. Rev.*, **108**, 2032–2044.

Chapman, D. C., and D. B. Haidvogel, 1992: Formation of Taylor caps over a tall isolated seamount in a stratified ocean. *Geophysical and Astrophysical Fluid Dynamics*, **64**, 31–65.

Comiso, J. C. and A. L. Gordon, 1987: Recurring polynyas over the Cosmonaut Sea and the Maud Rise. *J. Geophys. Res.*, **92**, 2819–2833.

De Steur, L., D. M. Holland, R. D. Muench, and M. G. McPhee, 2007: The warm-water "halo" around Maud Rise: Properties, dynamics and impact. *Deep-Sea Res.*, **54**, 871–896.

Drinkwater, M. R., 1996: Satellite microwave radar observations of climate-related sea-ice anomalies. *Workshop on Polar Processes and Climate Change*, Cancun, Mexico, Amer. Meteor. Soc., Boston, MA, 115–118.

Flanagan, J. D., T. Radko, W. Shaw, and T. Stanton, 2014: Dynamic and double-diffusive instabilities in a weak pycnocline: Part II, Direct numerical simulations and flux laws. *J. Phys. Oceanogr.*, **44**, 1992–2012.

Gargett, A. E., and G. Holloway, 1992: Sensitivity of the GFDL ocean model to different diffusivities for heat and salt. *J. Phys. Oceanogr.*, **22**, 1158–1177.

Gent, P., and J. McWilliams, 1990: Isopycnal mixing in ocean circulation models. *J. Phys. Oceanogr.*, **20**, 150–155.

Gnanadesikan, A., 1999: A simple predictive model for the structure of the oceanic pycnocline. *Science*, **283**, 2077–2079.

Gordon, A. L., 1978: Deep Antarctic convection west of Maud Rise. *J. Phys. Oceanogr.*, **8**, 600–612.

Gordon, A. L., 1981: Seasonality of southern ocean sea ice. *J. Geophys. Res.*, **86**(C5), 4193–4197.

Gordon, A. L., and B. A. Huber, 1984: Thermohaline stratification below the Southern Ocean sea ice. *J. Geophys. Res.*, **89**(C1), 641–648.

Gordon, A. L., and B. A. Huber, 1990: Southern Ocean winter mixed layer. *J. Geophys. Res.*, **95**(C7), 11,655–11,672.

Hallberg, R., & A. Gnanadesikan, 2006: The role of eddies in determining the structure and response of the wind-driven southern hemisphere overturning: results from the Modeling Eddies in the Southern Ocean (MESO) project. *J. Phys. Oceanogr.*, **36**, 2232–2252.

Hibler, III, W. D., 1979: A dynamic thermodynamic sea ice model. *J. Phys. Oceanogr.*, **9**, 815–846.

Holland, D. M., 2001: Explaining the Weddell Polynya: A large ocean eddy shed at Maud Rise. *Science*, **292**, 1697–1700.

Knauss, J. A., 1997: *Introduction to Physical Oceanography*. Prentice Hall, 320 pp.

Large, W. G., J. C. McWilliams, and S. C. Doney, 1994: Oceanic vertical mixing: a review and a model with a nonlocal boundary layer parameterization. *Rev. Geophys.*, **32**, 363–403.

Large, W. G., G. Danabasoglu, S. C. Doney, and J. C. McWilliams, 1997: Sensitivity to surface forcing and boundary layer mixing in a global ocean model: Annual-mean climatology. *J. Phys. Oceanogr.*, **27**(11), 2418–2447.

Lindsay, R. W., R. Kwok, L. de Steur, and W. Meier, 2008: Halo of ice deformation observed over the Maud Rise seamount. *Geophys. Res. Lett.*, **35**, L15501, doi: 10.1029/2008GL034629.

Lindsay, R. W., D. M. Holland, and R. A. Woodgate, 2004: Halo of low ice concentration observed over the Maud Rise seamount. *Geophys. Res. Lett.*, **31**, L13302, doi: 10.1029/2004GL019831.

Luyten, J. R., J. Pedlosky, and H. Stommel, 1983: The ventilated thermocline. *J. Phys. Oceanogr.*, **13**, 292–309.

Malkus, W. V. R., and G. Veronis, 1958: Finite amplitude cellular convection. *J. Fluid Mech.*, **4**, 225–260.

Manabe, S., K. Bryan, and M. J. Spelman, 1979: A global ocean-atmosphere climate model with seasonal variation for future studies of climate sensitivity. *Dyn. Atmos. Oceans*, **3**, 393–426.

Marshall, J., A. Adcroft, C. Hill, L. Perelman, and C. Heisey, 1997a: A finite-volume, incompressible Navier Stokes model for studies of the ocean on parallel computers. *J. Geophys. Res.,* **102** (C3), 5753–5766.

Marshall, J., C. Hill, L. Perelman, and A. Adcroft, 1997b: Hydrostatic, quasi-hydrostatic, and nonhydrostatic ocean modeling. *J. Geophys. Res.*, **102**(C3) 5733–5752.

Martinson, D. G., 1990: Evolution of the Southern Ocean winter mixed layer and sea ice: open ocean deepwater formation and ventilation. *J. Geophys. Res.*, **95**, 11641–11654.

Martinson, D. G., P. D. Killworth, and A. L. Gordon, 1981: A convective model for the Weddell Polynya. *J. Phys. Oceanogr.*, **11**, 466–488.

McDougall, T. J., 1987: Thermobaricity, cabbeling, and water-mass conversion. *J. Geophys. Res.*, **92**, 5448–5464.

McDougall, T. J., D. R. Jackett, D. G. Wright, and R. Feistel, 2003: Accurate and computationally efficient algorithms for potential temperature and density of seawater. *J. Atmos. Ocean. Technol.*, **20**, 730–741.

McPhee, M. G., C. Kottmeier, and J. H. Morison, 1999: Ocean heat flux in the central Weddell Sea during winter. *J. Phys. Oceanogr.*, **29**, 1166–1179.

McPhee, M. G. and the MaudNESS Science Group, 2006: The Maud Rise Nonlinear Equation of State Study (MaudNESS) in the Eastern Weddell Sea, Antarctica. Eos, **87**, Ocean Sciences Meeting Supplement, Abstract OS46B-01.

Merryfield, W. J., G. Holloway and A. E. Gargett, 1999: A global ocean model with double-diffusive mixing. *J. Phys. Oceanogr.,* **29**, 1124–1142.

Muench, R. D., J. H. Morison, L. Padman, D. Martinson, P. Schlosser, B. Huber, and R. Hohmann, 2001: Maud Rise revisited. *J. Geophys. Res.*, **106**, 2423–2440.

Munk, W., 1966: Abyssal recipes. *Deep-Sea Res.*, **13**, 707–730.

Munk, W., and C. Wunsch, 1998: Abyssal recipes II: energetics of tidal and wind mixing. *Deep-Sea Res. I*, **45**, 1977–2010.

Parkinson, C. L., and W. M. Washington, 1979: A large-scale model of sea ice. *J. Geophys. Res.*, **84**(C1), 311–337.

Pedlosky, J., 1987: *Geophysical Fluid Dynamics*, Springer, 710 pp.

Radko, T., 2003: A mechanism for layer formation in a double-diffusive fluid. *J. Fluid Mech.*, **497**, 365–380.

Radko, T., 2005: What determines the thickness of layers in a thermohaline staircase? *J. Fluid Mech.*, **523**, 79–98.

Radko, T., 2007a: Mechanics of merging events for a series of layers in a stratified turbulent fluid. *J. Fluid Mech.*, **577**, 251–273.

Radko, T., 2007b: A mechanism for establishment and maintenance of the meridional overturning in the upper ocean. *J. Mar. Res.*, **65**, 85–116.

Radko, T., 2013: *Double-Diffusive Convection*. New York: Cambridge University Press, 342 pp.

Radko, T., and J. Marshall, 2004: Eddy-induced diapycnal fluxes and their role in the maintenance of the thermocline. *J. Phys. Oceanogr.,* **34**, 372–383.

Radko, T., I. Kamenkovich, and P. Dare, 2008: Inferring the pattern of the oceanic meridional transport from the air-sea density flux. *J. Phys. Oceanogr.*, **38**, 2722–2738.

Radko, T., and I. Kamenkovich, 2011: Semi-adiabatic model of the deep stratification and meridional overturning, *J. Phys. Oceanogr.*, **41**, 757–780.

Radko, T., and M. E. Stern, 2011: Finescale instabilities for the double-diffusive shear flow. *J. Phys. Oceanogr.*, **41**, 571-585.

Radko, T. and D. P. Smith, 2012: Equilibrium transport in double-diffusive convection. *J. Fluid Mech.*, **692**, 5–27.

Rhines, P. B., and W. R. Young, 1982: A theory of the wind-driven circulation. Part I: Mid-ocean gyres. *J. Mar. Res.,* **40** (Suppl), 559–596.

Robinson, A. R., and H. Stommel, 1959: The oceanic thermocline and the associated thermohaline circulation. *Tellus*, **11**, 295–308.

Ruddick, B., 1983: A practical indicator of the stability of the water column to double-diffusive activity. *Deep-Sea Research,* **30***,* 1105–1107.

Salmon, R., 1990: The thermocline as an internal boundary layer. *J. Mar. Res.*, **48**, 437–469.

Samelson, R. M., and G. K. Vallis, 1997: Large-scale circulation with small diapycnal diffusion: The two-thermocline limit. *J. Mar. Res.*, **55**, 223–275.

Schmitt, R. W., 1979a: The growth rate of supercritical salt fingers. *Deep-Sea Research,* **26A***,* 23–44.

Schmitt, R.W., 1979b: Flux measurements in an interface. *J. Mar. Res.* **37***,* 419–436

Schmitt, R. W., 1981: Form of the temperature-salinity relationship in the central water: Evidence for double-diffusive mixing. *J. Phys. Oceanogr.*, **11**, 1015–1026.

Schmitt, R. W., 1994: Double diffusion in oceanography. *Annu. Rev. Fluid Mech.*, **26**, 255–285.

Schmitt, R. W., 2003: Observational and laboratory insights into salt finger convection. *Prog. Oceanogr.,* **56**, 419–433.

Schmitt, R. W., H. Perkins, J. D. Boyd, and M. C. Stalcup, 1987: C-SALT: an investigation of the thermohaline staircase in the western tropical North Atlantic. *Deep-Sea Res.*, **34**, 1697–1704.

Schmitt, R. W., J. R. Ledwell, E. T. Montgomery, K. L. Polzin, and J. M. Toole, 2005: Enhanced diapycnal mixing by salt fingers in the thermocline of the tropical Atlantic. *Science*, **308**, 685–688.

Semtner, Jr., A. J., 1976: A model for the thermodynamic growth of sea ice in numerical investigations of climate. *J. Phys. Oceanogr.*, **6**, 379–389.

Shaw, W. and T. Stanton, 2014: Dynamic and double-diffusive instabilities in a weak pycnocline: Part I, Observations of heat flux and diffusivity in the vicinity of Maud Rise, Weddell Sea. *J. Phys. Oceanogr.*, **44**, 1992–2012.

Smedsrud, L. H., and T. Martin, 2015: Grease ice in basin-scale sea-ice ocean models. *Annals of Glaciology*, **56**(69), 295–306.

St. Laurent, L., and R. W. Schmitt, 1999: The contribution of salt fingers to vertical mixing in the North Atlantic tracer release experiment. *J. Phys. Oceanogr.,* **29***, 1404–1424.

Stern, M. E., T. Radko, and J. Simeonov, 2001: 3D salt fingers in an unbounded thermocline with application to the Central Ocean. *J. Mar. Res.*, **59**, 355–390.

Timmermann, R., P. Lemke, C. Kottmeier, 1999: Formation and maintenance of a polynya in the Weddell Sea. *J. Phys. Oceanogr.*, **29**, 1251–1264.

Toggweiler, J. R., and B. Samuels, 1998: On the ocean's large-scale circulation near the limit of no vertical mixing. *J. Phys. Oceanogr.*, **28**, 1832–1852.

Turner, J. S., 1973: *Buoyancy Effects in Fluids*. New York: Cambridge University Press, 382 pp.

Walsh, D., and B.R. Ruddick, 2000: Double-diffusive interleaving in the presence of turbulence: the effect of a nonconstant flux ratio. *J. Phys. Oceano*gr., **30**, 2231–2245.

Welander, P., 1971: The thermocline problem. *Philos. Trans. R. Soc. London Ser.* **A.270**, 69–73.

Welander, P., 1986: Thermohaline effects in the ocean circulation and related simple models. in *Large-Scale Transport Processes in Oceans and Atmosphere*, ed. J. Willebrand and D. L. T. Anderson, 163–200. Dordrecht: Reidel.

Whitehead, J. A., 1995: Thermohaline ocean processes and models. *Annu. Rev. Fluid Mech.*, **27**, 89–113.

Wunsch, C., and R. Ferrari, 2004: Vertical mixing, energy, and the general circulation of the oceans. *Ann. Rev. Fluid. Mech.*, **36**, 281–314.

You, Y., 2002: A global ocean climatological atlas of the Turner angle: Implications for double-diffusion and water mass structure. *Deep-Sea Res.*, **49**, 2075–2093.

Zhang, J., R. W. Schmitt, and R. X. Huang, 1998: Sensitivity of GFDL Modular Ocean Model to the parameterization of double-diffusive processes. *J. Phys. Oceanogr.,* **28***, 589–605.

INITIAL DISTRIBUTION LIST

1.   Defense Technical Information Center
        Ft. Belvoir, Virginia

2.   Dudley Knox Library
        Naval Postgraduate School
        Monterey, California